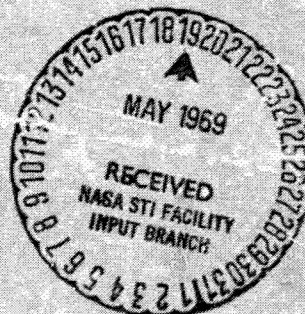


PHASE I/FINAL REPORT  
**STUDY OF A LOW ALTITUDE SATELLITE  
UTILIZING A DATA RELAY SATELLITE SYSTEM**

21 JANUARY 1969

Contract No. NAS 3-11605

Prepared By:  
Project Manager/Dennis Eggert  
Hughes Aircraft Company  
Space Systems Division  
Goddard Space Flight Center  
Greenbelt, Maryland



N69-24921

(ACCESSION NUMBER)	(THRU)
531	
(PAGE)	(CODE)
CR 110341	31
(NASA CR OR TMX OR AD NUMBER)	(CATEGORY)

**PHASE I/FINAL REPORT**  
**STUDY OF A LOW ALTITUDE SATELLITE**  
**UTILIZING A DATA RELAY SATELLITE SYSTEM**

**21 JANUARY 1969**

**Contract No. NAS 5-11602**

**Goddard Space Flight Center  
Contracting/Grafton Young  
Technical Monitor/Sheldon Wishna**

**Prepared By:**  
**Project Manager/Dennis Eggert**  
**Hughes Aircraft Company**  
**Space Systems Division**  
**For**  
**Goddard Space Flight Center**  
**Greenbelt, Maryland**





PRECEDING PAGE BLANK NOT FILMED.

## CONTENTS

	<u>Page</u>
1. INTRODUCTION	1-1
2. MISSIONS AND SENSORS	
2.1 Introduction	2-1
2.2 Missions	2-2
2.2.1 Earth Observation Data	2-2
2.3 Sensors	2-8
2.3.1 Optical Imaging	2-8
2.3.2 APT Camera	2-9
2.3.3 Radar Scatterometer	2-12
2.3.4 Synthetic Aperture Radar	2-12
2.3.5 Laser Altimeter	2-13
2.3.6 Remote Instrument Interrogation	2-14
2.3.7 Sensor Combination	2-14
2.4 Spacecraft Considerations	2-15
3. ORBITAL ANALYSIS AND GEOMETRICAL CONSIDERATIONS	
3.1 Introduction	3-1
3.2 Sun-Synchronous Orbit	3-3
3.2.1 Attitude and Inclination for Sun-Synchronous Orbit	3-3
3.2.2 Solar Eclipse	3-5
3.3 Global Coverage	3-9
3.3.1 Orbital Parameters for Sun-Synchronous Orbits	3-9
3.4 Orbital Information	3-19
3.4.1 Orbital Period and Velocity	3-19
3.4.2 Ground Velocity of Subsatellite Point	3-19
3.4.3 Range and Range Rate	3-20
3.4.4 Number of Orbits per Day	3-21
3.5 LAS-DRS Visibility	3-24
3.5.1 LAS Visibility by Single DRS	3-24
3.5.2 Two Data Relay Satellites - One Ground Station	3-27
3.5.3 Comment	3-30
3.6 Coordinate Systems	3-31
3.6.1 Inertial Reference ( $x, y, z$ )	3-31
3.6.2 Orbital Reference ( $i, j, k$ )	3-31
3.6.3 Body Reference ( $xyz$ )	3-31



3.6.4	Geomagnetic Reference ( $x_m, y_m, z_m$ )	3-31
4.	ANTENNA POINTING	
4.1	Introduction	4-1
4.2	Number of Antennas and Mounting Considerations	4-3
4.2.1	Continuous Data -- Two Antennas	4-3
4.2.2	Noncontinuous Data -- One Antenna	4-7
4.3	Gimbaling	4-11
4.3.1	Two-Gimbal Axes	4-11
4.3.2	Three-Gimbal System	4-19
4.3.3	Comment	4-21
4.4	Mathematical Gimbal Analysis	4-22
4.4.1	Line-of-Sight Vector	4-22
4.4.2	Three Gimbal -- Solar Panel-Mounted Antenna	4-23
4.4.3	Body-Mounted, Two-Gimbal Antennas	4-32
4.5	Antenna Steering	4-39
4.5.1	Continuous Ground Control	4-39
4.5.2	Updated Program	4-40
4.5.3	Autotrack With Ground-Controlled Changeover	4-40
4.5.4	Completely Automatic	4-41
4.6	Acquisition	4-42
4.7	Antenna-Spacecraft Dynamical Interaction	4-43
4.8	Recommendations	4-45
4.8.1	Two Antennas -- Continuous Data	4-45
4.8.2	One Antenna -- Interrupted Data	4-45
5.	ANTENNAS	
5.1	Introduction	5-1
5.2	Electronically Scanned Versus Mechanically Steered Antenna	5-2
5.2.1	Radiating Structure	5-2
5.2.2	Feed Network	5-3
5.2.3	Phase Shifters	5-3
5.2.4	Scan Controller	5-3
5.2.5	Quantitative Comparison -- Hemispherical Coverage	5-5
5.2.6	Conclusion	5-10
5.3	Planar Array of Slotted Waveguides	5-11
5.3.1	Description	5-11
5.3.2	Electrical Properties	5-11
5.3.3	Mechanical Properties	5-19
5.3.4	Effects of Tracking Method on Antenna Design	5-20
5.4	Arrays of Helical Radiators	5-22
5.4.1	Description	5-22
5.4.2	Electrical Properties	5-22
5.4.3	Mechanical Properties	5-31
5.4.4	Effects of Tracking Method on Antenna Design	5-34

5.5	Paraboloidal Reflectors and Feeds	5-35
5.5.1	Description	5-35
5.5.2	Electrical Properties	5-35
5.5.3	Mechanical Properties	5-41
5.5.4	Effects of Tracking Method on Antenna Design	5-41
5.5.5	Cassegrain Systems	5-41
5.6	Rectangular Horns	5-45
5.6.1	Description	5-45
5.6.2	Electrical Properties	5-45
5.6.3	Mechanical Properties	5-49
5.6.4	Effects of Tracking Method on Antenna Design	5-49
5.7	Comparison and Comments	5-52
5.8	References	5-58
6.	COMMUNICATIONS	
6.1	Introduction	6-1
6.2	Carrier Frequency	6-1
6.3	Range Equation	6-3
6.4	Information (Baseband) Structure	6-4
6.5	System Noise	6-7
6.5.1	Background Radiation -- External Noise	6-7
6.5.2	Internal Noise	6-7
6.6	Modulation Techniques	6-8
6.7	Frequency Division Multiplex/Frequency Modulation (FDM/FM)	6-8
6.8	Digital Transmission	6-13
6.9	DRS-LAS Broad Coverage Link	6-14
6.10	References	6-16
7.	CONTROL	
7.1	Introduction	7-1
7.2	Basic Attitude Control Concepts	7-2
7.2.1	Gravity-Gradient Stabilization	7-2
7.2.2	Mass Expulsion	7-2
7.2.3	Magnetic Control	7-2
7.2.4	Reaction Wheel System	7-2
7.2.5	Spin Stabilization	7-2
7.2.6	Momentum Bias System Type 1	7-3
7.2.7	Momentum Bias System Type 2	7-3
7.3	Disturbance Torques	7-4
7.3.1	Solar Radiation Torques	7-4
7.3.2	Aerodynamic Torque	7-5
7.3.3	Gravity-Gradient Torques	7-7
7.3.4	Magnetic Torques	7-9
7.3.5	Comments	7-10
7.4	Gravity-Gradient Control	7-11
7.4.1	Gravity-Gradient Torques	7-11

7.4.2	Control	7-11
7.4.3	Pointing Capability	7-12
7.5	Magnetic Torque Control	7-13
7.5.1	Earth's Magnetic Field	7-13
7.5.2	Magnetic Control Concepts	7-20
7.5.3	Implementation	7-23
7.5.4	Control Capability	7-25
7.6	Mass Expulsion Control	7-30
7.6.1	Specific Impulse and Propellants	7-30
7.6.2	Minimum Fuel Consumption	7-31
7.6.3	Impulsive Systems	7-31
7.6.4	System Implementation	7-34
7.7	Reaction Wheel Stabilization	7-35
7.7.1	Calculation of Wheel Inertia and Weight	7-37
7.7.2	Power Consumption	7-41
7.7.3	Motor Characteristics	7-43
7.7.4	System Implementation	7-43
7.8	Momentum Bias System Type 1	7-44
7.8.1	General Description and Stability	7-44
7.8.2	Despin Control System (DCS)	7-47
7.8.3	Velocity and Attitude Control	7-49
7.8.4	Pointing Accuracy	7-58
7.9	Momentum Bias System Type 2	7-62
7.9.1	Power Requirements	7-64
7.10	Comparison and Comments	7-65
7.11	References	7-68
8.	SUBSYSTEMS	
8.1	Telemetry and Command	8-1
8.2	Thermal Control	8-4
8.2.1	Thermal Control System Selection	8-4
8.2.2	High Internal Power Density	8-5
8.2.3	Infrared Camera Requirements	8-5
8.2.4	Ground Versus Automatic Control	8-5
8.3	Power System	8-7
8.3.1	Solar Array	8-7
8.3.2	Solar Array Steering System	8-7
8.3.3	Batteries	8-9
8.3.4	Charge-Discharge Controller	8-9
9.	CONFIGURATION	9-1
10.	CONCLUSIONS AND RECOMMENDATIONS	
10.1	Mission, Sensors, and Data Baseband	10-1
10.2	LAS-DRSS Visibility	10-1
10.3	Antenna Pointing	10-2
10.4	Antennas	10-3
10.5	Communications	10-4

10.6	Attitude Control	10-7
10.7	Subsystems	10-8
10.8	Configuration	10-10
GLOSSARY		G-1
APPENDIX I.	SOLAR RADIATION FORCES	I-1
APPENDIX II.	COMMUNICATION SYSTEM TECHNICAL ANALYSIS	II-1
APPENDIX III.	GRAVITY – GRADIENT TORQUES	III-1

## ILLUSTRATIONS

		Page
1	General LAS-DRSS Orbital Relationship	1-2
2	Resolution Versus Data Rate and Earth Coverage	2-6
3	Scan Pattern of Multispectral Scanning Camera	2-10
4	Synthetic Aperture Radar	2-13
5	Improved Thor-Delta Booster Shroud	2-15
6	Sun-Synchronous Orbit	3-2
7	Attitude and Inclination for Sun-Synchronous Orbit	3-2
8	Orbital Eclipse as Function of Orbit Normal/ Sunline Angle, $\lambda$	3-4
9	Portion of Orbit Eclipsed as Function of Angle, $\phi$ , Between Line of Nodes and Sun	3-4
10	Three-Dimensional Earth-Orbit-Sun Geometry	3-4
11	Two-Dimensional Earth-Orbit Geometry	3-4
12	Orbit-Sun Geometry	3-6
13	Swath and Equator	3-8
14	Earth Coverage Time	3-8
15	Earth Coverage Time as Function of Swath Width and Altitude	3-8
16	Equator Crossing Separation, $D$ , Versus Altitude	3-12
17	$dh/dD$ as Function of Altitude	3-12
18	$\Delta h_n$ as Function of $W_{eff}$ for Various Values of $n$	3-14
19	Equator Orbit Crossings	3-14
20	Example of Nonrelative Prime Numbers	3-18
21	$V_o$ and $T_o$ as Function of Altitude	3-18
22	Subsatellite Velocity Versus Altitude	3-22
23	Range and Range Rate Worst Case	3-22
24	Maximum Synchronous Satellite Range as Function of Circular Orbit Altitude	3-22
25	Number of Orbits Per Day as Function of Altitude	3-22
26	DRS Eclipse Worst-Case Geometry	3-24
27	LAS Eclipse by Earth From DRS	3-26
28	Angle Between DRS-Earth Line and LAS Line of Nodes for Complete Visability	3-26
29	Minimum Visibility of LAS by DRS	3-26
30	Geometry for Two DRSs and One Ground Station	3-28
31	$2Y$ and $\eta$ as Function of Altitude	3-28
32	Ground Elevation Angle Versus DRS Separation Angle	3-28



33	Geometry for Ground Station Not Located on Equator	3-28
34	Orbital and Inertial Reference Coordinate Systems	3-32
35	Magnetic and Inertial Reference Coordinate Systems	3-32
36	Orbital and Body Reference Coordinate Systems With Euler Angles	3-34
37	Necessity for Changeover	4-2
38	Sides of Earth-Oriented Body Available for Antenna Mounting	4-2
39	Possible Ways to Mount Two Antennas on Three-Axis Stabilized Solar Panels	4-4
40	Four Sides Available for Antenna Mounting	4-6
41	Two Antennas Mounted on MBS Type 1 Solar Panel	4-6
42	Alternate Configuration - Solar Panel Next to Earth-Oriented Body	4-6
43	Pointing a Single Antenna	4-6
44	Spacecraft Interference Forcing Changeover at Undesirable Orbit Position for Mounting as Shown	4-6
45	Worst-Case Geometry for Pointing Antenna Mounted to Side 4	4-8
46	Single Antenna Mounting Possibilities - MBS Type 1	4-8
47	Gimbal System Schemes	4-10
48	Geometric Determination of Gimbal Rates	4-10
49	Primary Gimbal Axis Rate Increase When LOS and Primary Axis Are in Close Proximity	4-10
50	Three Components of LOS-LAS Relative to Angular Velocity	4-12
51	Geometry for Maximum Magnitude of $\omega_L$	4-12
52	Polar Orbit With Primary Gimbal Axis Normal to LAS Orbit Plane and LOS and Primary Axis Nearly Coinciding	4-16
53	Geometry for Maximum LAS Orbit Inclination With Primary Gimbal Axis Normal to Orbit Plane	4-16
54	Polar Orbit With Primary Axis in LAS Orbit Plane	4-16
55	Polar Orbit and Worst-Case Geometry for Determining Closest Angular Approach of LOS and $g_1$	4-18
56	Pointing Vector Distances and Orbital Parameters	4-24
57	Solar Panel - Mounted Antenna Geometry	4-24
58	Two Geometrical Situations for Determining Maximum Angular Motion	
59	Two Gimbaling Schemes for Solar Panel- Mounted Antennas	4-26
60	Solar Panel Coordinates	4-26
61	Definition of Gimbal Angles	4-31
62	Antenna Pointing Angle in LAS Orbit Plane for Body-Mounted Antenna	4-34
63	Primary Axes in Orbit Plane for Avoiding Large Gimbal Rates	4-34
64	Two Orbit-Plane Gimbal Axes	4-34

65	Antenna Changeover Sequence for Two Antennas	4-35
66	Geometry of Primary Axis Normal to Orbit Plane	4-35
67	Body and Gimbal Axis Coordinates	4-38
68	Five Square Arrays Arranged on Frustum of Pyramid	5-4
69	Block Diagram of Phase Scanned Array Antenna System	5-4
70	X-Band Planar Array	5-12
71	Corporate Feed for One Quadrant of Planar Array Antenna	5-12
72	Typical H-Plane Power Divider	5-12
73	Square Planar Array Aperture Size Versus Antenna Gain	5-14
74	Antenna Gain Loss Versus Frequency	5-14
75	3-dB Beamwidth Versus Antenna Gain for Square Aperture With Uniform Illumination	5-14
76	Pattern of Uniformly Illuminated Square Aperture of Dimension L on a Side	5-15
77	Polarizing Sheets for Panel Polarization Converter	5-16
78	Panel Polarization Converter Configuration	5-16
79	Axial Ratio Versus Frequency Bandwidth	5-16
80	Typical Loop-Slot Configuration for Circular Polarization	5-16
81	Weight as Function of Antenna Gain for Square Aperture	5-18
82	Operation (on Reception) of Monopulse Sum and Difference Network	5-21
83	Helix Length as Function of Number of Helices, With Gain as Parameter	5-25
84	Array Gain as Function of Number of Helices for Array Diagonal Equal to Helix Length	5-25
85	Length of Helix and Array Diagonal as Function of Array Gain	5-26
86	Allowable Upper and Lower Limits of Helix Circumference as Function of Helix Length	5-26
87	Gain of Four-Helix Array as Function of Frequency	5-26
88	Patterns for Four-Element Array	5-29
89	Patterns for Seven-Element Array	5-29
90	3-dB Beamwidth Versus Antenna Gain for Square Array of Helices With Uniform Excitation	5-30
91	Five Bifilar Helix Array Axial Ratio as Function of Frequency Normalized to Transmit Frequency	5-30
92	Average Power Handling Capability of 50-ohm Line With Rexolite Dielectric as Function of Frequency	5-30
93	Helix Antenna -- UHF	5-32
94	High Frequency Helix Winding Support	5-32
95	Weight of Array of Helices as Function of Gain	5-33
96	Bifilar Helix Array	5-33
97	Seven-Helix Array	5-33
98	Paraboloidal Reflector and Feed	5-38
99	Aperture Size Versus Antenna Gain for Circular Aperture	5-38

100	Relative Efficiency of Reflector and Feed as Function of Frequency	5-39
101	Relative Gain of Reflector and Feed as Function of Frequency	5-39
102	3-dB Beamwidth as Function of Antenna Gain for Circular Aperture With 10-dB Taper	5-39
103	Pattern of Circular Aperture With 10-dB Parabolic Amplitude Taper Across Aperture	5-40
104	Aperture Blockage Effect on Sidelobe Level and Gain	5-40
105	Surveyor Altitude Marking Radar Reflector	5-42
106	Weight Versus Antenna Gain for Paraboloidal Reflector and Feed	5-43
107	Circularly Polarized Fin-Loaded Horn	5-45
108	Horn Length Versus Gain	5-46
109	Length of Horn, Polarizer, Load, and Transition Versus Gain	5-47
110	Aperture Side Dimension Versus Gain	5-48
111	Relative Gain of Optimum Horn as Function of Frequency	5-50
112	3-dB Beamwidth Versus Gain for Horn Antenna With Equal E- and H-Plane Beamwidths	5-50
113	E-Plane and H-Plane Patterns of Optimum Horn	5-50
114	Honeycomb Structural Material	5-50
115	Estimated Weight Versus Gain of Horn Antennas	5-51
116	Comparison of Antenna Size	5-53
117	Antenna Comparison	5-55
118	Weight Comparison	5-56
119	Communication Link	6-2
120	LAS-DRS Link	6-5
121	LAS EIRP Versus System Capacity	6-5
122	Data Link Model	6-6
123	LAS-DRS Link FDM/FM Modulation	6-10
124	Carrier-to-Noise Density, Bit Versus Rate	6-13
125	Low Data Rate Link	6-14
126	Broad Coverage Link	6-15
127	Reflection Geometry	7-6
128	Earth's Magnetic Field Magnitude Versus Altitude	7-8
129	Magnetic Cartesian and Spherical Coordinates	7-14
130	Coordinate Systems	7-14
131	Vector Relationships With Magnetic Torque Control Law	7-22
132	Magnetic Torquing Systems	7-24
133	G (3) Versus $\beta$	7-29
134	H (3) Versus $\beta$	7-29
135	One-Sided Limit Cycle	7-33
136	Two-Sided, Hard Limit Cycle	7-33
137	Mass Expulsion Control Block Diagram	7-34
138	Simplified Arrangement of Flywheels	7-36

139	Block Diagram of Single-Axis Flywheel Control System	7-36
140	Block Diagram of Single-Axis Dual-Mode Control System	7-38
141	Wheel Moment of Inertia Versus Unloading Interval for Various Disturbance Torques	7-40
142	Inertial Wheel Total Unit Weight Versus Rotating Parts Inertia	7-40
143	Wheel Assembly Weight Versus Unloading Interval for Various Disturbance Torques	7-40
144	Power Versus Motor Speed for Typical Inertia Wheel	7-40
145	Three-Axis Attitude and Velocity Control for Reaction Wheel Control	7-42
146	Representative Stabilization and Control Block Diagram Illustrating Crosscoupling	7-48
147	Typical Despin Control System Functional Block Diagram	7-48
148	Functional Block Diagram of Velocity and Attitude Control Subsystem	7-50
149	Ground Command Mode Block Diagram	7-52
150	Block Diagram of Autonomous On-Board Attitude Control System for MBS Type 1	7-52
151	On-Board Velocity and Attitude Control System Block Diagram	7-56
152	Momentum Wheel Sizing	7-64
153	Inertial Wheel Momentum Required to Limit Pointing Error Rate	7-64
154	Command System Simplified Block Diagram	8-2
155	Command Word Format	8-2
156	Solar Array Performance in Orbit	8-6
157	Gross Weight Efficiency for State-of-the-Art Solar Arrays	8-6
158	Average Silver-Cadmium Cell Voltage Versus Cycle as Function of Temperature	8-8
159	Estimated Open Circuit Stand Loss for Silver-Cadmium Batteries	8-8
160	Battery Capacity Versus Temperature	8-8
161	Silver-Cadmium Battery Weight Versus Capacity	8-8
162	MBS Type 1 With Two Platform-Mounted Antennas	9-3
163	Three-Axis Stabilized With Two Body-Mounted Antennas	9-4
164	MBS Type 1 With One Body-Mounted Antenna	9-5
165	Three-Axis Stabilized With Two Solar Panel-Mounted Antennas	9-6
I-1	Radiation-Surface Geometry	I-4
I-2	Cosine Law Diffusion Pattern	I-4
I-3	Pressure Geometry	I-4
I-4	Element of Hemispherical Surface	I-6
I-5	Solar Radiation Pressure Computation Flow	I-10

II-1	Lines of Constant Carrier-to-Noise Ratio	II-1
II-2	Possible Baseband for Data From LAS	II-5
II-3	Noise Approximation	II-12
II-4	Phasor Diagram of Carrier Plus Noise for Some Time, $t$	II-12
II-5	Noise Voltage and Power Spectrum at Output of Carrier Demodulator	II-16
II-6	Carrier Postdetection Spectrum With $i$ Modulating Channels	II-19
II-7	Antenna and Energy Source	II-26
II-8	Solar Radiation Flux Density Versus Frequency	II-26
III-1	General Gravity-Gradient Geometry	III-2
III-2	Orbital Coordinates	III-2



## TABLES

	<u>Page</u>
1 Applications of Earth Observation Data	2-4
2 Candidate LAS Sensor Characteristics	2-11
3 Spacecraft Weight and Power Estimates	2-16
4 Characteristics of 20 dB and 40 dB Planar Arrays to be Utilized in Hemispherical Coverage Scanned Antenna Array	5-6
5 Electronically Scanned Antenna Estimates	5-10
6 Mechanically Steered Antenna Estimates	5-10
7 Array Characteristics	5-34
8 Receiver Noise Figures and Noise Temperatures	6-7
9 Summary of LAS-DRS Link FDM/FM Modulation (DRS Antenna Gain Assumed Constant at 40 dB)	6-11
10 Summary of LAS-DRS Link FDM/FM Modulation (Varying DRS Antenna Gain)	6-12
11 Basic Attitude Control	7-3
12 Summary of DCS Operational Modes	7-49
13 Attitude Control Components	7-54
14 Attitude Control Mode Tradeoff Summary	7-57
15 Along-Track Pointing Error	7-59
16 Crosstrack Pointing Error	7-59
17 Three Viable Stabilization Methods	7-66
18 Attitude Control System Comparison	7-67
19 Attitude Control System Comparison Summary	7-67
20 Command Subsystem Weight, Power, and Volume	8-3
21 Summary of LAS-DRS Link FDM/FM Modulation (DRS Antenna Gain Assumed Constant at 40 dB)	10-5
22 Summary of LAS-DRS Link FDM/FM Modulation (Varying DRS Antenna Gain)	10-6
23 Attitude Control System Comparison	10-9
24 Attitude Control System Comparison Summary	10-9
II-1 Summary of Values used in Figure 123	II-8

## 1. INTRODUCTION

This document is a report of the results of Phase I of the Study of a Low Altitude Satellite Utilizing a Data Relay Satellite System conducted by Hughes Aircraft Company Space Systems Division for the National Aeronautics and Space Administration, Goddard Space Flight Center, under Contract NAS 5-11602.

The purpose of this 1-year study (19 July 1968 to 19 July 1969) is to investigate the technical considerations associated with a low altitude satellite (LAS) operating in conjunction with a data relay satellite system (DRSS). The study is being conducted in two phases. Phase I consists of analysis and trade studies dealing with LAS-DRSS communication and with LAS subsystems. Phase II consists of a spacecraft conceptual design based upon the results of Phase I.

The basic spatial relationships of an LAS-DRSS system are illustrated in Figure 1. The DRSSs are at geostationary altitude in an equatorial orbit, while the LAS is relatively near the earth. With two or more properly located DRSSs, an LAS is in view of one at all times. Further, all DRSSs can be seen from two ground stations. These properties make an LAS-DRSS system extremely attractive because they offer the potential for continuous communication between the LAS and a small number of ground stations. Two fundamental consequences of the continuous communication capability are:

- 1) Elimination of the need for LAS data storage
- 2) Reduction in the cost of ground tracking by providing continuous command, telemetry, tracking, and experiment data transmission with a small number of ground stations that transmit to and receive from geostationary relay satellites

To take advantage of the continuous communication potential of an LAS-DRSS, the satellites must be able to establish a communication link capable of handling the type and quantity of data required. A number of technical problems for the LAS and DRSS accompany this requirement. This study deals only with the LAS and with the impact on its design of providing the capability of transmitting data to and receiving from a system of DRSSs. In addition, a number of topics relevant to LAS design are presented in this report.

The LAS, in general, is earth-oriented and may have arbitrary orbital inclination. Data quantity requirements, discussed in Section 2, may require the LAS antenna gain to be relatively large — greater than 30 dB. Such an antenna is highly directive and must be steered in some manner to allow data transmission to a DRS. The gain of the antenna, communication system electronics, and antenna steering system are closely interrelated. Antenna size and steering requirements also influence the LAS structural configuration. Just as potent an influence on the configuration, however, is the method of stabilization or attitude control. Thus, there are a number of major areas which influence the LAS design. These study areas of major emphasis include:

- 1) Antenna pointing
- 2) Antennas
- 3) Communication system
- 4) Attitude control

Each of these topics is treated separately in this report, and the interrelationships are discussed.

Design of other spacecraft subsystems may be affected by the relay link. The telemetry and command system, power system, and thermal control system, are discussed briefly in Section 8. To provide a meaningful range of a number of spacecraft subsystems and data parameters, Section 2 deals with LAS missions and sensors. Several topics of general interest in support of the major study areas are treated in Section 3.

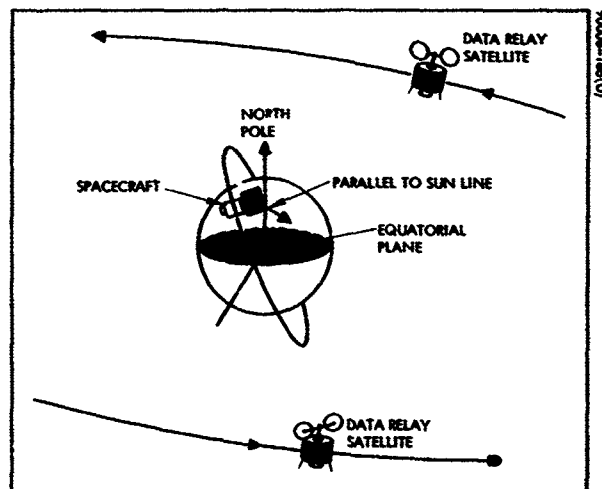


Figure 1. General LAS-DRSS Orbital Relationship

## 2. MISSIONS AND SENSORS

### 2.1 INTRODUCTION

The purpose of this chapter is to discuss potential applications for low-altitude satellites (LAS) operating in conjunction with a data relay satellite system (DRSS) in order to develop ranges for parameters associated with various spacecraft systems such as the communication, control, and power systems. A secondary purpose is to provide a completeness to this study by supplying some cogent reasons for employing LASs, and hence provide a partial justification for the study and a stimulus for additional programs and study.

The following section discusses LAS missions, and Section 2.3 deals with sensors associated with some of these missions. Section 2.4 discusses the ramifications of mission and sensor considerations on the spacecraft in terms of weight, power, and size and presents representative values for these parameters for a typical and popular mission.

## 2.2 MISSIONS

Missions for an LAS can be separated into several broad categories. Six of the major areas are listed below.

- 1) Earth observation — This category includes all missions requiring optical or microwave imaging of the earth's surface. High resolution will result in high data rates or, equivalently, large bandwidth.
- 2) Navigation — An LAS may be used as an aid to navigation by ships and aircraft. Furthermore, communication through an LAS/DRS system to a ground station may be more reliable in isolated areas such as midocean locations.
- 3) Science — This mission area includes scientific experiments in the extraterrestrial environment, the testing of new or modified spacecraft subsystem concepts, and astronomical observation.
- 4) Geodesy — Measurements of the earth's magnetic field or, in general, of the near-earth environment or topographical measurements of the earth's surface are examples of missions falling within this category.
- 5) Data collection — One of the most useful missions of an LAS will be the rapid gathering of data from many diverse remote sensors, such as river gauges, rain gauges, buoys, etc. The LAS will interrogate instrument packages on or near the earth's surface and relay the data to a ground station through a DRS.

Of the above missions, earth observation is probably the most popular. And, in general, earth observation data will, because of the large bandwidth required, present the greatest challenge to LAS design for operation with a DRSS. This study addresses itself to LAS design considerations associated with supporting sensors for such a mission and transmitting the data to the ground through a DRSS.

### 2.2.1 Earth Observation Data

In today's complex and highly developed societies, the collection and distribution of information concerning the earth is an increasingly important factor in technologically based economies. In the future, man's need for information will continue to increase as the expanding population and the desire for a better quality of life impose severe demands on the world's resources. Population projections for the United States range from 215 to 240 million for 1975 and from 270 to 380 million for the year 2000. World population by 2000 AD is expected to be above 6.3 billion unless population control methods are made effective. In 1955, the arable land per person



was about 1.25 acres; by 2000, it is expected to decrease to little more than one-half acre per person. Thus, the severe demand on the earth's resources in the future is clear. Information on the extent and distribution of the earth's resources on both a global and regional basis may allow optimum exploitation of these resources.

One of the most promising means of meeting future information requirements economically is a system of operational observation satellites. Carrying sensors at orbital altitudes, such earth observation satellites offer the potential of providing complete surveys of the earth's surface on a synoptic basis and detailed observations of selected areas. The nature of the sensing referred to here is the sensing of reflected or emanated electromagnetic radiation from the ultraviolet through the visible and infrared and into the microwave portion of the electromagnetic spectrum. One major advantage of satellite observation over aircraft or balloon observation is that complete coverage of the earth is possible within a matter of days, depending on the sensor, resolution, and cloud cover. Furthermore, access to some areas by aircraft is prohibited by local governments, but spacecraft are not subject to these restrictions.

A related advantage is that all data from a satellite will be collected by the same set of sensors, thus eliminating the errors due to sensor non-uniformity and calibration discrepancies which arise in aircraft or balloon observation systems.

Preliminary estimates<sup>1</sup> indicate that orbital earth observation will be considerably less expensive than even a single synoptic global coverage with airborne sensors.

Placing sensors in spacecraft precludes the fine resolution possible from lower altitudes. But many of the reasons for observing the entire earth or large portions of it do not require fine resolution. For the recognition of major crop distributions, ocean temperature mapping, and the detection of geologic lineaments, too fine a resolution would give detailed data, somewhat obscuring the desired information. Furthermore, there are many applications for data from presently available sensors.

#### Applications

The potential uses of earth observation data are many and varied. A discussion of some of the more obvious and important ones is given in the University of Michigan report<sup>1</sup>. Table 1, taken from that reference, summarizes the expected areas of application.

---

<sup>1</sup>Peaceful Uses of Earth Observation Spacecraft, Volumes I, II, and III, University of Michigan for NASA, NASA CR-586.

TABLE 1. APPLICATIONS OF EARTH OBSERVATION DATA

<u>Cartography</u>
Map preparation
Map revision
<u>Geographic Studies</u>
Land use studies (current distribution, trends, optimum use)
Urban areas
Rural settlement patterns
Forests
Transportation networks
Proxy measurements of levels of economic activity
Population estimates
<u>Food Resources</u>
Fisheries
Location of fishing grounds
Monitoring of fishing vessels
Agricultural resources
Soil treatment material surveys (limestone, fertilizer, etc.)
Agricultural land use studies
Soil classification and mapping
Soil conservation studies
Studies of site productivity, growth processes
Range management (evaluation of vegetative cover)
<u>Aids to Agricultural Operations</u>
Agricultural census
Crop prediction and control
Agricultural statistics
Crop-control compliance checks
Detection of disease or insect damage
Drought prediction
<u>Forest Resources</u>
Forest inventory
Protection against forest fires
Danger assessment
Early detection
Surveillance
<u>Oil and Mineral Resources</u>
Reconnaissance for new sources

Table 1 (continued)

<u>Wildlife and Recreation-Area Management</u>
Wildlife and waterfowl habitat assessment
Beach-area surveillance (water pollution, wind, and wave action)
Tracking wildlife (caribou, fur seals, African and Australian herd animals)
<u>Water Supply Prediction</u>
Water yield estimates
Streamflow estimates
Soil moisture conditions
Basin geomorphology
Flood prediction, assessment, and control
Prediction of runoff
Delineation of flooded areas
Distribution of water pollutants
<u>Weather Forecasting and Studies of Climatic Trends</u>
Sea surface temperatures
Ocean currents
Forest influences
Vegetative map
Measurement of biomass
Energy budget
Snow, ice, glacier reconnaissance
<u>Air Pollution</u>
Ship routing
Sea-state measurement
Sea-ice reconnaissance
Ship tracking
Sea rescue
<u>Aids to Engineering Projects</u>
Dam-site reconnaissance
Highway routing
<u>Detection of Unknown Archaeological Sites</u>

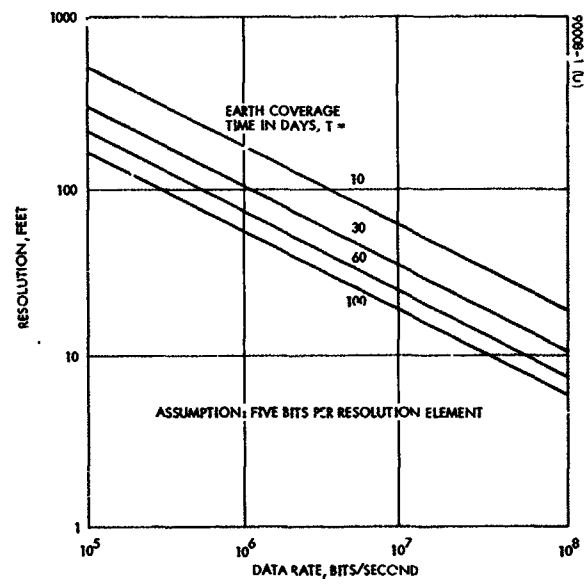


Figure 2. Resolution Versus Data Rate for Earth Coverage

### Resolution and Data

For earth imaging, a basic consideration, independent of the sensor used, is the relationship between ground resolution, earth-coverage time, and data rate. This relationship has an important bearing on the choice of communication equipment, and a brief study will allow ranges for the variables to be determined. There are approximately  $1.97 \times 10^8$  square miles of surface area; thus, if the resolution of a sensor is  $r$  linear feet, then there will be

$$\frac{(1.97 \times 10^8)(2.788 \times 10^7)}{r^2}$$

resolution elements. And if radiance level is encoded into a binary signal of  $b$  bits, then there will be  $(5.5 \times 10^{15}) b/r^2$  bits of information. Now if  $T$  denotes the time in days allowed to cover the entire earth, then the data rate  $D$  in bits per second is given by

$$D = \frac{(5.5 \times 10^{15}) b}{(8.64 \times 10^4) T r^2} = \frac{(6.36 \times 10^{10}) b}{T r^2} \text{ bps} \quad (1)$$

A common and usually adequate number for  $b$  is 5. Substituting this into the above formula

$$D = \frac{3.18 \times 10^{11}}{T r^2} \text{ bps} \quad (2)$$

Thus, if  $r = 100$  feet and  $T = 10$  days,  $D = 3.18 \times 10^6$  bps. Equation 2 is plotted in Figure 2 where it can be seen that for  $T = 30$  days and  $r = 100$  feet,  $D \approx 10^6$  bps.

If imaging in several spectral regions is implemented, the data associated with each spectral band will have a rate similar to the examples above. Thus, for good quality imaging in, say, five to seven spectral regions, a composite data rate of  $10^7$  bps is foreseeable. If higher resolution or shorter coverage time is desired, the data rate could easily increase to  $10^8$  bps or higher.

### Conclusion

The conclusion of importance to this study is that communication system analyses and trades should consider data rates in the range  $10^6$  to  $10^8$  bps or, equivalently, baseband bandwidths of 1 to 50 MHz.



## 2.3 SENSORS

Selection of sensors for the mission of the satellite will depend on the expected areas of data application such as geography, agriculture, forestry, hydrology, oceanography, geology, and meteorology. In this discussion, emphasis is placed on earth observation and data collection sensors since these have the most stringent requirements.

As mentioned previously, the most popular and generally agreed upon information is that obtained by multispectral imaging in the visible and infrared regions of the electromagnetic spectrum. Other techniques for obtaining useful information include radar scatterometry for sea-state determination, radio interrogation of surface sensors, radar mapping to penetrate cloud cover and complement optical imaging and, possibly, laser altimeter sensing for topographical studies and sea-state determination. Sensors and equipment required for these techniques are available, or can be readily developed, and are discussed below. Table 2 lists the sensors considered here and their weight, power, and data characteristics.

### 2.3.1 Optical Imaging

The basic problem in multispectral imaging is simultaneously obtaining the desired coverage and resolution. Film is precluded because of the desire to have the satellite in orbit for 1 or more years. To obtain a picture of an area 100 statute miles wide with 100 to 200-foot resolution requires roughly 3000 to 5000 television lines, compared with the 600 to 800 lines provided by present space TV systems. Two types of sensors currently in development appear to meet the requirements.

The first sensor is an extension of conventional TV techniques called the return beam vidicon, which shows promise of a 3500-TV line limiting resolution in the next year with improvement to more than 5000 lines foreseen for the future. To obtain the multispectral characteristics, three return beam vidicons would be used with a spectral filter in front of each. All three cameras would be simultaneously shuttered for several milliseconds to limit blurring from the motion of the satellite. The primary optics, system shutter, and vidicon tubes would have to be carefully synchronized and aligned so that the three colors could be recombined on the ground. Pictures would be read out from the vidicon surfaces every 24 seconds. In this way, a longitudinal swath of contiguous 100 by 100 statute mile picture frames would be produced.

The second imaging sensor operates on the same principle as the spin-scan camera developed by Hughes for taking color photographs from the Applications Technology Satellite (ATS). This device images a small spot field of view (i. e., 200 by 200 feet as projected on the earth's surface) onto a single-point detector such as a photomultiplier tube or photodiode. Pictures are taken by optically scanning this spot across the orbit track at a rate selected so that the vehicle progress along the track causes consecutive sweeps to be contiguous. The

crosstrack dimension of the picture is due to the optical scan of an oscillating mirror, and the longitude dimension of the picture is due to the satellite's orbit motion. The same 100-statute mile swath as described above would result. This type of imaging is shown schematically in Figure 3. The quality and reliability of this technique are illustrated by the 1-1/2 years of high quality black and white pictures from ATS-I and the 4 months of excellent color pictures from ATS-III.

A significant advantage of the multispectral scanning camera (MSSC) is that it can operate in the near-infrared and infrared regions as well as in the visible region to which the return beam vidicon is constrained. The reason is the optical simplicity of the device, which permits flexibility in adding detectors for operation in the visible and infrared. Hughes has configured a multispectral camera system that will operate in the red, green, 0.7 to 1.2-micron band, and 10-micron infrared band. The latter spectral interval will be of considerable use to earth resources scientists since it permits detection of self-radiation from earth temperature objects. The reference design would produce 900-foot resolution in the 10-micron region with a capability of discriminating 1°C temperature differences.

Detectors for imaging in the infrared must be cooled to temperatures less than 100°K. Coolers of this type have been under development at Hughes for several years. One candidate is a simple radiator that maintains low temperatures by radiating into cold space. The radiation to space method is reliable but entails preferential positioning in the spacecraft to minimize extraneous radiation from warm bodies. Another technique Hughes has developed for military applications is a miniature closed-cycle refrigeration machine. This machine is capable of meeting the infrared detector temperature requirements; its low power and weight and high reliability make it a preferred candidate.

Two versions of the multispectral scanning camera have been proposed. The most advanced version images in seven spectral bands with 70-foot resolution and weighs approximately 230 pounds including the required cooler. The data baseband from this device consists of 80 analog channels requiring 15 MHz bandwidth, and the power consumption is about 100 watts. The other version images in four spectral bands with 100-foot resolution and weighs 67 pounds. Its baseband consists of 28 analog channels requiring a total of 5 MHz bandwidth, and the power consumption is 35 watts. For good quality pictures, both of these cameras require a signal-to-noise ratio of 38 dB rms/rms. However, with a scale changing technique, this may be reduced to 30 dB.

### 2.3.2 APT Camera

The automatic picture transmission (APT) subsystem consists of a camera assembly, electronics module, automatic sync generator, and a VHF transmitter. The APTS is programmed for continuous operational cycles of picture-taking and transmission. The 1-inch vidicon tube is designed for a long-duration storage and slow readout of the cloud cover images viewed by a wide angle lens (108 degrees).

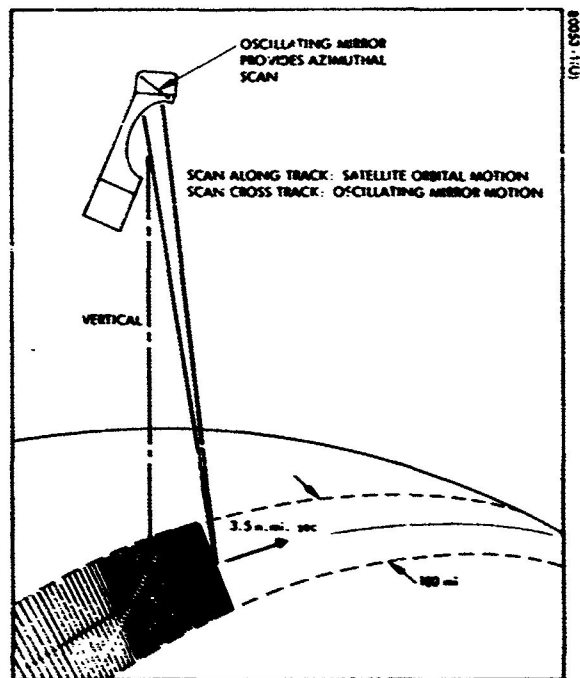


**Figure 3. Scan Pattern of Multispectral Scanning Camera**

TABLE 2. CANDIDATE LAS SENSOR CHARACTERISTICS

Sensor	Load Power, watts	Weight, pounds	Data Baseband	S/N (dB), rms/rms
Multispectral scanning camera (MSSC)				
Seven spectral bands 70-foot resolution limit (with cooler)	100	230	15 MHz	30 to 38
Four spectral bands 100-foot resolution limit	35	67	5 MHz	30 to 38
Return beam vidicon (RBV)				
3500-line frame	50	32	4 MHz	31
Automatic picture transmission (APT) camera	17	22	3.2 kHz	24
Remote instrument interrogation				
Information retrieval system (IRS)	6	35	1 kHz	10 to 12
Information retrieval and location system (IRLS)	40	35	20 kHz	10 to 12
Omega position location equipment (OPLE)	96	31	100 kHz	10 to 12
Radar scatterometer	50	50	200 Hz	Undetermined
Synthetic array rada				
150-n.mi. altitude				
60-km swath, 75-meter resolution	1000	100 to 200	30 to 1000 kHz	24
Laser altimeter	--	--	--	

The ground coverage for orbital altitude of 600 n. mi. is in the order of 1250 by 1250 n. mi. Assuming a circular orbit, the 208-second picture cycle will result in above ground coverage with overlaps of about 300 n. mi. For resolution capability of about 550 lines and from a height of 600 n.m. , the ground resolution will be approximately 2.4 n. mi. in the center of the picture at 100 percent contrast conditions.

The vidicon tube in the APTS camera is exposed by an electromechanical focal plane shutter for 10 milliseconds at F/9 lens opening. The image impinged on the vidicon face plate is stored electrically and, due to the nature of the vidicon tube, is available for a very slow readout (200 seconds).

During readout, the video information is sampled at a rate of 4800 Hz, which improves the signal-to-noise ratio. The resultant waveform is in a form of amplitude-modulated pulses. Next, this waveform is detected, which results in a continuous analog readout which in turn is used to amplitude-modulate the 2400-Hz subcarrier derived from the spacecraft clock or automatic sync generator in case of failure. The final, resultant waveform is the amplitude-modulated 2400-Hz subcarrier with sidebands extending 1600 Hz above and below.

The camera and associated electronics weigh approximately 22 pounds and require 17 watts of prime power. A signal-to-noise ratio of 24 dB rms/rms will result in good picture quality.

### 2.3.3 Radar Scatterometer

It has been suggested by various scientific investigators that sea state be measured from a satellite by means of a radar scatterometer. This device uses the strength of the radar signal return and the known angle of incidence to yield a signature that can be compared with a library of known sea states. From this comparison, wave height and wind conditions can be inferred. Preliminary studies indicate that such a device can be built weighing 50 pounds and requiring 50 watts of prime power. The data rate requires a 200-Hz bandwidth. Signal-to-noise ratio is undefined at present.

### 2.3.4 Synthetic Aperture Radar

Radar mapping of land masses offers the advantages of penetrating cloud cover and augmenting the information obtained through optical and infrared imaging. Together, radar and imaging sensors offer geological information not available from any one sensor. Disadvantages of conventional radar are the need for power to illuminate the area to be mapped and the basically poorer resolution.

The latter disadvantage can be alleviated through the use of synthetic aperture radar, a method for storing and combining several returns from the same earth point as the vehicle moves, giving the effect of a longer antenna (and hence higher resolution) than could actually be carried. Ordinary radar

would require an antenna 1000 feet long to provide 250-foot resolution at 500 n.mi.; whereas synthetic aperture radar processing can image with similar resolution using relatively small antennas. Theoretically, these antennas could be quite small, but, practically, the longest antenna the vehicle can accommodate would be used so that power can be minimized.

The technical aspects of these radars are well-known; however, their value for earth resources is controversial. Wavelengths in the 4 to 10-inch region give images deemed valuable by geologists for disclosing hydrological features and ice formations; while less than an inch is favored by agriculture experts for crop discrimination and by geologists for disclosing lineament. In either case, the power penalty caused by high altitudes makes it clear that a synthetic aperture radar sensor must be used at as low an orbit as possible. Figure 4 shows the effects of antenna size, orbit altitude, and swath width on power requirements for the radar.

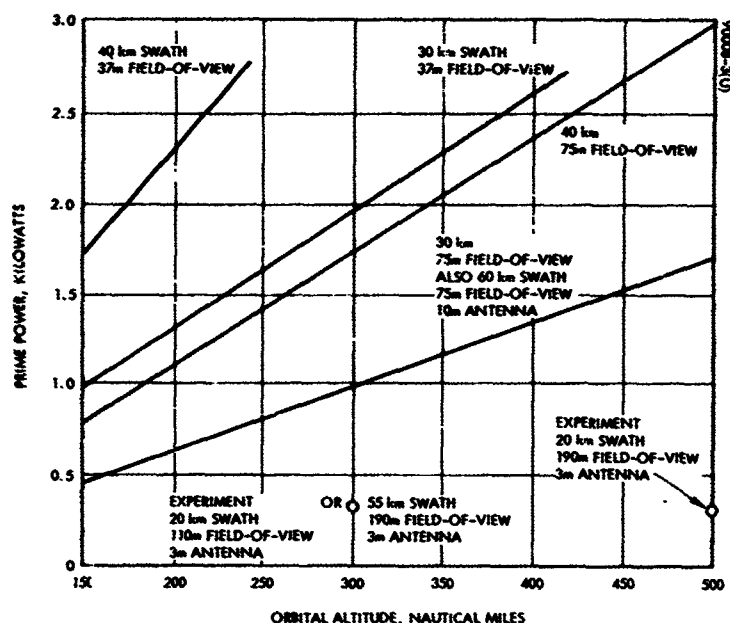


Figure 4. Synthetic Aperture Radar  
5-m antenna except where otherwise noted

### 2.3.5 Laser Altimeter

It has been postulated that a laser altimeter would provide information useful for sea-state determination and orographical mapping with higher resolution than possible with radar. At present, since no information exists on weight, power, or data requirements, this device represents an extremely interesting experiment.

### 2.3.6 Remote Instrument Interrogation

There are two basic concepts currently under consideration for interrogation of remote instrument packages. The first, called information retrieval and location system (IRLS), interrogates by radio command instrument packages on the ground, on buoys, or on balloons. Such a system, designed for operation on the Nimbus vehicle, weighs 35 pounds and requires 128 watts of power and a 20-kHz data baseband. A simplification of this information retrieval system is possible by eliminating the position determining feature. Such a device will interrogate instruments whose locations are known or can be estimated by other means. A preliminary study indicates a weight of 35 pounds, a requirement of 6 watts power, and a 1-kHz data baseband.

The second system, designated omega position location equipment (OPLE), utilizes the present omega navigation system (ONS). This system consists of ground-based stations transmitting synchronized signals which may be phase-compared for position determination. Transmission of the signals received by the instrument package, together with the instrument data to the satellite and then back to the ground station, will allow determination of the package location. Such a system can be built weighing 31 pounds, requiring 96 watts of power and a 100-kHz data baseband for 40 interrogation channels.

### 2.3.7 Sensor Combination

In order to arrive at a representative spacecraft payload which will lead to meaningful design analysis and trade studies for an LAS, a combination of sensors has been selected. The combination consists of the four-band MSSC, a radar scatterometer, and the IRLS remote instrument interrogation system.

Although the laser altimeter would be an interesting experiment, at present, lack of information precludes consideration here. From Table 2, it can be seen that a synthetic array radar is in a different class from other sensors in terms of power and weight. Thus, the choice that remained was which sensor to choose in the optical imaging group and the instrument interrogation group. The IRLS is one of the better of the three, and the camera chosen is much superior to the APT camera, but somewhat lower in quality than the seven-band MSSC. Note the saving in both power and weight as a result of choosing the four-band MSSC over the seven-band MSSC.

The combination of the three sensors — four-band MSSC, IRL instrument interrogation system, and a radar scatterometer — is a very attractive payload.

## 2.4 SPACECRAFT CONSIDERATIONS

To provide a guideline, especially for configuration concepts, the power and weight of subsystems were estimated for a spacecraft capable of carrying the sensor combination discussed above. The results are shown in Table 3. It can be seen that such a spacecraft is within the capability of Thor-Delta boosters. This class of spacecraft is attractive because of the good mission or data potential without the high cost of the larger boosters.

The spacecraft weight estimate has led to the Thor-Delta booster, which in turn imposes constraints on the spacecraft's size. Figure 5 illustrates the shroud dimensions for the two-stage Thor-Delta. These dimensions, together with the power requirement of approximately 275 watts, indicate a need for an extended solar array. Furthermore, if antennas must be packaged between the spacecraft structure and the sides of the shroud, the dimensional limit will be about 36 inches.

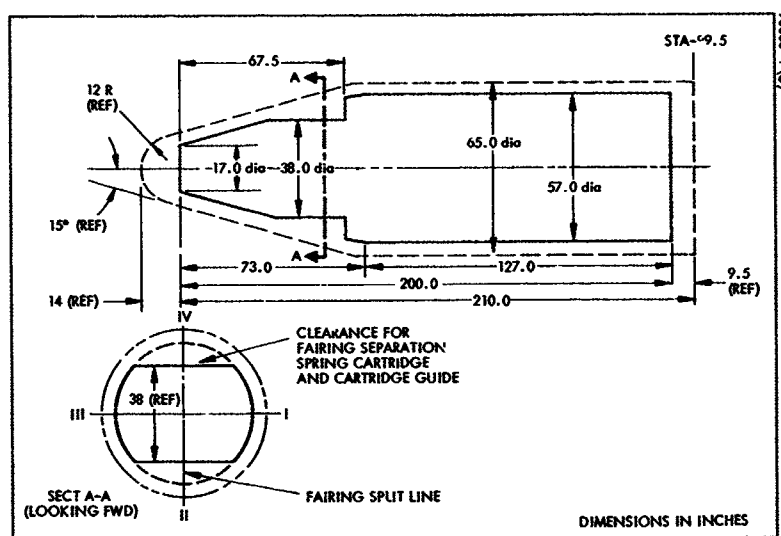


Figure 5. Improved Thor-Delta Booster Shroud  
Payload capability = 1170 pounds



TABLE 3. SPACECRAFT WEIGHT AND POWER ESTIMATES

Spacecraft Component	Weight, pounds	Load Power, watts
Payload		
Multispectral camera	66	35
Interrogation system	35	40
Radar scatterometer	50	50
Data transmission		
Steerable antennas	30 (two), 15 (one)	— —
Antenna steering systems	15	20
Transmitters (two)	40	60
Command system	30	4
Omniantenna	10	—
Attitude control system (sensors, controllers, and processing)	60	30
Orbit control system		
Dry hardware	15	—
Propellant	80	—
Power subsystem		
Solar array	60	—
Batteries	40	—
Drive system	35	20
Electronics	9	5
Structural and thermal control	140	10
Adapter and despin	48	—
Total	748-763	274
Improved Thor-Delta booster capability	1170	—

### 3. ORBITAL ANALYSIS AND GEOMETRICAL CONSIDERATIONS

#### 3.1 INTRODUCTION

There are a number of topics of interest which are related to low-altitude satellite (LAS) orbital considerations. Standard orbital analysis can be found in many study reports and texts and has application mainly when more specific mission and orbital requirements are defined. The rather general nature of this study and the emphasis upon the low-altitude satellite/data relay satellite system (LAS/DRSS) communication link dictates a limited study of orbital characteristics. Thus, two of the sections in this section deal with orbital considerations associated with the mission (Sections 3.2 and 3.3), and Section 3.5 treats the geometrical relationships between an LAS and DRSS. Section 3.4 presents some general information for reference, and Section 3.6 defines coordinate systems associated with the spacecraft and several frames of reference.

An orbit is determined by six basic quantities: the semimajor axis, the eccentricity, the inclination, the longitude of the ascending node, the argument of perifocus, and the time of perifocal passage. However, in this study only circular orbits are considered, and for these orbits the above six quantities reduce to three: the altitude, the inclination, and the longitude of the ascending node. These are the three quantities which appear as parameters in orbit related analyses. For a sun synchronous orbit, discussed in the following section, the inclination is determined by the altitude, and the ascending node longitude is determined by the desired sun aspect angle. The point to be made is that the orbital altitude is a primary parameter in LAS orbits, and in the following sections its effect should be noted.

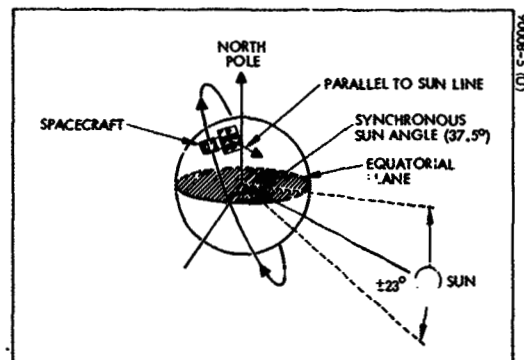


Figure 6. Sun-Synchronous Orbit

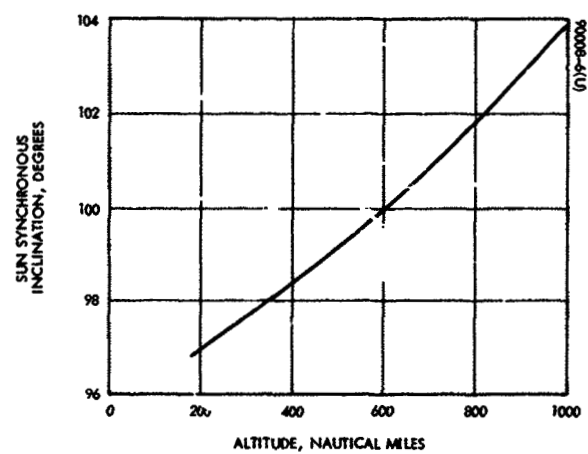


Figure 7. Attitude and Inclination for Sun-Synchronous Orbit

### 3.2 SUN-SYNCHRONOUS ORBIT

A sun-synchronous orbit is characterized by an orbital precession rate (caused by the oblateness of the earth) equal to the angular rate of the earth's travel about the sun. Thus, the sunline makes a constant angle with the spacecraft orbital plane throughout the year. The main advantage of such an orbit is that lighting conditions on the ground can be maintained at the desired level for optical imaging missions. In addition, this orbit is desirable from the standpoint of solar power and thermal control design aspects of the spacecraft. Figure 6 portrays a 9:30 a. m. sun-synchronous orbit. Such an orbit gives the fixed 37.5-degree angle between the orbit plane and the sunline shown in the sketch.

When, in order to make an analysis, trade study, or configuration decision meaningful, it becomes necessary to be more specific concerning the orbit, a sun-synchronous orbit is assumed. This is consistent with the representative optical imaging mission discussed in Section 2.

#### 3.2.1 Attitude and Inclination for Sun-Synchronous Orbit

Due to the earth's oblateness, a perturbing force is applied to a satellite which causes its orbit to rotate in inertial space. That is, the line of nodes rotates and its angular rate,  $\dot{\Omega}$ , is a function of the semi-major axis,  $a$ , eccentricity,  $e$ , and orbit inclination,  $i$ . The relationship is

$$\dot{\Omega} = -C \frac{\cos i}{a^{7/2} (1 - e^2)} \quad (1)$$

For circular orbits under consideration here,  $a = R_o = R_e + h$  and  $e = 0$ . Then Equation 1 becomes

$$\dot{\Omega} = -C \frac{\cos i}{(R_e + h)^{7/2}}$$

where  $C = 3.939 \times 10^{13}$  deg-miles<sup>7/2</sup>/day. For a sun-synchronous orbit,

$$\dot{\Omega} = 0.041068 \text{ deg/hour}$$

Combining these numbers

$$\cos i = -(4.09099 \times 10^{-14})(R_e + h)^{7/2}$$

where  $R_e$  and  $h$  are in nautical miles. This relationship between  $i$  and  $h$  is illustrated in Figure 7.

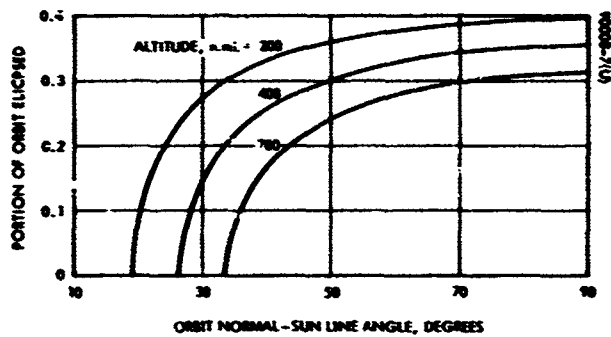


Figure 8. Orbital Eclipse as Function of Orbit Normal/Sunline Angle,  $\lambda$

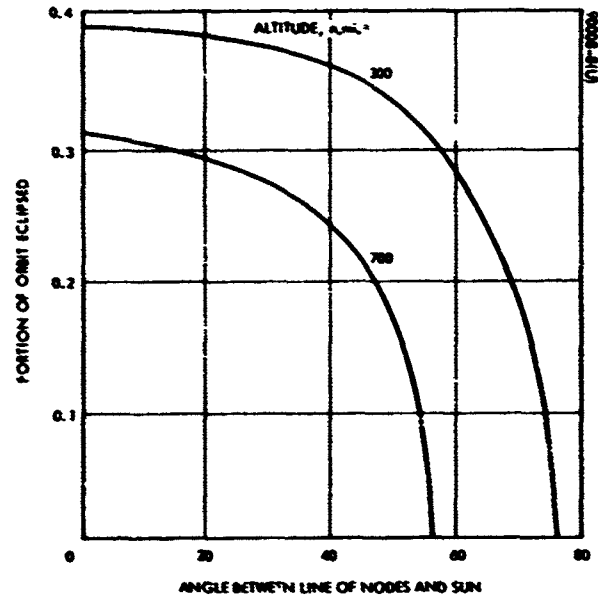


Figure 9. Portion of Orbit Eclipsed as Function of Angle,  $\phi$ , Between Line of Nodes and Sun

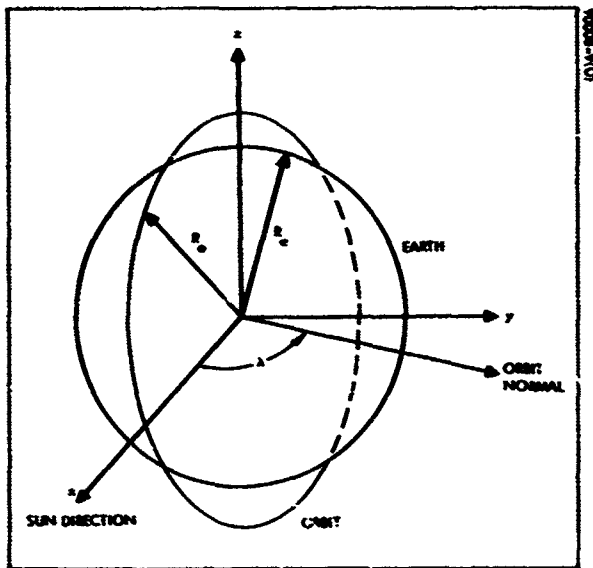


Figure 10. Three-Dimensional Earth-Orbit-Sun Geometry

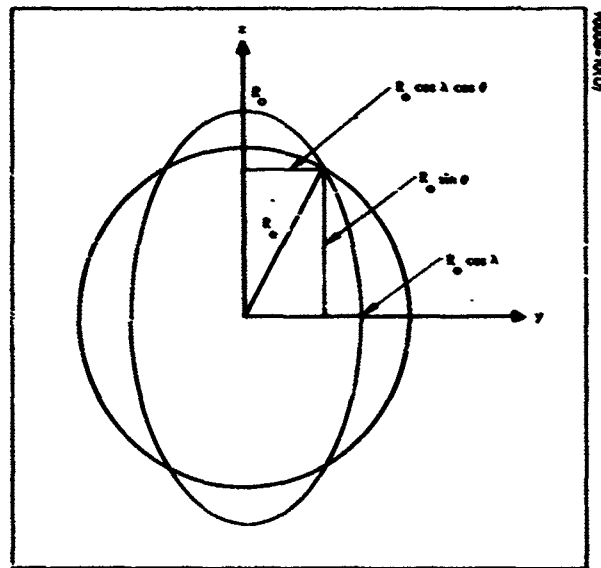


Figure 11. Two-Dimensional Earth-Orbit Geometry

### 3.2.2 Solar Eclipse

For a given sun-synchronous orbit, the solar eclipse time due to earth shadowing is the same every orbit. This eclipse time is a function of the LAS altitude and the relationship of the sun to the LAS orbit plane. This relationship is developed below, and the results are shown in Figures 8 and 9.

Consider Figure 10 where the basic geometrical relationships between the earth, orbit, and sun are illustrated. The angle between the earth-sun line (the x-axis) and the orbit normal is denoted by  $\lambda$ . For developing the desired relationships, only the projection of the earth and orbit onto the y-z plane need be considered because this is the plane perpendicular to the sun direction. Thus, referring to Figure 11

$$y = R_o \cos \lambda \cos \theta$$

$$z = R_o \sin \theta$$

where  $\theta_o$  is the orbital position angle measured from the y-axis. An eclipse begins at  $\theta_o = \theta$  where

$$(y^2 + z^2)^{1/2} = R_e = \text{the earth's radius}$$

That is, where

$$\begin{aligned} R_e^2 &= R_o^2 (\sin^2 \theta + \cos^2 \lambda \cos^2 \theta) \\ &= R_o^2 (\sin^2 \theta \sin^2 \lambda + \cos^2 \lambda) \end{aligned} \quad (2)$$

Denote

$$A = \frac{R_e}{R_o} \quad (3)$$

From Equations 2 and 3

$$\sin^2 \theta = \frac{1}{\sin^2 \lambda} (A^2 - \cos^2 \lambda) \quad (4)$$

Thus,  $\theta$  is a function of orbital altitude and the angle  $\lambda$ .

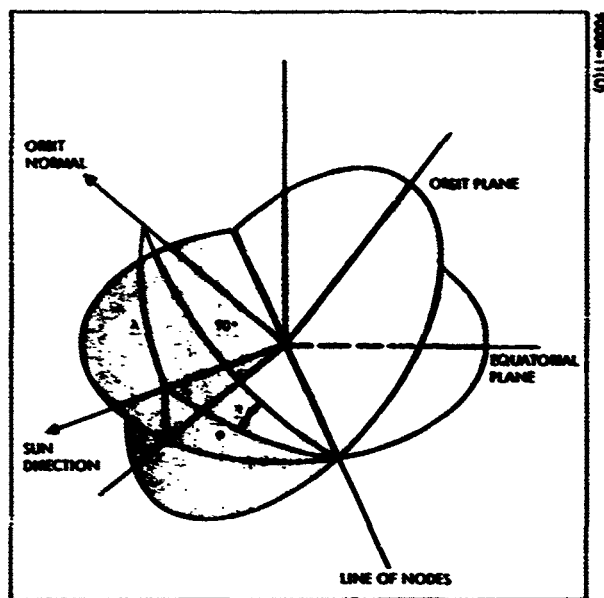


Figure 12. Orbit-Sun Geometry

For machine computation where frequently only the inverse tangent is an available internal function, the tangent of  $\theta$  is a useful quantity. Using Equation 4

$$\tan \theta = \frac{\sin \theta}{(1 - \sin^2 \theta)^{1/2}} = \left( \frac{A^2 - \cos^2 \lambda}{1 - A^2} \right)^{1/2}$$

or

$$\theta = \tan^{-1} \left( \frac{A^2 - \cos^2 \lambda}{1 - A^2} \right)^{1/2} \quad (5)$$

The value of interest of  $\theta$  determined from Equation 5 is the value which lies between 0 and  $\pi/2$ . The percentage of eclipse time,  $E$ , is given by

$$E = \frac{2\theta}{2\pi} = \frac{\theta}{\pi}$$

This percentage is plotted in Figure 8 as a function of  $\lambda$  and orbital altitude  $h$ .

The relationship between  $\lambda$  and the angle between the line of nodes and the sun line can be determined from a simple spherical trigonometrical identity. Consider Figure 12, where these geometrical relationships are illustrated. The illustrated quantities are related by

$$\cos \lambda = \sin \phi \cos \eta$$

For simplification, only the case where the sun lies in the equatorial plane will be dealt with here. For this case,  $\eta = i - 90$  degrees, so that

$$\cos \lambda = \sin \phi \cos \eta = \sin \phi \sin i$$

must be substituted in Equation 5 to determine  $\theta$  as a function of  $\phi$  and  $h$  during the equinoxes. In Figure 9,  $\theta$  is plotted as a function of  $\phi$  and  $h$ .



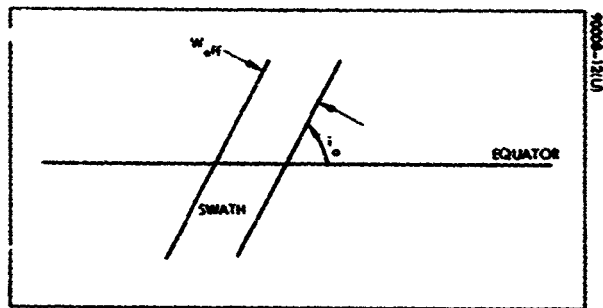


Figure 13. Swath and Equator

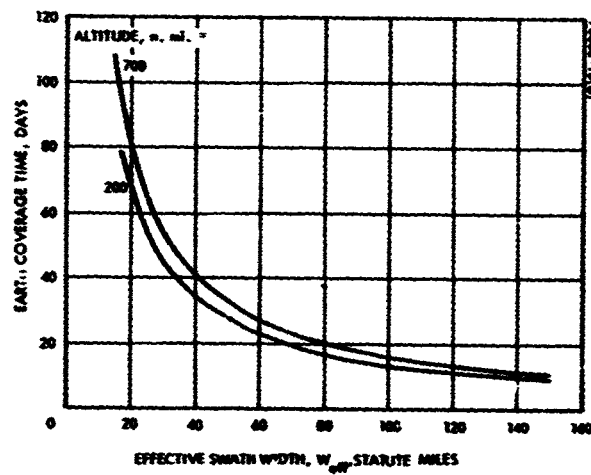


Figure 14. Earth Coverage Time

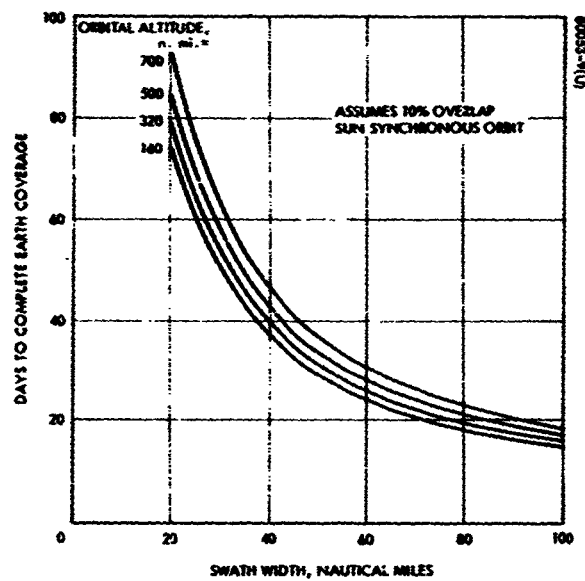


Figure 15. Earth Coverage Time as Function of Swath Width and Altitude

### 3.3 GLOBAL COVERAGE

Related to the mission, but also related to the LAS orbit, are global coverage considerations. This section treats the problem of achieving maximum possible earth coverage in minimum time.

For the representative mission assumed here, which includes optical imaging, the camera field of view or scan pattern sweeps a path or swath centered about the subsatellite orbit track on the earth's surface.

The swath width is defined as the distance on the earth's surface perpendicular to the orbit track corresponding to the field of view of the imaging device. This swath is illustrated in Figure 3. Of interest is the relationship between swath width,  $W$ , satellite altitude,  $h$ , and minimum time,  $T_e$ , to cover the entire earth. One other parameter of lesser importance is the amount of overlap. This parameter can be easily accommodated by merely subtracting the overlap from the swath width to obtain the effective swath width,  $W_{eff}$ .

It should be noted at the outset that unless the orbit is polar (inclination of 90 degrees), complete coverage of the earth is impossible. For instance, for a sun-synchronous orbit with an inclination of 99 degrees, the areas near the poles above 81 degrees latitude will not be covered. However, earth coverage time will be defined as the time required to cover the amount of the earth's surface area consistent with the orbit inclination. Earth coverage under this definition occurs when the equator has been completely covered. Referring to Figure 13, the minimum earth coverage time is given by

$$T_e = \left( \frac{2\pi R_e}{W_{eff}} \sin i \right) T_o \quad (6)$$

where

$$T_o = 2\pi \frac{(R_e + h)^{3/2}}{G^{1/2}} = \text{orbital period}$$

This relationship is shown in Figure 14. If a swath width,  $W$ , and overlap factor,  $f_o$ , are specified, then  $W_{eff} = (1 - f_o)W$ . Figure 15 is a plot of coverage time as a function of  $W$  for 10 percent overlap.

#### 3.3.1 Orbital Parameters for Sun-Synchronous Orbits

The next topic is the method by which total ground coverage is accomplished in minimum time. One method is to choose an orbital altitude very near one of the altitudes which result in an integer number of orbits. But if this integer is  $n$ , then the altitude should deviate just enough so that

the point where the  $n + 1$  orbit crosses the equator is a distance away from the first orbit crossing of one effective swath width,  $W_{eff}$ , in either an easterly or westerly direction. The arc distance,  $\theta$ , at the equator between successive LAS orbit crossings is given by

$$\theta = \frac{T_o}{8.64 \times 10^4} (2\pi) \text{ radians}$$

where  $T_o = \left[ (2\pi)(1.1508)^{3/2} / G^{1/2} \right] (R_e + h)^{3/2}$  and where  $R_e = 3444$  n. mi.,  $h$  is the LAS altitude in nautical miles, and  $G = 9.563 \times 10^4 \text{ mi}^3/\text{sec}^2$ . The conversion factor from nautical miles to statute miles is 1.1508.

The linear distance,  $D$ , between two consecutive orbit crossings of the equator is given by

$$\begin{aligned} D &= \theta R_e = 3963 \theta \text{ statute miles} \\ &= K(R_e + h)^{3/2} \text{ statute miles} \end{aligned} \quad (7)$$

where  $R_e$  and  $h$  are in nautical miles and

$$K = \frac{(2\pi)^2 (3963)(1.1508)^{3/2}}{(8.64 \times 10^4) G^{1/2}} = 7.229 \times 10^{-3} \frac{\text{mi.}}{(\text{n. mi.})^{3/2}}$$

Figure 16 is a plot of  $D$  versus altitude.

According to the above mentioned method, for an integer,  $n$ , orbits per day, the distance,  $D$ , between consecutive orbit crossings must be

$$D = \frac{2\pi R_e + W_{eff}}{n} \quad (8)$$

Combining Equations 7 and 8, the relationship between  $h$ ,  $W_{eff}$  and  $n$  is given by

$$h = \left( \frac{2\pi R_e + W_{eff}}{nK} \right)^{2/3} - R_e \quad (9)$$

Another approach to determining  $h$  is to determine the change in  $h$  to produce a small change in  $D$ . From Equation 7

$$h = \left( \frac{D}{K} \right)^{2/3} - R_e \quad (10)$$

Differentiating

$$\frac{dh}{dD} = \frac{2}{3K^{2/3}} D^{-1/3}$$

And substituting from Equation 7

$$\frac{dh}{dD} = \frac{2}{3K} (R_e + h)^{-1/2}$$

Figure 17 shows  $dh/dD$  as a function of altitude.

Denoting  $\Delta h_n$  as the deviation of altitude from that value which results in  $n$  orbits per day, and  $\Delta D_n$  as the deviation from the corresponding equator crossing separation

$$\Delta h_n = \frac{2}{3K} (R_e + h_n)^{-1/2} \Delta D_n$$

The equator crossing separation deviation is given simply by

$$|\Delta D_n| = \frac{W_{eff}}{n}$$

where  $W_{eff}$  is in statute miles. If  $\Delta D_n$  is made negative, the  $n + 1$  equator crossing will fall short (to the east) of the first crossing by a distance equal to  $W_{eff}$ , and if  $\Delta D_n$  is positive, the  $n + 1$  equator crossing will fall to the west of the first. Thus,

$$\Delta h_n = \frac{2}{3nK} (R_e + h_n)^{-1/2} W_{eff} \quad (11)$$

it is shown in Section 3.4.4

$$h_n = \left[ \left( \frac{8.64 \times 10^4}{2\pi} \right)^2 \frac{G}{n^2} \right]^{1/3} - R_e \quad (12)$$

Substituting Equation 12 into 11

$$\Delta h_n = \frac{2}{3KH^{1/3}G^{1/6}} \frac{W_{eff}}{n^{2/3}}$$

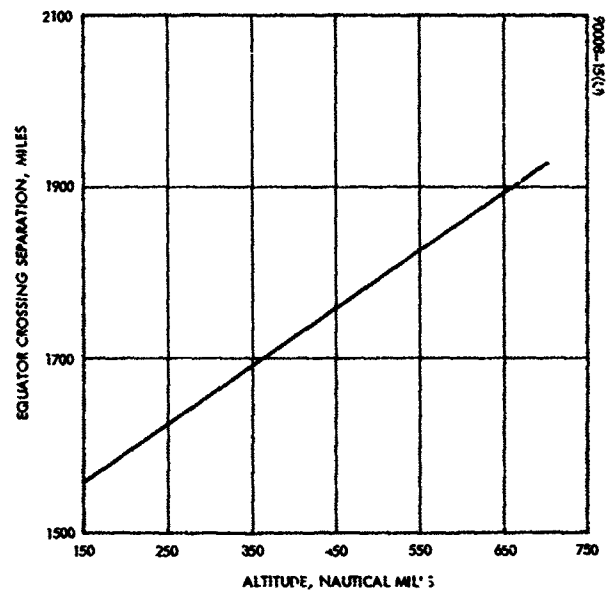


Figure 16. Equator Crossing Separation, D, Versus Altitude

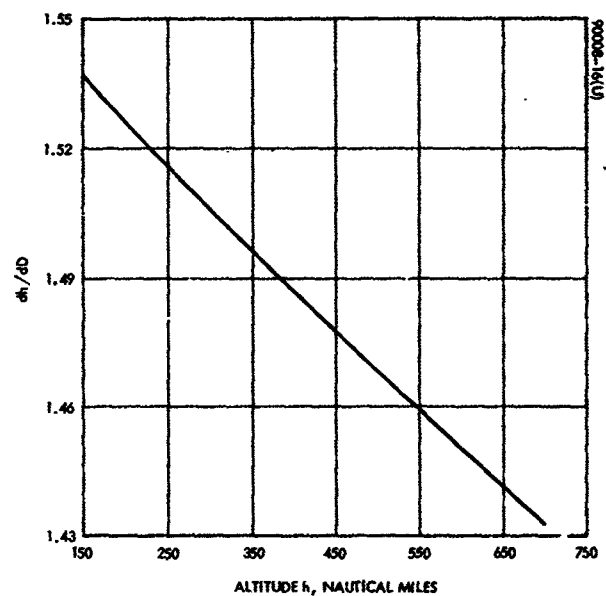


Figure 17.  $dh/dD$  as Function of Altitude

where

$$H = \frac{8.64 \times 10^4}{2\pi} = 1.3751 \times 10^4 \quad \text{sec/rad}$$

and  $W_{\text{eff}}$  is in statute miles.

Below is a list of values of  $\Delta h_n/W_{\text{eff}}$  and  $h_n$  for values of  $n$  corresponding to low altitude orbits, and Figure 18 is a plot of  $\Delta h_n$  as a function of  $W_{\text{eff}}$  for these values of  $n$ .

<u>Number of Orbits per Day</u>	<u><math>h_n</math></u>	<u><math>\Delta h_n/W_{\text{eff}}</math></u>
12	907.76	0.1086
13	781.65	0.10296
14	482.79	0.09799
15	306.28	0.09359
16	148.36	0.086097

As an example, suppose a swath width of 100 miles with 10 percent overlap and an altitude near 500 n. mi. is desired. Then, choosing  $n = 14$ , which corresponds to an altitude,  $h_{14}$ , of 482.79 n. mi., and with  $W_{\text{eff}} = 100 - 10 = 90$  statute miles,  $\Delta h_{14} = 8.82$  n. mi., and so

$$h = 482.79 + 8.82 = 491.61 \text{ n. mi.}$$

The above method has the disadvantage that for a given swath width there are only a few altitudes which yield the type of earth coverage described, namely, altitudes near the integer orbit altitudes. Suppose for reasons related to the spacecraft mission some other altitude is desired. Is it possible to achieve earth coverage in minimum time at this altitude or at some altitude very near it?

In order to understand the following analysis, consider Figure 19 where the equator is represented by the circle and several LAS orbit crossings are indicated.  $D$  is the equatorial distance between equator crossings and is determined by the altitude (see Equation 7). The number  $\alpha$  is the fraction of  $D$  corresponding to the distance between the first orbit crossing and  $n^{\text{th}}$  crossing, where  $n$  is the largest integer smaller than  $2\pi R_e/D$ . Thus,  $n$  is the integer part of  $2\pi R_e/D$ , while  $\alpha$  is the fractional or decimal part.

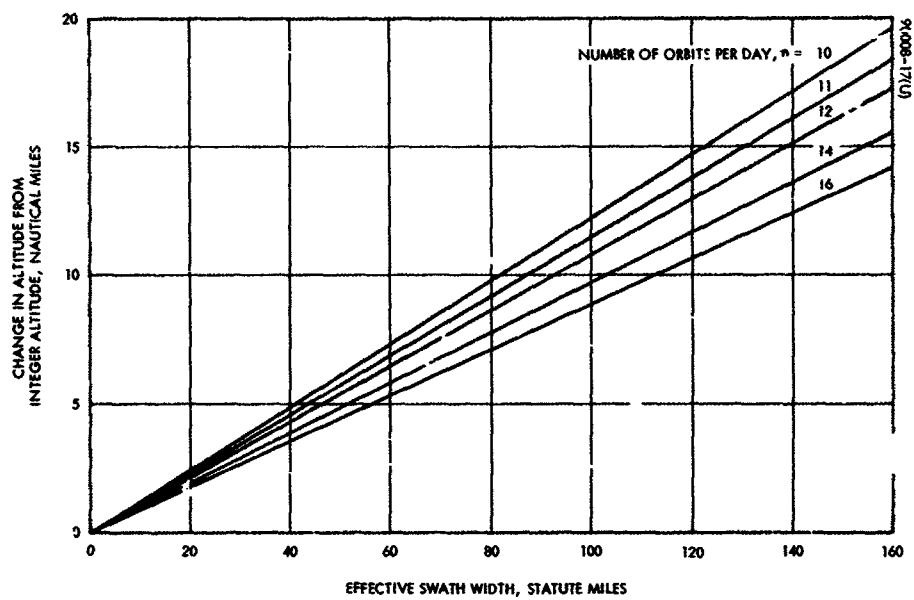


Figure 18.  $\Delta h_n$  as Function of  $W_{eff}$  for Various Values of  $n$

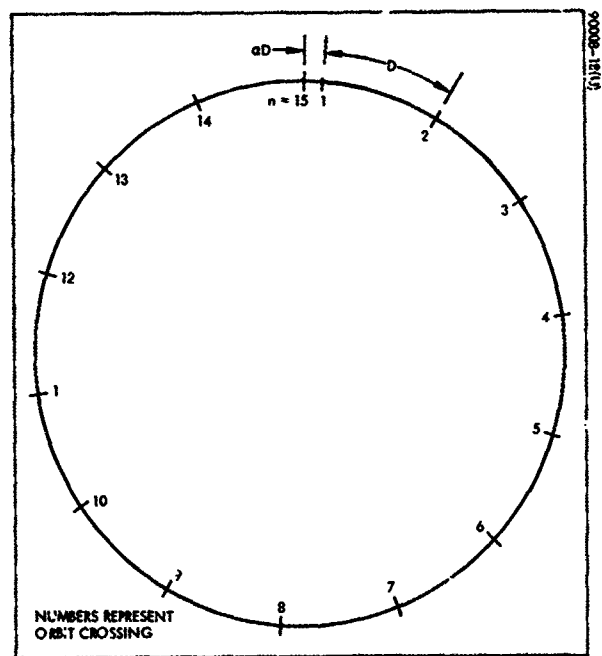


Figure 19. Equator Orbit Crossings

Suppose  $\alpha = 0.5$ ; then the  $2n + 1$  crossing will coincide exactly with the first, and the sequence will repeat with large areas not covered by the orbit swath.

Define  $N$  as the largest integer less than  $D/W_{\text{eff}}$  and  $\beta$  as the fractional part or remainder, i. e.,

$$\beta = \frac{D}{W_{\text{eff}}} - N$$

Total earth coverage, or equator coverage, as it is defined here will require  $N + 1$  days, since this is the number of gaps between any two successive orbit crossings of approximately  $W_{\text{eff}}$  width. That is, each day a different gap between orbits 1 and 2 will be covered. The problem that arises is how to ensure that all the gaps are covered. The conditions are discussed and developed below.

First define

$$\epsilon = \frac{1 - \beta}{N + 1}$$

This quantity  $\epsilon W_{\text{eff}}$  is just the play or slack allowable per crossing because  $D$  is not an integer number of swath widths.

It can be shown that if  $p$  and  $N + 1$  are relatively prime, i. e., they have no common divisor except unity, and if

$$p - \epsilon \leq \alpha \frac{D}{W_{\text{eff}}} \leq p + \epsilon \quad (13)$$

then the entire space between any two consecutive orbits will be subsequently covered, and this occurs naturally in minimum time, and the entire equator is covered. The condition in Equation 13, in essence, ensures there will be no repeating sequences within the required number of days to cover all the gaps.

A case of interest is that situation where  $D$ , or equivalently  $h$ , is given along with  $W_{\text{eff}}$ , and the values of  $\alpha$  or  $h$  nearest those given values to ensure complete coverage in the minimum time are desired. The procedure below deals with this situation and is based upon the above concepts.

1) Compute  $n$ ,  $\alpha$ ,  $N$ ,  $\beta$ , and  $\epsilon$  from

$$n + \alpha = 2\pi R_e / D$$

$$N + \beta = D / W_{\text{eff}}$$

$$\epsilon = \frac{1 - \beta}{N + 1}$$



where  $2\pi R_e = 24,902$  miles.

- 2) Determine  $p$ , the relative prime of  $N + 1$  nearest in value to

$$\sigma(N + \beta)$$

- 3) Define:

$$s = \begin{cases} +1 & \text{if } p < \sigma(N + \beta) \\ -1 & \text{if } p \geq \sigma(N + \beta) \end{cases}$$

- 4) Calculate  $D^*$ , the required value of  $D$ , according to the applicable formula below.

$$D^* = \frac{1}{n} \left| 2\pi R_e - (p + s\epsilon)W_{\text{eff}} \right| \quad (14)$$

The previously developed procedure is a special case of this one and corresponds to  $\epsilon = 0$  and  $p = N$ .

The following example will illustrate the above procedure. Suppose the desired altitude is 540 n. mi. and a swath width of 100 miles with 10 per cent overlap is desired. Then  $W_{\text{eff}} = 90$  miles and  $D = 1817.85$  miles. Following the above procedure:

$$n + \alpha = \frac{2\pi R_e}{D} = \frac{24,902}{1817.85} = 13.6987$$

$$N + \beta = \frac{D}{W_{\text{eff}}} = \frac{1817.85}{90} = 20.1983$$

$$\epsilon = \frac{1 + \beta}{N + 1} = \frac{1 + 0.1983}{21} = 0.0381762$$

Thus,  $\alpha = 0.6987$ , and so

$$\sigma(N + \beta) = 14.1125$$

The nearest prime number to this number, which is also a relative prime of 21 is 13. And since

$$p = 13 < \sigma(N + \beta) = 14.1125,$$

$$s = +1.$$

Thus,

$$\begin{aligned} D^* &= \frac{1}{13} \left| 2\pi R_e - (5 + 0.03818)(90) \right| \\ &= 1825.2^\circ \end{aligned}$$

and the corresponding altitude is computed from Equation 10 to be

$$H^* = 550.861 \text{ n. mi.}$$

Thus, only a 10 n. mi. deviation from the originally desired altitude is required for total coverage.

If the effect of  $\epsilon$  is ignored, i. e.,  $\epsilon = 0$  in Equation 14, then

$$H^* = 551.247$$

So that  $\epsilon$  can be ignored in most instances because its effect is very small.

This example can be used to illustrate the necessity of the relative prime condition for  $p$ . Suppose  $p$  were taken as 14, the closest integer to  $(N + \beta) = 14.1125$ . Then orbit  $3n + 2 = 41$  will coincide with the first orbit and there will be large areas not covered. This is illustrated in Figure 20. Suppose  $p = 15$ , which is close to 14 but shares 3 as a common divisor with 21. If the effective swath width gaps between orbits 1 and 2 are numbered from 1 to 21, with orbit 1 numbered as 1 and orbit 2 representing 22, the sequence in which these gaps are covered will be as follows:

1, 7, 13, 19, 4, 10, 16, 1, 7, . . .

Consequently, the sequence begins to repeat before all the gaps are covered. The gap number increases by  $21 - 15 = 6$  modulo 21 each day, so that on the eighth day the LAS would be in the same position with respect to the earth's surface as on the first day. If  $p$  and  $N + 1$  are relative primes, this will not happen.

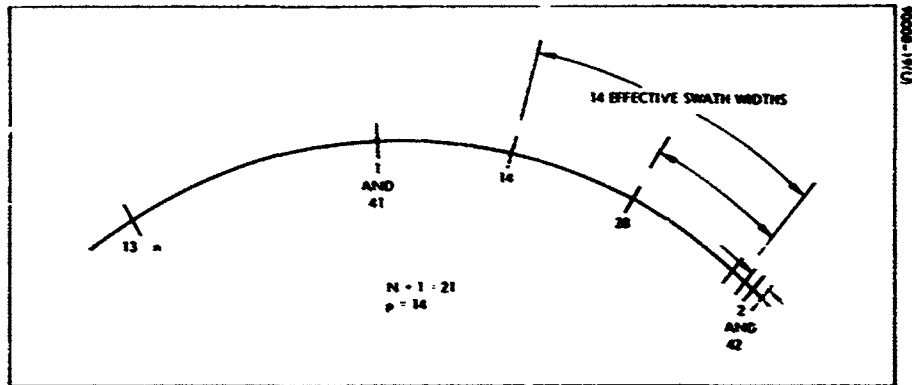


Figure 20. Example of Nonrelative Prime Numbers

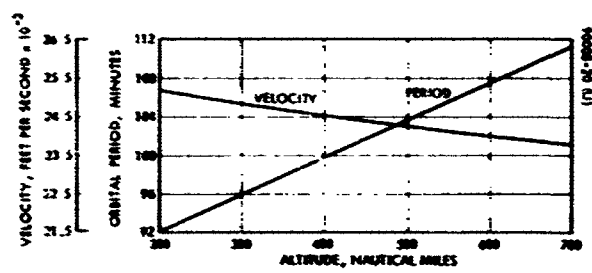


Figure 21.  $V_o$  and  $T_o$  as Function of Altitude

### 3.4 ORBITAL INFORMATION

For completeness as well as convenient reference, several LAS orbit related quantities of interest are discussed here. These include orbital period, L/S velocity, number of orbits per day, and range and range rate between a LAS and DRS. These topics are treated separately below.

#### 3.4.1 Orbital Period and Velocity

The orbital period and velocity are determined by the altitude, and the respective relationships are easily developed from the law of gravitation. This law can be expressed as

$$\omega^2 = \frac{G}{R^3} \quad (15)$$

where  $\omega$  is the orbital angular velocity,  $G$  is the earth's gravitational constant, and  $R$  is the orbital radius. The orbital velocity,  $V_o$ , and the period,  $T_o$ , are given by

$$V_o = \omega R = \left(\frac{G}{R}\right)^{1/2} \quad (16)$$

$$T_o = \frac{2\pi}{\omega} = 2\pi \left(\frac{R^3}{G}\right)^{1/2} \quad (17)$$

where

$$G = 9.563 \times 10^4 \text{ mi}^3/\text{sec}^2$$

Figure 21 is a plot of  $V_o$  and  $T_o$  as a function of altitude.

#### 3.4.2 Ground Velocity of Subsatellite Point

The linear velocity,  $v_s$ , of a satellite in a circular orbit at a radius,  $R_s$ , from the earth's center is given by

$$v_s^2 = \frac{G}{R_s}$$

The orbital angular velocity,  $\omega$ , is related to  $v_s$  and  $R_s$  by

$$\omega = \frac{v_s}{R_s}$$

and the velocity,  $v_e$ , of the subsatellite point on the earth is given by

$$v_e = R_e \omega$$

where  $R_e$  is the distance from the center of the earth to the surface. Nominally,  $R_e = 3963$  miles. Thus,

$$v_e = v_s \frac{R_e}{R_s} = \frac{G^{1/2} R_e}{R_s^{3/2}} \text{ miles/second}$$

Using the nominal value of  $R_e$

$$v_e = \frac{12.255 \times 10^5}{(R_e + h \text{ (mi)})^{3/2}} = \frac{12.255 \times 10^5}{(R_e + h \text{ (mi)})^{3/2}} \text{ miles/second}$$

where  $h \text{ (mi)}$  is the satellite altitude in statute miles. It is common practice, however, to specify the altitude in nautical miles (n. mi.); in which case,

$$\begin{aligned} v_e &= \frac{12.255 \times 10^5}{(3441 + h \text{ (n. mi.)})^{3/2} (1.1508)^{3/2}} \\ &= \frac{9.94 \times 10^5}{(3441 + h \text{ (n. mi.)})^{3/2}} \text{ miles/second} \end{aligned}$$

This relationship is plotted in Figure 22.

### 3.4.3 Range and Range Rate

Of interest here is the worst case situation which occurs when the DRS lies on the line of nodes. The geometry is shown in Figure 23.

$$r_{\text{max}} = (R_s^2 - R_e^2)^{1/2} + R_o \sin \beta$$

where

$$\cos \beta = \frac{R_e}{R_o}$$

Thus

$$\rho_{\max} = (R_s^2 - R_e^2)^{1/2} + (R_o^2 - R_e^2)^{1/2}$$

But

$$R_o = R_e + h, \text{ where } h \text{ is the altitude}$$

So

$$\rho_{\max} = (R_s^2 - R_e^2)^{1/2} + (2R_e h + h^2)^{1/2} \quad (18)$$

Clearly, the minimum range is given by

$$\rho_{\min} = R_s - R_o = R_s - R_e - h \quad (19)$$

Figure 24 is a plot of the maximum range as a function of altitude.

The maximum range rate is just the orbital velocity and is shown in Figure 21.

#### 3.4.4 Number of Orbits per Day

An orbital period,  $T_o$ , is given by Equation 17. The number of orbits,  $n$ , per day is given by

$$n = \frac{(24)(3600)}{T_o} = \frac{(24)(3600)}{2\pi} \left( \frac{G}{R_o^3} \right)^{1/2} \quad (20)$$

This is plotted in Figure 25 as a function of altitude.

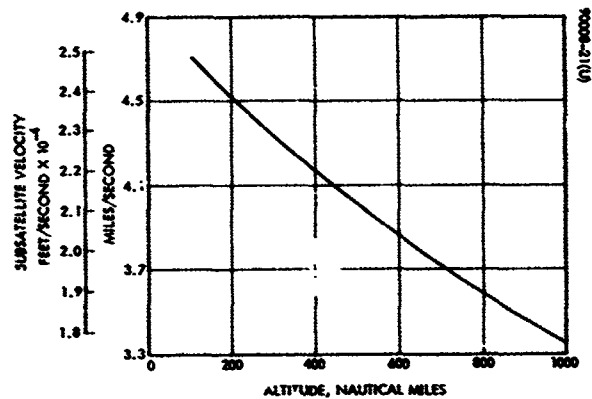


Figure 22. Subsatellite Velocity Versus Altitude

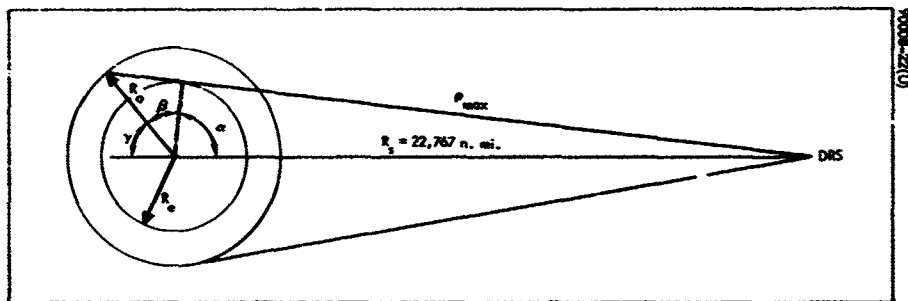


Figure 23. Range and Range Rate Worst Case

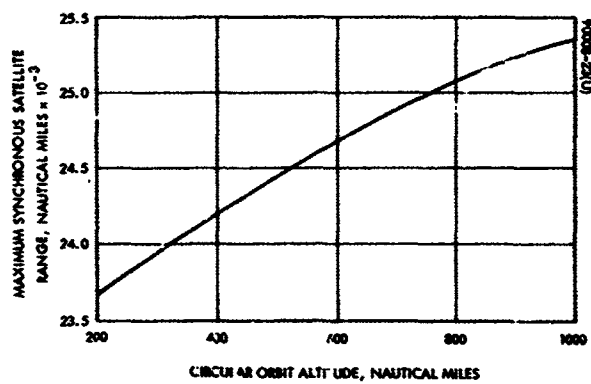


Figure 24. Maximum Synchronous Satellite Range as Function of Circular Orbit Altitude

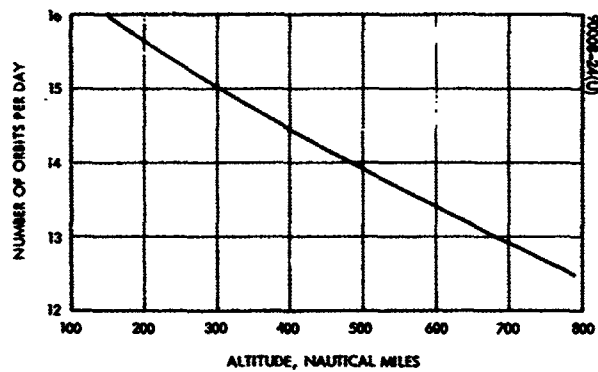


Figure 25. Number of Orbits Per Day as Function of Altitude

If it is desired that  $n$  be an integer, then certain altitudes are dictated. These can be found by solving Equation 20 for the altitude,  $h$ , ( $R_o = R_e + h$ ).

$$R_{on} = \left\{ \left[ \frac{(24)(3600)}{2\pi} \right]^2 \frac{G}{n^2} \right\}^{1/3} = R_e + h_n$$

or

$$h_n = \left\{ \left[ \frac{(24)(3600)}{2\pi} \right]^2 \frac{G}{n^2} \right\}^{1/3} - R_e$$

The low altitudes are listed below.

<u>Number of Orbits Per Day</u>	<u>Altitude (n. mi.)</u>
12	907.76
13	681.65
14	482.79
15	306.28
16	148.36



### 3.5 LAS-DRS VISIBILITY

Of major interest for this study are the considerations associated with line-of-sight visibility of the LAS by one or more DRSs. With three DRSs, an LAS is visible to at least one of them at all times, and at least two ground stations are required. Two DRSs and one ground station is a situation with limitations. The visibility relationships between an LAS and a single DRS are of interest because this is the fundamental link in an LAS-DRS system. These latter two subjects are discussed below.

#### 3.5.1 LAS Visibility by Single DRS

The worst case relative positions of the LAS and DRS for visibility occur when the DRS lies in the LAS orbit plane; i.e., the DRS lies on the line of nodes. The corresponding geometry is shown in Figure 26. For the case where the DRS is not in the orbit plane, geometrical relationships similar to those used for solar eclipse may be developed.

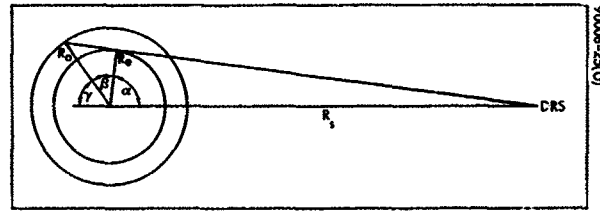


Figure 26. DRS Eclipse  
Worst-Case Geometry

From Figure 26

$$\cos \beta = \frac{R_e}{R_o} = A \quad (21)$$

$$\cos \alpha = \frac{R_e}{R_s} = B \quad (22)$$

$$\gamma = 180 - \beta - \alpha$$

$$\sin \gamma = \sin (\alpha + \beta) = \sin \alpha \cos \beta + \cos \alpha \sin \beta \quad (23)$$

where

$$\sin^2 \alpha = 1 - B^2 \quad (24)$$

$$\sin^2 \beta = 1 - A^2 \quad (25)$$

Similar to the solar eclipse analysis, eclipse of the DRS begins when

$$R_o^2 \sin^2 \gamma = R_o^2 (\sin^2 \theta + \cos^2 \lambda \cos^2 \theta) \quad (26)$$

where  $\theta$  is the orbit angle and  $\lambda$  is the angle between the earth-DRS line and the orbit normal.

From Equations 21 through 25

$$\sin \gamma = (1 - B^2)^{1/2} A + (1 - A^2)^{1/2} B \quad (27)$$

and by using the identity  $\cos^2 \theta = 1 - \sin^2 \theta$ , Equation 26 becomes

$$\sin^2 \gamma = \sin^2 \theta \sin^2 \lambda + \cos^2 \lambda \quad (28)$$

The relationship between the angle,  $\lambda$ , and the DRS orbit angle,  $\phi$  (angle between the line of nodes and the DRS-earth line), is given by

$$\cos \lambda = \sin \phi \cos \eta$$

where  $\eta = i - 90$  degrees, and  $i$  is the orbit inclination angle and also varies with altitude for a sun-synchronous orbit. Thus,

$$\cos \lambda = \sin \phi \sin i \quad (29)$$

Substituting Equation 29 into 28

$$\sin^2 \theta = \frac{\sin^2 \gamma - \sin^2 \phi \sin^2 i}{1 - \sin^2 \phi \sin^2 i} \quad (30)$$

The solution of Equation 30, which lies between 0 and  $\pi/2$ , is the value of interest, and the portion  $P$  of the orbit not visible by the DRS is given by

$$P = \frac{\theta}{\pi} \quad (31)$$

Figure 27 is a plot of  $P$  versus  $\phi$  for several orbital altitudes. Note:  $R_s = 22,767$  n. mi. and  $R_o = 3,444$  n. mi.

The value of  $\phi$ , where  $\theta = 0$ , is determined by using Equations 28 and 29 to solve for  $\phi$ . The result is

$$\sin \phi_o = \frac{\sin \gamma}{\sin i} \quad (32)$$

Figure 28 is a plot of  $\phi_o$  versus orbital altitude.

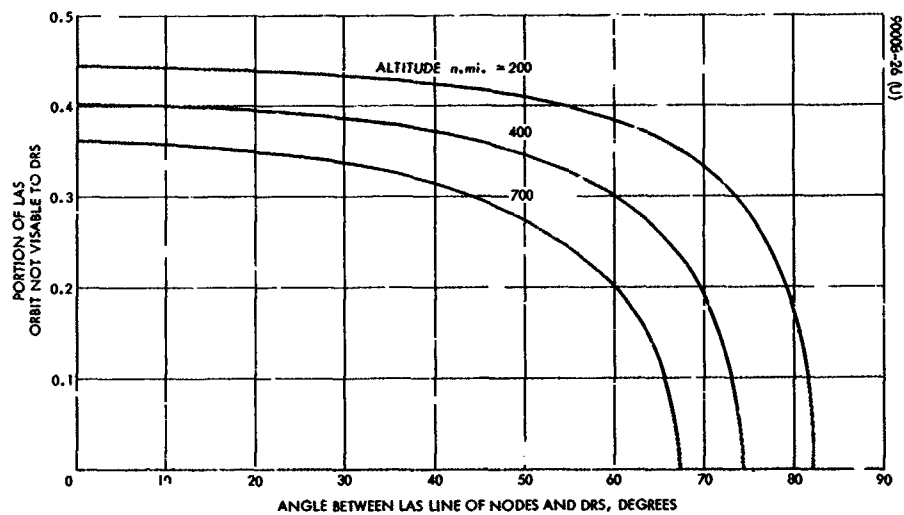


Figure 27. LAS Eclipse by Earth From DRS

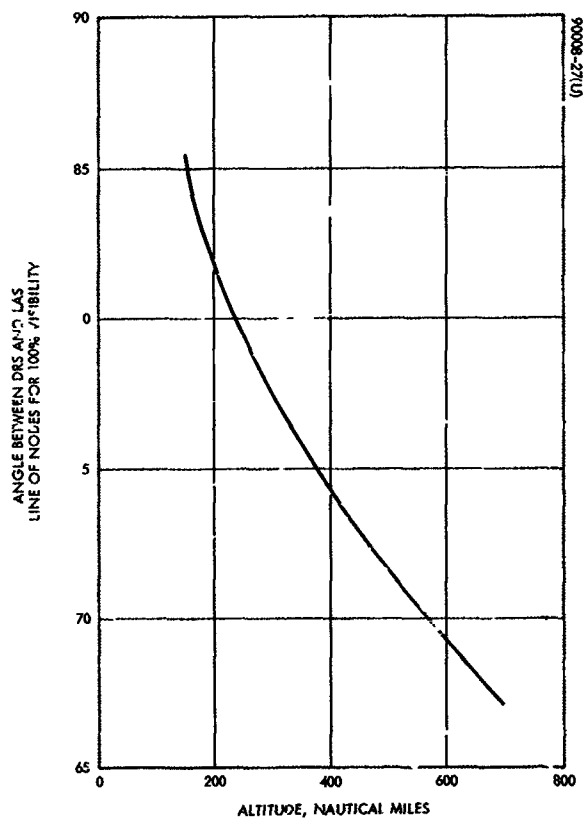


Figure 28. Angle Between DRS-Earth Line and LAS Line of Nodes for Complete Visibility

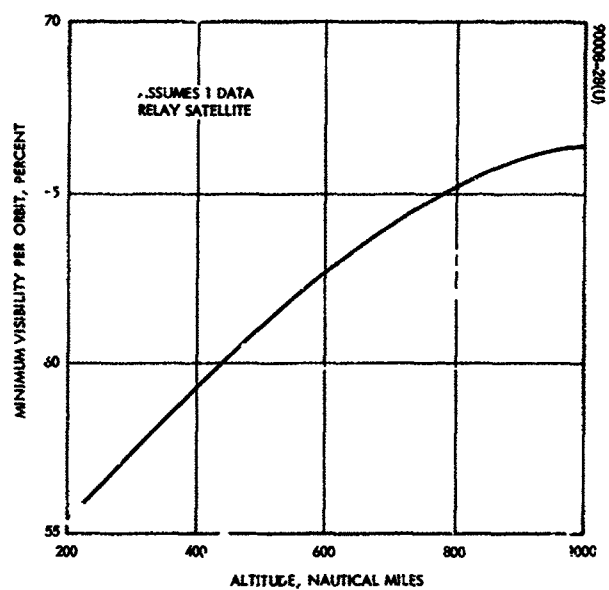


Figure 29. Minimum Visibility of LAS by DRS

As mentioned previously, the worst case or minimum visibility situation occurs when the DRS lies in the orbit plane and, thus, on the line of nodes. This can be seen from Figure 27, where this condition corresponds to  $\phi = 0$ . Substituting  $\phi = 0$  into Equation 30, it can be seen that  $\sin^2 \gamma = \sin^2 \theta$ , and so the minimum visibility condition requires only the solution of Equation 27, and then substituting  $\gamma = \theta$  into Equation 31. Thus, minimum visibility is a function of LAS altitude, and is shown in Figure 29.

The above analysis assumes that the DRS is stationary with respect to the LAS orbit during one orbit. Actually, the DRS will move through about 25 degrees of its orbit. This will slightly increase the actual visibility for the worst case. For various other LAS-DRS spatial relationships, the visibility may be slightly increased or decreased from the values of Figure 27.

### 3. 5. 2 Two Data Relay Satellites — One Ground Station

Consider Figure 30, where the geometry for two DRSs is shown. The plane of the drawing is the equatorial plane, and the circle around the earth is the intersection of the orbit sphere with this plane. The constraining relationships are shown. The angle  $2\gamma$  is the angular separation necessary for continuous coverage of the low altitude satellite. The angle  $\eta$  is the antenna elevation angle for an equatorial ground station.

As in previous analysis, define

$$\cos \alpha = \frac{R_e}{R_s} = A \quad (33)$$

$$\cos \beta = \frac{R_e}{R_e + h} = B \quad (34)$$

Then

$$\gamma = 180 - \alpha - \beta$$

Figure 31 is a plot of  $2\gamma$  as a function of altitude.

Turning to the elevation angle,  $\eta$ , the law of sines and the law of cosines yield

$$\frac{R_g}{\sin \gamma} = \frac{R_s}{\sin (90 + \eta)} = \frac{R_s}{\cos \eta} \quad (35)$$

$$R_g^2 = R_s^2 + R_e^2 - 2R_e R_s \cos \gamma \quad (36)$$

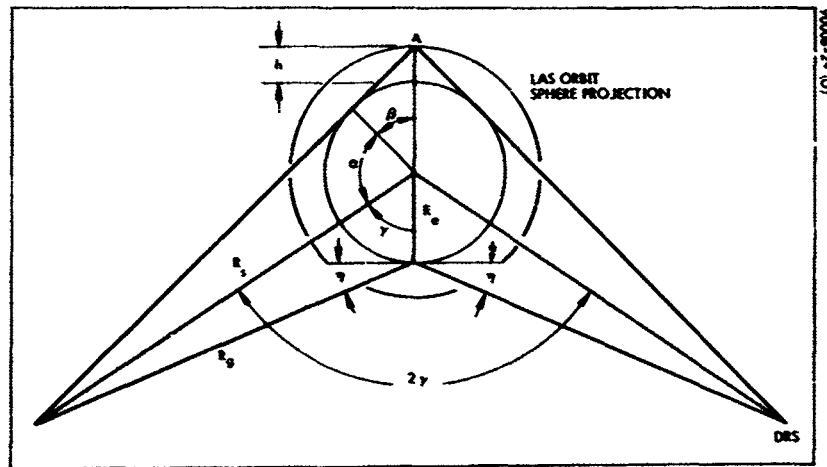


Figure 30. Geometry for Two DRSs and One Ground Station

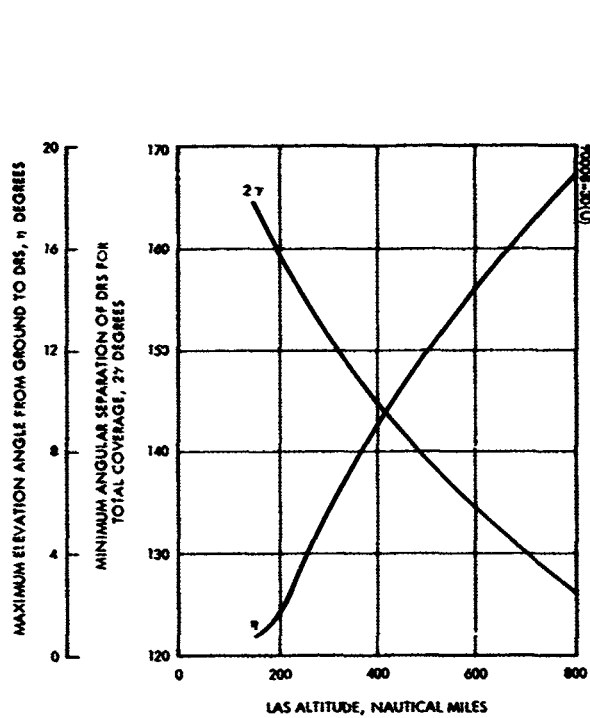


Figure 31.  $2\gamma$  and  $\eta$  as Function of Altitude

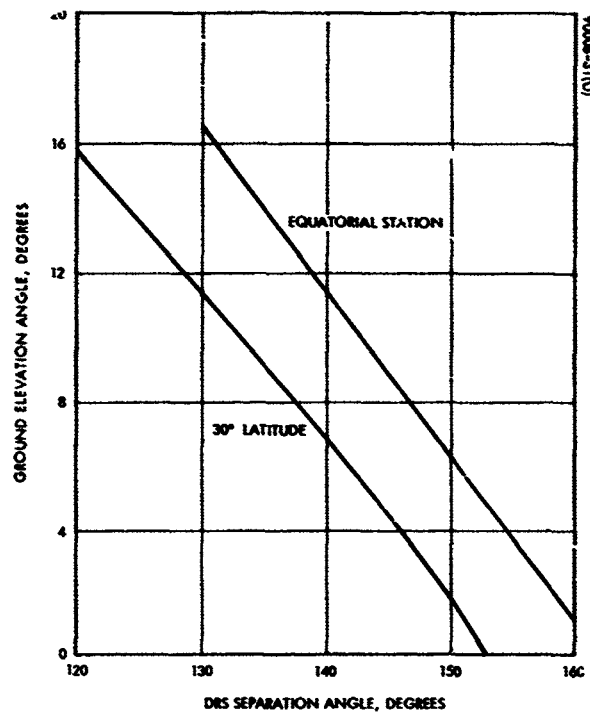


Figure 32. Ground Elevation Angle Versus DRS Separation Angle

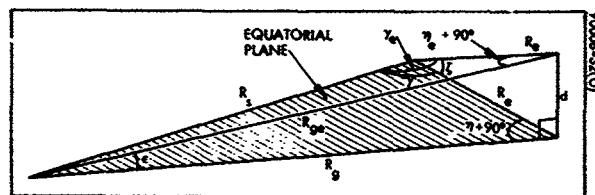


Figure 33. Geometry for Ground Station Not Located on Equator

Combining Equations 35 and 36

$$\cos \eta = \left[ 1 + A^2 - 2A \cos \gamma \right]^{-1/2} \sin \gamma \quad (37)$$

Figure 31 is also a plot of  $\eta$  as a function of LAS altitude. Figure 32 plots  $\eta$  as a function of  $2\gamma$ . Note that in order for the elevation angle,  $\eta$ , to be larger than 5 degrees, the LAS altitude must be greater than 280 n. mi.

Consider the situation where the ground station is not located on the equator but at some latitude,  $\zeta$ . The geometry for this case is illustrated in Figure 33, where it can be seen that

$$R_{ge}^2 = R_g^2 + d^2 \quad (38)$$

and

$$d = 2R_e \sin \frac{\zeta}{2} \quad (39)$$

Using the law of sines

$$\cos \eta_e = \frac{R_s}{R_{ge}} \sin \gamma_e \quad (40)$$

And from spherical trigonometry

$$\cos \gamma_e = \cos \gamma \cos \zeta \quad (41)$$

Furthermore, from Equation 35

$$R_g = R_s \frac{\sin \gamma}{\cos \eta} \quad (42)$$

The angle  $\eta_e$  is the ground elevation angle to each of the DRSs from the ground station at latitude,  $\zeta$ , and this angle must be found as a function of  $\gamma$  and  $\zeta$ . In order to do this, Equations 39 and 42 are substituted into Equation 38 to yield

$$R_{ge} = R_s \left( \frac{\sin^2 \gamma}{\cos^2 \eta} + 4A^2 \sin^2 \frac{\zeta}{2} \right)^{1/2} \quad (43)$$

and from Equation 41

$$\sin \gamma_e = (1 - \cos^2 \gamma_e)^{1/2} = (1 - \cos^2 \gamma \cos^2 \zeta)^{1/2} \quad (44)$$

Substituting Equations 43 and 44 into 40

$$\cos \eta_e = \cos \eta \left[ \frac{1 - \cos^2 \gamma \cos^2 \zeta}{\sin^2 \gamma + 4A^2 \cos^2 \eta \sin^2 \frac{\zeta}{2}} \right]^{1/2} \quad (45)$$

where  $\cos \eta$  is given by Equation 37. Substituting this expression into Equation 45 yields

$$\cos \eta_e = \left[ \frac{1 - \cos^2 \gamma \cos^2 \zeta}{1 + A^2 - 2A \cos \gamma + 4A \sin^2 \frac{\zeta}{2}} \right]^{1/2} \quad (46)$$

Figure 32 shows the relationship between the DRS separation angle and the elevation angle,  $\eta_e$ , for a ground station located at  $\zeta = 30^\circ$  latitude.

To illustrate the use of Figures 31 and 32, suppose an altitude of 500 n. mi. is desired. Then, from Figure 31 the DRS separation,  $2\gamma$ , must be at least 139 degrees, and the elevation is 12 degrees. However, rather than require the geometry of Figure 30, where the communication link is marginal when the LAS is at position A, the separation should be increased somewhat to provide overlap on the far side of the LAS orbit. Using Figure 32, if  $2\gamma$  were increased to 148.5 degrees, then  $\eta$  is reduced to 7 degrees for an equatorial ground station, and to about 5 degrees for a ground station at  $30^\circ$  latitude.

### 3.5.3 Comment

Figures 31 and 32 and the above example indicate that a DRS system with only two satellites has very strict limitations. Ground antenna elevation angles are small and accurate stationkeeping will be required.

### 3.6 COORDINATE SYSTEMS

In order to provide reference frames for relating orbital parameters to antenna pointing requirements and spacecraft motion, several reference coordinate systems are necessary. For consideration of the earth's magnetic field as a source of control torques, a geomagnetic reference is also needed.

#### 3.6.1 Inertial Reference ( $x_i y_i z_i$ )

This reference is an inertial coordinate set with the origin at the center of the earth; the  $x_i z_i$  plane the earth's equatorial plane; and the  $z_i$  axis along the line of the equinoxes, directed toward the autumnal equinox. For situations where only short-time dynamics are of interest and the sun's position is important, the  $z_i$  axis can be defined as the intersection of the  $y_i$ -sun vector plane and the equatorial plane (see Figure 34). This is particularly useful when considering the effects of solar radiation or for analyzing the behavior of a vehicle with steerable solar arrays.

#### 3.6.2 Orbital Reference ( $i, j, k$ )

This reference is a coordinate set with the origin at the center of the earth; the  $ik$  plane the orbit plane (which in general regresses in inertial space); and the  $i$  axis along the radius vector,  $r_o$ , directed from the center of the earth to the vehicle center of mass. The angle,  $i$ , is the inclination of the orbit plane to the equatorial plane. The angle between the line of nodes (intersection of the orbit plane with the equatorial plane) and the  $z_i$  axis is  $\lambda_o - \omega_\lambda t$ , where  $\lambda_o$  is this angle at  $t = 0$ , and  $\omega_\lambda$  is the nodal regression rate of the orbit plane. For convenience, define  $\lambda_o - \omega_\lambda t = \lambda$ . The angle  $\theta$  defines the angular position of the satellite relative to the ascending node. For the case where  $z_i$  is defined as the projection of the sun vector on the equatorial plane as mentioned above, and the orbit is sun synchronous,  $\omega_\lambda = 0$ ; i.e., both  $z_i$  and the line of nodes rotate with the same angular velocity, namely, the earth's angular velocity about the sun.

#### 3.6.3 Body Reference ( $xyz$ )

This reference is an orthogonal coordinate set fixed in the satellite with the origin at the vehicle center of mass. Usually this coordinate system is chosen to coincide with the principal axes of inertia of the vehicle or of some portion of the vehicle.

#### 3.6.4 Geomagnetic Reference ( $x_m, y_m, z_m$ )

This reference is an earth-fixed reference coordinate system with the origin at the center of the earth; the  $y_m$  axis directed toward the magnetic north pole;  $x_m z_m$  plane the magnetic equatorial plane, and the  $z_m$  axis coinciding with the intersection of the magnetic equatorial plane and the equatorial plane (see Figure 35). The angle between the  $z_m$  axis and the  $z_i$  axis is  $\psi = \psi_o + \Omega t$ , where  $\Omega$  is the earth's rotation rate. The angle between the  $y_i$  and  $y_m$  axes is approximately 11 degrees.



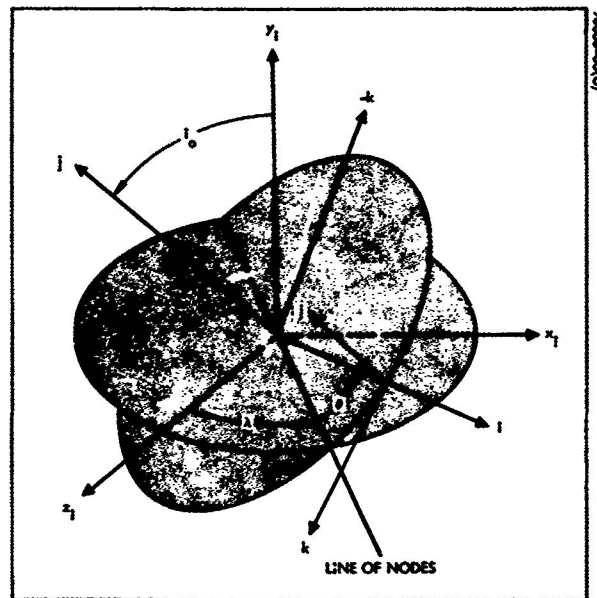


Figure 34. Orbital and Inertial Reference Coordinate Systems

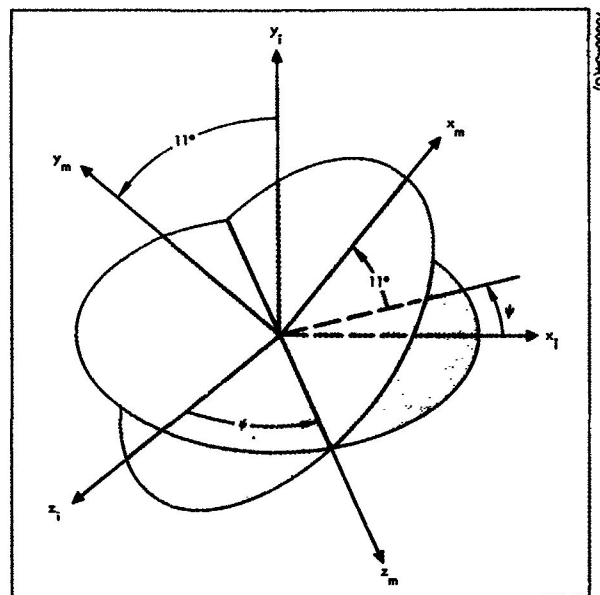


Figure 35. Magnetic and Inertial Reference Coordinate Systems

The transformation between vectors expressed in terms of the magnetic reference coordinates to inertial coordinates is given by

$$\begin{pmatrix} x_i \\ y_i \\ z_i \end{pmatrix} = H \begin{pmatrix} x_m \\ y_m \\ z_m \end{pmatrix} \quad (47)$$

where

$$H = \begin{pmatrix} \cos \psi & 0 & \sin \psi \\ 0 & 1 & 0 \\ -\sin \psi & 0 & \cos \psi \end{pmatrix} \begin{pmatrix} \cos 11^\circ & -\sin 11^\circ & 0 \\ \sin 11^\circ & \cos 11^\circ & 0 \\ 0 & 0 & 1 \end{pmatrix}$$

Denoting  $\cos 11^\circ = c_m$ ,  $\sin 11^\circ = s_m$

$$H = \begin{pmatrix} c_m \cos \psi & -s_m \cos \psi & \sin \psi \\ s_m & c_m & 0 \\ -c_m \sin \psi & s_m \sin \psi & \cos \psi \end{pmatrix} \quad (48)$$

The transformation of vectors from the  $x_i, y_i, z_i$  system to the  $i, j, k$  system is given by

$$\begin{pmatrix} i \\ j \\ k \end{pmatrix} = G \begin{pmatrix} x_i \\ y_i \\ z_i \end{pmatrix} \quad (49)$$

where

$$G = \begin{pmatrix} \sin \theta & 0 & \cos \theta \\ 0 & 1 & 0 \\ -\cos \theta & 0 & \sin \theta \end{pmatrix} \begin{pmatrix} \cos i & \sin i & 0 \\ -\sin i & \cos i & 0 \\ 0 & 0 & 1 \end{pmatrix} \begin{pmatrix} \cos \lambda & 0 & -\sin \lambda \\ 0 & 1 & 0 \\ \sin \lambda & 0 & \cos \lambda \end{pmatrix} \quad (50)$$

and so

$$\begin{aligned} g_{11} &= \sin \theta \cos i \cos \lambda + \cos \theta \sin \lambda \\ g_{12} &= \sin \theta \sin i \\ g_{13} &= \cos \theta \cos \lambda - \sin \theta \cos i \sin \lambda \\ g_{21} &= -\sin i \cos \lambda \\ g_{22} &= \cos i \\ g_{23} &= \sin i \sin \lambda \\ g_{31} &= \sin \theta \sin \lambda - \cos \theta \cos i \cos \lambda \\ g_{32} &= -\cos \theta \sin i \\ g_{33} &= \cos \theta \cos i \sin \lambda + \sin \theta \cos \lambda \end{aligned} \quad (51)$$

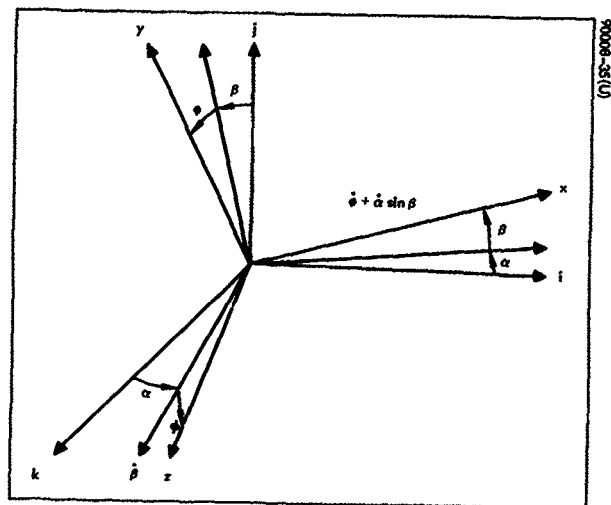


Figure 36. Orbital and Body Reference Coordinate Systems With Euler Angles

The body axes may be related to the ijk axes by means of Euler angles defined by three successive rotations. These Euler angles are illustrated in Figure 36 where the order of rotation as shown is  $\alpha - \beta - \phi$ .

The transformation of vectors in the body coordinate system (xyz) to the orbit system (ijk) is given by

$$\begin{pmatrix} i \\ j \\ k \end{pmatrix} = A \begin{pmatrix} x \\ y \\ z \end{pmatrix} \quad A = \begin{pmatrix} a_{11} & a_{12} & a_{13} \\ a_{21} & a_{22} & a_{23} \\ a_{31} & a_{32} & a_{33} \end{pmatrix} \quad (52)$$

where

$$\begin{aligned} a_{11} &= \cos \alpha \cos \beta \\ a_{12} &= \sin \alpha \sin \phi - \cos \alpha \sin \beta \cos \phi \\ a_{13} &= \cos \alpha \sin \beta \sin \phi + \sin \alpha \cos \phi \\ a_{21} &= \sin \beta \\ a_{22} &= \cos \beta \cos \phi \\ a_{23} &= -\cos \beta \sin \phi \\ a_{31} &= -\sin \alpha \cos \beta \\ a_{32} &= \sin \alpha \sin \beta \cos \phi + \cos \alpha \sin \beta \\ a_{33} &= \cos \alpha \cos \phi - \sin \alpha \sin \beta \sin \phi \end{aligned}$$

All of the above matrices are unitary and possess the following properties:

$$A^T = A^{-1} \quad (A^T = \text{transpose of } A)$$

$$\sum_{j=1}^3 a_{ij}^2 = 1 = \sum_{i=1}^3 a_{ij}^2$$

## 4. ANTENNA POINTING

### 4.1 INTRODUCTION

"Antenna pointing" means the method and procedure for following the data relay satellite (DRS) with a directive, mechanically steered antenna mounted on the low-altitude satellite (LAS). The motion of the antenna must compensate for the orbital and rotational motion of the LAS and the motion of the DRS. Antennas may be mounted on either the body of the spacecraft or on the solar panels; the geometry involved in each method is significantly different.

The number of antennas, a major consideration, is discussed in the following subsection. Methods of gimbaling one or more antennas, also of major interest, are discussed in Section 4.3. Subsections following these deal more specifically with particular gimbaling and antenna-mounting methods.

In the following sections, it will be seen that antenna pointing requires consideration of spacecraft structure and configuration and of LAS-DRS geometry. Discussion of spacecraft structure and configurations is restricted in this section to only those general aspects that influence antenna pointing.

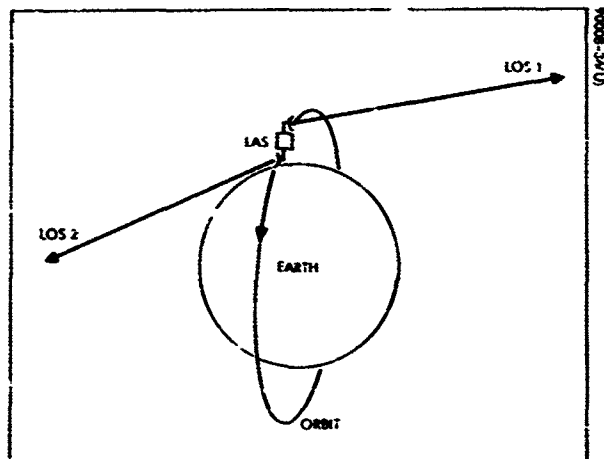


Figure 37. Necessity for Changeover  
LOS 1 about to be intercepted by earth

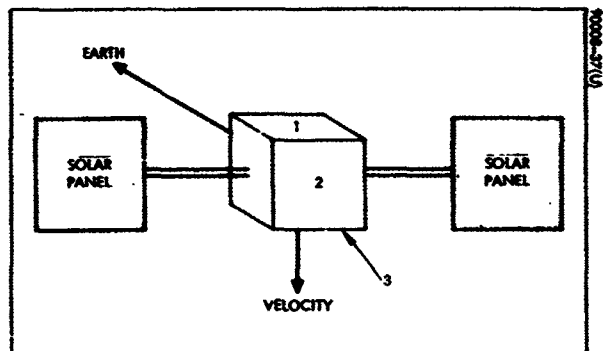


Figure 38. Sides of Earth-Oriented  
Body Available for Antenna Mounting  
Three-axis stabilized

## 4.2 NUMBER OF ANTENNAS AND MOUNTING CONSIDERATIONS

The number of antennas to be used on the LAS depends on the data transmission requirements. If continuous, uninterrupted communication is required, then two antennas are needed, whereas only one is needed if blackout periods during each orbit are acceptable.

Future LAS missions may require optical or infrared imaging of the entire earth including the polar regions. Or relayed data from ground instrument packages may be desired on a global basis. The first and possibly the latter mission will require uninterrupted data transmission if data storage is to be avoided, which is a fundamental assumption of this study.

On the other hand, for many earth observation missions, the polar regions may be ignored which would allow time to steer an antenna from one DRS toward another. And some optical imaging missions may require data transmission only on the sunlit side of the earth which would allow one-half of an orbit to reposition a single antenna.

### 4.2.1 Continuous Data — Two Antennas

The necessity for two antennas for continuous data is obvious from a consideration of the changeover problem. As the earth interrupts the line of sight (LOS) between an LAS antenna and a DRS, another antenna must be pointed at another DRS ready for changeover. This changeover situation is illustrated in Figure 37 where LOS 1 is about to be intercepted by the earth, while LOS 2 will be the transmission path after changeover. Note that two antennas are mounted on booms extended on opposite sides of the spacecraft on an axis coinciding with the velocity vector. That is, the antennas are attached to the sides of the spacecraft that are perpendicular to the z-axis defined in Section 3.6. There are several reasons this is a preferred configuration for two body-mounted antennas. These reasons are based on orbital geometry and spacecraft configuration considerations.

There are two fundamental spacecraft structure types — the momentum bias system type 1 and the three-axis stabilized spacecraft which here includes the momentum bias system type 2 (see Section 7).

#### Three-Axis Stabilized Spacecraft

Consider a three-axis stabilized spacecraft that is earth-oriented with solar panels. The primary solar array drive is normal to the orbit plane; so, if the spacecraft is visualized as a six-sided box, this drive protrudes from the two sides parallel to the orbit plane. Of the remaining four sides, one is facing the earth (an antenna mounted on this side would severely interfere with the sensors). The three remaining sides — the side facing away from the earth and the two sides perpendicular to the velocity vector — are viable candidates for mounting antennas and are shown numbered in Figure 38. For continuous data, requiring two antennas, these are most naturally and symmetrically mounted on the opposite sides of the spacecraft

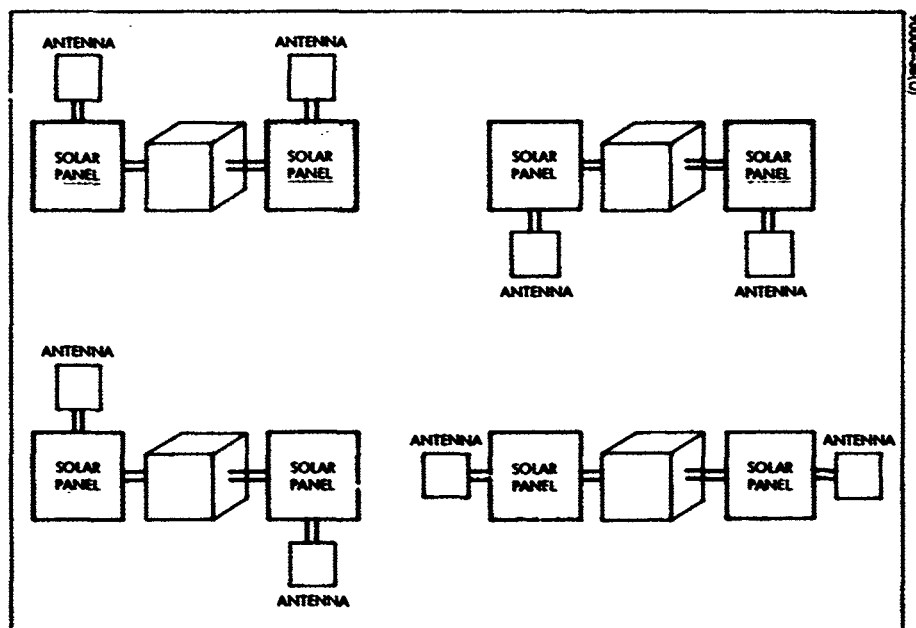


Figure 39. Possible Ways to Mount Two Antennas on Three-Axis Stabilized Solar Panels



that are perpendicular to the velocity vector (sides 1 and 3). Although one antenna could be mounted on the outward side and one on a side perpendicular to the velocity vector, no apparent advantage is gained by this configuration, but mounting, gimbaling, and steering symmetry are lost. Hence, the preference for two body-mounted antennas to be extended away from the spacecraft in opposite directions along the axis defined by the velocity vector, i.e., the z-axis (see Section 3.6).

As mentioned previously, the antennas may be mounted on the solar panels which gives some gimbaling advantages discussed later along with several disadvantages. For the three-axis stabilized spacecraft with two solar panels, structural interference considerations as well as symmetry preference require that one antenna be mounted on each solar panel.

To eliminate shadowing of the solar panels, the antennas must be mounted off the edges. Three edges are available — the two that extend away from the body of the spacecraft and the outer edge farthest from the body. Defining the upper edge as that edge parallel to the ecliptic plane but above the other in the direction of the ecliptic normal and the lower edge as the opposite edge, it is possible to mount, 1) both antennas on the upper edges, 2) both on the lower edges, 3) one on a lower and one on an upper edge, or 4) one on each of the outer edges. These four possibilities are shown in Figure 39. None of these configurations has any particular pointing advantage. However, antennas attached to upper or lower edges must be mounted on booms long enough to eliminate interference of the radiated energy by the corner of the solar panel.

There are a number of disadvantages to mounting antennas on the solar panels; principally, 1) the structural complexities, 2) the more complex solar panel drive and antenna drive systems, 3) longer antenna feed distances and more rotary joints, and 4) greater packaging problems. In addition, the advantages of solar panel mounting can be obtained with body-mounted antennas without most of these disadvantages, as will be pointed out in the next subsection.

#### Momentum Bias System Type 1 (MBS Type 1)

The MBS Type 1 is significantly different from a three-axis stabilized spacecraft in that the basic body cannot be considered as a single box or structural volume. Rather the basic spacecraft consists of two bodies — one spinning and the other earth-oriented. The spin axis is normal to the orbit plane and so the asymmetry is along this axis. Since the primary solar drive must also be normal to the orbit plane, putting a solar panel on each side of the two-body spacecraft would require two independent solar panel drives or complex drive electronics to rotate each solar panel with respect to the two bodies which themselves are rotating with different speeds. These complexities are reduced if only a single solar panel is employed.

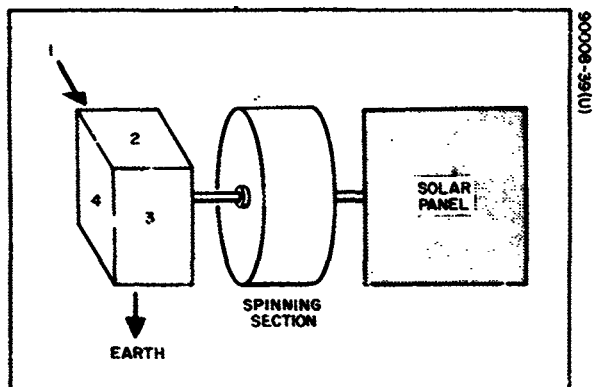


Figure 40. Four Sides Available for Antenna Mounting

MBS Type 1

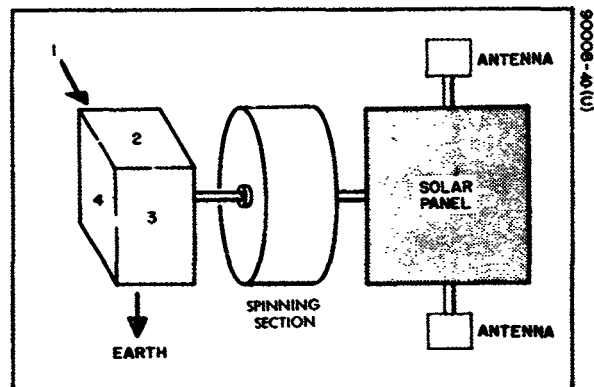


Figure 41. Two Antennas Mounted on MBS Type 1 Solar Panel

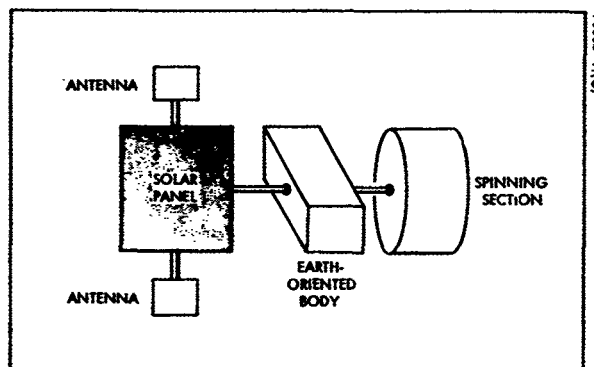


Figure 42. Alternate Configuration – Solar Panel Next to Earth-Oriented Body

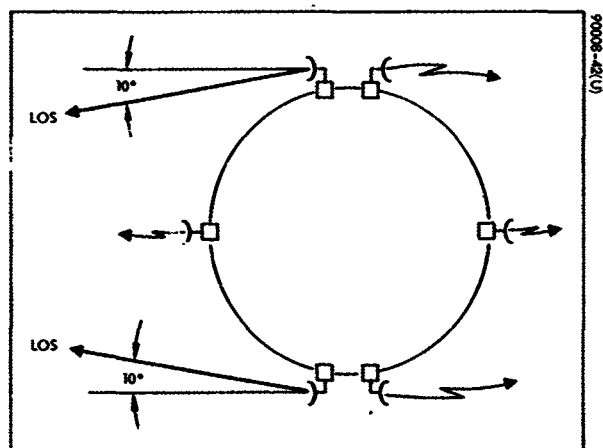


Figure 43. Pointing a Single Antenna

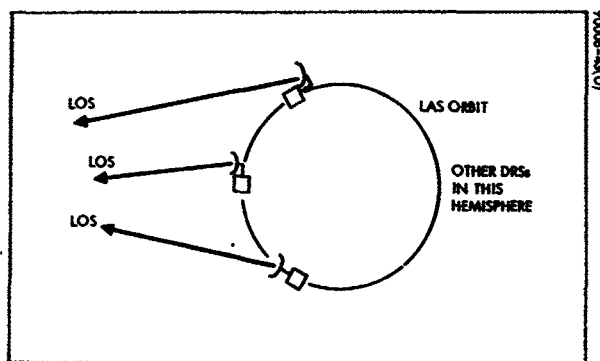


Figure 44. Spacecraft Interference Forcing Changeover at Undesirable Orbit Position for Mounting as Shown

Two antennas may be mounted to the earth-oriented body with the same considerations as with a three-axis stabilized spacecraft. The same three sides of the earth-oriented body are available for antenna mounting. In addition, if the solar panel is placed next to the spinning body, then the opposite side of the earth-oriented body from the spinning section is also available. The four sides available for antenna mounting are shown numbered in Figure 40. For the two-antenna requirement being considered here, symmetry and interference considerations indicate a preference for sides 1 and 3, i.e., the sides perpendicular to the velocity vector.

Mounting antennas on the single solar panel is a possibility, but for the configuration shown in Figure 41, the antenna feed lines will be undesirably long. An alternate configuration shown in Figure 42, with the solar panel driven from the earth-oriented body, allows shorter feed lines, but still entails the additional mechanical difficulties.

#### 4.2.2 Noncontinuous Data -- One Antenna

If an LAS mission will allow periods of data interruption, then only one directive antenna is necessary. For many optical imaging missions, the regions near the poles will be of less importance than lower latitude areas. This is due to poorer lighting conditions near the poles as well as the fact that these regions are relatively uninhabited. Such a mission may only require high data quantity transmission on the sunlit side of the earth. In either case, time is allowed to steer the antenna from one DRS to another to provide communications during the required portions of the orbit. Since for the majority of missions blackout over or near the poles is more acceptable than over other regions, the mounting and steering considerations associated with this case will be discussed here.

##### Three-Axis Stabilized Spacecraft

If changeover begins within 10 orbit degrees of the nearest point to the poles and the DRSS consists of three data relay satellites, then a DRS will always lie in the outward satellite-fixed hemisphere. That is, the half-space defined by the plane through the LAS, normal to the x-axis, (local vertical) facing outward away from the earth will always contain a DRS. Thus, the side of the earth-oriented body away from the earth is an attractive location for mounting a single body-mounted antenna. Figure 43 illustrates the mounting and resultant pointing geometry as well as changeover.

Figure 38 shows the available sides for antenna mounting on a three-axis stabilized spacecraft. If a single antenna were mounted on sides 1 or 3, spacecraft interference would force changeover at an undesirable position; when this interference occurs, there may be no other DRS within view. This problem is illustrated in Figure 44.

Solar panel mounting is also a possibility, but symmetry is lost when the single antenna is mounted on one of the solar panels. The drive and structure of the two panels will be significantly different, and the antenna feed will be longer than that needed for a body-mounted antenna. Moreover,

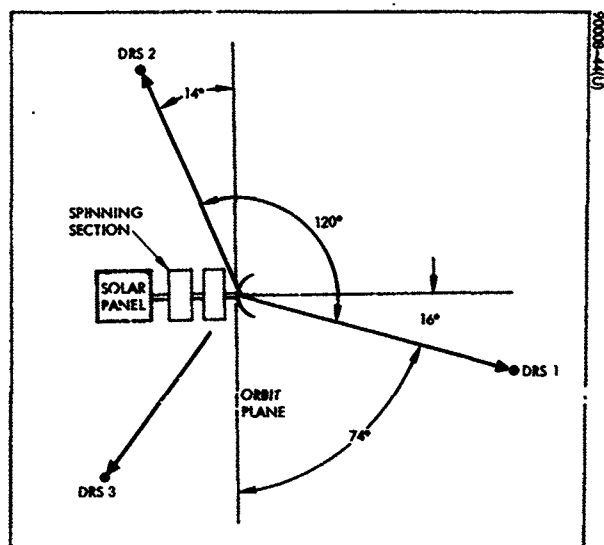


Figure 45. Worst-Case Geometry for Pointing Antenna Mounted to Side 4 (see Figure 40)

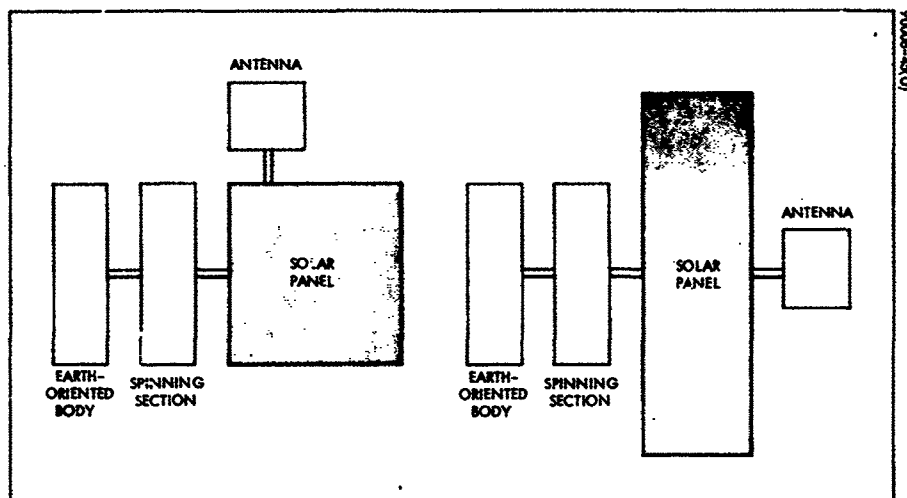


Figure 46. Single Antenna Mounting Possibilities - MBS Type 1

the gimbaling advantage of a solar-panel-mounted antenna can be achieved with a body-mounted antenna with only slight increase in complexity, while eliminating the above mentioned problems. Thus, for a three-axis stabilized spacecraft, a single solar-panel-mounted antenna is not recommended.

#### MBS Type 1

The four available sides for a body-mounted antenna are shown in Figure 40. Sides 1 and 3 are not recommended for the same reason as presented for the three-axis stabilized spacecraft. The two remaining sides are possibilities with side 2 being attractive for the same reasons as mentioned above. The principal difference between the MBS Type 1 and a three-axis stabilized satellite is that the MBS Type 1 offers an additional "free" side. This side, numbered 4 in Figure 40, is also an attractive candidate for mounting an antenna.

The side parallel to the orbit plane is only useful for antenna mounting if there are three or more DRSs. Consider a three-DRS system and an LAS altitude of 400 n.mi. From Figure 28, total orbit visibility of a DRS by the LAS is possible only if the angle between the LAS line of nodes and the DRS is greater than 74 degrees. Thus, the worst case or design geometry for pointing capability is shown in Figure 45. The antenna must be able to look back on one side of the orbit plane 14 degrees in addition to covering all of the other side. This look-back angle increases to about 22 degrees for a 200-n.mi. orbit altitude. This angle when compared to the look-down angle of about 10 degrees, shown in Figure 43 indicates that an antenna mounted on side 4 must have slightly greater pointing capability. If there are more than three DRSs, it can have less pointing capability. It should be noted that mounting an antenna on side 4 is desirable only if more than two DRSs are available, and the required pointing capability depends both on the number of DRSs and the LAS altitude.

For solar panel mounting, two general configurations are shown in Figure 46. The disadvantages have been mentioned above.

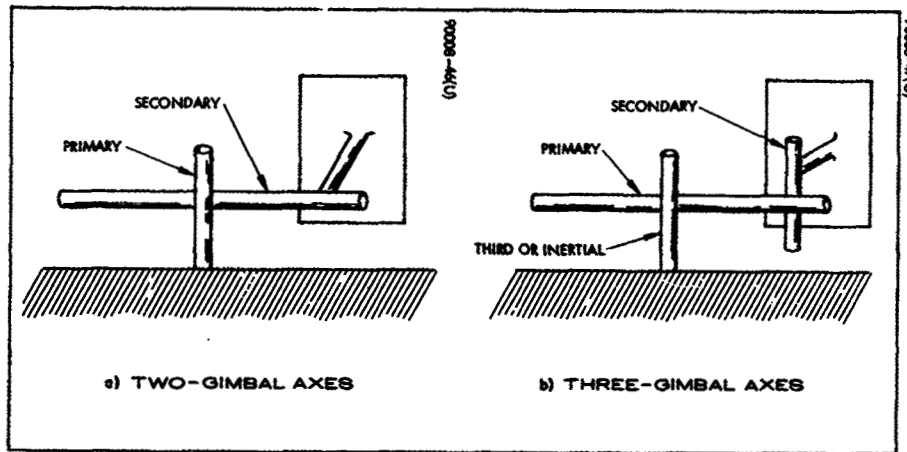


Figure 47. Gimbal System Schemes

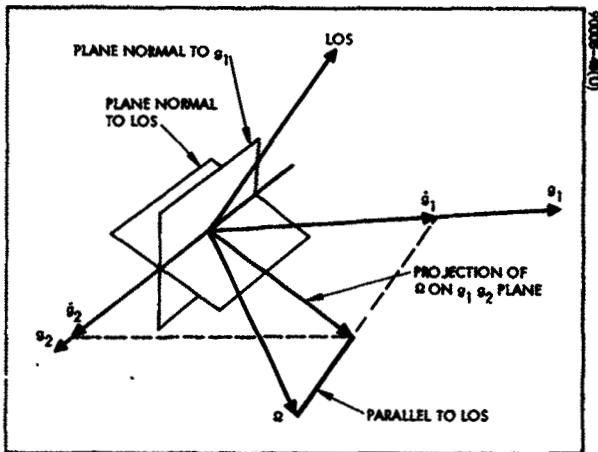


Figure 48. Geometric Determination of Gimbal Rates

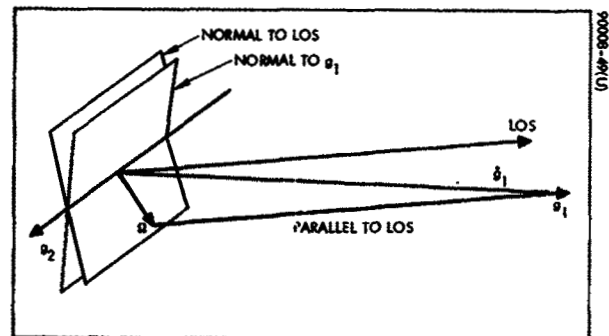


Figure 49. Primary Gimbal Axis Rate Increase When LOS and Primary Axis Are in Close Proximity

### 4.3 GIMBALING

Gimbaling here refers to the methods of providing the required antenna rotational motion. To mechanically rotate an antenna with respect to the spacecraft or a part of the spacecraft, there must be one axis of rotation fixed rigidly to the spacecraft and one axis fixed rigidly to the antenna. If these are the same axis, then only rotation about that axis is possible. If there are two axes, the axis fixed to the spacecraft is called the primary axis, and the axis fixed to the antenna is called the secondary axis. If there are three axes of rotation, the axis attached to the antenna is again called the secondary axis, and the axis that orients the secondary axis is again called the primary. The axis that is attached to the spacecraft and orients the primary axis is called the third axis or inertial axis for reasons to be discussed later. Thus, for the three-gimbal system, the primary axis is the middle axis that connects the two axes which are attached to the spacecraft and the antenna. These two schemes are illustrated in Figure 47.

#### 4.3.1 Two-Gimbal Axes

Theoretically, an antenna can be pointed in any direction if it has two connected axes of rotation — one fixed in inertial space (the primary) and the other fixed to the antenna (the secondary). One heuristic argument supporting this statement is based on the fact that rotational motion about the axis defined by the line of sight (LOS) is unnecessary and/or unimportant; hence, only two other degrees of rotational motion are required. Practical considerations of structural design and mounting methods limit the antenna motion to less than the ideal. However, this limitation occurs for any antenna steering system. The major problem with a two-gimbal system is that the angular rate about the primary axis can be very large. To see how and why this occurs, consider the following heuristic discussion.

Denote the primary axis of an orthogonal two-gimbal system by  $g_1$  and the secondary axis by  $g_2$ . Orthogonal means that  $g_1$  is perpendicular to  $g_2$ . Let the antenna pointing direction be perpendicular to  $g_2$ . Such a configuration is shown in Figure 47a. Since the pointing direction must coincide with the LOS to the target,  $g_2$  lies in the plane normal to the LOS, but also must lie in the plane normal to  $g_1$  because of the orthogonal design. Thus, the rotation of  $g_2$  about  $g_1$  must be such as to make  $g_2$  coincide with the intersection of these two planes. But in addition to this positioning requirement about  $g_1$ , the relative angular rate of the LOS with respect to the body to which  $g_1$  is fixed must be compensated.

It was mentioned previously that rotational motion about the LOS is unimportant. Thus, the angular rates  $\dot{g}_1$  and  $\dot{g}_2$  must compensate for the component of the LOS angular rate,  $\Omega$ , which is normal to the LOS. As just explained,  $g_2$  is defined by  $g_1$  and the LOS. And consistent with the above argument,  $\dot{g}_1$  and  $\dot{g}_2$  are defined by the projection of the  $\Omega$  vector along the LOS onto the  $g_1$ - $g_2$  plane. This geometric interpretation is illustrated in Figure 48. The gimbaling problem occurs when the LOS and  $g_1$  coincide or nearly coincide. Figure 49 indicates geometrically why  $\dot{g}_1$  becomes very

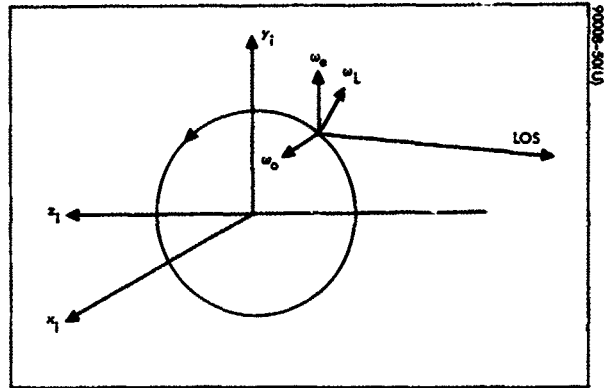


Figure 50. Three Components of LOS-LAS  
Relative to Angular Velocity

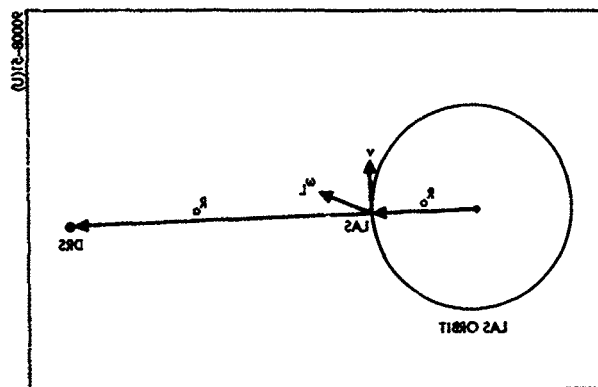


Figure 51. Geometry for Maximum  
Magnitude of  $w_L$



large; namely, the projection of the LOS angular rate,  $\Omega$ , along the LOS onto the  $g_1$ - $g_2$  plane results in a large value of  $\dot{g}_1$ . Theoretically, when the LOS and  $g_1$  coincide,  $\dot{g}_1$  must be infinite in order to point the antenna at the target.

Furthermore, the gimbal angle rates must satisfy

$$\dot{g}_1^2 + \dot{g}_2^2 = (\text{component of } \Omega \text{ normal to LOS})^2$$

so that when the primary gimbal rate becomes relatively large, the secondary must provide compensatory motion and, hence, becomes large also. Thus, when  $g_1$  and the LOS coincide, both  $\dot{g}_1$  and  $\dot{g}_2$  must be infinite in order to follow the DRS.

In order to make further discussion of this problem meaningful, an approximate quantitative analysis is necessary. The relative angular velocity,  $\Omega$ , between the earth-oriented body and the LOS vector must be analyzed. This angular velocity can be separated into three quantities expressed in inertial coordinates (see Section 3.6): 1) the angular velocity  $\omega_o$ , of the earth-oriented body, 2) the angular velocity,  $\omega_L$ , of the LOS due to the orbital motion of the LAS, and 3) the angular velocity,  $\omega_d$ , of the LOS due to the orbital motion of the DRS.

Referring to Figure 50 where these three components are illustrated, each can be evaluated as shown below. The LAS orbit is chosen to be polar with the line of nodes coinciding with the  $z_1$  axis.

- 1) LAS angular velocity -- This angular velocity in inertial coordinates is merely the orbital angular velocity because the LAS is earth-oriented. For a 400-n.mi. altitude, referring to Figure 21

$$|\omega_o| = \frac{360}{100} = 3.6 \text{ deg/min} \quad (1)$$

Thus,

$$\omega_o = \begin{pmatrix} 3.6 \\ 0 \\ 0 \end{pmatrix}$$

- 2) LOS angular motion due to LAS orbital motion -- the maximum value of  $\omega_L$  occurs under the geometrical circumstances shown in Figure 51.

$$|\omega_L|_{\max} = \frac{v}{R_a} = |\omega_o| \frac{R_o}{R_a} \leq 0.23 |\omega_o| \quad (2)$$

At other times, the component of linear velocity normal to the LOS will be less and  $R_a$  will be greater. This angular velocity vector is normal to the plane containing the LAS velocity vector and the LOS ( $R_a$ ). In vector algebra

$$\bar{\omega}_L = \frac{\bar{v} \times \bar{R}_a}{|\bar{R}_a|^2} = \frac{(\bar{\omega}_o \times \bar{R}_o) \times \bar{R}_a}{|\bar{R}_a|^2} \quad (3)$$

- 3) LOS angular velocity due to DRS motion – This quantity is given approximately by

$$|\omega_d| \approx \frac{v_d}{R_a} = \omega_e \frac{R_s}{R_a} \quad (4)$$

where  $\omega_e$  is the earth's rotational speed (0.25 deg/min) and  $R_s$  is distance from the earth's center to the DRS (22,767 n.mi). The maximum value of  $|\omega_d|$  occurs when the DRS lies along the line of nodes.

$$|\omega_d|_{\max} = \omega_e \frac{R_s}{(R_a)_{\min}} = 1.24 \omega_e = 0.31 \text{ deg/min} \quad (5)$$

#### Case A

Consider now a polar orbit with the primary gimbal axis normal to the LAS orbit plane and the LOS and primary axis nearly coinciding, as shown in Figure 52. The three angular velocity components just discussed are shown. The relative angular velocity  $\bar{\Omega}$  between the LAS and LOS is given by

$$\bar{\Omega} = \bar{\omega}_d + \bar{\omega}_L - \bar{\omega}_o \quad (6)$$

As shown in Figure 52, the primary gimbal axis rate  $\dot{g}_1$  is given approximately by

$$\dot{g}_1 = |\omega_o| + |\omega_d| \csc \epsilon \approx 3.6 + 0.3 \csc \epsilon \text{ deg/min} \quad (7)$$

If the angular proximity effect is ignored, the primary gimbal rate varies between  $|\omega_o| - |\omega_L|_{\max}$  and  $|\omega_o| + |\omega_L|_{\max}$ . This latter will be used as a basic comparison value

$$|\omega_o| + |\omega_L|_{\max} = 1.23 |\omega_o| = 4.5 \text{ deg/min}$$

Then in order that the additional angular rate due to the proximity of  $g_1$  and the LOS be equal to or less than this value

$$0.3 \operatorname{cosecant} \epsilon \leq 4.5$$

or

$$\operatorname{cosecant} \epsilon \leq 15$$

$$\epsilon \geq 3.8 \text{ degrees}$$

The primary axis will always be separated from the LOS by more than 4 degrees if the inclination of the LAS orbit is less than 76 degrees or greater than 104 degrees. The geometry for this result is shown in Figure 53. However, for inclinations in the range 80 to 100 degrees which include polar and sun-synchronous orbits, there is no body-fixed axis that does not at some time during the LAS orbit coincide with a possible LOS to a DRS.

#### Case B

Now, consider a polar orbit with the primary axis in the LAS plane with near-coincidence as shown in Figure 54a. The three angular velocity components are shown, and it can be seen that

$$\dot{g}_1 \approx |\omega_d| \csc \epsilon \approx 0.31 \csc \epsilon \text{ deg/min} \quad (8)$$

In Figure 54a, the LOS is shown in the orbit plane. Suppose the LOS is in the equatorial plane, as shown in Figure 54b. For this situation,  $g_2$  is normal to the equatorial plane, and it can be seen that the projection on the  $g_1 g_2$  plane results in large values of the gimbal rates.

$$\dot{g}_1 \approx |\omega_o + \omega_L| \csc \epsilon$$

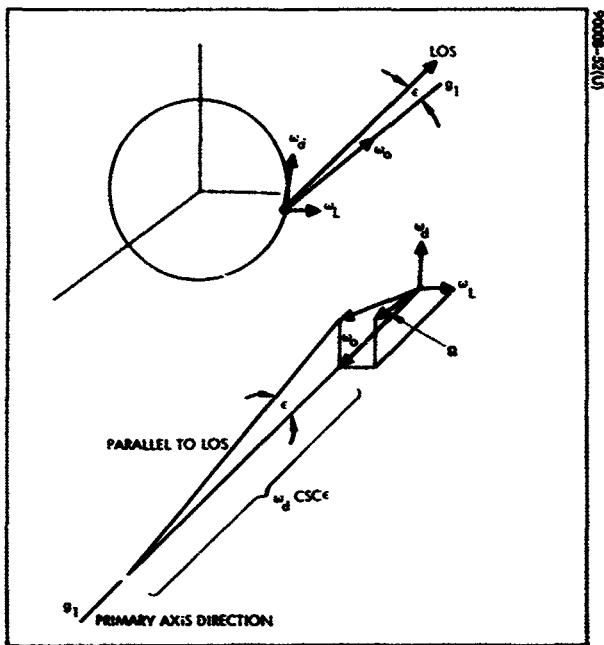


Figure 52. Polar Orbit With Primary Gimbal Axis Normal to LAS Orbit Plane and LOS and Primary Axis Nearly Coinciding

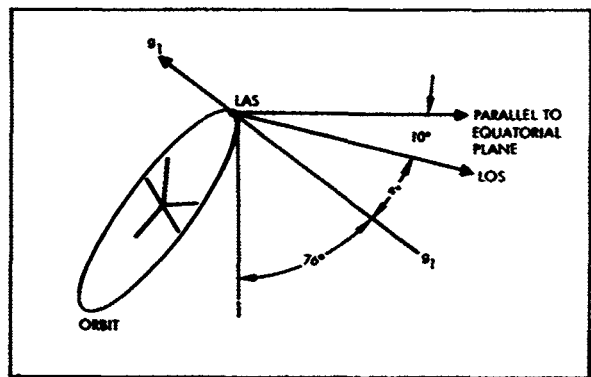
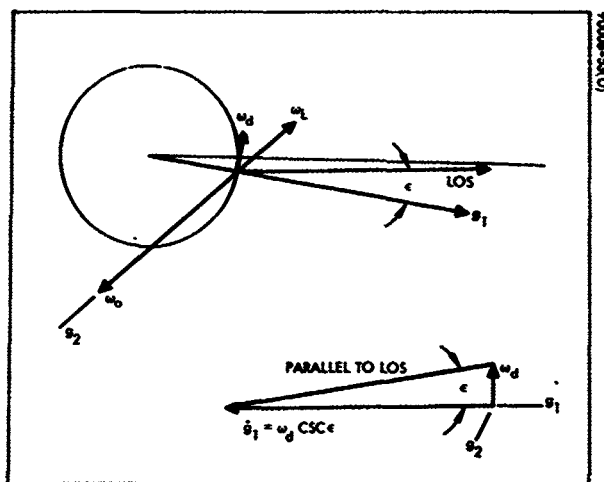
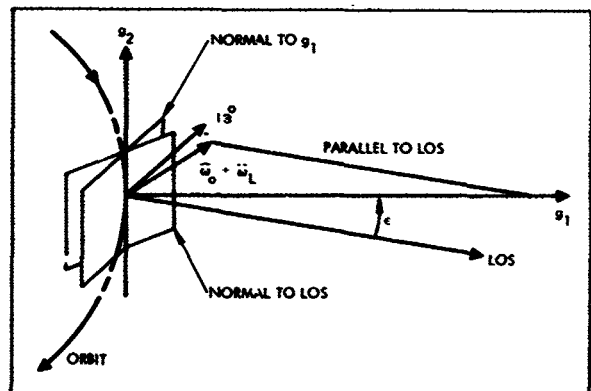


Figure 53. Geometry for Maximum LAS Orbit Inclination With Primary Gimbal Axis Normal to Orbit Plane



a) LOS in Orbit Plane



b) LOS in Equatorial Plane

Figure 54. Polar Orbit With Primary Axis in LAS Orbit Plane

For this case, in order that  $\dot{g}_1$  not exceed twice its nominal minimum and comparison value  $|\omega_0 + \omega_L|$

$$\csc \epsilon \leq 2 \text{ or } \epsilon \geq 30 \text{ degrees}$$

#### Comments

The above angles, limiting the angular proximity of the primary gimbal axis and the LOS, ensure that the maximum gimbal rate is limited to approximately twice the minimum value. These angles can be reduced if motors large enough to produce the higher angular rates can be readily incorporated into the pointing system design. However, provision for such a large variation of required angular rates is usually weight-inefficient.

As just shown above, if the primary gimbal axis is normal to the orbit plane, it will always be separated from the LOS by more than 4 degrees if the inclination of the LAS orbit is less than 76 degrees or greater than 104 degrees. However, for inclinations in the range 80 to 100 degrees which include polar and sun-synchronous orbits, there is no body-fixed axis that does not at some time during the LAS orbit coincide with a possible LOS to a DRS. That is, for these LAS orbit inclinations, any arbitrarily chosen axis fixed in the earth-oriented body will at some time point toward a location in space at geostationary altitude where a DRS could be. This occurs because the earth-oriented body is rotating about the orbit normal and because its orbital motion corresponds to a  $\pm 10$  degrees as seen from a DRS. Since these inclinations are popular for many earth observation missions, the gimbal rate problem is a consequence of the orbital geometry.

There are several ways to eliminate or minimize this problem.

- 1) Two antennas — If two antennas are used, their primary axes can be fixed in the earth-oriented body in different directions so that during the portions of the LAS orbit in which each is used their respective primary axes are adequately separated from the LOS. Or alternatively the primary axes of the antenna can be made parallel, and when the axis of the transmitting antenna begins to approach the LOS so that the angular rate becomes excessive, the other antenna is pointed to another DRS and transmission is switched to this antenna. These methods are treated in somewhat greater detail later.
- 2) Off-target pointing — An obvious method to avoid the high gimbal rates is to refuse to point the antenna in a direction close to the primary axis. That is, the antenna pointing direction will not coincide with the LOS when the LOS is near to the primary gimbal axis. If the target DRS lies along the primary axis or very near it, then the antenna will not be pointing the center of its directive beam at the DRS — hence, the term "off-target pointing." This method is not applicable if the antenna is highly directive,

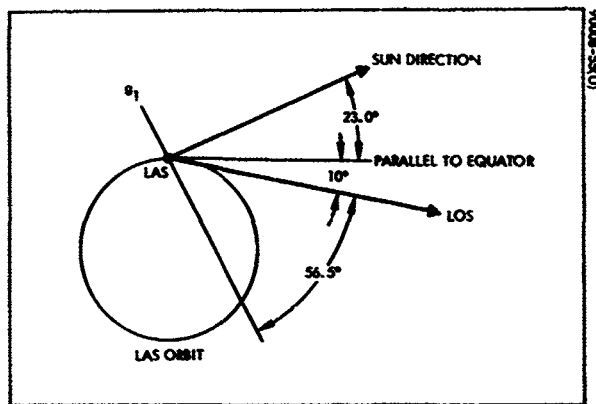


**Figure 55. Polar Orbit and Worst-Case Geometry for Determining Closest Angular Approach of LOS and  $g_1$**

i. e. , the beamwidth is small. For optical imaging missions, such as the representative mission chosen in Section 2, the data rates and bandwidths will be large, and analysis of the communication link indicates that required antenna gain will probably be 30 dB or greater which means that the 3-dB beamwidth will be less than 5 degrees. Such an antenna must be pointed to within 2.5 degrees or less of the LOS; for this case, off-target pointing is dubious.

For instance, in order to point within 2 degrees of the primary axis, according to the previous analysis, Case A, a gimbal rate of approximately 12.2 deg/min is required which is nearly 3-1/2 times the LAS orbital angular rate. For an antenna with a 2-degree beamwidth, only 1-degree of deviation from the LOS can be allowed which requires a gimbal rate of 20.8 deg/min — nearly six times the LAS orbit angular rate.

If the antenna gain is less than about 24 dB corresponding to a 3 dB beamwidth of 10 degrees, the antenna can be allowed to deviate from the LOS by 4 or 5 degrees, which, for Case A, according to the above analysis, ensures that the maximum gimbal rate is reasonable.

- 3) Solar panel mounting — An antenna may be mounted to a solar panel as discussed in the preceding subsection. Since the solar panel is oriented so that its surface is perpendicular to the sun direction, there is an axis parallel to this surface which is also parallel to the LAS orbit plane. Orienting the primary gimbal axis in this direction ensures that it will always be separated from the LOS by at least 56.5 degrees which eliminates the gimbaling problem of concern here. The worst-case conditions yielding this result are shown in Figure 55.
- 4) Three-gimbal axes — Providing an additional gimbal axis allows another degree of rotational freedom and eliminates the gimbal rate problem. In this case, the third axis keeps the primary axis always pointed away from the LOS, possibly and ideally normal to it, thereby eliminating the gimbal rate problem. This subject is treated below as a separate topic because of its potential.

#### 4.3.2 Three-Gimbal System

As just discussed, a three-gimbal system eliminates the problem of large gimbal rates, but it introduces additional complexity into the antenna steering mechanical and electronic design. As mentioned previously, mathematically only two rotational degrees of freedom are required and the two gimbal angles can be expressed uniquely as time-varying functions. Adding an additional gimbal axis introduces nonuniqueness, i. e. , there is no unique way to rotate about the three-gimbal axes in order to follow a DRS, but an

infinite number of ways. In order to make a three-gimbal system attractive, a simple steering method should be adopted, minimizing the added complexity due to the third gimbal axis and eliminating the nonuniqueness problem.

The nonuniqueness problem can be solved by letting the third axis be controlled by some external reference such that the primary axis is in a known position and does not lie near an LOS. A very desirable reference is the equator, with the third axis rotating the primary axis so that it is always perpendicular to the equatorial plane. However, providing sensing devices and/or command capability to implement this primary axis control is complex.

An alternate scheme is to use the ecliptic plane in place of the equatorial plane. A very convenient object, the sun, is available to establish this reference. The third axis is controlled by a sun sensor to orient the primary axis normal to the sun vector and parallel to the LAS orbit plane. But, recalling the previous discussion of solar panel mounting, this method is equivalent. The very same control signals used to position the solar panels can be used to control the third gimbal axis, which will be normal to the orbit plane. Furthermore, the antenna can be mounted on the earth-oriented body, and all the disadvantages of the solar panel mounting are removed.

There is one possible disadvantage to such a three-gimbal system in addition to increased complexity. If the solar panel control system has a pointing accuracy less than one-half the antenna beamwidth, then programmed control of the antenna is not possible and ground control is dubious. For high data rates, it is entirely possible that an antenna with a 2-degree beamwidth may be used. If the solar array steering system has an accuracy less than 1 degree, then program control of the primary and secondary gimbal axes based on the assumed position of the third (normal to the ecliptic) will result in a serious degradation of the data. Ground control, however, is possible if angular position data are available from all three-gimbal axes, but the control is more complex because all three axes must now be steered from the ground rather than just two. Automatic antenna steering with a monopulse system will give the required pointing accuracy. In such a system, only the primary and secondary gimbal axes are controlled by the monopulse system, just as in a two-gimbal system, while the inertial axis is controlled by the inaccurate solar panel steering system. For this reason, the third gimbal axis will be referred to as the inertial axis.



#### 4.3.3 Comment

It must be remembered that for a two-gimbal system the primary gimbal rate becomes large when the primary axis and the LOS are in angular proximity. It was shown previously that if the primary axis were placed normal to the orbit plane and the inclination  $i$  satisfied

$$0 \leq i \leq 76 \text{ degrees}$$

$$104 \leq i \leq 180 \text{ degrees}$$

then the gimbal rate will not become excessive. Thus, all the above discussion dealing with solutions to the gimbal rate problem is of interest only if  $76 \text{ degrees} \leq i \leq 104 \text{ degrees}$ , which includes polar and sun-synchronous orbits.

#### 4.4 MATHEMATICAL GIMBAL ANALYSIS

To provide greater detail, several of the above concepts are discussed more fully here. In particular, mathematical analyses of two gimbaling methods are presented.

##### 4.4.1 Line-of-Sight Vector

To mathematically analyze gimbaling systems, the mathematical expression for the LOS must be known. The vector distance between the LAS and a DRS can be described in terms of the orbital parameters which include 1)  $\lambda$ , the angle between the LAS orbit line of nodes and the vernal equinox, 2)  $\theta$ , the orbit angle of the LAS from the line of nodes, 3)  $i$ , the inclination of the LAS orbit plane, and 4)  $\phi$ , the orbit angle of the DRS from the vernal equinox. The first three are defined in Section 3.6 and shown in Figure 34. The vector distances and orbital parameters are shown in Figure 56. In the following analysis, all vectors are expressed in inertial coordinates shown in Figure 56.

$$\bar{R}_O = R_O \begin{pmatrix} \cos \theta \sin \lambda + \sin \theta \cos i \cos \lambda \\ \sin \theta \sin i \\ \cos \theta \cos \lambda - \sin \theta \cos i \sin \lambda \end{pmatrix} \quad (9)$$

$$\bar{R}_s = R_s \begin{pmatrix} \sin \phi \\ 0 \\ \cos \phi \end{pmatrix}$$

$$\bar{R}_a = \bar{R}_s - \bar{R}_O \quad (10)$$

$$R_a = \begin{pmatrix} R_s \sin \phi - R_O \cos \theta \sin \lambda - R_O \sin \theta \cos i \cos \lambda \\ -R_O \sin \theta \sin i \\ R_s \cos \phi - R_O \cos \theta \cos \lambda + R_O \sin \theta \cos i \sin \lambda \end{pmatrix} \quad (11)$$

where

$$R_O \equiv |\bar{R}_O| \quad \text{and} \quad R_s \equiv |\bar{R}_s| .$$

Then it may be shown that

$$R_a^2 = |R_a|^2 = R_s^2 + R_o^2 - 2 R_s R_o \left[ \cos \vartheta \cos (\varphi - \lambda) + \cos i \sin \vartheta \sin (\varphi - \lambda) \right] \quad (12)$$

#### 4.4.2 Three Gimbal — Solar-Panel-Mounted Antenna

This subsection treats the gimbaling system for a solar-panel-mounted antenna and the three-gimbal system discussed above where the third or spacecraft-fixed axis is normal to the orbit plane and is controlled by solar panel steering signals. These two systems are mathematically equivalent. First, the two-gimbal solar-panel-mounted antenna will be discussed, and then the equivalence of the three-gimbal system will be treated.

A solar-panel-mounted antenna will not require as much angular motion in the orbital plane as a body-mounted antenna because the rotational motion of the spacecraft is compensated for by the solar panel pointing system. The antenna pointing system must compensate for the LAS orbital motion, the DRS orbital motion, and the motion of the sun with respect to the LAS and DRS orbits. The range of pointing angles can be determined by referring to Figure 57 where the basic geometry is illustrated.

It is important to note that an oriented solar panel is positioned so that it is perpendicular to the sun vector,  $v$ , which serves as a fundamental reference. Thus, there are two references associated with the solar panel — the LAS orbit plane, or equivalently its normal, and the sun vector.

In Figure 57, the two extreme conditions for a polar orbit are shown; they occur at the summer and winter solstices. The angular motion illustrated is in the plane containing the sun vector,  $v$ , and ecliptic normal, i. e., the plane perpendicular to the ecliptic plane containing the sun vector which coincides with the LAS orbit plane. The maximum required angular motion in this plane is seen to be  $47 \text{ degrees} + 2\alpha_m$ , and it takes 1 year to realize this range of motion. Since the motion of the sun during any single LAS orbit is relatively small, the variation during one LAS orbit will be  $2\alpha_m$ .

At the two times of year shown, the plane containing the sun vector and the ecliptic normal is perpendicular to both the ecliptic and equatorial planes.  $\alpha_m$  represents the maximum angular deviation of the LOS from the equatorial plane. Figure 58 shows two geometrical situations for determining  $\alpha_m$ . From the case shown in Figure 58a, for LAS altitudes less than 800 n.mi.,  $\alpha_m \leq 10.3 \text{ degrees}$ ; for the case in Figure 58b,  $\alpha_m \leq 10.8 \text{ degrees}$ .

From the above analysis, the conclusion is that pointing capability in the LAS orbit plane for a polar orbit should allow a range of at least  $47 + 22 \text{ degrees} = 69 \approx 70 \text{ degrees}$  of motion. This range should be

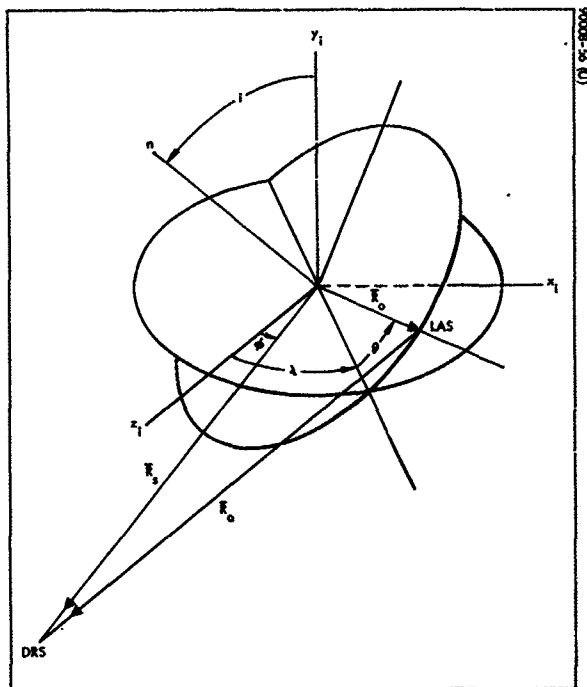


**Figure 56. Antenna Pointing Vector Distances and Orbital Parameters**

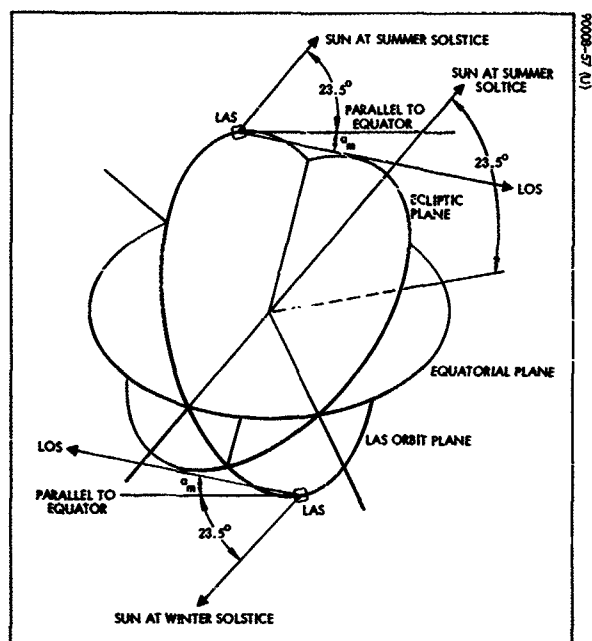


**Figure 57. Solar Panel – Mounted Antenna Geometry**

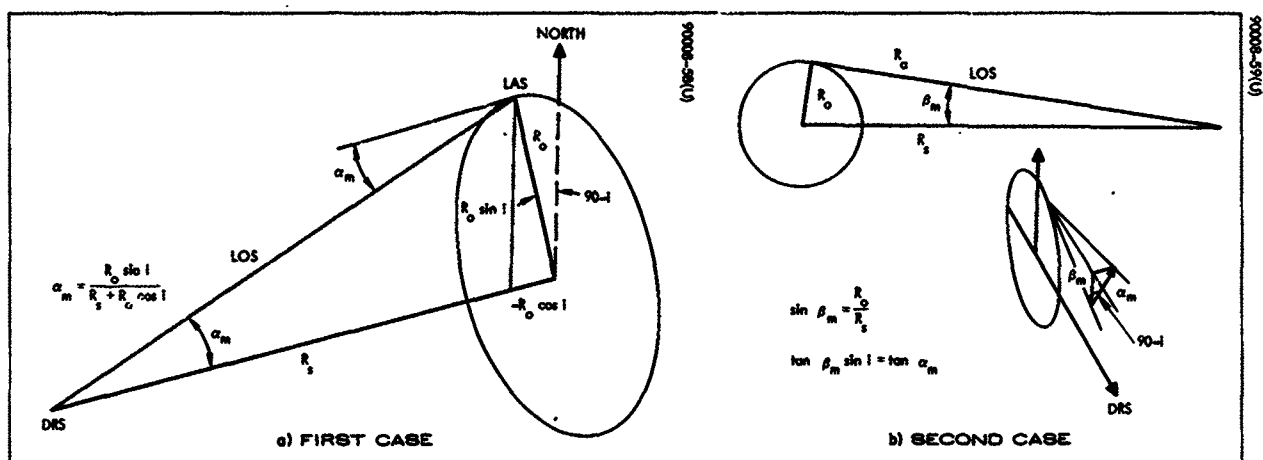


**Figure 58. Two Geometrical Situations for Determining Maximum Angular Motion**

centered about the sun vector so that angular deviation from this vector is  $\pm 35$  degrees.

This discussion has dealt so far with the motion in the LAS orbit plane or equivalently motion about its normal. For total antenna coverage, another plane of motion must be chosen, and the most natural choice is the ecliptic plane. Although pointing capability in the orthogonal plane is limited to  $\pm 35$  degrees, the motion in the ecliptic should be unlimited and, indeed, can be made so because the orthogonal motion is limited.

As mentioned in Section 4.3, the axes in a two-gimbal system can theoretically be oriented arbitrarily except that they must not be colinear. However, as was shown in that section, when the LOS is in angular proximity to the primary gimbal axis, the angular rate about that axis increases with a term involving the cosecant of the separation angle. Thus, a desirable gimbaling scheme should not allow the primary axis and LOS to approach each other. But, as was shown for certain LAS orbit inclinations, this cannot be avoided if a two-gimbal system is mounted on the body. Mounting an antenna on a solar panel eliminates this problem.

The two natural references have been described above. It is geometrically logical to orient the primary gimbal axis with respect to the solar panel such that it is normal to one of these references. Thus, two configurations are possible as shown in Figure 59. Note that in system A, the primary axis coincides with the sun vector, which means that there will be two times of the year such that when the LAS crosses the equatorial plane, the primary axis and LOS may coincide, i. e., the primary axis lies in the equatorial plane. Considering the translational orbit motion, the period during which the primary axis may lie undesirably near an LOS is a significant portion of a year. Using simple spherical trigonometric relationships, for a polar orbit, the primary axis in system A can lie within 4 degrees of a possible LOS for 41.6 percent of the year.

In system B of Figure 59, the  $g_1$  - LOS proximity problem is eliminated. In this system, the primary axis is oriented with respect to the solar panel so that it always remains normal to the sun vector and parallel to the LAS orbit plane. Then, as is mentioned in the previous section and illustrated in Figure 55, the LOS and primary axis are always separated by at least 56.5 degrees for a polar orbit. For LAS orbits which deviate considerably from a polar orbit, there is a body-mounted two-gimbal system which is applicable (see subsection 4.3.1). Thus, it is this system which is preferred for LAS orbit inclinations in the range 75 to 105 degrees.

In spite of this gimbaling advantage, there are a number of disadvantages that detract from the solar panel mounting of an antenna. These disadvantages include:

- 1) Extension of antenna feed lines resulting in additional signal power losses

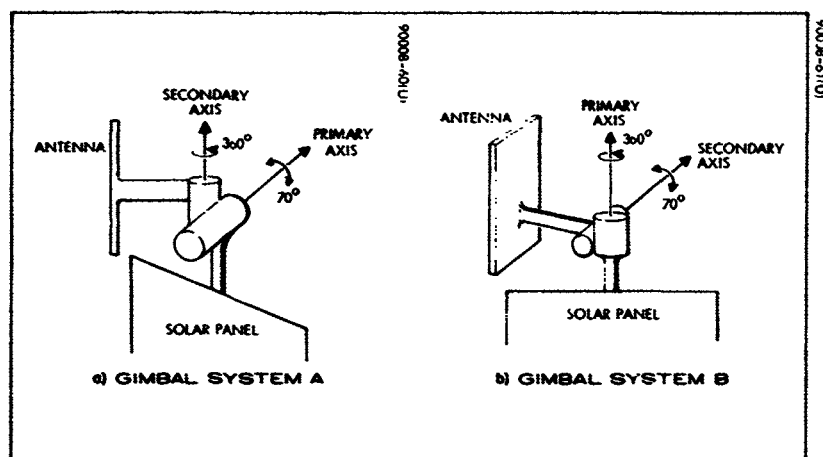


Figure 59. Two Gimbal Schemes for Solar Panel-Mounted Antennas

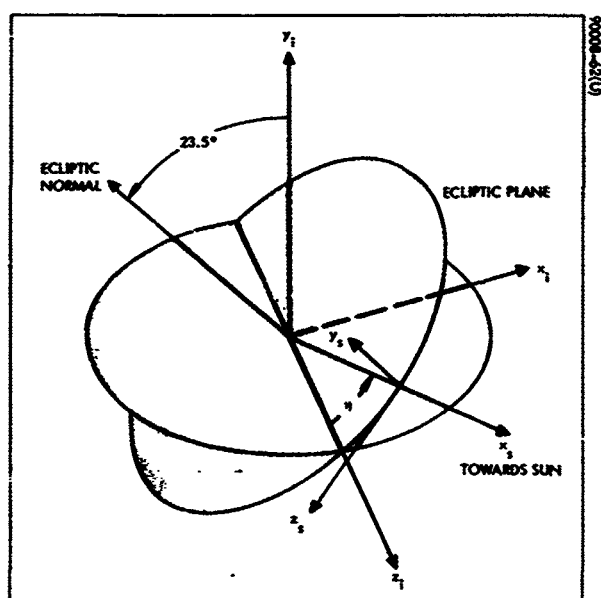


Figure 60. Solar Panel Coordinates

- 2) Possible interaction between the solar panel steering system and the antenna steering system
- 3) Additional structural complexity of solar panel in order to mount the antenna

But all of these disadvantages are removed with a body-mounted three-gimbal antenna.

A body-mounted antenna will be attached to a structural extension, itself attached to the earth-oriented body. The gimbal axes and torquing devices are located at the end of this extension. Instead of attaching a two-gimbal system to a solar panel which by its directivity toward the sun keeps the primary axis normal to the sun vector, just add another torquing device at the end of the antenna extension which performs the same function. This additional torquing device, providing motion about a third axis attached rigidly to the structural extension and oriented normal to the orbit plane and, hence, parallel to the solar drive, maintains the primary axis normal to the sun vector just as the solar panel would. This torquing device can be controlled with the same electrical signals that control the solar panel drive, or, alternately, it can be "slaved" to the solar panel steering system. With this three-gimbal system, the solar-panel-mounted antenna and the three-gimbal antenna are conceptually equivalent.

#### Approximate Angular Rates

For purposes of approximating the gimbal angle rates of such a system, assume that the LAS orbit is polar. Then there are two orthogonal components of rotation not compensated by the solar panel or inertial gimbal steering system. Referring to Figure 60,

$$\dot{g}_1 = \dot{\Omega}_2 \cos 23.5^\circ + \dot{\Omega}_1 \cos \lambda \sin 23.5^\circ \quad (13)$$

$$\dot{g}_2^2 + \dot{g}_1^2 = \dot{\Omega}_1^2 + \dot{\Omega}_2^2 \quad (14)$$

Now

$$(\dot{\Omega}_1)_{\max} = \left(\frac{d\alpha}{dt}\right)_{\max} = \frac{v_o}{(Ra)_{\min}} = \frac{\omega_o R_o}{R_s - R_o} = \frac{G^{1/2}}{R_o^{1/2} (R_s - R_o)} \quad (15)$$

$$(\dot{\Omega}_2)_{\max} = \frac{v_s}{(Ra)_{\min}} = \frac{\omega_e R_s}{R_s - R_o} = \frac{G^{1/2}}{R_s^{1/2} (R_s - R_o)} \quad (16)$$

where

$$G \approx 6.275 \times 10^4 \frac{(\text{n. mi.})^3}{\text{sec}^2}$$

For

$$R_o = 500 \text{ n. mi. and } \lambda = 35 \text{ degrees}$$

$$(\dot{\Omega}_1)_{\max} \approx 2.12 \times 10^{-4} \text{ rad/sec}$$

$$(\dot{\Omega}_2)_{\max} = 8.8 \times 10^{-5} \text{ rad/sec} \quad (17)$$

And so

$$(\dot{g}_1)_{\max} \approx 1.51 \times 10^{-4} \text{ rad/sec} = 8.66 \times 10^{-3} \text{ deg/sec}$$

$$(\dot{g}_2)_{\max} \approx 1.2 \times 10^{-4} \text{ rad/sec} = 6.9 \times 10^{-3} \text{ deg/sec} \quad (18)$$

#### Gimbal Angle Analysis

As discussed above, the preferred gimbaling scheme (system B in Figure 59) has the primary axis mounted orthogonal to the inertial axis and is rotated by that axis so that it remains normal to the sun vector. The antenna axis corresponding to the principal direction of radiation must be controlled to coincide with the LOS ( $R_a$ ). Thus there are three fundamental vector quantities which define the two gimbal angles: the LOS vector,  $R_a$ , which is given by Equation 11, the sun vector,  $x_s$ , and the orbit normal,  $n$ . These latter two are shown in Figures 60 and 56, respectively, and are expressed in inertial coordinates by

$$x_s = \begin{bmatrix} q \sin \eta \\ p \sin \eta \\ \cos \eta \end{bmatrix} \quad (19)$$

$$n = \begin{bmatrix} -\sin i \cos \lambda \\ \cos i \\ \sin i \sin \lambda \end{bmatrix} \quad (20)$$

where  $p = \sin (23^\circ 27')$ ;  $q = \cos (23^\circ 27')$



Denoting the primary gimbal axis by  $g_1$ , the above mentioned orthogonality conditions imply that

$$g_1 \cdot x_s = g_{1x} q \sin \eta + g_{1y} p \sin \eta + g_{1z} \cos \eta = 0 \quad (21)$$

$$g_1 \cdot n = -g_{1x} \sin i \cos \lambda + g_{1y} \cos i + g_{1z} \sin i \sin \lambda = 0 \quad (22)$$

A third equation defines the magnitude of  $g_1$

$$g_{1x}^2 + g_{1y}^2 + g_{1z}^2 = 1 \quad (23)$$

Solving Equations 21, 22, and 23 with considerable algebraic manipulation

$$g_1 = \frac{1}{K} \begin{bmatrix} p \sin \eta \sin \lambda \sin i - \cos \eta \cos i \\ \cos \eta \sin i \cos \lambda - q \sin \eta \sin i \sin \lambda \\ \sin \eta (q \cos i - p \sin i \cos \lambda) \end{bmatrix} \quad (24)$$

where

$$K = \left\{ \sin^2 i \left[ \cos^2(\eta + \lambda) + p^2 \cos^2 \lambda \sin^2 \eta \right] + \sin^2 \eta (p^2 \cos^2 \lambda + q^2 \cos^2 i) + \cos^2 i \cos^2 \eta - \sin^2 i \left( \sin \eta \cos \eta \sin \lambda + pq \cos \lambda \right) \right\}^{1/2} \quad (25)$$

The antenna is attached to the secondary gimbal axis,  $g_2$ , so that the radiation beam center is orthogonal to it. And since  $\bar{R}_a$  and the beam center must coincide,  $g_2$  is orthogonal to  $\bar{R}_a$ . By construction,  $g_2$  is orthogonal to  $g_1$ . The relationship between these three vectors is shown in Figure 61a where the secondary gimbal angle,  $\alpha_2$  is also shown. It can be seen from this figure that

$$g_1 \cdot \bar{R}_a = |g_1| |R_a| \cos(90^\circ + \alpha_2)$$

Thus

$$\sin \alpha_2 = -\cos(90 + \alpha_2) = \frac{-g_1 \cdot \bar{R}_a}{|g_1| |\bar{R}_a|} \quad (26)$$

Performing the vector multiplication of Equation 26

$$\begin{aligned} \sin \alpha_2 = \frac{1}{QK} \left\{ \sin \theta (\cos \eta \cos i - p \sin \eta \sin \lambda \sin i) \right. \\ + \cos \theta \sin \eta (p \sin i \cos \lambda - q \cos i) + B(p \cos \theta \sin \eta \sin i \cos 2 \lambda \\ + \sin \theta \cos \eta \cos \lambda \cos 2 i - p \sin \theta \sin \eta \sin i \cos i \sin 2 \lambda \\ \left. + q \sin \eta \sin \theta \sin \lambda) \right\} \quad (27) \end{aligned}$$

where

$$Q = \frac{|\bar{R}_a|}{R_s} = \left\{ 1 + B^2 - 2 B \left[ \cos \theta \cos(\varphi - \lambda) + \cos i \sin \theta \sin(\varphi - \lambda) \right] \right\} \quad (28)$$

$$B = \frac{R_o}{R_s}$$

The primary gimbal angle  $\alpha_1$ , is defined as the deviation of the projection  $\bar{R}_{ap}$  of  $R_a$  onto the plane normal to  $g_1$  from the vector normal to both  $n$  and  $g_1$ . This seemingly complex definition is illustrated in Figure 61b, from which it follows that

$$\begin{aligned} \bar{R}_{ap} \cdot n &= |\bar{R}_{ap}| |n| \cos(90 - \alpha_1) \\ &= |\bar{R}_{ap}| \sin \alpha_1 \end{aligned}$$

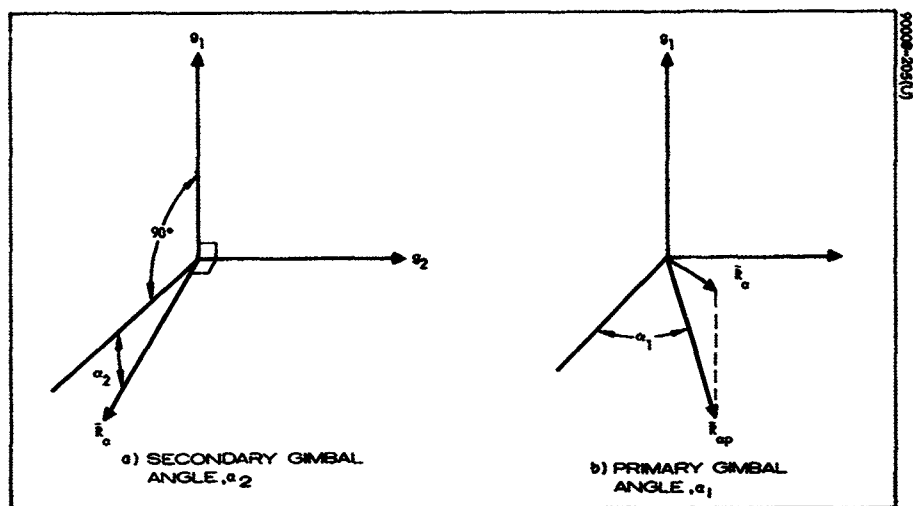


Figure 61. Definition of Gimbal Angles

since

$$|n| = 1$$

Thus

$$\sin \alpha_1 = \frac{\bar{R}_{ap} \cdot n}{|\bar{R}_{ap}|}$$

$$\bar{R}_{ap} = (g_1 \times \bar{R}_a) \times \frac{g_1}{|g_1|} = (g_1 \times \bar{R}_a) \times g_1$$

By a vector identity and Equation 26

$$\bar{R}_{ap} = \bar{R}_a - g_1(g_1 \cdot \bar{R}_a) = \bar{R}_a + g_1 |\bar{R}_a| \sin \alpha_2$$

Thus

$$\sin \alpha_1 = \frac{(\bar{R}_a + g_1 |\bar{R}_a| \sin \alpha_2) \cdot n}{|\bar{R}_{ap}|} \quad (29)$$

#### 4.4.3 Body-Mounted, Two-Gimbal Antennas

##### Geometry and Gimbal Axes

For the three-gimbal or solar-panel-mounted antenna, the solar panel steering compensates for the rotation of the spacecraft, but a body-mounted antenna must move so as to compensate for this motion as well as the LAS orbital translation motion and DRS motion. The basic reference for the solar-panel-mounted antenna is the sun vector, but for a body-mounted antenna, the reference is the LAS orbit plane and the primary gimbal axis may, most naturally, lie either in or normal to this plane.

Consider the geometry of Figure 62 where the pointing angle limits in the LAS orbit plane are shown. The maximum angular movement between the body-fixed x-axis and the LOS is  $2\zeta_{\max}$  which varies from 218 to 248 degrees for LAS altitudes from 200 to 700 n.mi. For the relative positions of the LAS orbit and the DRS shown in Figure 62, the rate of change of  $\zeta$  is much greater than the rate of change of the angle between the LOS and body axis normal to the orbit plane. Since the orbital angular velocity of the LAS is 12 to 15 times greater than that of the DRS, the orbit plane will be the plane of the most rapid LOS relative angular motion. This was shown in subsection 4.3.1.

Two natural choices are available for primary gimbal axis orientation— in the orbit plane or normal to it. Any axis lying in the orbit plane when rotated through more than 180 degrees will coincide with a possible LOS. Since rotation in this plane is in the vicinity of 240 before eclipse of the DRS, the gimbal rate problem, discussed at length in subsection 4.3.1, exists. However, the problem can be eliminated by providing two antennas whose primary gimbal axes during use rotate through less than 180 degrees and are positioned with respect to the spacecraft so as to never coincide with a possible LOS during the respective antenna's use. Figure 63 shows the choice of two primary gimbal axes, and Figure 64 shows their movement with respect to a LOS and the orbit. Figure 65 illustrates how the antennas would be switched at the equator and near the poles.

The alternate gimbaling method consists of choosing the primary axis normal to the orbit plane. Angular motion about this axis performs the task of the solar panel steering system for a solar-panel-mounted antenna as well as compensating for the LAS translational orbit motion. However, for LAS orbit inclinations between 80 and 100 degrees, the primary axis will coincide with a possible LOS resulting in excessive primary gimbal rates unless two antennas are again provided. The fundamental geometry is shown in Figure 66. The following mathematical analysis pertains to this type of system.

#### Gimbal Angle Analysis — Primary Axis Normal to Orbit Plane

Similar to the analysis for the solar-panel-mounted antenna, the gimbal angles can be related to the orbital parameters. Since the sun is not involved in this situation as it was earlier, the angle  $\lambda$  between the LAS line of nodes and vernal equinox can be set to zero except that the DRS orbit angle,  $\phi$ , must be replaced by  $\phi - \lambda = \Omega$ . That is, the inertial axis  $z_i$  now rotates with the line of nodes, but substituting  $\phi - \lambda = \Omega$  accounts for the movement of the line of nodes. The important quantity is the angular rate

$$\frac{d}{dt} (\phi - \lambda) = \omega_{\text{sync}} - \omega_{\text{sun}} = \dot{\Omega}$$

Thus

$$\phi - \lambda = \Omega_0 + \dot{\Omega}t$$

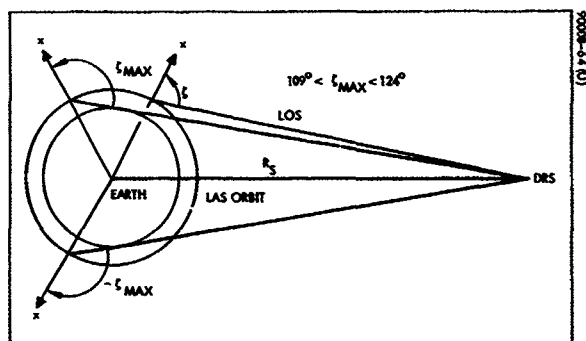


Figure 62. Antenna Pointing Angle in LAS Orbit Plane for Body-Mounted Antenna

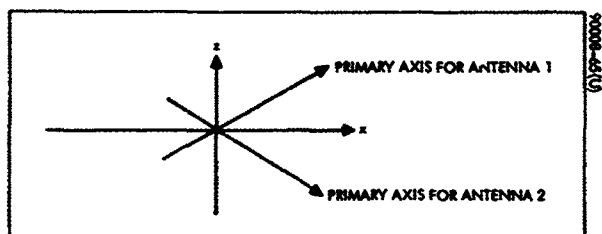


Figure 63. Primary Axes in Orbit Plane for Avoiding Large Gimbal Rates

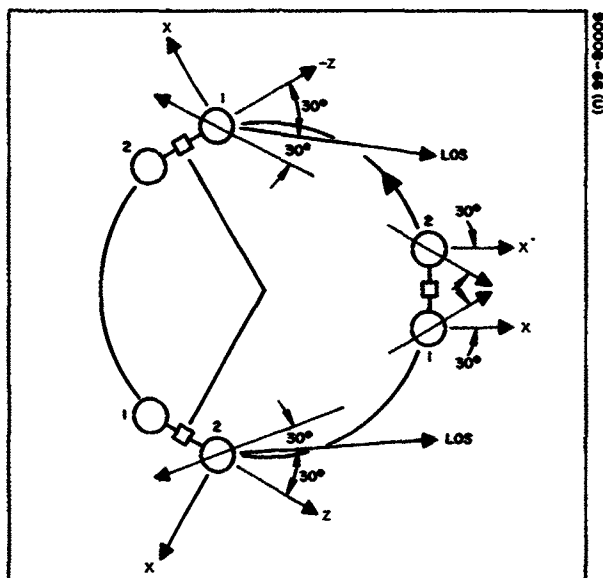


Figure 64. Two Orbit-Plane Gimbal Axes

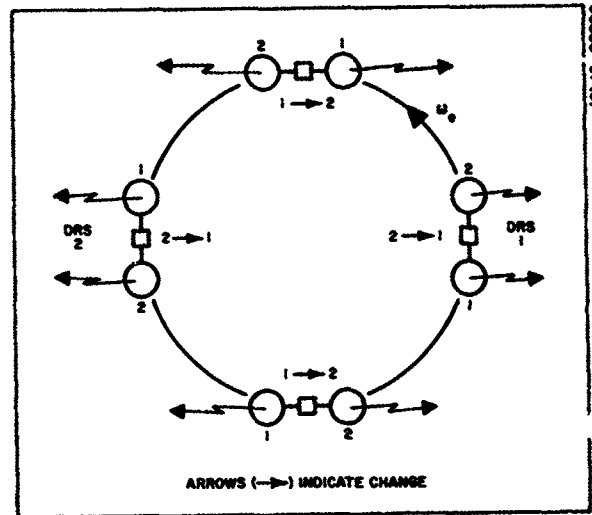


Figure 65. Antenna Changeover Sequence for Two Antennas

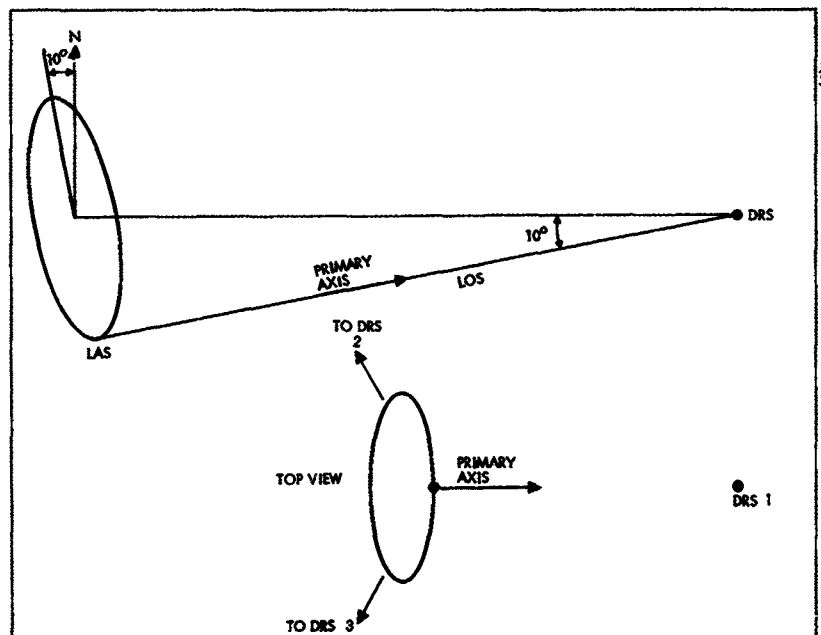


Figure 66. Geometry of Primary Axis Normal to Orbit Plane

The above simplification is possible because only the relative positions of the LAS and DRS are of concern and the sun is not a consideration. However, the line of nodes of the LAS orbit will rotate; this accounted for the relative LAS orbit-DRS angle  $\Omega$  and its rate of change. With this simplification, Equation 11 becomes

$$\overline{R}_a = \begin{pmatrix} R_s \sin \Omega - R_o \sin \theta \cos i \\ -R_o \sin \theta \sin i \\ R_s \cos \Omega - R_o \cos \theta \end{pmatrix} \quad (30)$$

In Section 3.6, the relationship between the inertial and orbital coordinates is given as

$$\begin{pmatrix} i \\ j \\ k \end{pmatrix} = G \begin{pmatrix} x_i \\ y_i \\ z_i \end{pmatrix} \quad (31)$$

where with  $\lambda = 0$

$$G = \begin{pmatrix} \sin \theta \cos i & \sin \theta \sin i & \cos \theta \\ -\sin i & \cos i & 0 \\ -\cos \theta \cos i & -\cos \theta \sin i & \sin \theta \end{pmatrix} \quad (32)$$

And assuming that the orbit and body axes are kept in close alignment by the attitude control system

$$\begin{pmatrix} x \\ y \\ z \end{pmatrix} = \begin{pmatrix} i \\ j \\ k \end{pmatrix} \quad (33)$$

Then

$$(\overline{R}_a)_{\text{body}} = G(\overline{R}_a)_{\text{inertial}}$$



So combining Equations 30 through 33

$$(\bar{R}_a)_{\text{body}} = \begin{pmatrix} R_s (\sin \Omega \sin \theta \cos i + \cos \Omega \cos \theta) - R_o \\ -R_s \sin \Omega \sin i \\ R_s (\cos \Omega \sin \theta - \sin \phi \cos \theta \cos i) \end{pmatrix} \quad (34)$$

The relationship of the antenna axes  $x_a, y_a, z_a$  to the body axes is shown in Figure 67 which is almost identical to Figure 61.

$$\begin{pmatrix} x \\ y \\ z \end{pmatrix} = \begin{pmatrix} \cos g_1 \cos g_2 & -\cos g_1 \sin g_2 & \sin g_1 \\ \sin g_2 & \cos g_2 & 0 \\ -\sin g_2 \cos g_2 & \sin g_1 \sin g_2 & \cos g_2 \end{pmatrix} \begin{pmatrix} x_a \\ y_a \\ z_a \end{pmatrix} \quad (35)$$

The  $x_a$  vector must coincide with  $\bar{R}_a$  and must equal a unit vector in the  $\bar{R}_a$  direction. Using the defining Equations 24 and 25, the body coordinate components of  $x_a$  and  $u_a$  can be equated, yielding

$$\cos g_1 \cos g_2 = Q [\sin \Omega \sin \theta \cos i + \cos \Omega \cos \theta - B] \quad (36)$$

$$\sin g_2 = -Q \sin \Omega \sin i \quad (37)$$

$$-\sin g_1 \cos g_2 = Q [\cos \Omega \sin \theta - \sin \Omega \cos \theta \cos i] \quad (38)$$

where

$$B = \frac{R_o}{a} = \left\{ 1 + B^2 - 2B [\cos \theta \cos \Omega + \cos i \sin \theta \sin \Omega] \right\}^{-1/2} \quad (39)$$

The secondary gimbal angle position,  $g_2$ , is specified by Equation 37 and the primary gimbal angle is found by dividing Equation 38 by 36 yielding

$$\tan g_1 = \frac{\sin \Omega \cos \theta \cos i - \cos \Omega \sin \theta}{\sin \Omega \sin \theta \cos i + \cos \Omega \cos \theta - B} \quad (40)$$

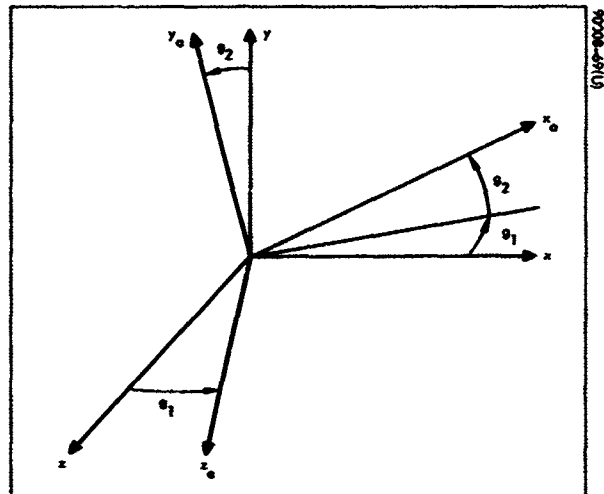


Figure 67. Body and Gimbal Axis Coordinates

## 4.5 ANTENNA STEERING

The directive antenna must be pointed at a DRS within view of the LAS. Nominally, the center of the antenna beam pattern and the line of sight coincide. The problems and considerations associated with mounting an antenna and with orienting the axes of rotation have been considered in the previous three subsections. The question now arises — given an antenna mounting and gimbaling configuration, how should the torquing devices be controlled? Four methods are discussed below in order of increasing sophistication and complexity.

### 4.5.1 Continuous Ground Control

One of the first and most obvious methods of steering one or two antennas is by command from a ground station through the DRS relay link. If accurate pointing is required, the command rate will be high.

First consider a body-mounted antenna with the primary axis in the orbit plane, but oriented such that during use it always remains separated from a LOS by 30 degrees. Such a system is discussed in subsection 4.4.3 and is illustrated in Figures 63 and 64. To evaluate the gimbal rates precisely, a detailed mathematical analysis is necessary, but estimates are possible from simple geometrical considerations. Referring to Figure 53 with  $\epsilon = 30$  degrees, the primary gimbal rate is given by

$$\dot{g}_1 = 0.31 \csc \epsilon = 0.62 \text{ deg/min}$$

and the secondary gimbal rate is given by

$$\dot{g}_2 = |\bar{\omega}_d - \bar{\omega}_L| = |\omega_d| + |\omega_L| = 1.23|\omega_d| = 4.43 \text{ deg/min}$$

If the gimbal axis must be controlled to within  $\xi$  degrees, the time between commands is given by

$$t_{\xi 1} = 1.61 \xi \text{ minutes}$$

$$t_{\xi 2} = 0.226 \xi \text{ minutes}$$

Thus if  $\xi = 1$  degree, commands for the primary axis must be sent every 1.61 minutes and commands for the secondary axis about every 13 seconds.

Now, consider a polar orbit and a three-gimbal system at the vernal equinox. The primary gimbal axis is normal to the equator and the secondary axis is normal to the LOS. The primary axis must compensate for the DRS orbital motion ( $\omega_d$ ) and the secondary axis must compensate for the LAS translational orbit motion ( $\omega_L$ ), where the inertial axis automatically compensates for LAS rotation.

From Section 4.3.1

$$\omega_d \leq 0.31 \text{ deg/min}$$

$$\omega_L \leq 0.083 \text{ deg/min}$$

Thus if each gimbal axis must be controlled to within  $\xi$  degrees the minimum time between commands is given by

$$t_{\xi 1} = \frac{\xi}{0.31} = 3.22\xi \text{ minutes}$$

$$t_{\xi 2} = \frac{\xi}{0.083} = 12\xi \text{ minutes}$$

Thus, in order to control each axis to within 1 degree, commands for the primary axis must be sent every 3.22 minutes and commands for the secondary axis every 12 minutes.

A comparison of these two examples reveals another advantage of the three-gimbal system — the two externally controlled axes have low gimbal rates and thus require commands relatively infrequently. The inertial axis must be accurately controlled by the solar panel steering system.

#### 4.5.2 Updated Program

It is possible to have an on-board program which controls the primary and secondary gimbal axes for a length of time. Periodically, commands from the ground will change program parameters, and the changeover from one DRS to another will be controlled by ground command. For a two-gimbal system, the analysis results of subsection 4.3.1 indicate that the programmer may be complex and/or the updating commands will have to be sent frequently, but much less frequently than with pure ground control. The three-gimbal system again offers an advantage because the motions about the primary and secondary axes are relatively simple. For this system, the primary axis rate is nearly constant, but has a small additive sinusoidal term, while the secondary is sinusoidal in nature. With such a system, it appears that no updating would be necessary between changeovers.

The basic advantage of this concept over the pure ground control method is that fewer ground commands are necessary.

#### 4.5.3 Autotrack With Ground-Controlled Changeover

The autotrack with ground-controlled changeover method requires that the LAS be able to track the DRS automatically using a monopulse or equivalent tracking scheme. Control signals from the autotrack electronics will be applied to the primary and secondary gimbal motors between

changeover, but the slewing of the antenna from one DRS to another is performed by ground command as in the two previous methods. Just prior to changeover, the autotrack system is turned off. The changeover maneuver is performed and then the autotrack system is re-engaged.

This system is considerably more complex than the previous two methods requiring both the autotrack electronics as well as more complex antenna design. But, in general, antenna pointing is much more accurate which is extremely desirable for a highly directive antenna, and fewer ground commands are necessary than are required with the two previous systems.

#### 4.5.4 Completely Automatic

The completely automatic method is the ultimate method. Ground control is not required. The antenna steering system automatically tracks a DRS, performs the changeover maneuver, and then reactivates the autotrack system. One or two antennas may be controlled automatically by such a scheme. The difference between this method and the previous one is that the changeover maneuver is performed automatically.

In order that the complexity of such a system be kept within reasonable bounds, the data relay satellites must be located symmetrically in the equatorial plane, which for full LAS coverage requires three or more DRSs. With such symmetry, the changeover consists of a preprogrammed maneuver.

To illustrate how such a system might operate, consider a simple case. The LAS is in a polar orbit with a single three-gimbal antenna mounted away from the outward facing side. There are three DRSs located in the equatorial plane spaced symmetrically 120 degrees apart. If the time of year is one of the equinoxes, the primary gimbal axis is normal to the equatorial plane. When the LAS approaches either the north or south pole, the autotrack system is deactivated, the antenna is rotated approximately 120 degrees toward another DRS, and the autotrack is reactivated. Admittedly, at some other time of year and for a nonpolar LAS orbit, this maneuver is somewhat more complex, involving the secondary gimbal axis, but the maneuver can be preprogrammed.

Establishing communications following a changeover in the above systems has implied that after the changeover maneuver, the antenna is pointing at the DRS with the required accuracy for transmission, or that turning on the autotrack will correct any small residual pointing errors. However, the acquisition problem, discussed below, may not be that simple.

#### 4.6 ACQUISITION

The requirement for some type of acquisition system depends primarily on the beamwidth of the antenna. For very small beamwidths, pointing capability by ground command or programmed maneuver may not be sufficient to ensure that the DRS lies within the antenna beamwidth following changeover. If this is the case, then some automatic acquisition method must be employed.

One candidate method requires that after changeover, portions of the antenna be deactivated resulting in a broader beamwidth. With this beamwidth, the autotrack system is activated and the antenna is automatically pointed toward the DRS within the capability of the crude pointing system. Then the unused portions of the antenna are reactivated, providing the fine pointing and tracking mode. The antenna design is complicated by this method.

Another method is to search for the DRS by mechanically scanning the antenna over some angular search area determined by the expected residual errors following the changeover maneuver. This method requires added electronic complexity.

In the representative LAS mission chosen in Section 2, structural design and packaging limitations will probably limit LAS antenna gains to less than about 38 to 40 dB. In general, the beamwidths will be greater than 2 degrees. With beamwidths in this range, it appears possible to provide command or autotrack control of the antenna such that an acquisition scheme is unnecessary.

#### 4.7 ANTENNA - SPACECRAFT DYNAMICAL INTERACTION

The following analysis pertains to a three-axis stabilized vehicle which has a very small angular momentum associated with the LAS orbital angular velocity. Assuming this angular momentum is negligible, the law of conservation of angular momentum can be expressed as

$$T = \frac{dH}{dt} = 0$$

where T represents external torque and H represents the angular momentum of the satellite. This is just Newton's second law expressed in angular dynamical terms. If there are no external torques except the natural disturbance torques which may be considered separately, then any angular momentum produced by rotating the antenna must be offset by a compensating angular momentum due to motion of the spacecraft. Thus

$$I_a \omega_a = I_s \omega_s \quad (41)$$

where  $I_a$  and  $I_s$  are the corresponding moments of inertia of the antenna and the spacecraft, and  $\omega_a$  and  $\omega_s$  are the respective angular velocities. Thus, the angular rate induced in the spacecraft is the antenna rate, reduced by the ratio of their moments of inertia with respect to axes through their respective centers of mass parallel to the axis of rotation. Integrating this relationship

$$\theta_s = \frac{I_a}{I_s} \theta_a \quad (42)$$

In order to estimate quantitatively the effects of antenna movement on a spacecraft of the type being considered here within the boost capability of the Thor Delta, the following assumptions will be made:

- 1) The antenna is a planar array, 30 inches on . side with a moment of inertia about the gimbal axes of approximately 0.5 slug-ft<sup>2</sup>.
- 2) The spacecraft weighs 1000 pounds which for Delta shroud packaging yields moments of inertia about the center of mass usually in excess of 200 slug-ft<sup>2</sup> (see Figure 5).

Now if two antennas are employed, while one is being used, the other will be maneuvered at a rate corresponding to 180 degrees during one-quarter of an orbit, which is approximately 25 minutes. Thus

$$(\omega_a)_{\max} = \frac{180}{25} = 7.2 \text{ deg/min} = 0.12 \text{ deg/sec} \quad (43)$$

And from Equation 41

$$(\omega_s)_{\max} = \frac{0.5}{200} (\omega_a)_{\max} = 0.018 \text{ deg/min} = 3 \times 10^{-4} \text{ deg/sec} \quad (44)$$

A single antenna will be moved at its maximum rate during changeover over the poles. If this changeover maneuver is performed during 20 LAS orbit degrees corresponding to about 5.5 minutes and represents a 140-degree rotation, then

$$(\omega_a)_{\max} = \frac{140}{5.5} = 25.4 \text{ deg/min} \quad (45)$$

and so

$$(\omega_s)_{\max} \approx 0.064 \text{ deg/min} \quad (46)$$

This value is substantially larger than that of Equation 44, but since no data are being transmitted during this period, degradation of the data due to this motion is unimportant.

During data transmission, the maximum relative angular rate is approximately

$$(\omega_o) + (\omega_a) \approx 4.4 \text{ deg/min}$$

which results in

$$(\omega_s)_{\max} = (4.4) \frac{0.5}{200} = 0.011 \text{ deg/min} = 1.83 \times 10^{-4} \text{ deg/sec}$$

which is quite small.

If the above angular rates are excessive for a particular mission or sensor, they can be reduced by providing counterrotating inertias to compensate for the antenna motion. Spin stabilization with the gyrostator or a momentum wheel will also minimize these disturbance effects.



## 4.8 RECOMMENDATIONS

This section began by distinguishing between the two major antenna considerations based on transmission requirements.

Uninterrupted data require two antennas, but with allowable interruptions a single antenna may be used. Based on the discussion of Sections 4.2 and 4.3, the following recommendations are made for these cases.

### 4.8.1 Two Antennas — Continuous Data

#### LAS Orbit Inclination Between 75 and 105 Degrees

The antennas should be mounted on extensions outward from the earth-oriented body in opposite directions along the axis coinciding with the velocity vector. These antennas should have two-gimbal steering systems with the primary axes in the LAS orbit plane oriented as shown in Figures 63 and 64.

#### LAS Orbit Inclination Less Than 75 Degrees and Greater Than 105 Degrees

The mounting should be same as above, but the primary gimbal axes should be normal to the LAS orbit plane.

### 4.8.2 One Antenna — Interrupted Data

#### LAS Orbit Inclination Between 75 and 105 Degrees

The antenna should be mounted on an extension outward from the side of the spacecraft which faces away from the earth. The antenna should have three gimbal axes with the inertial axis (the one rigidly attached to the body-fixed extension) controlled by the solar panel steering system such that the primary axis remains normal to the sun vector.

#### LAS Orbit Inclination Less Than 75 Degrees and Greater Than 105 Degrees

The mounting should be the same as above, but a two-gimbal system can now be used with the primary axis normal to the orbit plane.

## 5. ANTENNAS

### 5.1 INTRODUCTION

A critical element in the low-altitude satellite data relay satellite (LAS-DRS) communication link is the LAS antenna. There are two fundamental antenna concepts: the electronically steered antenna and the mechanically steered antenna. The following section compares the two concepts for use on an LAS, concluding that the mechanically steered antenna is preferable.

Sections 5.3 through 5.6 deal with specific types of mechanically steered antennas which will provide gains that range from 10 to 50 dB over frequencies ranging from 2.25 to 35.0 GHz. Both electrical and mechanical aspects are considered, and quantities such as pertinent dimensions, efficiencies, patterns, impedances, bandwidths, and weights are discussed. The antenna arrays examined here are slotted planar arrays, arrays of helices, paraboloidal reflectors and feeds, and rectangular horns. At the lower frequencies especially, the dimensions and weights of the antennas become extremely large for the largest gains considered. However, these characteristics have been included for comparison purposes.

## 5.2 ELECTRONICALLY SCANNED VERSUS MECHANICALLY STEERED ANTENNA

This section discusses primarily the electronically scanned antenna concept, but both a qualitative and quantitative comparison are made with an equivalent mechanically steered antenna. The comparison of these two types is hindered somewhat by the fact that for the electronically scanned antenna many of the electronic and RF components are closely associated with the radiating structure and cannot be separated from it as can be done with a mechanically steered antenna.

Briefly, the main radiation beam of an electronically scanned antenna is steered, or scanned, by causing a progressive change in the phase of a wavefront across the aperture of the array, whereas the beam of a mechanically steered array is scanned by physically rotating the array, orienting the beam in the desired direction.

An electronically scanned antenna consists of four functional subportions: the radiating structure, the phase shifting devices (or their equivalent) with their actuators or drivers, the feeding network, and the scan controller. The subportions are discussed below.

### 5.2.1 Radiating Structure

The magnitude of angular motion of the line of sight (LOS) with respect to the LAS depends on the inclination of the LAS orbit and the number of data relay satellites (DRSs). For a polar LAS orbit and a two-DRS system, the LOS may lie in an angular region greater than a hemisphere (see Figure 30).

If there are three DRSs, this region is somewhat reduced, but is still approximately a hemisphere symmetric about the LAS body-fixed local vertical. Figures which may help to visualize this antenna pointing requirement include 37, 45, 62, and 64. Because of this large required angular coverage, an electronically scanned antenna has a number of disadvantages.

Because of the reduction of effective aperture that occurs when the beam is scanned off the array normal, a single planar array is not sufficient to achieve the desired coverage. Consequently, a number of separate arrays must be used. As the beam is scanned, only one array will be active at a time. Analyses have shown that when a maximum scanning loss of 3 dB is desired, approximately five or six arrays are needed to provide hemispheric coverage with the minimum number of elements. Each array covers a different but equal portion of the hemisphere. It is estimated that about 400 radiating elements, each with a peak gain of 7 dB, would be required on each array to obtain a 30 dB gain at the extreme edge of its coverage region. Consequently, the radiating structure itself will be larger and heavier than that of a mechanically steered antenna. That is, for the same gain, the radiating structure for the electronically steered antenna will be at least five or six times the weight of that for an equivalent mechanically steered antenna.

### 5.2.2 Feed Network

The main beam of an array is scanned by the creation of a progressive change in the phase of a wavefront across the aperture of the array. To accomplish this phase change, the elements require excitations whose phase can be independently controlled by electronic means. Shifting the phase between the elements by a controlled amount will change the progressive phase of the common wavefront by the desired magnitude.

Phase control of the individual elements can be accomplished by using parts of the array structure or by using separate components, called phase shifters, or their equivalent. These phase shifters are inserted between elements or in the feeding structure that connects the elements. In mechanically steered arrays, the layout of the feeding structure is affected by such factors as size of array, polarization, shape of elements, physical size and weight limitations, power handling requirements, conductor losses, input impedance, bandwidth, and frequency of operation. In scanned arrays, additional factors to be considered are the required phase change and loss in the phase shifter, systematic errors, and control circuitry.

### 5.2.3 Phase Shifters

The required phase shifting can be performed either at RF or at IF. If the phase shifters are broadband, 400 will be required for 30 dB gain. They can be shared among the five or six arrays, since only one array operates at a time. If RF diode phase shifters built into microstrip circuits are used at 8 GHz to provide only 2-bit phase shifts (90-degree steps), the weight would be about 1 ounce per phase shifter. This weight corresponds to a total phase shifter weight of 25 pounds, which exceeds by a factor of more than 16 the weight of a mechanically steered planar array to provide the same gain and coverage.\* The control power per phase shifter is 0.1 watt, so 40 watts of control power will be needed to steer the beam.

If IF phase shifters are used, a low-noise mixer is required for each of the 400 elements in the array. These mixers add about 25 pounds to the weight of the antenna in addition to the weight of the IF phase shifters.

### 5.2.4 Scan Controller

A scan controller serves at least two functions: it must accept perhaps a single-channel input command and multiply or convert it to as many individual commands to the phase shifter as are needed to operate the array. The provision of such a multiplicity of commands, perhaps several hundred from a single input, is a function that is not common in computers.

The second function is one of performing computations necessary to provide the correct specific actuating signals to the phase shifter drivers. Since, in general, the computations must be made for each different setting

---

\*The planar array weight does not include the weight of the mechanical torquing devices.

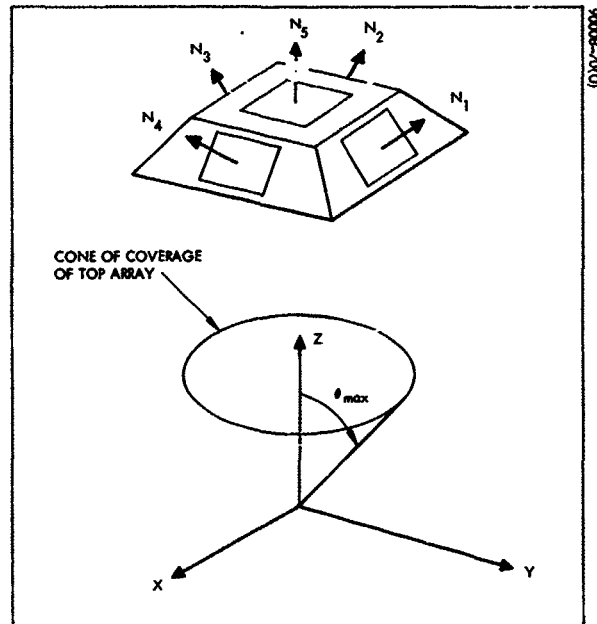


Figure 66. Five Square Arrays Arranged on Frustum of Pyramid

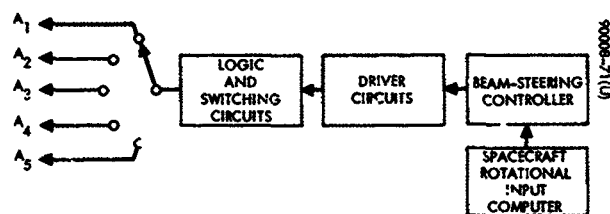


Figure 69. Block Diagram of Phase Scanned Array Antenna System

of the phase shifters, either sufficient speed must be achieved in the computations or the computations must be made in parallel.

The complexity of the controller depends on the number of elements and on the number of bits of phase shift employed. The device adds additional weight to the antenna and requires additional prime power.

#### 5.2.5 Quantitative Comparison -- Hemispherical Coverage

Based on the results of Reference 1, an array of five or six identical square arrays arranged on a pyramidal frustum will give the most efficient gain coverage of a hemisphere. Figure 68 shows a five-array combination and illustrates the coverage it provides. It is assumed that the gain reduction resulting from scanning the pencil beam from broadside of an array to its cone edge of coverage is 3 dB. This assumption is a good approximation for an array composed of elements with approximately a  $\cos \theta$  power pattern. A waveguide slot element in a multislot array has a pattern that satisfies this approximation.

Weight estimates are based upon a planar array design of slotted waveguides. The electrical and mechanical characteristics of a planar array of slotted waveguides designed for high gain, lightweight applications are well known (see Section 5.3).

Only one planar array is "on" at any one time. If the beam generated by one array is scanned beyond its maximum scan angle of coverage into the coverage range of an adjacent array, logic circuits automatically switch to the adjacent array and activate it, while the first array is deactivated. Figure 69 is a block diagram of the antenna system. The logic is controlled by a spacecraft rotational input computer (SRIC) which always knows the spacecraft position relative to the DRS in view. The SRIC also has an output which goes to the beam steering controller (BSC). The BSC converts beam position, relative to a fixed coordinate system of the spacecraft, to a set of digital settings for all phase shifters in an array. The digital command outputs of the BSC are converted to appropriate currents or voltages, and distributed to N phase shifters of N-element array by driver and switch circuits. Logic and switch circuitry directs driver signals to only one of the five arrays.

Estimates of power, weight, and space for the above-mentioned electronically scanned antenna system components are made below.

#### Single Array and Feed

Two antenna sizes are considered for the weight, power, and size estimates. The frequency of transmission is assumed to be 8.0 GHz. The frequency of reception is assumed to be 7.5 GHz. Circular polarization is assumed. These estimates are shown in Table 4.

TABLE 4. CHARACTERISTICS OF 20 dB AND 40 dB PLANAR  
ARRAYS TO BE UTILIZED IN HEMISPHERICAL COVERAGE  
SCANNED ANTENNA ARRAY

Number of Elements	$\theta = 0^\circ$ $G_{\max}$ (lin. pol.), dB		Scan Loss, dB*		Max Circular Polarizer Loss, dB		Weight of Array and Feed Only, ounces	Array Side D. M., inches	3 dB Beam- width $\theta = 0^\circ$ , degrees
	7.5 GHz	8.0 Hz	$N_A = 5$	$N_A = 6$	$\theta = 0^\circ$	$\theta_{\max}$			
			$\theta_{\max} = 47^\circ$	$\theta_{\max} = 41^\circ$					
16	19	20	3.5	3.0	0.5 dB	assume 1 dB	3.5-5	4.8	16
1600	39	40					$\approx 500$	48	1.5

\*due to element pattern only.

#### Spacecraft Rotational Input Computer (SRIC)

Weight  $\approx$  5 pounds

Volume @ 25 in<sup>3</sup>/lb  $\approx$  125 cubic inches

Power dissipation

$$P_{\max} = 1 \text{ watt/in}^3 \times 125 \text{ in}^3 = 125 \text{ watts}$$

Assuming safety factor  $> 2$  results in

$$P_{\text{SRIC}} \approx 50 \text{ watts}$$

#### Beam Steering Computer (BSC)

Assume slow scan, on order of several seconds, for low orbiting spacecraft. Worst-case estimate of digital scan rate

$$T_{\text{orbit}} \approx 90 \text{ minutes}, \frac{360^\circ \text{ scan}}{90} = 4 \text{ deg/min} = 1 \text{ deg/15 sec}$$

If the beam is scanned in increments of one-half of the 3 dB beamwidth, the fastest scan rate is (15 sec/1°)  $\times$  1/2(1.5°)  $\approx$  10 seconds hold per beam.

Assume a square array with uniform rectangular spacing. Then the basic arithmetic function for the computer is

$$\phi_{xy} = f(x, \theta, \phi) + g(y, \theta, \phi)$$

$$\{\text{sets of bits}\} = h(\phi_{xy})$$

$$1) \quad N = N_x N_y = 1600$$

3 or 4 bits/ $\phi$ -shifter

Require 1000 to 1200 integrated circuits

$$\text{Size} \approx 1/3 \text{ ft}^3 = 575 \text{ in}^3$$

Weight  $\approx$  10 pounds

$$P_{\text{Diss}} \approx 100 \text{ watts}$$

$$2) \quad N = N_x N_y = 100$$

4 bits/ $\phi$ -shifter

Have  $\approx 1/3$  complexity of computer for D above, therefore,  $1/3$  number of ICs.

$$\text{Size} \approx 1/4 \text{ ft}^3 = 430 \text{ cubic inches}$$

Weight  $\approx$  3.5 pounds

$$P_{\text{Diss}} \approx 30 \text{ watts}$$

#### Driver Circuits

Assume 1 driver/ $\phi$ -shifter, therefore have N drivers/array.  
Assume diode  $\phi$ -shifters only (not enough information on ferrites at this time).

##### 1) 1600 element array

2 bits/ $\phi$ -shifter (i. e.,  $\Delta\phi = 90$ -degree increments) believed adequate for good pattern control

$$\text{Weight} = 0.002 \text{ lb/driver} \times 1600 = 4 \text{ pounds}$$



Volume  $\approx$  12 cubic inches (epoxy and copper)

$$P_{\text{Diss}} \approx 1 \text{ watt each (from Esaira - 70 ma per diode)} \\ \times 1600 = 1600 \text{ watts}$$

A multilayered distribution board for simple pin connections and structural rigidity would weigh  $\approx$  1 pound.

## 2) Comments

- a) Heat dissipators add to complexity, since driver has its own losses; e. g., pull up resistors and limiter resistors.
- b) Driver would be attached to  $\phi$ -shifter, therefore need cabling from distribution board to switching circuits to  $\phi$ -shifters.

## Logic and Switching Circuits

Needed are  $N_E \times N_A$ -position, single throw switches; i. e.,  $\approx 16 \times$  five-position switches (diode type) to 1600  $\times$  five-position switches (diode type). Electromechanical switches would probably consume less power and be simpler in construction.

## Power Supplies

- 1) 1600 elements (2 bits)

$$\begin{aligned} P_{\text{Diss}} &\approx 1600 \text{ watts} - \phi\text{-shifter drivers} \\ &\approx 50 \text{ watts} - \text{SRIC} \\ &\quad 100 \text{ watts} - \text{BSC} \\ &\quad \underline{0 \text{ watts} - \text{logic and switching circuits}} \\ &> 1750 \text{ watts} \end{aligned}$$

Assuming  $\eta = 60$  percent efficiency

$$P_{\text{Diss}} > 3000 \text{ watts}$$

$$\text{Size} \approx P_{\text{Diss}} / 1 \text{ watt/in}^3 \approx 3000 \text{ cubic inches}$$

$$\text{Weight} \approx (0.24 \text{ lb/in}^3) \times (3000 \text{ in}^3) \approx 120 \text{ pounds}$$

2) 16 elements (4 bits)

$P_{\text{Diss}} \approx 32 \text{ watts} - \phi\text{-shifter drivers}$   
50 watts - SRIC  
30 watts - BSC  
0 watts - logic and switching circuits  
112 watts

Assuming  $\eta = 60$  percent efficiency

$P_{\text{Diss}} > 190 \text{ watts}$

Size  $\approx 190$  cubic inches

Weight  $\approx (0.04 \text{ lb/in}^3) \times (190 \text{ in}^3) \approx 8 \text{ pounds}$

Phase Shifters Weight (Excluding Drivers)

1)  $N_E = 1600$

Assume  $< 1 \text{ ounce} = 1/16 \text{ pound each}$

Weight  $\approx 100 \text{ pounds}$

Volume each  $\approx 0.5 \text{ in}^2$  by 3 to 6 inches long

2)  $N_E = 16$

Weight  $\approx 1 \text{ pound}$

Volume each  $\approx 0.5 \text{ in}^2$  by 3 to 6 inches long

Combining the above results, estimates of total weight and prime power required by the two electronically scanned arrays can be made. These estimates are shown in Table 5.

For comparison, similar estimates can be made for a mechanically steered array. In addition to the weight and size of a single array, the total antenna weight must include the weight of the gimbaling system and a portion of the mounting structure. The power required for steering is that required by the torquing devices and control electronics. Conservative estimates were made, and the combination of these considerations is presented in Table 6.

TABLE 5. ELECTRONICALLY SCANNED ANTENNA ESTIMATES

Design Frequency = 8 GHz

Number of Elements	Minimum Gain, dB		Planar Array Side Dimension, inches	Weight, pounds*	Power Dissipation, watts*
	Receive	Transmit			
16	14.5	15.5	4.8	14	> 112
1600	34.5	35.5	48	770	> 3000

\*Excludes cables and logic-switch circuits

TABLE 6. MECHANICALLY STEERED ANTENNA ESTIMATES

Design Frequency = 8 GHz

Gain, dB	Side Dimension, inches	Weight, pounds	Power, watts
16	4	5	< 8
3	36	25	< 15

#### 5.2.6 Conclusion

Referring to Tables 5 and 6, it can be seen that the power required by the electronically steered antenna is several orders of magnitude larger than that required by the mechanically steered antenna for high gains. The weight difference is not great for low gain antennas, but for a gain of 35 dB, which is a very real possibility for anticipated optical imaging data rates, the difference in weight is considerable. From an examination of Table 5, it can be seen that for high gains in the vicinity of 35 dB, both the power requirement and weight of the electronically steered antenna is way out of proportion compared to the total spacecraft, payload, and other subsystem weights and powers.

Electronically scanned arrays are desirable where mechanical motion of the antennas cannot be tolerated or the rapidity of the required beam steering exceeds that which can be obtained by mechanical movement of the antenna. Under those conditions it may be necessary to pay the price of additional weight and prime power. In the application of interest here, however, neither of the above requirements for mechanical motion or rapidity of beam steering apply. For this reason it is felt that further study of electronically steered arrays at this time is unwarranted, and further study effort is directed to mechanically steered antennas.

### 5.3 PLANAR ARRAY OF SLOTTED WAVEGUIDES

#### 5.3.1 Description

The antenna discussed in this section consists of a planar array of shunt slots cut in the broadwall of rectangular waveguides. Antennas of this type are extremely efficient and, consequently, display very high-gain characteristics for a given aperture size.

The low-gain antennas (10 to 20 dB) consist of from two to four linear arrays that are fed by a single feedguide across the back of the array. The coupling is accomplished by means of a slot cut in the center of each linear array. The feedguide can be fed either by waveguide or a coaxial connector properly matched to the feedguide. The thickness of the low-gain planar arrays is on the order of a half of a free space wavelength. An X-band planar array with 20 dB peak gain is shown in Figure 70.

The higher gain antennas are obtained by connecting many of the low-gain antennas or modules that were described above. These modules are fed by a corporate feed consisting of rectangular waveguide and H-plane power dividers. The corporate feed for one quadrant of a high gain planar array is shown in Figure 71 and a typical H-plane power divider is shown in Figure 72. The thickness of the antennas with gains between 20 and 35 dB will be approximately one-half of a free-space wavelength. For the antennas with gains between 35 and 50 dB, the thickness will be approximately one free space wavelength.

Circularly polarized planar arrays are in general rather complex; thus, it is usually advantageous to use a polarized planar array of slots. Various types of polarization converters that will convert linear polarization to circular polarization are discussed in another section of this document. These polarization converters are attached to the front face of the planar array and will add to the overall thickness of the antenna.

In all of the discussions and calculations that follow, the aperture was assumed to have a square shape, since square planar arrays are simpler to design and fabricate than are planar arrays of other shapes. This, however, does not mean that planar arrays with other shapes could not be considered for this application.

#### 5.3.2 Electrical Properties

Since the frequency range of operation has not been chosen, this discussion will include predicted antenna performance characteristics for four representative frequency ranges. The four transmitting frequencies were assumed to be 2.25, 8.0, 15.0, and 35.0 GHz.

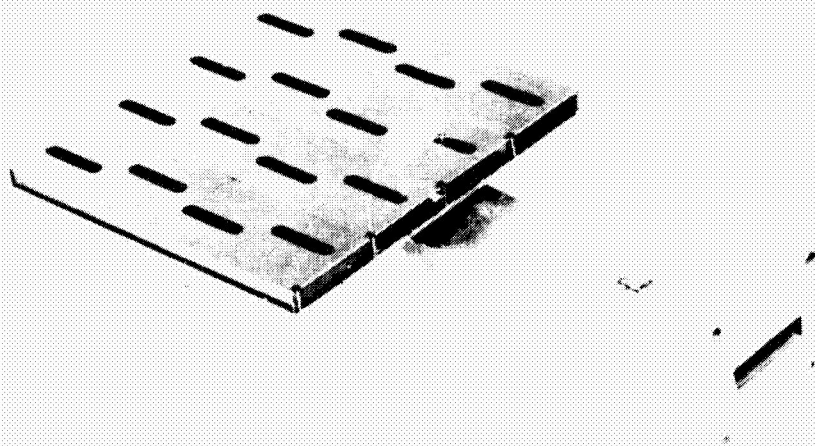


Figure 70. X-Band Planar Array  
(Photo 4R02113)

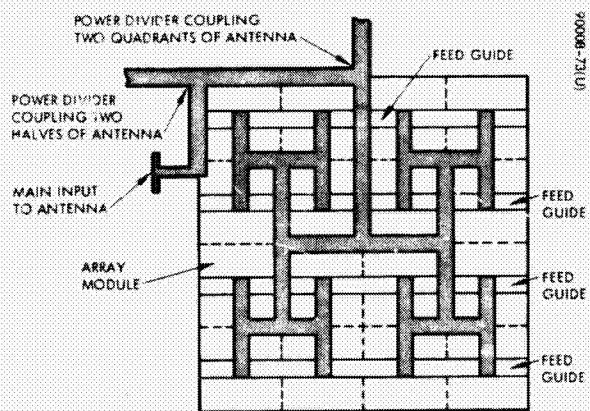


Figure 71. Corporate Feed for  
One Quadrant of Planar Array  
Antenna

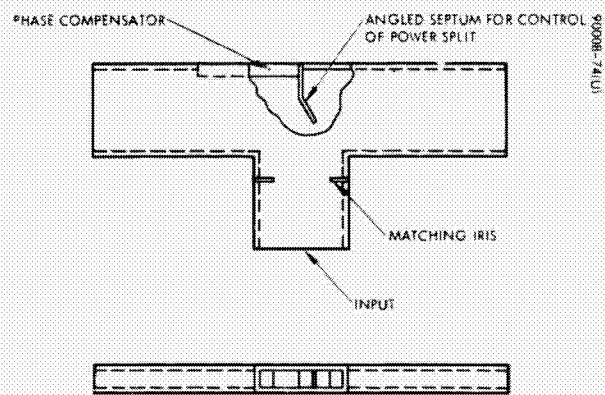


Figure 72. Typical H-Plane  
Power Divider

### Gain (Efficiency)

As was mentioned previously, slotted waveguide planar arrays are extremely efficient devices; efficiencies of greater than 80 percent have been measured on planar arrays that operate at frequencies as high as  $K_u$ -band, and greater than 70 percent for frequencies as high as 60 GHz. Antenna aperture size as a function of antenna gain for the four operating frequencies being considered is shown in Figure 73. Although the curves are shown as continuous, this is not really the case for low gain antennas, since the slots are discrete elements with a fixed element pattern. However, for antenna gains greater than 20 dB, these curves can be considered to be continuous.

Planar arrays can be designed to provide very efficient operation over a 12 to 15 percent frequency band. The estimated gain loss as a function of percent frequency bandwidth is plotted in Figure 74. The three main factors that contribute to this gain degradation are a decreasing effective aperture for decreasing frequencies, a high voltage standing wave ratio (VSWR), and slot-to-slot phase and amplitude errors.

### Beamwidth

The 3-dB beamwidth as a function of antenna gain is plotted in Figure 75. These beamwidths were calculated for a square aperture with a uniform aperture illumination. If a tapered aperture distribution is required in order to lower the sidelobes, the beamwidth will increase by a factor that is dependent on the sidelobe level and the type of amplitude taper being utilized.

### Sidelobes

All of the gain and beamwidth data presented in the two previous sections were based on a square-shaped aperture with a uniform amplitude distribution. This configuration provides a  $(\sin X/X)^2$  far-field radiation pattern with a first sidelobe 13.2 dB down from the peak of the main beam. The pattern is shown in Figure 76. Lower sidelobe levels may be obtained by changing the shape of the antenna, (e. g., a circular aperture with a uniform amplitude distribution has a first sidelobe 17.6 dB down from the peak of the main beam), by exciting the aperture with a tapered amplitude distribution, or a combination of the two.

For the large planar arrays with gains between 35 and 50 dB, very low sidelobe levels (30 to 35 dB down) may be obtained with a minimal gain loss by utilizing efficient amplitude tapers such as the Taylor distributions. The antennas with less than 35 dB of gain do not have a sufficient number of elements across the aperture to approximate these sophisticated amplitude tapers. This means that a simpler amplitude taper, such as a linear or parabolic taper, would have to be utilized. Minimum sidelobe levels that could be realized would be approximately 25 dB down for antennas with gains between 25 and 30 dB, and on the order of 20 to 22 dB down for antennas with 25 dB of gain or less.

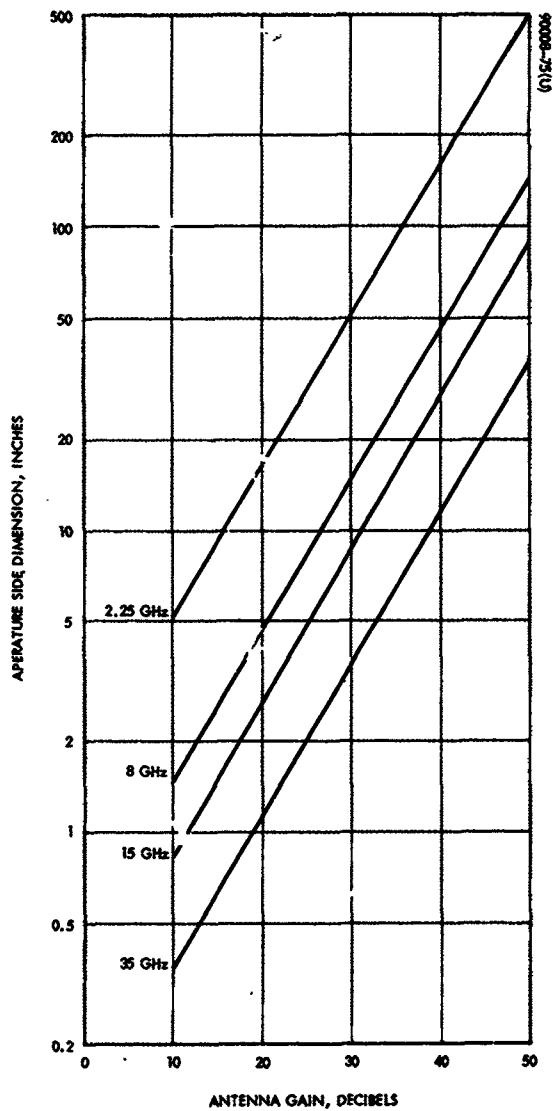


Figure 73. Square Planar Array Aperture Size Versus Antenna Gain

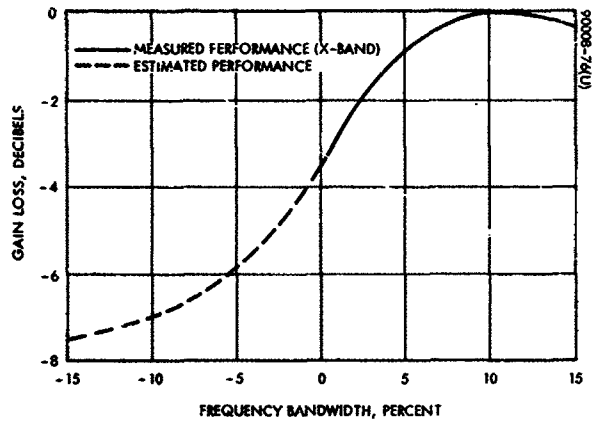


Figure 74. Antenna Gain Loss Versus Frequency

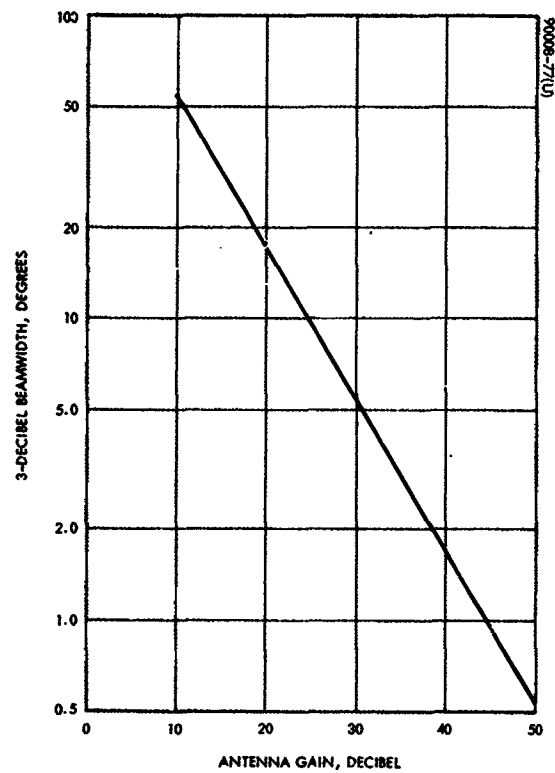


Figure 75. 3-dB Beamwidth Versus Antenna Gain for Square Aperture With Uniform Illumination

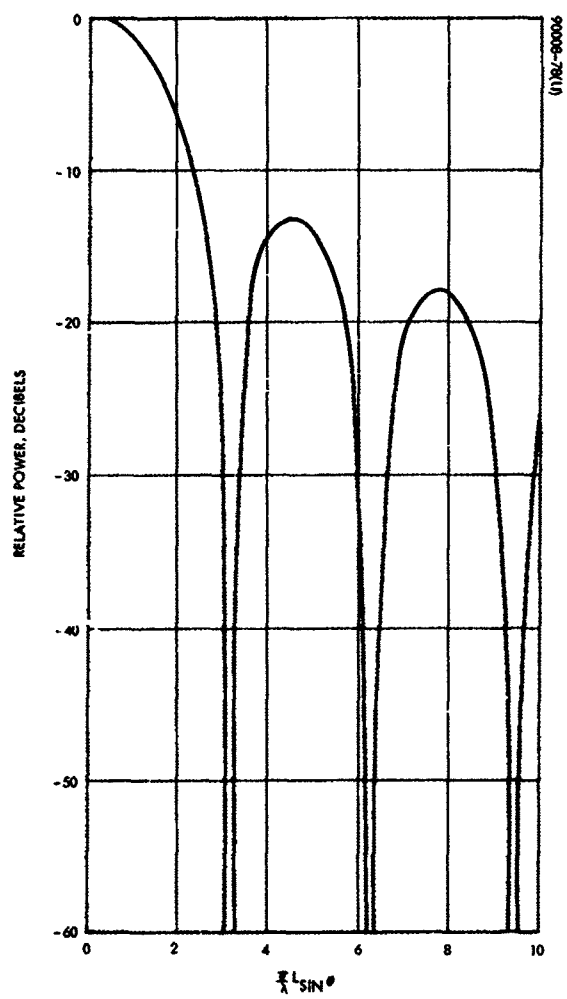


Figure 76. Pattern of Uniformly Illuminated Square Aperture of Dimension  $L$  on Side



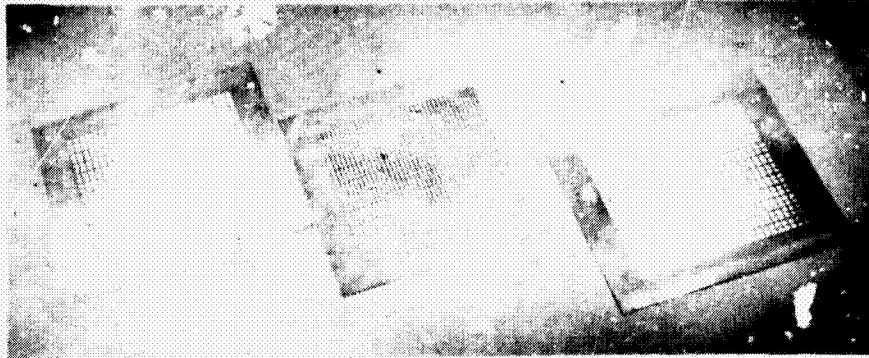


Figure 77. Polarizing Sheets  
for Panel Polarization  
Converter  
(Photo 5R0330d)

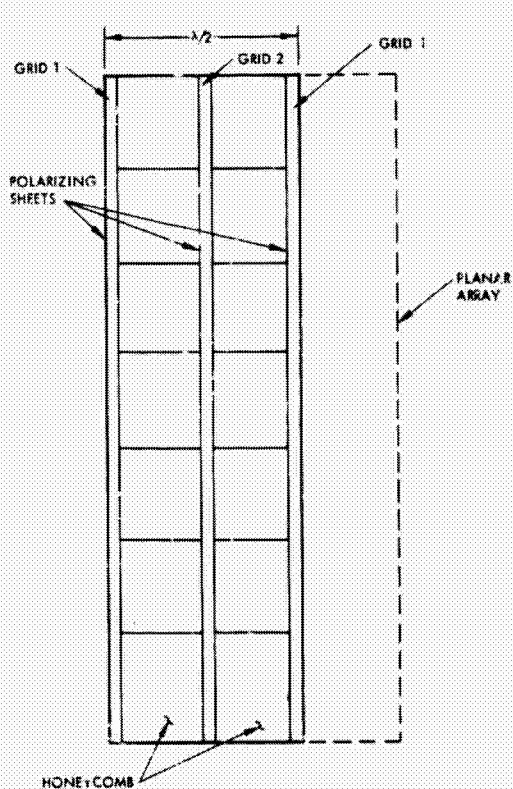


Figure 78. Panel Polarization  
Converter Configuration

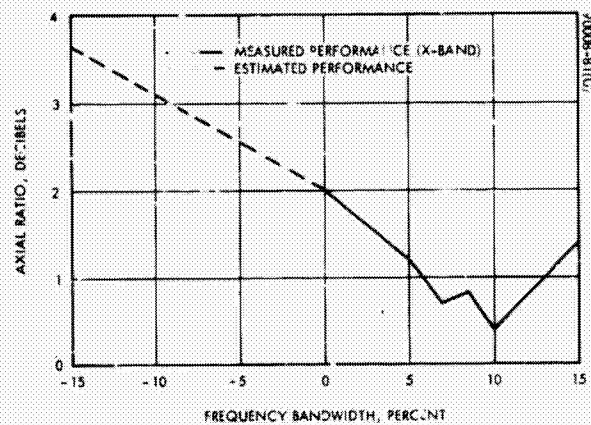


Figure 79. Axial Ratio Versus  
Frequency Bandwidth

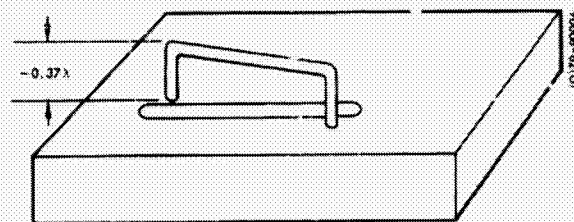


Figure 80. Typical Loop-Slot  
Configuration for Circular  
Polarization

As was the case with the gain characteristics, good sidelobe performance could be maintained over an 8 to 12 percent frequency band, but there would be some degradation for a larger frequency band. The amount of sidelobe degradation is difficult to estimate without a detailed computer analysis

#### Voltage Standing Wave Ratio (VSWR)

Slotted waveguide planar array antennas have been designed with a VSWR of less than 1.50:1.0 for a 13-percent frequency band. Outside of this frequency band, measurements indicate that the VSWR tends to oscillate between 2.0:1.0 and 4.0:1.0. The planar array could be designed so that the low VSWR occurred in the transmitting frequency band and that the degradation occurred in the receiving frequency band.

#### Polarization

The slotted waveguide planar arrays are linearly polarized, so some method of polarization conversion must be added to provide the required sense of circular polarization. For the present application there appears to be two attractive methods that can be used to obtain circular polarization with an array of linearly-polarized slots. Both of these techniques have been demonstrated by personnel at Hughes.

The first method is a panel-type polarization converter consisting of three polarizing sheets separated by a specific electrical distance. The three polarizing sheets with the critical separation convert the linearly-polarized electric field into two orthogonal components and delay the phase of one component 90 electrical degrees with respect to the other, resulting in circular polarization. The three polarizing sheets are shown in Figure 77, and the panel-type polarization converter configuration is shown in Figure 78. An experimental polarization converter of this type was designed and fabricated for operation with an X-band planar array. The device provided a circularly polarized wave with an axial ratio of less than 2.0 dB over a 20-percent frequency band. A plot of the axial ratio as a function of frequency bandwidth is shown in Figure 79.

The second method involves making the slot itself a circularly polarized radiating element. This is accomplished by placing a conducting loop across the slot, as is shown in Figure 80. Planar arrays of this type of element have exhibited axial ratios of less than 2.5 dB over a 12-percent frequency band. The axial ratio performance over a 25-percent frequency band would be comparable to that of the panel-type polarization converter.

From a practical standpoint, the panel type polarization converter could be used on all sizes of planar arrays, but the loop-slot radiator may not be desirable for antennas with gains over 30 dB, since the number of slots becomes very large.

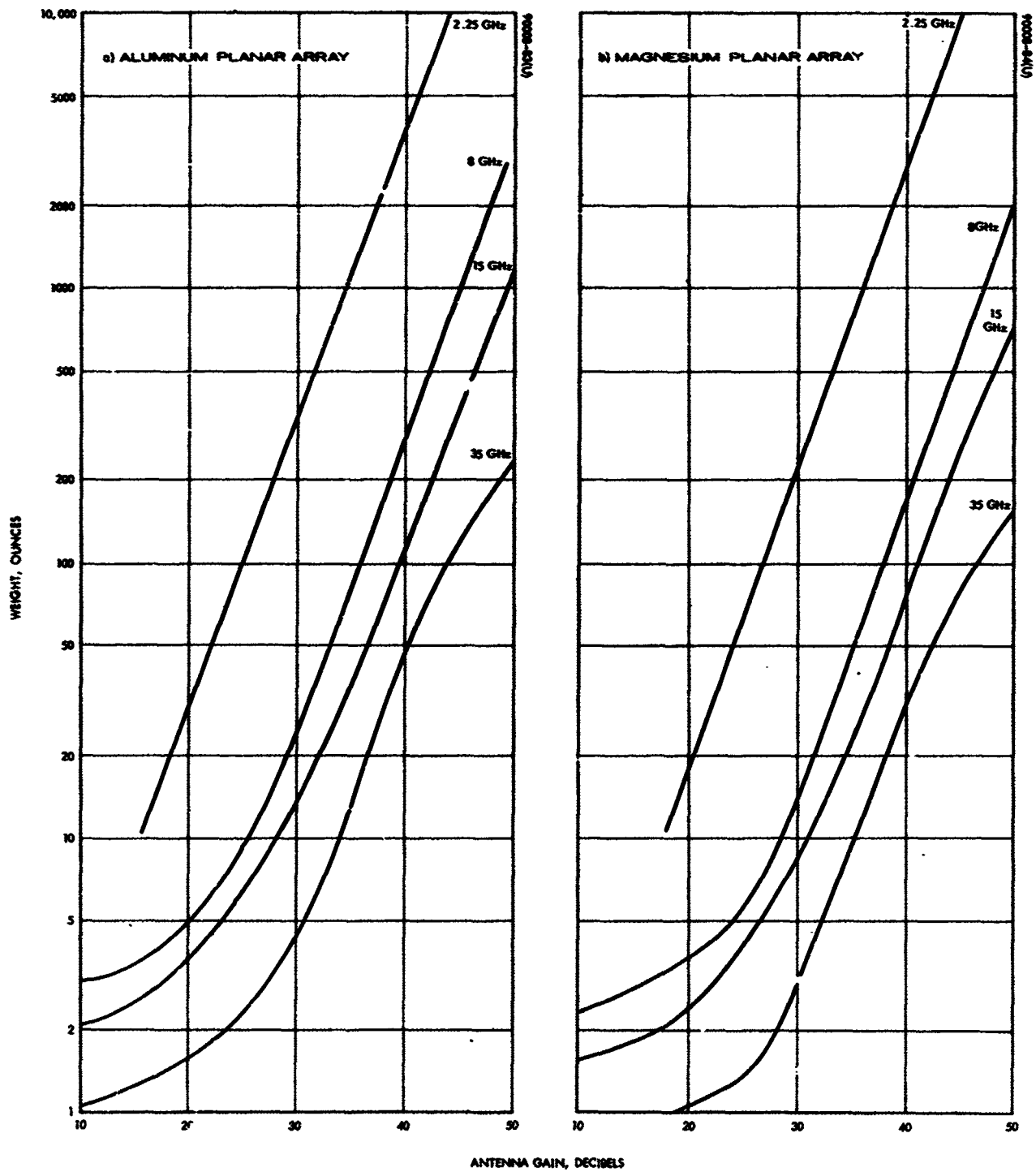


Figure 81. Weight as Function of Antenna Gain for Square Aperture

### Power Handling Capabilities

The factor that will determine the power handling capability of the planar array is the method by which it is fed. For frequencies up through X-band, the planar array could be fed either by waveguide or a coax-to-waveguide transition. For frequencies higher than X-band, the planar array would probably be fed by waveguide since coaxial cable starts to get very lossy at the higher frequencies. The breakdown that might occur is multipactor breakdown. This effect depends on the peak voltage across a region, the dimension of that region, and the frequency of operation. For waveguide of the height-to-width ratios employed in the planar arrays, power handling capabilities, as limited by multipactor breakdown, are of the order of tens of kilowatts or more. For the radiating and coupling slot dimensions of interest, multipactor breakdown should not occur for power levels less than the order of kilowatts.

In the case of the lower frequencies where coaxial feed lines might be used, multipactor effects will not be a problem in dielectric filled lines. In air-filled lines of 50-ohm impedance, multipactor effects should not occur for the power levels of interest.

### 5.3.3 Mechanical Properties

#### Materials and Weight

As is the case with all spacecraft hardware, it is desirable to make the antenna as lightweight as possible. In order to attain this goal the planar arrays would be fabricated from thin (0.016 inch) sheets of aluminum or magnesium. The predicted antenna weights as a function of antenna gain for the four operating frequency ranges under discussion are plotted in Figure 81, for aluminum and magnesium, and the aperture shape is assumed to be square. For some applications, planar arrays have been fabricated with a combination of magnesium and aluminum and in that case the weight would fall between corresponding values taken from these two figures.

#### Fabrication Techniques

For the purpose of discussing fabricating techniques, the planar array can be considered to consist of four basic parts: the slotted radiating plate, the main body containing the array of waveguides minus the slotted top-wall, the feedguides, and in the case of the higher gain antennas, the corporate feed containing the power dividers.

The slotting of the thin radiating plate has been accomplished successfully by either milling with a numerically controlled milling machine or by a chemical milling process. A precise method of fabricating the main body containing the array of waveguides consists of straddle-milling the entire panel from a sheet of magnesium or aluminum. The feedguide is a simple U-shaped channel, machined or formed from the desired material. The method of fabricating the power dividers, if they are utilized, is somewhat

dependent on the number required. For a relatively small quantity they would probably be fabricated from thin-wall waveguide with the septums and matching irises either bonded or dip-brazed into place. For a large quantity it would be more economical to make tooling for investment castings and then cast the power dividers.

Electron-beam welding is used to attach the radiating plate to the main body of the planar array. Both aluminum and magnesium have been electron-beam-welded with excellent results. This technique is desirable because it provides strong joint with minimum distortion, since very little heat is generated. The feedguides can be either electron-beam-welded or bonded to the back of the planar array. The technique that is used for bonding is a two-step operation; first a nonstructural, silver filled, conductive adhesive is used in order to maintain a continuous conductive path, then a structural epoxy is used to provide the necessary mechanical integrity. With the higher gain antennas, the corporate feed is bonded to the feedguides in the same manner as just described.

The panel-type polarization converter is also constructed as a very lightweight unit. The polarizing sheets are fabricated from thin dielectric sheets clad with a 0.001-inch layer of metal. The required polarizing pattern is photo-etched onto the metallic coating of the dielectric sheets. The spacing between the polarizing sheets can be maintained by placing a lightweight phenolic honeycomb between them, as shown in Figure 78. This structure is then attached to the planar array.

In the case of the planar array of loop-slots, it is only necessary to attach the loop to the slotted radiating plate. This can be accomplished by bonding or electron-beam welding.

#### 5.3.4 Effects of Tracking Method on Antenna Design

##### Command or Programmed Steering

Since these two types of antenna steering involve sending electrical signals to a motor that drives the positioning mechanism without feedback from the satellite-to-satellite communication link, there is no effect on the RF design of the planar array antenna.

##### Monopulse Autotracking

Once the two communication antennas (one on each satellite) are aligned within their 3 dB beamwidths, a monopulse autotracking scheme can be utilized to keep them aligned as long as there is a signal transmitted between the two antennas. From an antenna design standpoint the only special feature required on a monopulse antenna is a sum-and-difference circuit. The microwave circuit shown schematically in Figure 82 can be used to obtain the sum-and-difference signals necessary for a dual-plane phase monopulse tracking system. The basic element of this network is a four-port hybrid junction that has the property of combining two input signals

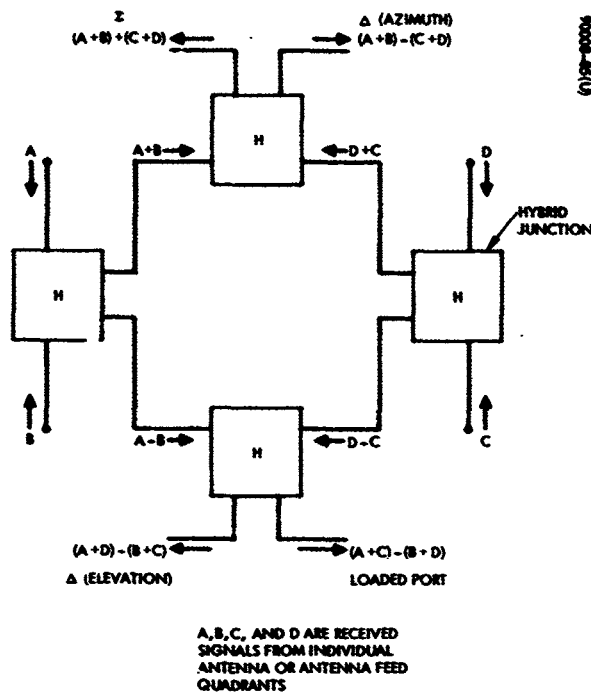


Figure 82. Operation (on Reception) of Monopulse Sum and Difference Network

in phase at one output port, and 180 degrees out of phase at the other output port. Four such hybrids are arranged, as shown in Figure 82, to provide difference signals in two orthogonal planes in addition to the pencil beam sum signal. More than 30 dB of isolation can be obtained between the sum port and either of the difference ports. The four-port hybrid junctions can be designed in waveguide, coax, or stripline.

The only limitation involved with utilizing the planar array as a monopulse tracking unit is that the radiating aperture must be able to be divided into four identical subapertures or quadrants. This implies that it would be rather difficult to mechanize a planar array with less than sixteen slots (a 20 dB gain antenna) for monopulse tracking operation. But this is consistent with the conclusion of Section 4.5; that automatic tracking is necessary only for high-gain, narrow-beam antennas where command or programmed steering is inadequate.

## 5.4 ARRAYS OF HELICAL RADIATORS

### 5.4.1 Description

Arrays of end-fire radiators or volumetric arrays such as the helical radiator have the advantage of being smaller in cross section than the other types of radiators and are less complex than dipole or slot arrays. The axial mode helical radiator is formed by winding a wire in a helix with a pitch angle of from 11 to 16 degrees and a diameter of the order of  $\lambda/3$ . A metallic ground plane whose dimensions are of the order of  $\lambda$  is placed at one end of the helix. The helix is usually fed by a coaxial line whose outer conductor terminates on the ground plane and whose inner conductor passes through the ground plane to form the helix. The helix itself may be wound on a dielectric tube or supported by dielectric spokes extending from a metal tube along the longitudinal axis of the helix. Several helices can be connected by a network of transmission lines to form an array. The design and performance of suitable arrays of helices are discussed in some detail in succeeding paragraphs.

### 5.4.2 Electrical Properties

The design parameters of helical radiators scale linearly with wavelength, hence the dimensions of both the individual helices and arrays of helices are given in terms of wavelength in the following discussion. It is emphasized that when dealing with helices, mutual coupling effects are significant for practical spacings. These effects are very difficult to predict. The curves of size, weight, etc., given are extrapolations of existing data, with mutual coupling neglected. Consequently, they are only gross estimates of these properties.

#### Gain

The gain of an array of helical radiators is dependent on the number of helices in the array, the spacing between the helices, and the gain of the individual helix. If the helices are spaced sufficiently far apart so that mutual coupling is then negligible to a first approximation, the gain of an array of  $N$  helices is simply the product  $NG$ , where  $G$  is the gain of a single helix.

The gain of a helical radiator is related in a rather complex fashion to the helix diameter, pitch angle, and the length of the helix (Reference 2). The gain also depends on whether the helix has one or more windings. The gain of a bifilar helix (Reference 3) is greater than that of a unifilar helix of the same length, and for that reason is preferred over the unifilar helix. The relation  $G = 10 L/\lambda$ , where  $L$  is the overall helix length, has been found to give the gain of a bifilar helix within 1 dB over the frequency range in which the helix radiates in the axial mode.

The spacing between helices in the array should be greater than  $\sqrt{L/\lambda}$  wavelengths in order to reduce mutual coupling effects. Assuming that the spacing between radiators is greater than  $\sqrt{L/\lambda}$ , the gain of an array of N helices is approximately

$$G = 10 NL/\lambda$$

where L is the length of an individual helix. The variation of array gain with the number and length of the helices is illustrated in Figure 83.

If it is assumed that the helices of the array are arranged in rows to form a square array and that the spacing between rows is  $\sqrt{L/\lambda}$ , then the diagonal of the array is given by

$$\Delta = \sqrt{2}(\sqrt{N}-1) \sqrt{L/\lambda} \text{ wavelengths}$$

On setting the array diagonal equal to the length of an individual helix, the following relation is obtained for the number of helices in the array

$$20 N^2 - 40 N\sqrt{N} + 20 N = G$$

The number of helices required for an array whose diagonal equals the length of an individual helix is shown in Figure 84 as a function of G. The array diagonal as a function of gain is plotted in Figure 85.

The resistive losses on a helical radiator are usually completely negligible, and the efficiency of an array of helices is determined by the attenuation in the transmission line network connecting the helices. Efficiencies greater than 90 percent have been achieved by arrays of four and five helices.

#### Bandwidth of Helix

The bandwidth of a helix radiating in the axial mode is given by Kraus (Reference 2) and is determined by the requirement that  $2/3 < C_\lambda < 4/3$ , where  $C_\lambda$  is the circumference of the helix in terms of wavelength. This relation holds true for helical radiators with pitch angles of 13 to 15 degrees and axial lengths up to approximately two wavelengths. The relation is not correct for helices much longer than two wavelengths, since the upper frequency limit is a function of the length of the helix (see Reference 4).

The lower frequency limit depends on the effective launching of the axial mode along the helix. For pitch angles of 13 to 15 degrees, the lower limit is given approximately by  $C_\lambda = 0.8$ , and is substantially constant with helix length. The upper frequency limit for a given helix depends on the relationship of the phase velocity along the helix conductor to that required



by the Woodyard-Hansen criterion. As the length of the helix is increased the phase velocity required for optimum gain increases and the phase relationship between turns of the helix is no longer optimum. The variation of  $C_\lambda$ , and hence the upper frequency limit, with length is shown in Figure 86 for a 13-degree helix. The peak helix gain occurs for  $C_\lambda$  a few percent less than the limit shown in Figure 86, hence, in general, the length of a helix should be less than 7 or  $8\lambda$  so that at the receive frequency,  $C_\lambda$  is greater than 0.8. The gain of a four-helix array is shown in Figure 87 as a function of frequency. At higher frequencies where the percentage bandwidth requirements are less, this length restriction on the helices no longer applies.

#### Minimum Length

The limitations on the minimum length of a helical radiator operating in the axial mode result from a combination of impedance sensitivity, pattern degradation, and polarization degradation.

The frequency insensitivity of the input impedance of axial mode helices depends on the fact that the current distribution at the input is not appreciably affected by the open end. This condition requires that the helix conductor length be at least 1.5 wavelengths (Reference 2). For an axial mode helix, the circumference ranges from 0.75 to 1.3 wavelengths so that the helix must have at least one turn or more. However, from the point of view of pattern symmetry, a one-turn helix is not very satisfactory. The two orthogonal components of the electric field have patterns that are quite different and have high back lobes so that even if circular polarization were obtained for some direction it would not be maintained over a very large coverage region.

The axial ratio on the axis of a helix is given approximately by the relation (see Reference . ,

$$\text{axial ratio} = \frac{2n + 1}{2n}$$

where  $n$  is the number of turns. For a small number of turns, the axial ratio would be further degraded at other angles as a result of the pattern asymmetry discussed above. Consequently, it appears that three turns is the minimum number that should be used. This number of turns corresponds to a minimum helix length of approximately three-quarters of a wavelength. These conclusions are based on the properties of a single conductor helix. No data is available on short bifilar helices. It appears that the bifilar helix would improve the pattern symmetry somewhat and might allow even shorter axial mode helices to be used.

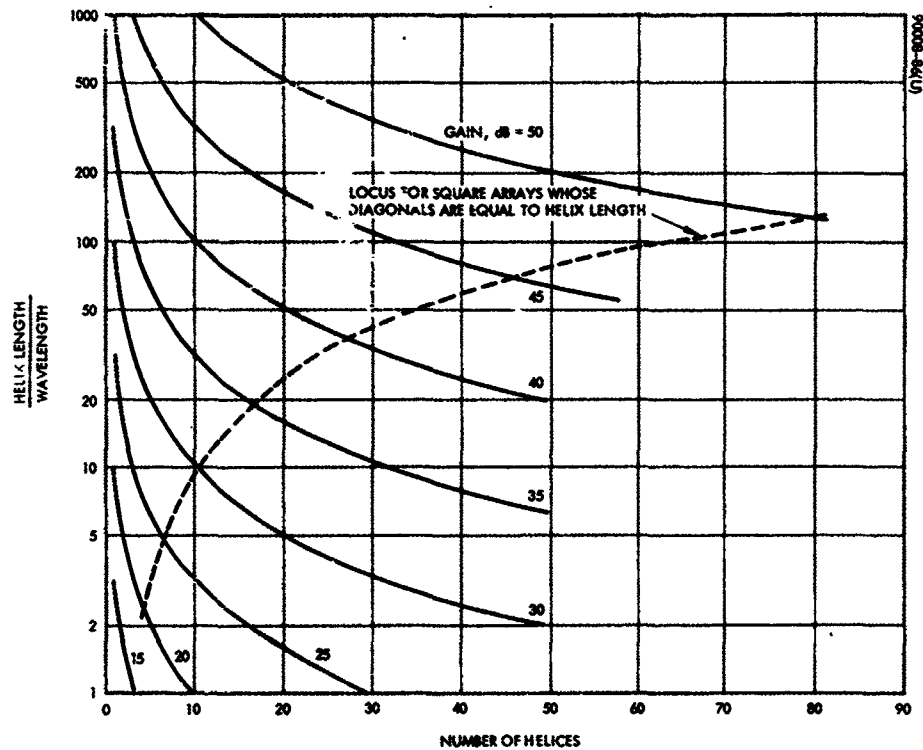


Figure 83. Helix Length as Function of Number of Helices, With Gain as Parameter

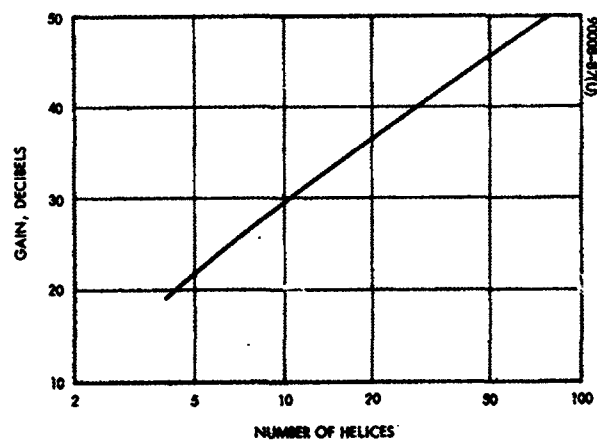


Figure 84. Array Gain as Function of Number of Helices for Array Diagonal Equal to Helix Length

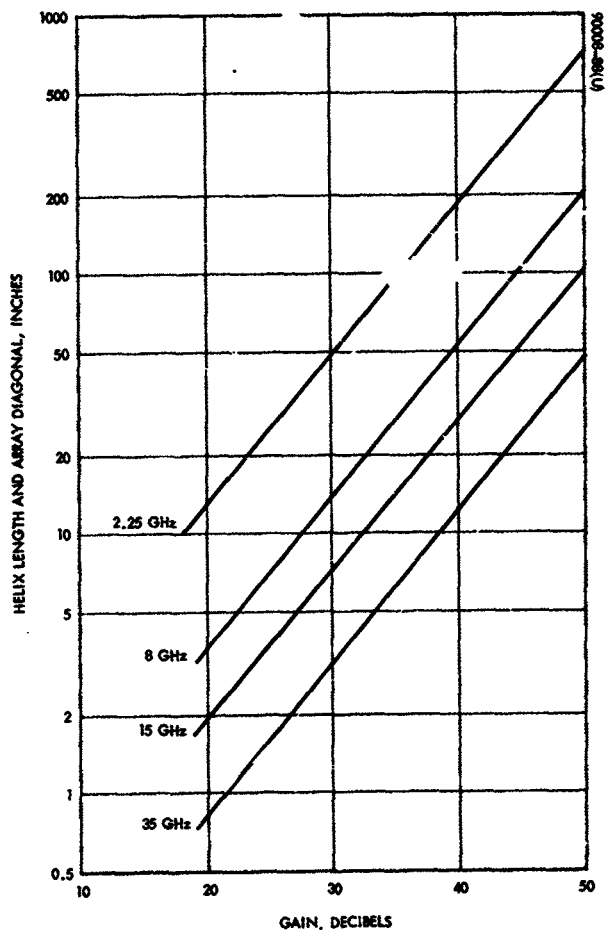


Figure 85. Length of Helix and Array Diagonal as Function of Array Gain

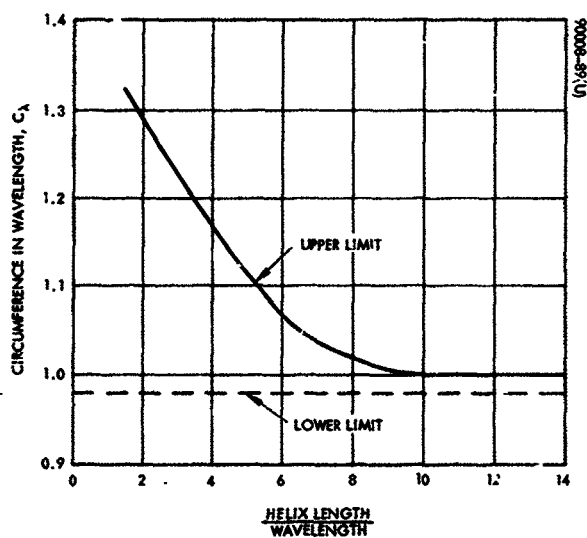


Figure 86. Allowable Upper and Lower Limits of Circumference as Function of Helix Length

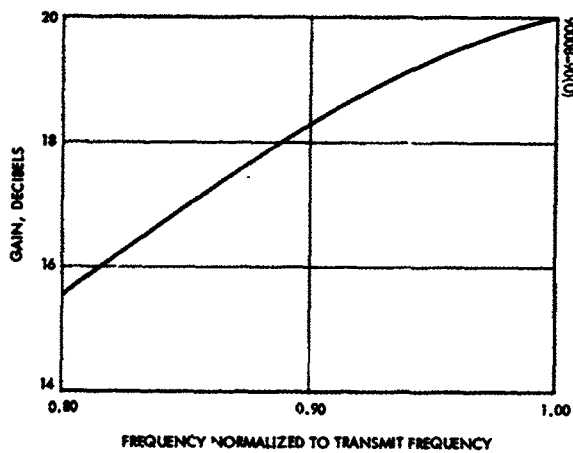


Figure 87. Gain of Four-Helix Array as Function of Frequency

### Beamwidth and Sidelobe Level

The radiation pattern of an array of helices can be computed using array theory, provided the radiation patterns of the individual helices in the array are known. If the helices are spaced sufficiently far apart so that mutual coupling can be neglected, the array patterns can be computed, using for the pattern of the individual helix the relation (see Reference 2)

$$E(\theta) = \sin\left(\frac{\pi}{2n}\right) \frac{\sin[\pi n (S_\lambda (1 - \cos \theta) + 1/2)]}{\sin[\pi (S_\lambda (1 - \cos \theta) + 1/2)]} \cos \theta$$

where

$n$  = the number of turns in the helix

$S_\lambda$  = the separation between turns in wavelengths

The patterns computed in this fashion are useful at the transmit frequency where mutual coupling between the helices is not great. At frequencies deviating far from the design frequency, the mutual coupling between helices cannot be neglected and the measured radiation patterns have a broader beam and higher sidelobes than indicated by the computed patterns.

Patterns for four and seven element arrays of helices are shown in Figures 88 and 89. The patterns for the seven-helix array are computed patterns using the theoretical patterns of Kraus.

It is evident from the foregoing discussion that the exact beamwidth and sidelobe level of the radiation patterns of arrays of helices must be determined by actual measurement. However, the beamwidth may be determined approximately from the relation

$$\theta^2 = \frac{26000}{G}$$

This beamwidth is plotted as a function of gain in Figure 90.

Antennas with low sidelobe levels have amplitude distributions which are tapered toward the edges of the aperture. Taylor tapers give low sidelobes with minimum loss of gain. This type of distribution cannot be used effectively in arrays of helices, since such arrays are usually composed of a relatively small number of helices.

The sidelobe level of arrays of helices fall in the range of 10 to 15 dB below the main beam. Lower sidelobes (15 to 20 dB below) can be obtained by using more helices with closer spacing and tapering the distribution stepwise so that the helices on the outer periphery receive less power than the inner helices. This method results in an antenna which is much heavier and more complex, and in effect nullifies one advantage of arrays of helices over a dipole or slot array.

#### Voltage Standing Wave Ratio

Arrays of four and five helices have been built with an input VSWR less than 1.5:1 over a 25 percent frequency band. This performance can also be achieved with larger arrays; however, the design of the branching structure becomes increasingly difficult as the number of elements is increased.

#### Polarization

The axial mode helical antenna radiates right or left-hand elliptically polarized waves depending on the screw sense of the helix winding. The polarization is very nearly circular for helices with eight or more turns. The axial ratio or ellipticity at the beam peak of an array of five bifilar helices is shown as a function of frequency in Figure 91. The axial ratio increases for angles off the beam peak and may be very nearly linearly polarized for angles much greater than the 3 dB beamwidth.

#### Power Handling Capability

The peak power handling capability of helical array antennas for space applications is limited by multipactor breakdown. The feed network used to distribute power to the helices and the input to helices themselves are most susceptible to multipactor breakdown. The multipactor effect is a resonance phenomenon which is frequency sensitive, and the dimensions of the branching network and input to the helices must be chosen so small or so large that multipactor breakdown cannot occur. The peak power handling capability of stripline with a characteristic impedance of 50 ohms is of the order of 1 kilowatt for frequencies in the range 2 to 35 GHz.

The average power handling capability of the stripline components is limited primarily by the allowable temperature rise at the center of the line. For a given rise in temperature the power handling capability decreases with frequency. The average power handling capability of 50-ohm line with a Rexolite dielectric is shown as a function of frequency in Figure 92 for a 39°C rise in temperature.

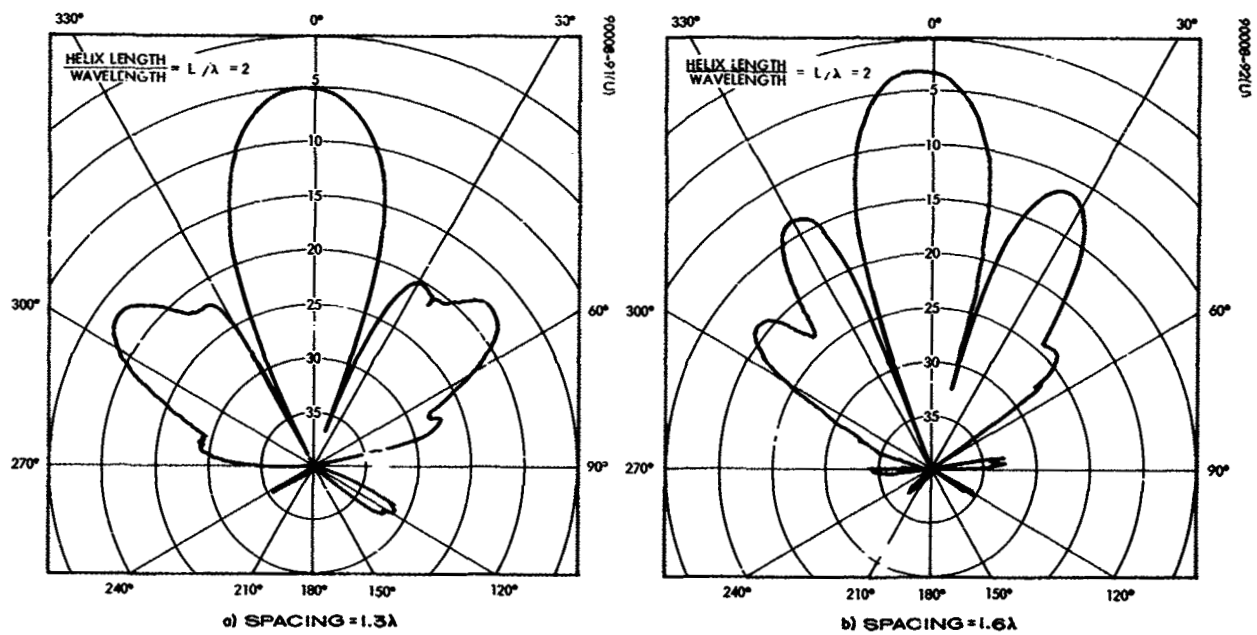


Figure 88. Patterns for Four-Element Array

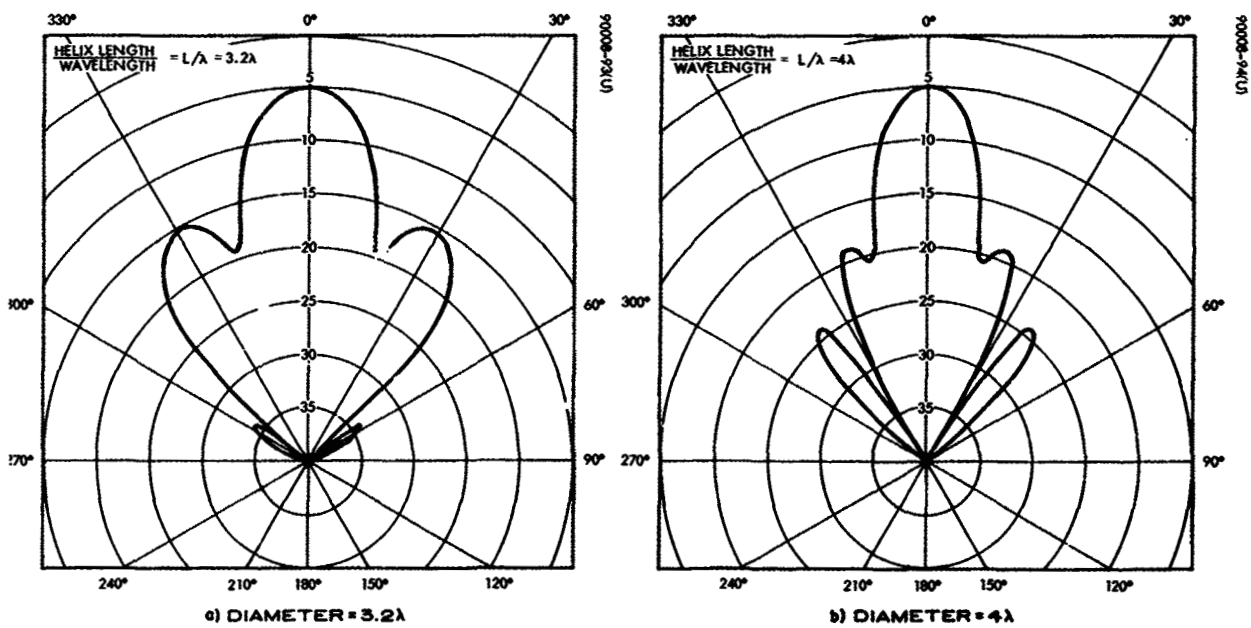


Figure 89. Patterns for Seven-Element Array

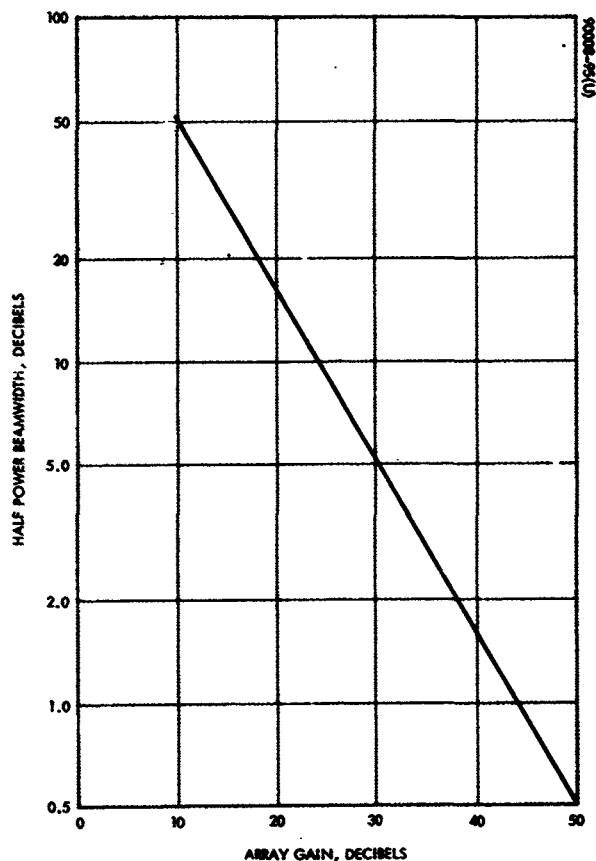


Figure 90. 3-dB Beamwidth Versus Antenna Gain for Square Array of Helices With Uniform Excitation

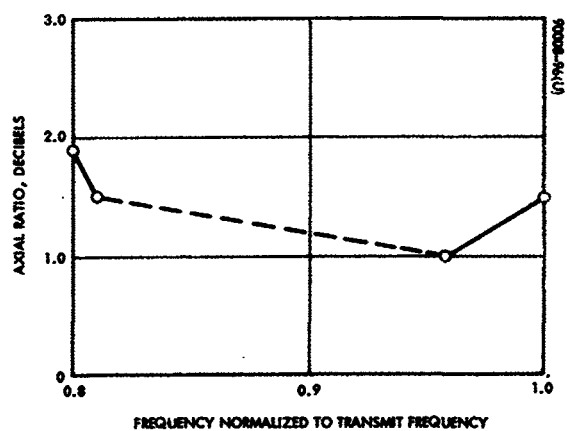


Figure 91. Five Bifilar Helix Array Axial Ratio as Function of Frequency Normalized to Transmit Frequency

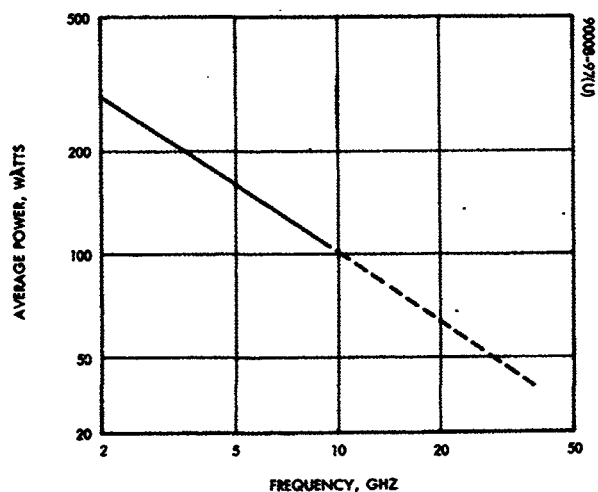


Figure 92. Average Power Handling Capability of 50-ohm Line With Rexolite Dielectric as Function of Frequency

### 5.4.3 Mechanical Properties

#### Materials and Weight

The materials best suited for the fabrication of an array of helices depend on the environment in which the antenna is expected to survive and operate. For spacecraft applications, lightweight, high-strength materials such as beryllium and magnesium, and dielectric materials such as fiberglass and teflon are used.

The materials and fabrication techniques are dependent on the frequency of operation as well as the environment. The dimensional tolerances required at the higher frequencies are more severe and may necessitate different fabrication techniques. The windings of helical arrays operating at S-band and below can be supported by a metallic cylinder with dielectric spokes, as shown in Figure 93. Helices operating at X-band and above usually employ a dielectric tube to support the winding, as shown in Figure 94.

The branching network used to feed the helices in an array is formed of stripline components which are less bulky and much simpler to fabricate than a coaxial feed network.

Weights of the arrays were estimated for the dielectric tube construction. The weights of arrays of helices to operate at the four frequencies of interest are shown in Figure 95 as a function of gain. The weights of the large arrays, especially, are only rough estimates, and specific designs have not been made for these antennas.

The characteristics of a quad-helix array are compared to those of a seven-helix array in Table 7. The dimensions of two such arrays suitable for operation in the 1800 MHz to 2250 MHz are shown in Figures 96 and 97, respectively. The gain and pattern data in Table 7 for the quad-helix array are based on measured data for a somewhat smaller quad-helix array. The gain given in Table 7 can be obtained with lower sidelobes than those indicated by using more helical elements with closer spacing between elements. The VSWRs given in the table are at the input to the power divider or branching structure and do not include the discontinuities contributed by components such as rotary joints or multiplexers.

#### Fabrication Techniques

The stripline branching network used to connect the helices in an array is most simply fabricated by the chemical milling technique. The stripline components are made from two thin sheets of dielectric, each of which has metallic foil, usually copper, bonded to both sides. Portions of the metal are etched away from one side of each of these laminated sheets to form the center conductor of the branching structure, leaving a complete copper plate on the other side to form a ground plane. This technique is also applicable to the helix shown in Figure 94. The helix winding can be fabricated by etching the undesired metal from a thin fiberglass tube to which a metallic foil has been bonded.



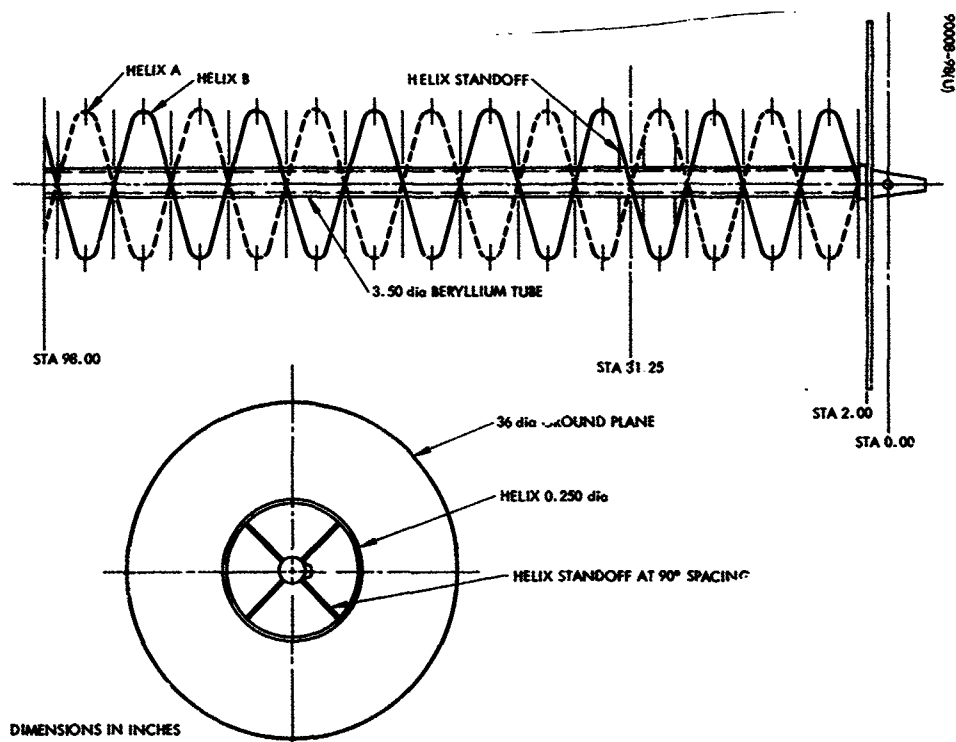


Figure 93. Helix Antenna - UHF

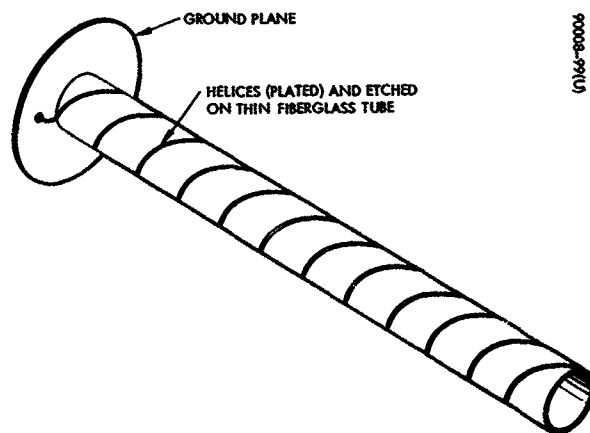


Figure 94. High Frequency Helix Winding Support

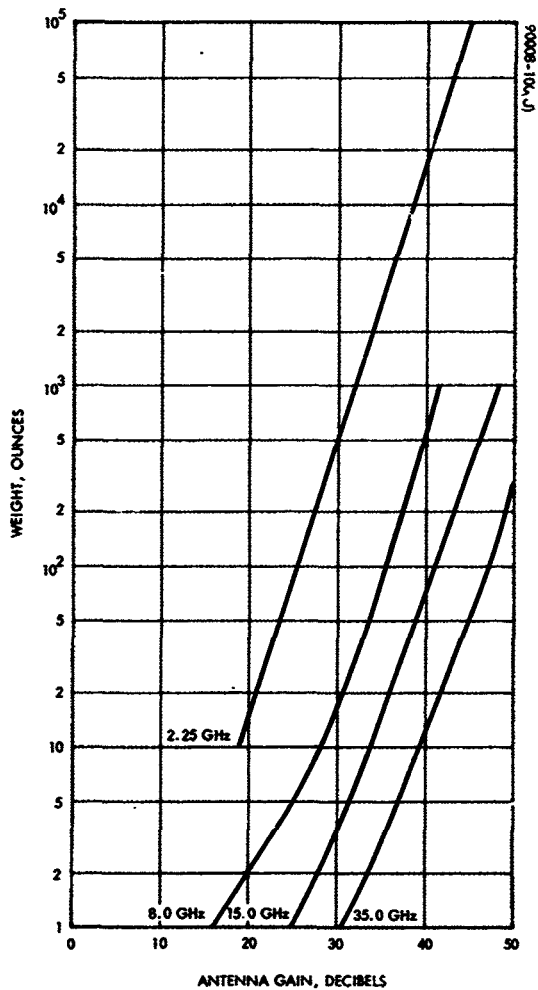


Figure 95. Weight of Array of Helices as Function of Gain

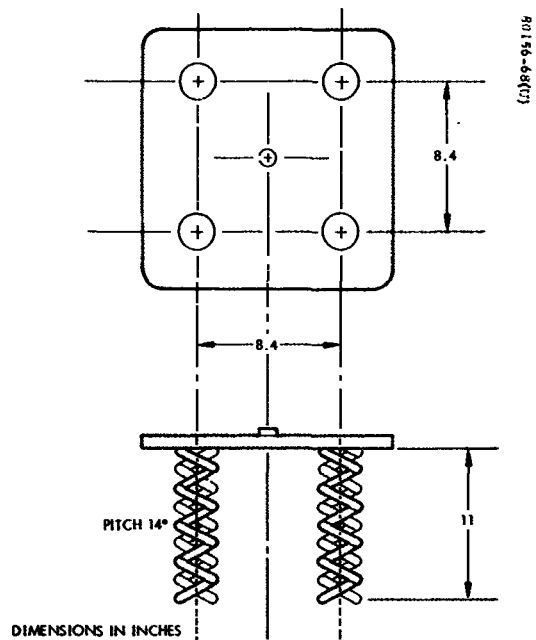


Figure 96. Bifilar Helix Array

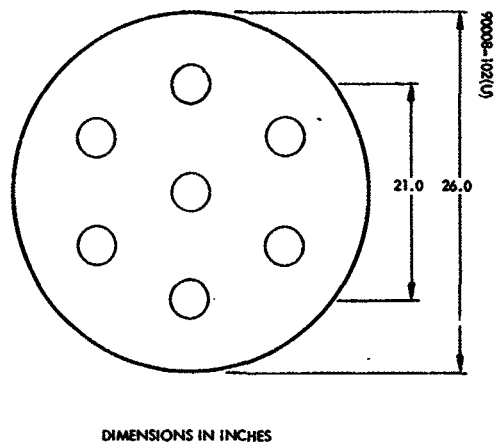


Figure 97. Seven-Helix Array

TABLE 7. ARRAY CHARACTERISTICS

	Quad-Helix Array	Seven-Helix Array
Transmit gain, dB	20	23.5
Transmit beamwidth, degrees	16.5	12
Maximum sidelobe level- transmit, dB	9	14
VSWR at transmit	<1.5	<1.5
Receive gain, dB	15.5	19.5
Receive beamwidth, degrees	20.5	17
Maximum sidelobe level- receive, dB	12	10.2
VSWR at receive	<2.0	<2.0
Helix length, inches 2250 to 1800 MHz array	11	21
Maximum array dimension, inches	17	26
Estimated weight, pounds 2250 to 1800 MHz array	2.5	9

Fabrication tolerances are dependent on the operating frequency of the antenna. It is desirable to hold dimensional tolerances of the helices to within  $\lambda/1000$  in order to obtain optimum performance from the array. For frequencies above X-band the chemical milling technique is not suitable because of the close tolerances required, and machine milling must be used.

#### 5.4.4 Effects of Tracking Method on Antenna Design

##### Command or Programmed Steering

These two types of steering have no effect on earth design, since the steering scheme is independent of the antenna.

##### Monopulse Tracking

In a monopulse tracking array, the array is divided into four quadrants, the outputs of which are fed to sum and difference circuits, as shown schematically in Figure 82. Hence, the effects of this tracking method on the antenna design are the addition of the stripline sum and difference circuits to the feed network and the requirement that the number of elements in the array be an integral multiple of four.

## 5.5 PARABOLOIDAL REFLECTORS AND FEEDS

### 5.5.1 Description

A typical antenna is illustrated in Figure 98. Antennas of this type are generally not as efficient as planar slot arrays, so the area required to obtain a given gain with the paraboloidal reflector and feed is greater than that required to obtain the same gain with a planar array. The reasons for the lower efficiency of the paraboloidal reflector and feed combination are that there are effects such as aperture blockage and spillover losses. Aperture blockage occurs because the feedhorn and its support intercepts a portion of the incident energy. Spillover losses result because the pattern of the feedhorn extends beyond the angular region subtended by the reflector. In order to keep spillover losses small, the pattern of the feed horn is tapered. This taper across the reflector reduces the aperture efficiency still further. The effects of aperture blockage are more severe for low gain antennas. For the higher gain antennas (30 dB) the effects are not so significant.

Reflector and feed antennas are inherently broadband radiators since they are essentially optical devices. The bandwidth is limited by the characteristics of the feed rather than by the reflector.

Circular polarization is obtained by selecting a circularly polarized feed horn. The reflector itself is insensitive to the polarization characteristics of the antenna.

The thickness, or depth, of the reflector and feed antenna is significantly greater than that of the planar array. The feed horn is placed at the focus of the reflector. Typical values of the ratio  $f/D$ , where  $f$  is the focal distance and  $D$  is the reflector diameter, range from 0.25 to 1.0. The feed horn and microwave circuitry necessary to obtain circular polarization extend further out along the axis of the antenna, further increasing its depth. Consequently, the depth of the antenna may equal or exceed its aperture dimension.

### 5.5.2 Electrical Properties

This discussion includes estimated antenna performance characteristics for the same representative frequency ranges as were considered for the planar array, namely, 2.25, 8.0, 15.0, and 35.0 GHz.

#### Gain (Efficiency)

The efficiencies of paraboloidal reflectors and feeds are generally lower than those of planar arrays of slots. For a typical reflector with a horn feed, efficiencies of from 55 to 60 percent may be obtained. This range of efficiency values is a result of a number of contributing factors, and these factors depend on the specific design requirements.

The main factors that contribute to the reduced efficiency are amplitude taper, spillover, aperture blockage, feed phase error, and errors in reflector surface. Losses due to dissipation are relatively small because the system is basically an optical system and the feeding system is relatively simple. The loss due to amplitude taper across the aperture results from attempts to minimize spillover losses. These latter losses result from the loss of energy in radiation from the feed that is not intercepted by the reflector. Aperture blockage losses result from the presence of the feed and supporting structure in the aperture. Blockage losses are less serious for very high gain antennas, since the feed size does not depend on the required gain but on the ratio of focal distance to reflector diameter and on the required illumination taper.

The conflicting requirements of low spillover loss and small taper loss can be obviated to some extent by using special feeding techniques that shape the primary illumination pattern to give a more uniform aperture illumination and yet reduce rapidly to a low value the energy radiated toward the reflector edge. This shaping, however, requires larger feeds than normal and hence increases aperture blockage. In all but high gain, narrow-beam antennas, such shaping techniques are not very practical and are not considered for this application.

The overall design is a compromise to achieve maximum gain. Reasonable values often employed in practice result in an amplitude taper of 10 dB from center to edge of the reflector. This taper, then, is a determining factor in arriving at the feed horn dimensions. When all factors have been accounted for, an overall efficiency of about 60 percent results. Plots of antenna aperture size versus gain for the four operating frequencies being considered are presented in Figure 99. An overall efficiency of 60 percent has been assumed for computing these curves.

Reflectors with horn feeds can be designed to operate over broad bandwidths. Over these bandwidths the efficiency varies for several reasons. First, as the frequency goes down, the primary feed pattern broadens, thereby making the illumination more nearly uniform and tending to increase gain. At the same time, however, the broadening of the primary feed pattern increases spillover losses, thereby tending to reduce gain. In addition, phase errors in the primary feed time pattern are sensitive to frequency and contribute to the change in efficiency. The exact form of the variation of efficiency with frequency depends on the details of the feed system. An estimated curve of relative efficiency versus frequency is illustrated in Figure 100. In arriving at the curve in the figure, it has been assumed that at  $f_0$ , the design frequency, the feed has been adjusted to give a 10-dB taper to the aperture illumination. It has also been assumed that the phase variation of the feed pattern is negligible across the aperture and that the feed gain is therefore proportional to the square of the frequency. The corresponding gain variation with frequency is illustrated in Figure 101. Different shapes of these curves will be obtained for different assumptions concerning the primary pattern characteristics.

### Beamwidth

The 3-dB beamwidth as a function of antenna gain is plotted in Figure 102. These beamwidths were calculated for a 10-dB taper across the aperture and are not very sensitive to aperture blockage.

### Sidelobes

The antennas considered have been assumed to have an amplitude taper across the aperture that falls to 10 dB below its peak value at the edge of the reflector. The pattern of such an antenna for a taper of the form  $1$  to  $0.6838 (2r/D)^2$  is shown in Figure 103. The pattern does not include the effect of aperture blockage. Aperture blockage tends to raise the sidelobes somewhat as shown in Figure 104, the amount depending on the amount of aperture blockage. The sidelobe level increase will probably not exceed 3 dB for antennas in the 30 dB gain range. For lower gain antennas the blockage becomes more significant, and it is difficult to obtain low sidelobes. The effect for an aperture with a 10-dB taper would be somewhat less than shown in Figure 104.

### Voltage Standing Wave Ratio

Paraboloidal reflectors with circularly polarized horn feeds can be designed with low VSWR over very broad bands. The reason for this is that the circularly polarized waves from the feed that are reflected from the paraboloid have their sense of polarization reversed from that of the incident waves and, hence, are not seen by the feed. The impedance bandwidth will be limited by the device used to obtain circular polarization.

### Polarization

A number of devices are available for obtaining circularly polarized waves in the feed horn. The bandwidths over which these devices may operate differ from device to device. For narrow bandwidths, the polarizer can be simply an orthomode transducer that has a 90-degree phase shift between the two inputs. However, to maintain the 90-degree phase shift over wide bandwidths some additional device is required. One such device consists of irises in square waveguide that carries two orthogonal dominant modes. The irises are spaced at various intervals and are adjusted to retard one mode while providing a phase advance for the orthogonal mode. One such device using five irises can be operated for over a 35 percent bandwidth with VSWR of less than 1.2:1, and over a 45 percent bandwidth with an axial ratio less than 3 dB. The insertion loss is on the order of 0.04 dB at X-band. The length of the device is 1.6 wavelengths at the design frequency.

### Power Handling Capabilities

The power handling capabilities of the reflector type antenna will be determined by the power handling capabilities of the feed horn polarizer and waveguide. The most critical component will probably be the polarizer.

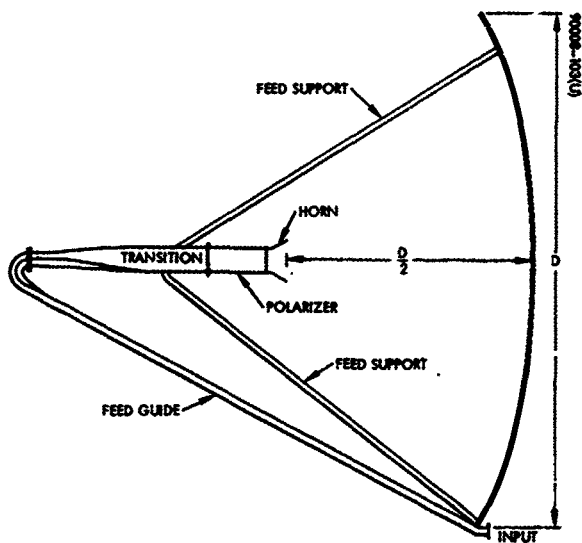


Figure 98. Paraboloidal Reflector and Feed

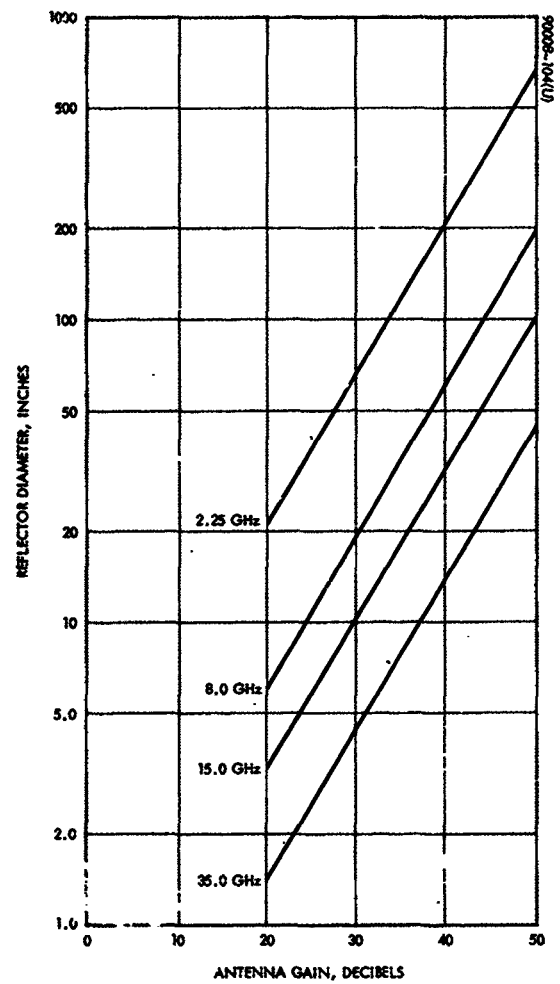


Figure 99. Aperture Size Versus Antenna Gain for Circular Aperture

(Assumed efficiency = 60 percent)

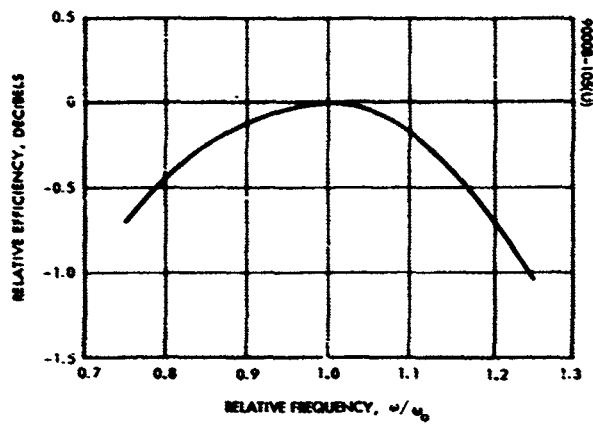


Figure 100. Relative Efficiency of Reflector and Feed as Function of Frequency

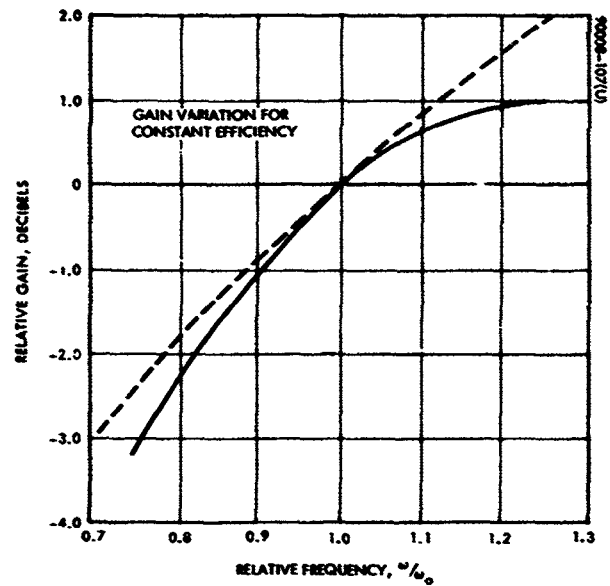


Figure 101. Relative Gain of Reflector and Feed as Function of Frequency

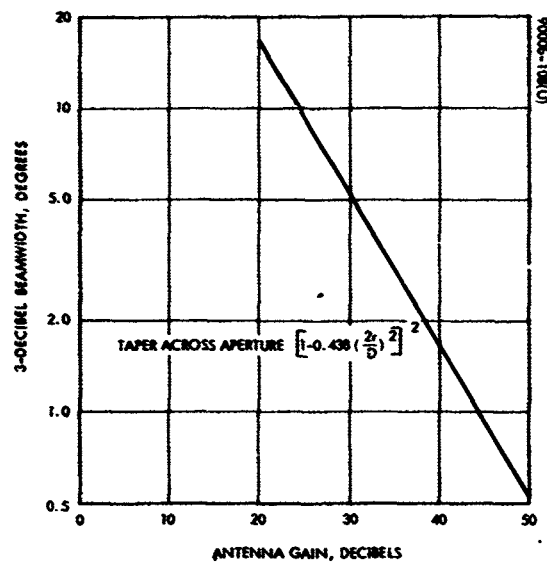


Figure 102. 3-dB Beamwidth as Function of Antenna Gain for Circular Aperture With 10-dB Taper



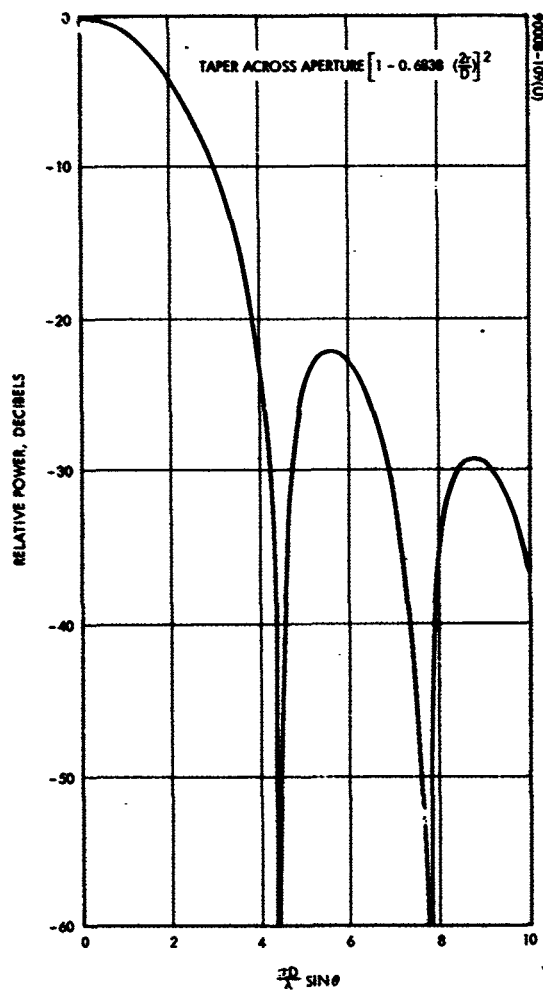


Figure 103. Pattern of Circular Aperture With 10-dB Parabolic Amplitude Taper Across Aperture

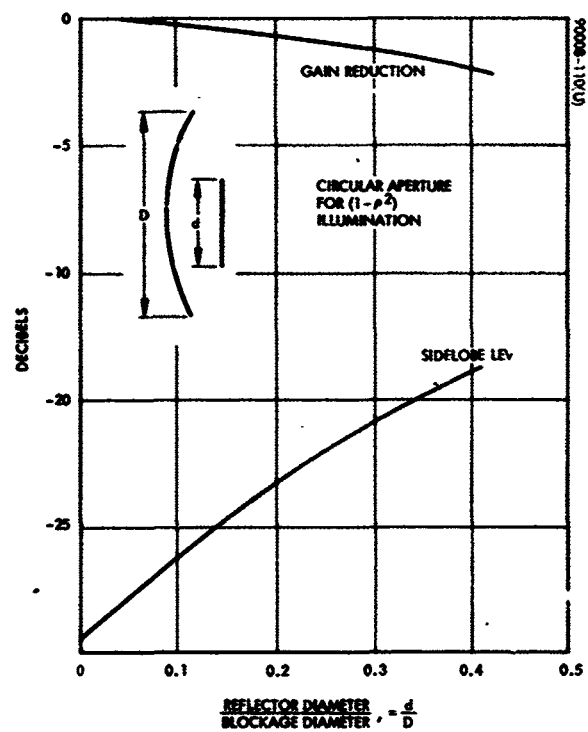


Figure 104. Aperture Blockage Effect on Sidelobe Level and Gain

Based on the discussion presented for the planar array case, however, power handling capabilities of the waveguide feeds should not be a limitation of these antennas.

### 5.5.3 Mechanical Properties

#### Materials and Weights

The basic construction of the paraboloid will be a honeycomb sandwich consisting of a lightweight aluminum foil core and bonded epoxy-fiberglass faces. This construction is illustrated in Figure 105 which shows the 28-inch diameter radar reflector used on the Surveyor spacecraft.

To ensure high dimensional accuracy, the reflective surface of the paraboloid can be fabricated over an accurately made cast steel tool. The inner and outer surfaces can each be made of three plies of 0.002-inch thick fiberglass cloth impregnated with a space-approved epoxy-resin impregnant. The laminating resin will also act as the bonding agent for attachment of the honeycomb core. This construction will result in a weight of 0.36 lb/ft<sup>2</sup>.

The feed waveguides and horns are assumed to be made of 0.020-inch thick aluminum or magnesium. The feed supports are also aluminum or magnesium. Figure 106 shows the estimated weights of the reflector, feed, and feed supports as a function of gain at the four frequencies of interest. The weights have been estimated for both aluminum and magnesium feeds, horns, and supports.

### 5.5.4 Effects of Tracking Method on Antenna Design

#### Command or Programmed Steering

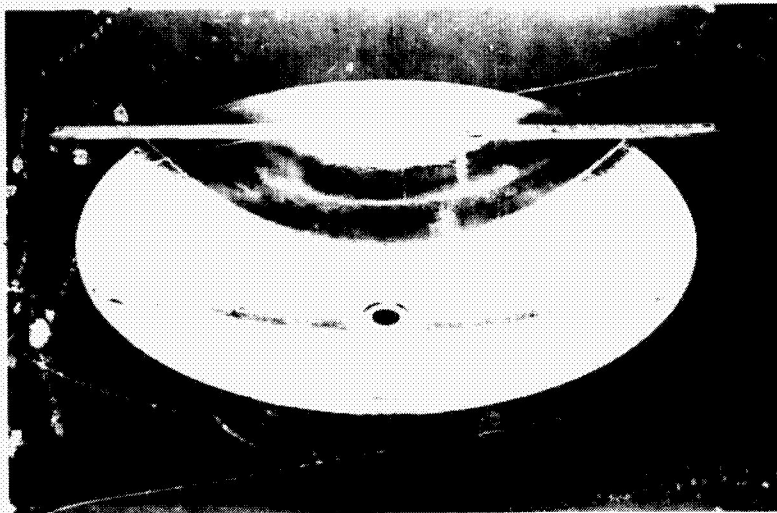
Since these methods of antenna steering do not use any antenna output to direct the antenna, their use has no effect on antenna design.

#### Monopulse Autotracking

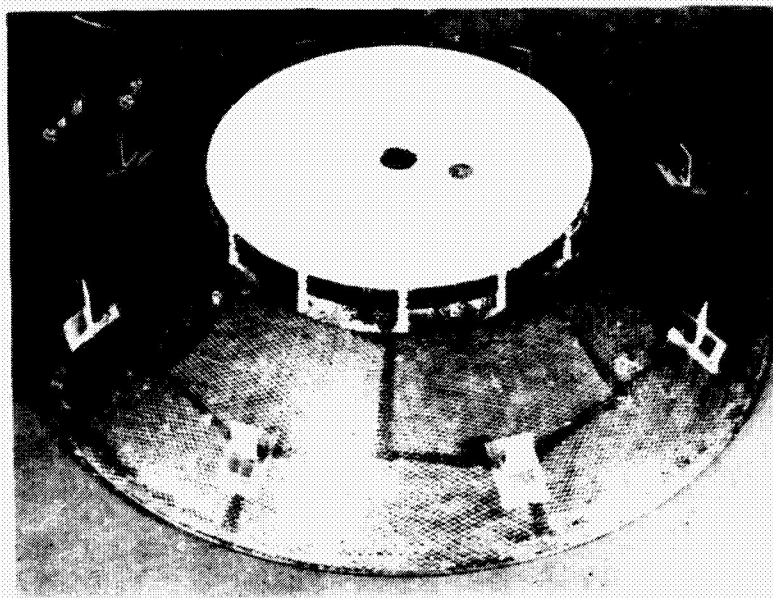
The use of monopulse tracking with a reflector and feed antenna requires a significant modification of the feed horn. The single horn must be replaced by a cluster of four horns. The proper placement of the four horns requires careful horn design, since it would be necessary to modify the primary sum pattern to obtain desirable difference patterns. The use of monopulse also requires the addition of hybrid circuits that would complicate the feed and increase the weight of the antenna. However, the technique is feasible and has been implemented in other paraboloidal reflector antennas.

### 5.5.5 Cassegrain Systems

The Cassegrain system is the most common two-reflector system. It consists of a paraboloidal primary reflector, a hyperboloidal secondary reflector, and a feed. The secondary reflector is located between the primary reflector and its focus. The primary feed is located between the



a) Top View  
(Photo R112139)



b) Bottom View  
(Photo R112138)

Figure 105. Surveyor Altitude Marking  
Radar Reflector

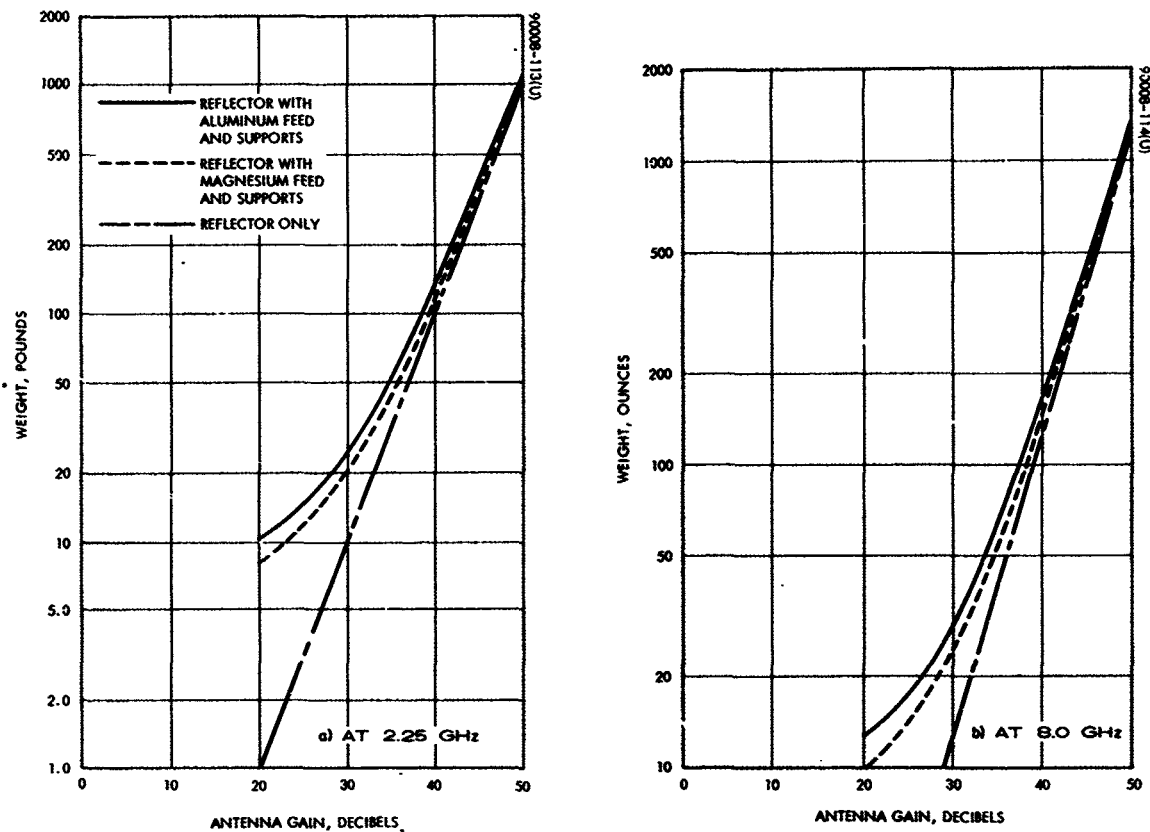


Figure 106. Weight Versus Antenna Gain for Paraboloidal Reflector and Feed

primary and secondary reflectors near the vertex of the primary reflector. Consequently, the depth of the system along its axis is less than that of the single reflector paraboloidal system. This configuration provides a second advantage. Since the feed does not require long transmission lines out to the focus of the primary reflector, dissipation losses are reduced and higher efficiencies can be obtained. When low noise temperatures are required, this reduced dissipation aids in the achievement of these low temperatures. Because of the presence of the secondary reflector, the aperture blockage of the Cassegrain antennas is somewhat larger than for single reflector antennas, and the greater efficiency is achievable only for systems sufficiently large that aperture blockage is not too significant; that is, for high-gain antennas. The weight of a high-gain Cassegrain system should be somewhat less than that of a high-gain single reflector system because of the increased efficiency of the Cassegrain system. Consequently, Cassegrain systems, with their increased efficiencies and reduced axial depths, are also of interest for the 30 to 50 dB gain range.

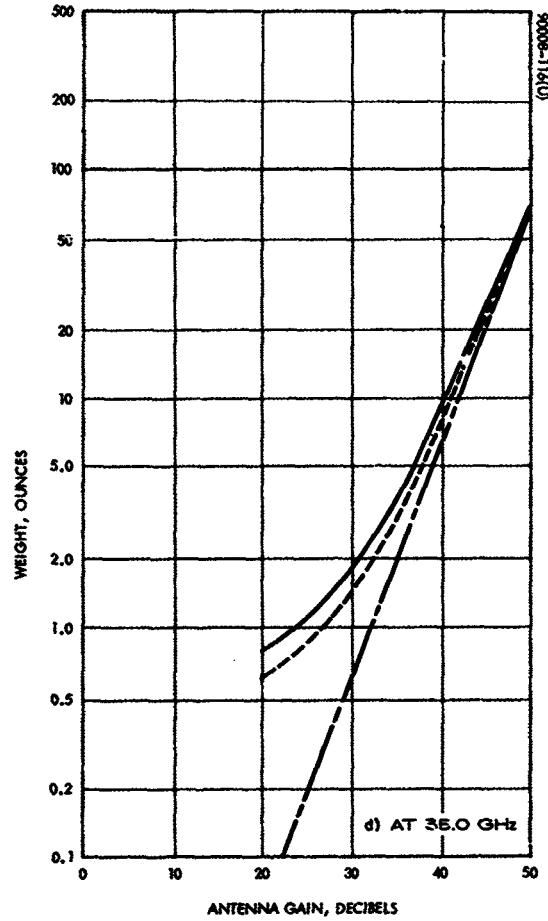
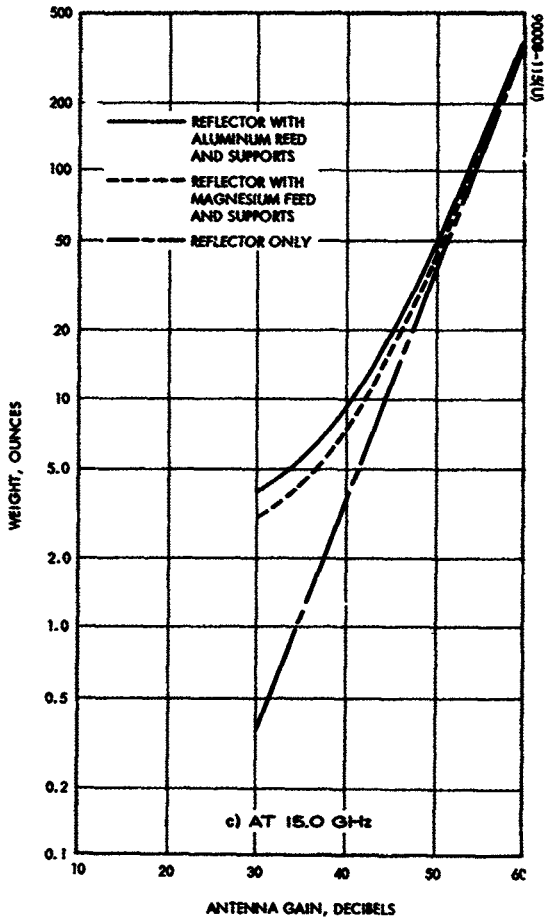


Figure 106 (continued). Weight Versus Antenna Gain for Paraboloidal Reflector and Feed

## 5.6 RECTANGULAR HORNS

### 5.6.1 Description

The type of antenna discussed in this section is a pyramidal horn of square cross section and fin loaded to give independent control of E- and H-plane beamwidths for both orthogonal polarizations. The horn is fed by a square waveguide containing a circular polarizer. Single-horn antennas are considered over the gain ranges required. However, for the higher gain range a number of lower gain horns could be combined to obtain the desired performance. This modification would decrease the required horn length by the reciprocal of the number of horns used, but would add the complication of a corporate feeding device. The total weight of the array of low-gain horns would probably not be much different than that of a single high-gain horn.

It is assumed that the feed guide contains a circular polarizer and a transition to go from a rectangular feed waveguide with linear polarization to the square feed guide with circular polarization. The arrangement is shown in Figure 107.

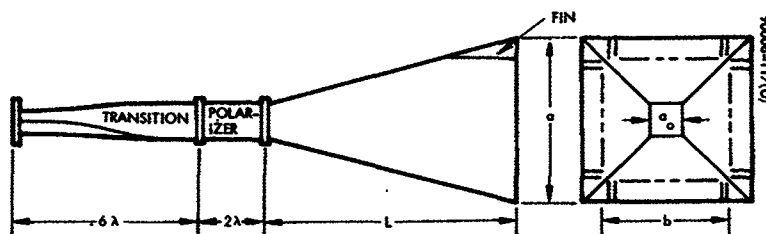


Figure 107. Circularly Polarized  
Fin-Loaded Horn

### 5.6.2 Electrical Properties

This discussion will include predicted antenna performance for the same representative frequency range as for the other antennas considered. The four frequencies of interest are 2.25, 8.0, 15.0, and 35.0 GHz.

#### Gain (Efficiency)

From the standpoint of dissipative losses, the pyramidal horn antenna is a very efficient device. However, because of the modal structure of the fields in such horns, the aperture efficiency is low. This low efficiency arises from the sinusoidal taper in the H-plane aperture field and from the phase error across the aperture that is a consequence of the horn taper. If the phase error were eliminated, an aperture efficiency of 81 percent is the best that could be realized. The aperture phase error depends on both the aperture dimensions and the horn length. By making the horn

long, with a resultant small horn taper, the phase error can be made as small as desired. However, the length rapidly becomes much greater than the aperture dimensions. The horns considered in this report are optimum horns in that their lengths are the shortest possible for a given gain. While optimum horns do not have exactly the same 3-dB beamwidths in both E- and H-planes, the difference in beamwidths is not great. The E-plane beamwidth can be adjusted to equal the H-plane beamwidth by adjustment of the fin dimensions with no change in horn dimensions. The maximum phase errors across the aperture of an optimum horn are  $3/8\lambda$  in the H-plane and  $1/4\lambda$  in the E-plane. Under these conditions the aperture efficiency is about 48 percent.

Figure 108 is a plot of horn length versus gain, while Figure 109 includes the polarizer, load, and transition versus gain. Figure 110 shows the aperture side dimension as a function of gain. These curves were computed for an assumed overall efficiency of 46 percent. These curves were not extended beyond a gain of 30 dB because the horn lengths increase much more rapidly than the aperture dimensions, usually making poor use of available space.

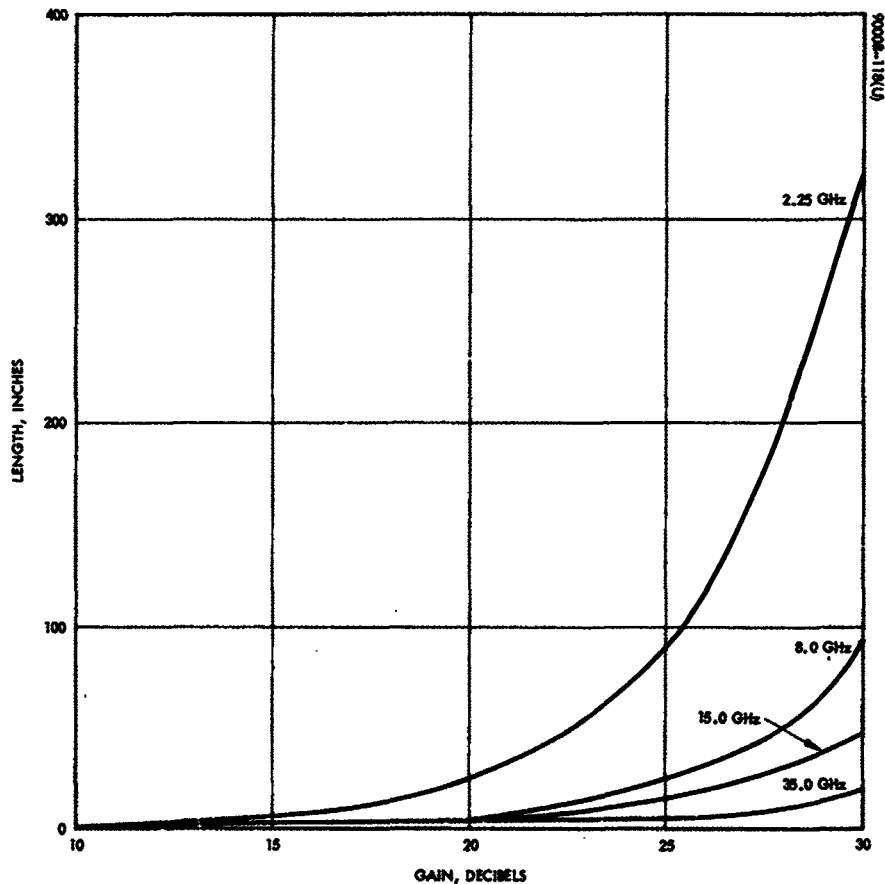


Figure 108. Horn Length Versus Gain

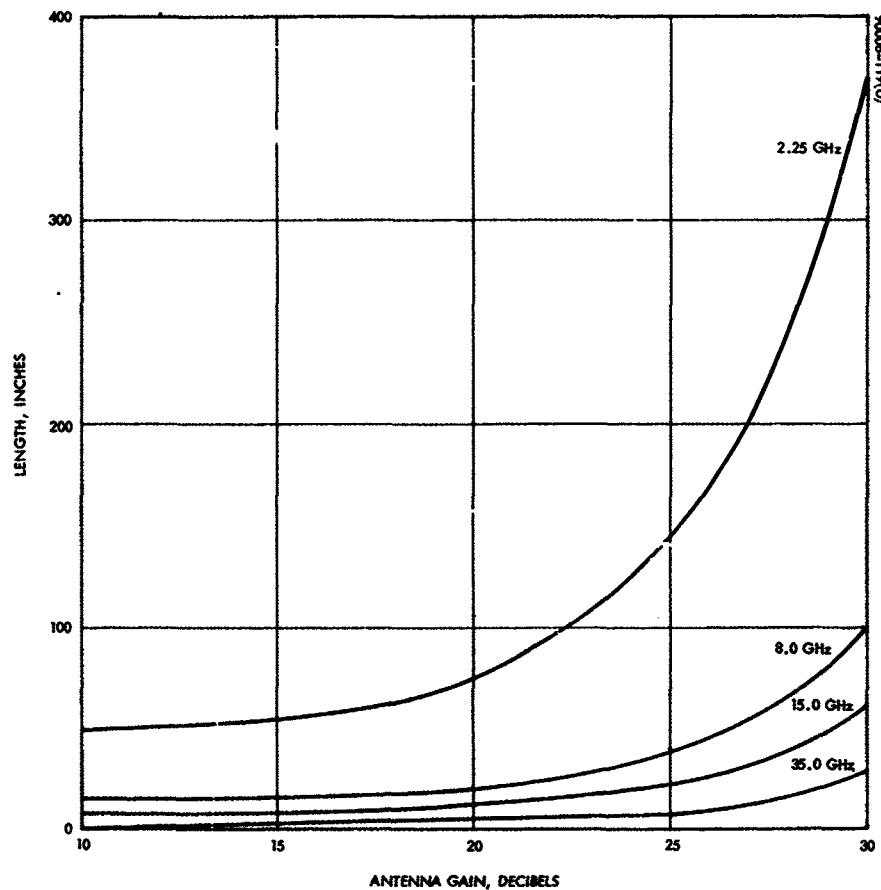


Figure 109. Length of Horn, Polarizer, Load, and Transition Versus Gain

Pyramidal horns can be operated over wide bandwidths. Their impedance characteristics arise from reflections at both the aperture and at the point where the horn joins the waveguide. However, optimum horns having gains of 20 dB or more are usually well matched. The variation of gain with frequency due to mismatch for such horns is small. Even a VSWR of 1.4, which is an approximate value for open ended waveguide, affects the gain by less than 0.13 dB, and unless the VSWR changes significantly with frequency, the gain fluctuation due to mismatch will be less than this value as the frequency is changed. The main change in gain with frequency arises from the change in aperture phase error with frequency and from the inherent change in the aperture area proportional to  $\lambda^2$ . The gain variation with frequency due to these latter effects is shown in Figure 111.

#### Beamwidth

The 3-dB beamwidth as a function of horn gain is plotted in Figure 112.

#### Patterns and Sidelobes

The E-plane and H-plane radiation patterns of optimum horns are shown in Figure 113. There are no deep nulls in the pattern because of the phase errors that occur in the aperture. The E-plane pattern exhibits



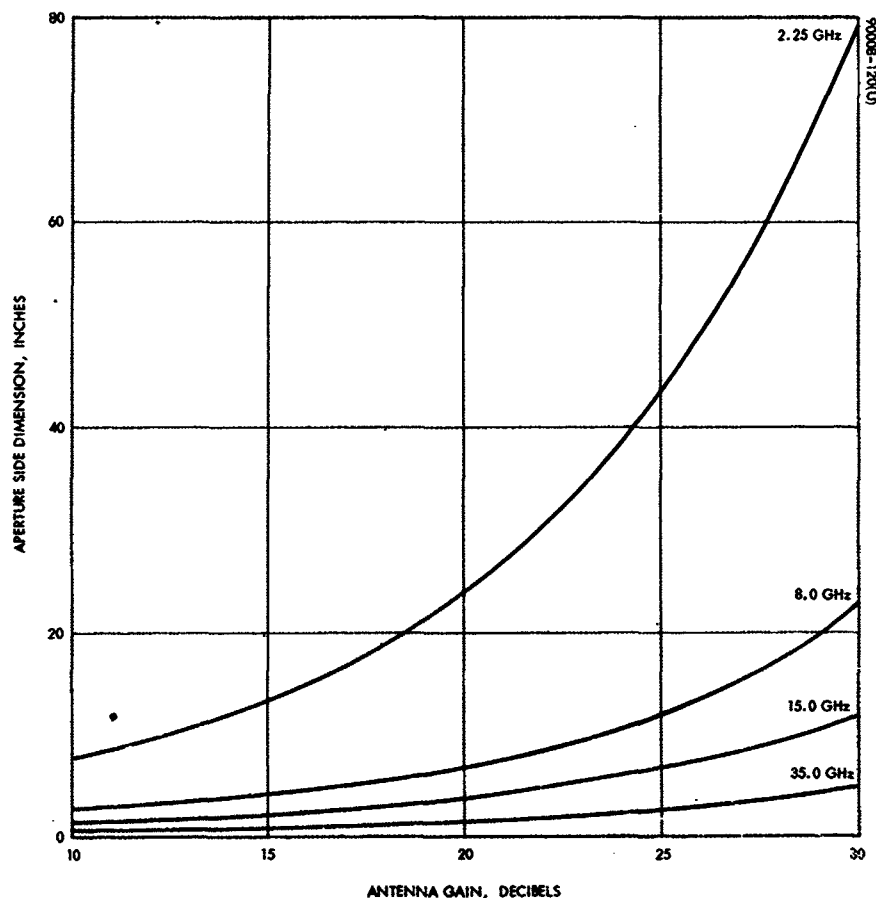


Figure 110. Aperture Side Dimension Versus Gain

approximately an 8 dB first sidelobe level as compared to a 13 dB first sidelobe level for the uniform planar array, and approximately a 20 dB first sidelobe level to be expected from a paraboloidal reflector and feed.

#### Voltage Standing Wave Ratio

Pyramidal horns such as optimum horns having a gain of 20 dB or more and having a dominant mode waveguide feed are usually well matched over very broad bandwidths. Even low-gain horns can be expected to have a VSWR of less than 1.5:1 over a 25 percent band.

#### Polarization

The same polarization considerations as for the polarizer considered for the paraboloidal reflector feed apply here.

#### Power Handling Capabilities

The power handling capabilities of horn radiators will be the same as those for the feeds of the paraboloidal reflectors.

### 5.6.3 Mechanical Properties

#### Materials, Weight, and Construction

As is the case with all spacecraft hardware, antenna weight is an important consideration. Depending on the size of the horn, it will be constructed from one of several materials. Small horns in the range of less than 2.5 inches square by 4 inches long will be made from fiberglass and epoxy molded on a mandril with aluminum vacuum deposited on the inside surface. The wall thickness will be approximately 30 mils, and the weight per square inch of surface, about 0.002 pound. Horns in the range larger than the above sizes, but not exceeding 9.6 inches square and 20 inches long, will be made of quarter-inch thick honeycomb sandwich molded on a mandril. The structure of the material is illustrated in Figure 114. The weight of this honeycomb structure is approximately 0.36 pound per square foot ( $0.0025 \text{ lb/in.}^2$ ). For horns up to 24 inches square to 34 inches long, the same type of material would be used. However, it would be  $1/2$  inch thick and the cell size would be  $3/8$  inch, rather than  $1/8$  inch. Its weight per unit area would be about the same as the other honeycomb structure. Horns much larger than these sizes are somewhat impractical when their lengths are compared to the depths of other antenna types, but are included here for comparison purposes. They were assumed to be constructed of 1-inch thick honeycomb with a  $3/8$  inch Hexcell, with additional cross ribs of the same material. The weight would be approximately  $1.1 \text{ lb/ft}^2$ . The estimated curves of weight versus gain of horn antennas and feeds at each of the frequencies of interest are shown in Figure 115. Breaks in the curves (shown as broken lines) indicate regions in which a change takes place from one construction material to another. The feed guides, polarizer, and transition are assumed to be made from aluminum guide with a wall thickness of 0.020 inch. In practice, the guide at 2.25 GHz might be constructed of a honeycomb material, but its weight would not be significantly altered from the estimates presented in the figure.

### 5.6.4 Effects of Tracking Method on Antenna Design

#### Command or Programmed Steering

Since these methods of antenna steering do not use any antenna output to direct the antenna, their use has no effect on antenna design.

#### Monopulse Autotracking

The use of monopulse tracking with horn antennas can be accomplished using a cluster of four horns. This type of tracking would not be required for low-gain antennas because of their broad beamwidths. For the higher gain antennas the use of four (or more) horns in a cluster, in addition to providing the monopulse capability, would, as previously discussed, significantly shorten the overall antenna length for a given gain. The addition of hybrid circuits, as discussed for planar arrays, would provide the signals required to implement the monopulse technique.

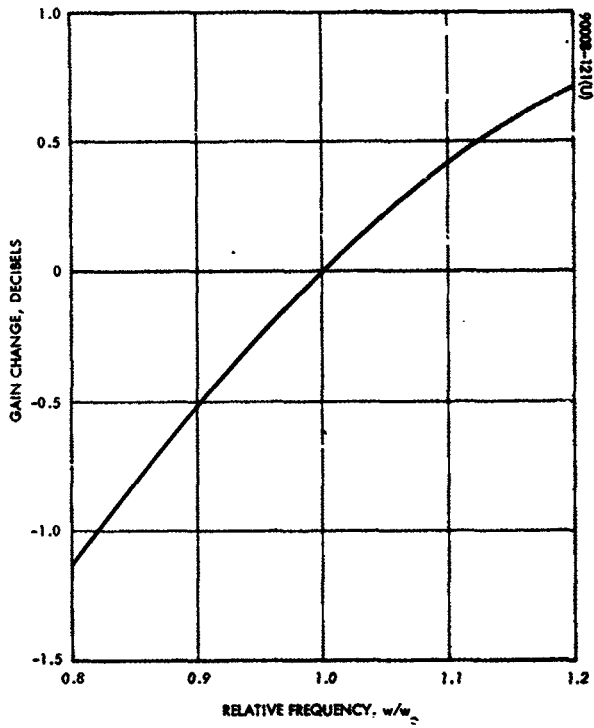


Figure 111. Relative Gain of Optimum Horn as Function of Frequency

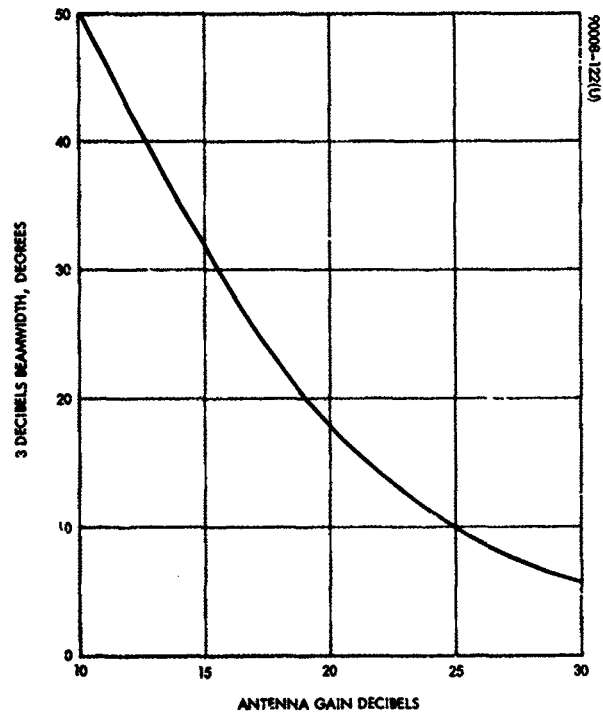


Figure 112. 3-dB Beamwidth Versus Gain for Horn Antenna With Equal E- and H-Plane Beamwidths

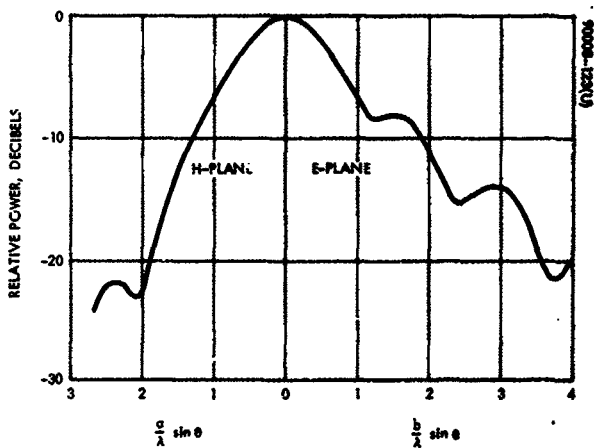


Figure 113. E-Plane and H-Plane Patterns of Optimum Horn

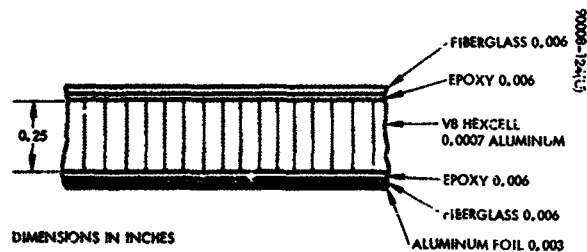


Figure 114. Honeycomb Structural Material

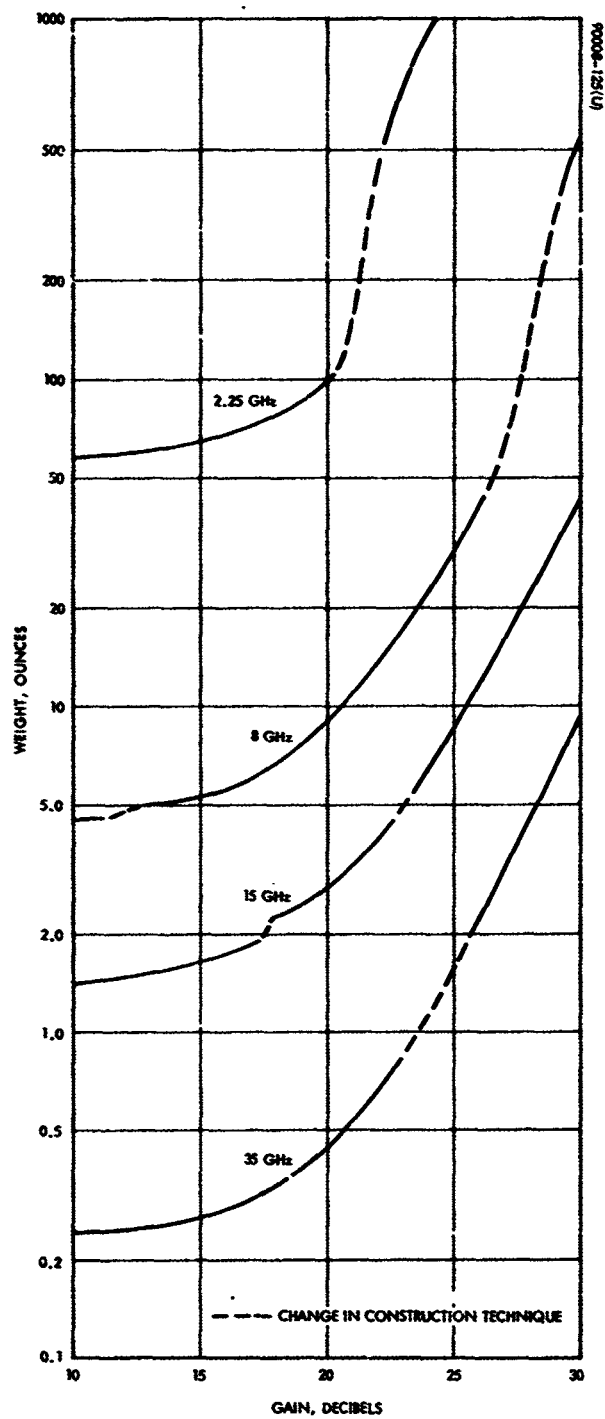


Figure 115. Estimated Weight Versus Gain of Horn Antennas

## 5.7 COMPARISON AND COMMENTS

Selection of one of the types of antennas discussed in the four preceding sections to be used on the LAS involves a number of factors, including:

- Shroud and packaging limitations
- Antenna size and shape
- Weight
- Radiation pattern and sidelobes
- Gimbal and steering problems

Figure 116 presents four sets of curves corresponding to the four frequencies of interest in this study. These curves are a combination of Figures 73, 85, 99, and 109, and allow a comparison of size. The first feature which may be noted is that the relative relationships are nearly the same in all four sets of curves. For a given gain, the length of a horn is considerably greater than the maximum dimension of the other antennas. Similarly, the parabolic reflector diameter is somewhat larger than a helical array length or planar array side. However, at about 50 dB gain, the helical array length surpasses the reflector diameter. Above about 35 dB gain, the planar array side is smaller than the principal dimension of the other antennas.

Figure 117 allows a very crude comparison of radiation patterns and sidelobes. From this figure, which is a combination of Figures 76, 89a, 103, and 113, it can be seen that the parabolic reflector antenna has the lowest sidelobes, while the horn has the largest. This figure also reveals that for a given size, the helical array and planar array have better directivity than the horn or parabolic reflector, i.e., higher gain, which corresponds to the results of Figure 116. Although conclusions are difficult to reach, Figure 117 allows a comparison which may be meaningful for particular applications.

Figure 118 shows a weight comparison for each frequency. From these four figures it can be seen that for every value of gain there is at least one antenna type which weighs less than a horn antenna. Thus, this antenna looks unfavorable on the basis of weight comparison. Also notice from these figures that for every value of gain, either a helical array or parabolic reflector weighs less than a planar array, except for the lower frequencies. Figure 118 indicates that for 2.25 GHz there is a range of gain in the vicinity of 30 dB where the planar array weighs the least.

For design frequencies above 15 GHz, all antennas except the horn weigh less than 7 pounds for gains less than 40 dB, and this holds true at 8 GHz for gains less than 36 dB. Thus, for most applications, packaging considerations will influence the choice from among these antennas.

If a significant portion of the spacecraft has one or more flat exterior surfaces, the planar array is favored because it may be packaged within the booster shroud against the flat surface. If the stowed spacecraft structure can more easily accommodate volume rather than area, then either the helical array or parabolic reflector may be the best choice. For instance, the open conical structure of the Nimbus satellite can more easily accommodate a helical array than a planar array for a range of antenna gain. Figure 116 indicates that the helical array length and diagonal is less than the planar array side for gains less than 40 dB.

There are no obvious gimbaling or steering problems with any of the antennas about which general statements can be made.

Thus, from among the planar array, helical array, and parabolic reflector, for X-band frequencies and higher, the choice will depend mainly on the spacecraft structure and configuration and booster shroud limitations. For instance, for the Thor-Delta shroud shown in Figure 5, if the spacecraft has a box shape, a rigid, nonfoldable, square planar array must have a side dimension of less than about 36 inches if it is packaged between the spacecraft and shroud.

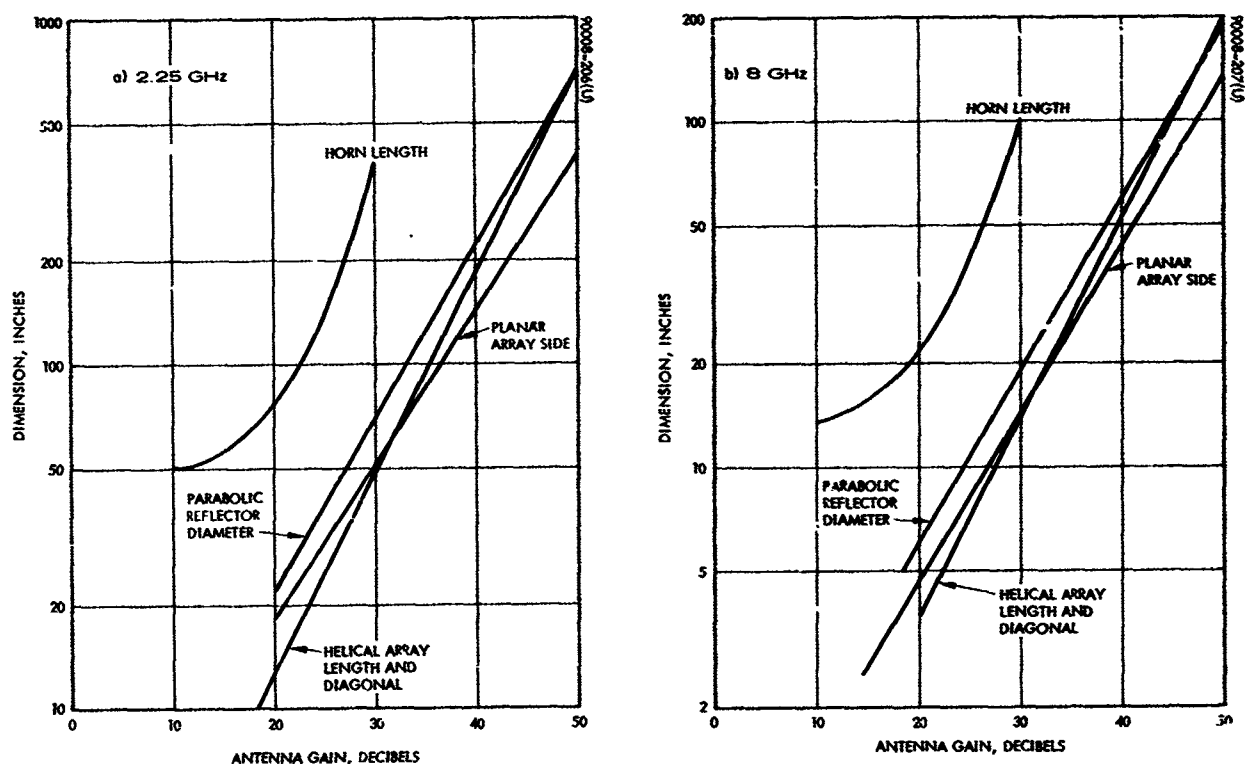


Figure 116. Comparison of Antenna Size

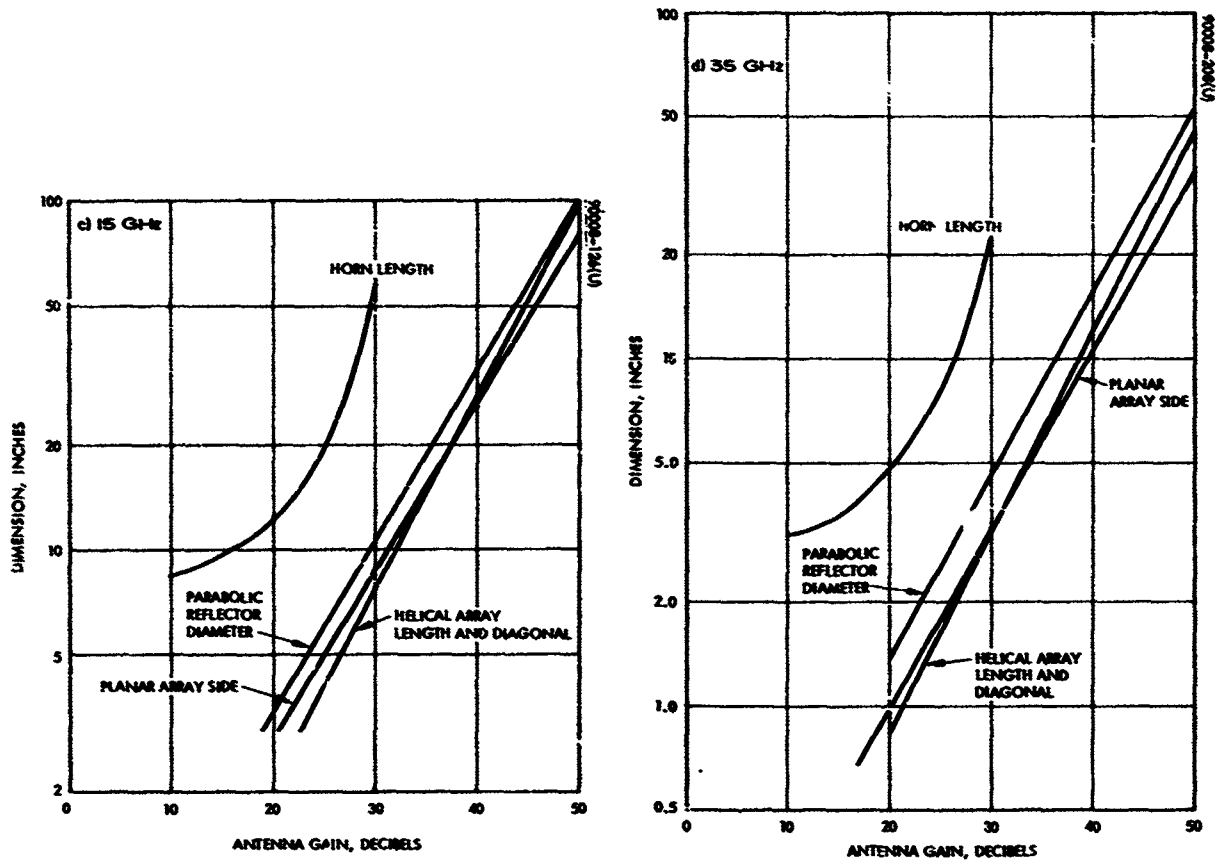


Figure 116 (continued). Comparison of Antenna Size

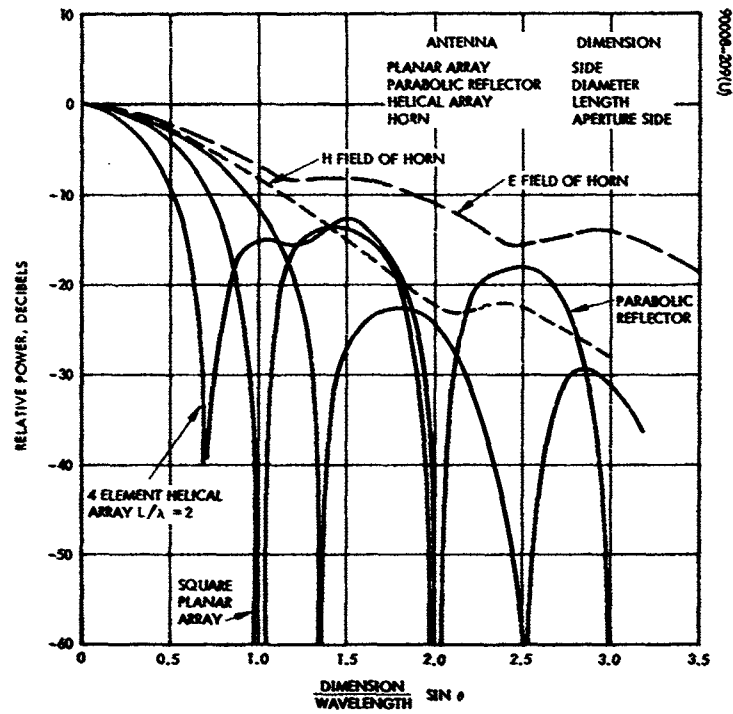


Figure 117. Antenna Comparison



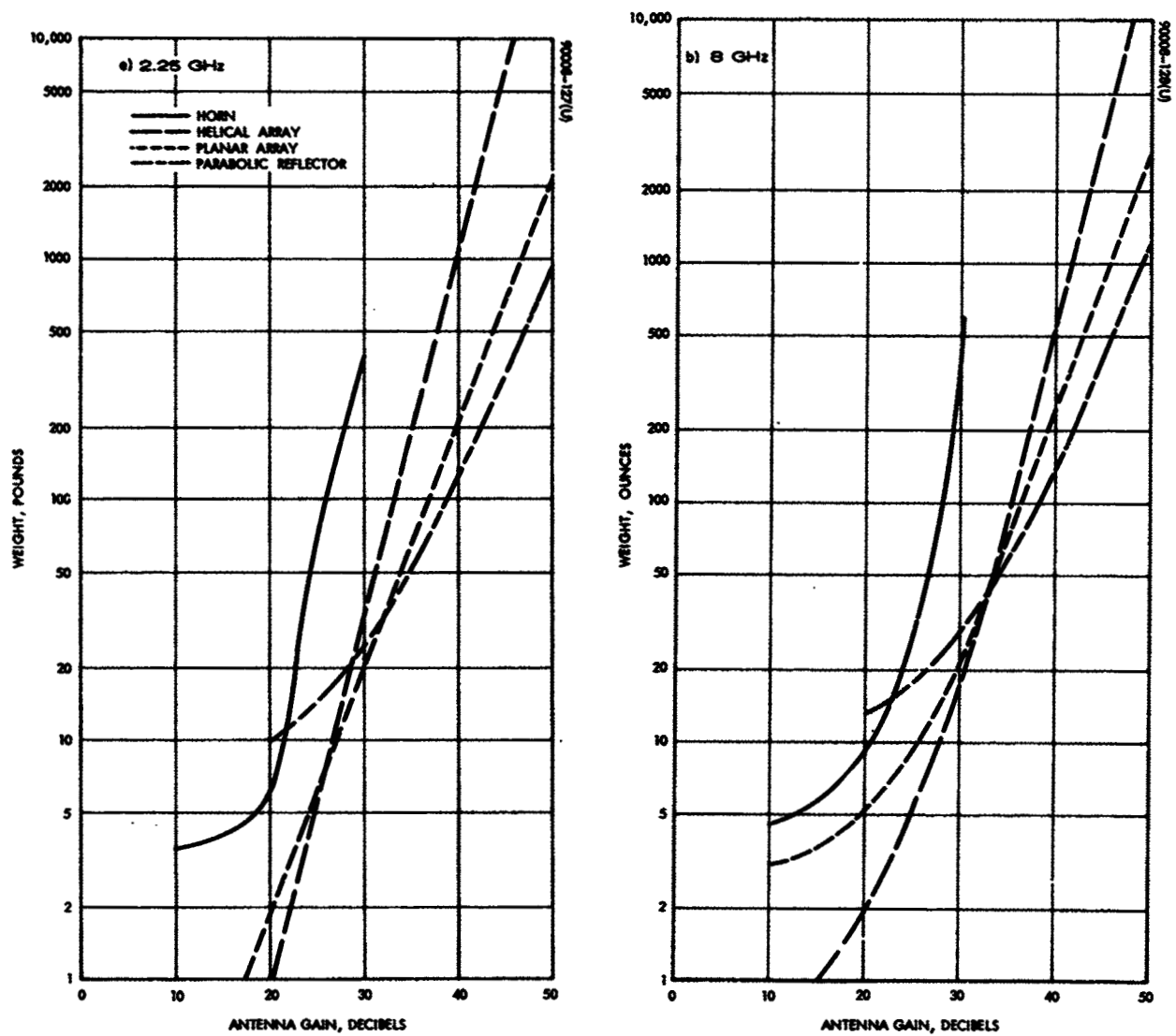


Figure 118. Weight Comparison

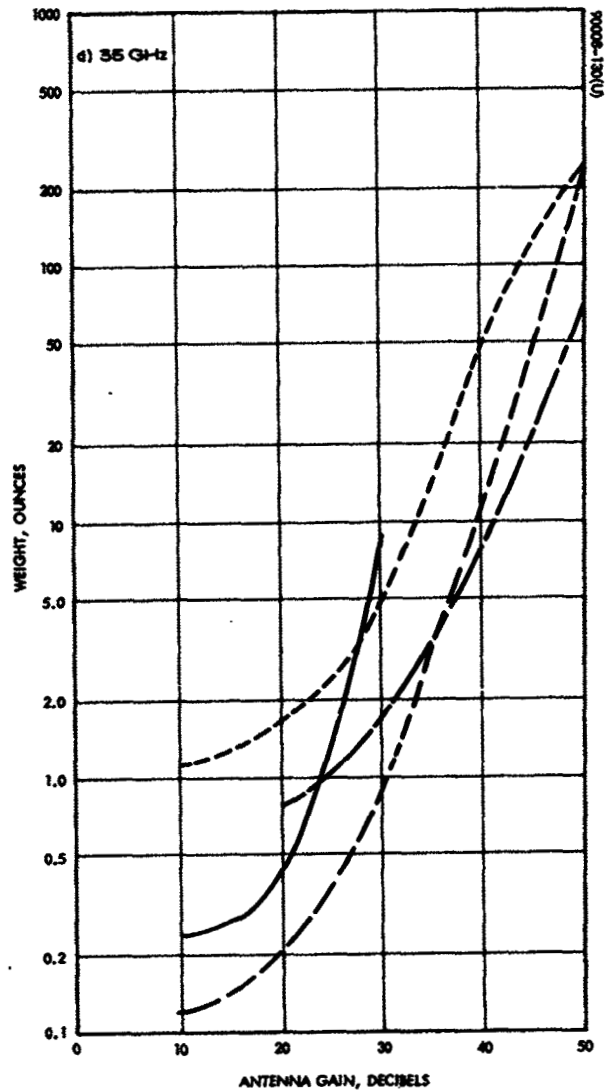
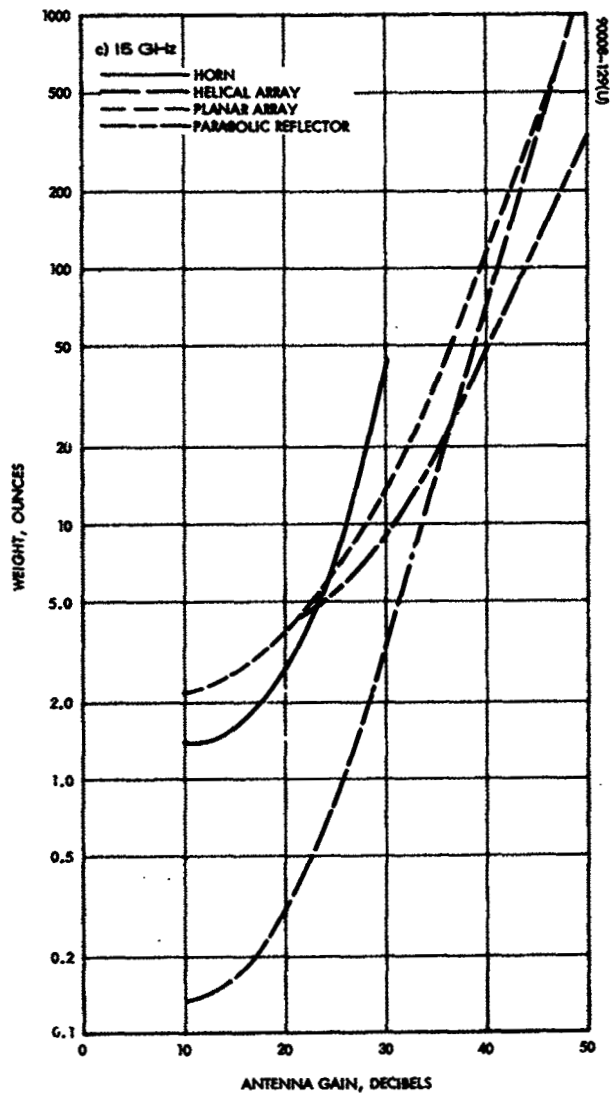


Figure 118(continued). Weight Comparison

## 5.8 REFERENCES

1. G. H. Knittel, "Choosing the Number of Faces of a Phased-Array Antenna for Hemisphere Scan Coverage," IEEE Trans. Antennas and Propagation, AP-13, 1965, pp. 878-882.
2. J. D. Kraus Antennas, McGraw-Hill, Book Co., Inc., New York, 1950.
3. A. G. Holtum, "Improving the Helical Beam Antenna," Electronics, April, 1960.
4. MacLean and Kouyoumjian, "The Bandwidth of Helical Antennas," IRE Trans. Antennas and Propagation, December, 1959.

## 6. COMMUNICATIONS

### 6.1 INTRODUCTION

The major communication requirement of the low-altitude satellite (LAS) is direct transmission of payload information to the data relay satellite (DRS). Station and housekeeping information, together with tracking and command capability, will also be required.

An elementary diagram of the communications link is shown in Figure 119. Present payload information bandwidth may approach 5 MHz, and future growth may require an information bandwidth of more than 20 MHz. It is anticipated that telemetry and command will require approximately 500 bits/sec and 200 bits/sec, respectively, and that the Goddard Range and Range Rate (GRARR) system may be used for tracking.

In this report, attention is focused on the payload information requirement since this will be the major factor for sizing the communication link. It is assumed that the DRS to ground link will have a negligible effect on the LAS-DRS link although it can be accounted for eventually.

The general system parameters considered are frequency, bandwidth, power, and antennas. The information will be sufficient to enable the next phase of this study to be adequately concluded.

### 6.2 CARRIER FREQUENCY

The following frequencies are available, according to EARC, Geneva, 1963:

1750 to 1850 MHz	15.25 to 15.35 GHz
2200 to 2290 MHz	31.00 to 31.3 GHz
7300 to 7750 MHz	34.2 to 35.2 GHz
8400 to 8500 MHz	

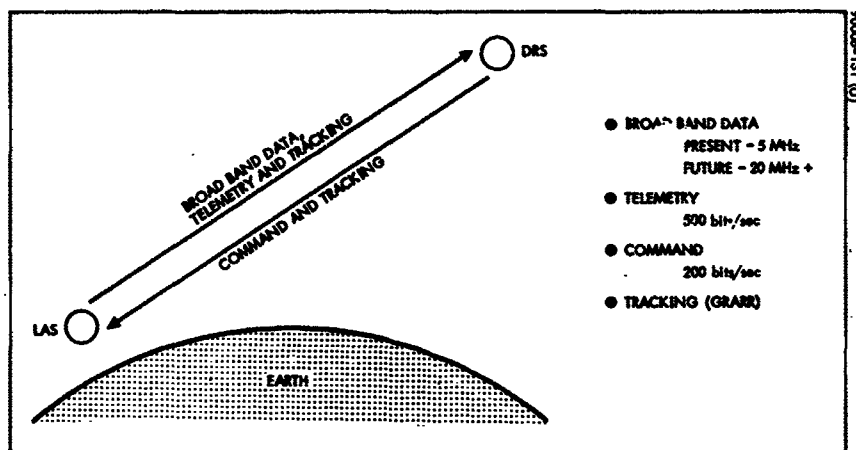


Figure 119. Communication Link

In this analysis, 2.2, 8.0, and 15.3 GHz have been considered in some detail from the point of view of present and potential hardware considerations. The basic analysis can be applied to any other carrier frequency, however, should available hardware suggest it.

### 5.3 RANGE EQUATION

The range equation

$$C = \frac{P_t G_t G_r \lambda^2}{L_t (4\pi R)^2} = \frac{\text{EIRP} \cdot A_e}{4\pi R^2} \quad (1)$$

where

$C$  = receiver carrier power, watts  
 $P_t$  = transmitter power, watts  
 $G_t$  = transmitter antenna effective gain  
 $L_t$  = transmitter losses  
 $G_r$  = receiver antenna effective gain  
 $\lambda$  = wavelength, meters  
 $R$  = range, meters

$\text{EIRP} = \frac{P_t G_t}{L_t}$  = effective isotropic radiated power, watts

$A_e = \frac{G_r \lambda^2}{4\pi}$  = effective aperture, square meters

shows the interrelationships of the various fundamental factors that are considered in sizing the communications system. Some of these factors are known, and others will be varied over a practical spread for tradeoff purposes.

The noise in a system is measured by the equivalent noise spectral density and the predetection bandwidth.

$$N = \eta B \quad (2)$$

where

$N$  = noise power, watts

$\eta$  = predetection noise spectral density, watts/Hz

$B$  = predetection bandwidth, Hz

The ratio of Equations 1 to 2 is a measure of the quality of the system and is (in decibel form)

$$\frac{C}{N} = \text{EIRP} + A_e - 4\pi R^2 - \eta - B \quad (3)$$

A fundamental and basic illustration of the range equation is shown in Figure 120. It is assumed that the DRS carrier-to-noise (C/N) ratio is 10 dB and that the DRS system noise temperature is (nominal) 1000°K. In addition, the range is assumed to be (worst-case) 45,500.0 km. Figure 120 and its describing functions interrelate most of the major communication system parameters.

The ration  $C/\eta$  is sometimes called the capacity of a system. An example of its use in tradeoff form is shown in Figure 121.

#### 6.4 INFORMATION (BASEBAND) STRUCTURE

For the purpose of system analysis, it will be necessary to assume a model baseband structure which represents the payload information. The model chosen for this analysis is a frequency division multiplex (FDM) using a test tone (TT) format. The use of this structure allows great flexibility in its application.

A simplified diagram of the model baseband structure is shown in Figure 122. It is assumed that the information is stacked frequency-wise in a number of equal channels. The information in each channel is represented by a TT of equivalent power. Even though equal channels and equal TT are shown in the transmitted baseband, it is obvious that they can be combined or subdivided in any required fashion. The basic information in each channel or group of channels can be in any format, either analog or digital.

Having established the model baseband structure, it is required to transmit this structure to a user. There is inevitably a degradation in the quality of the baseband as received, and this is measured by the amount of

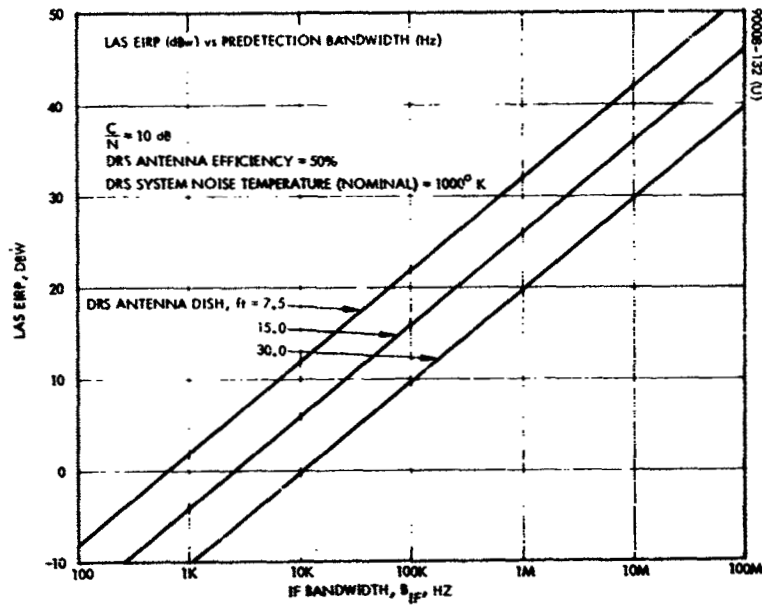


Figure 120. LAS-DRS Link

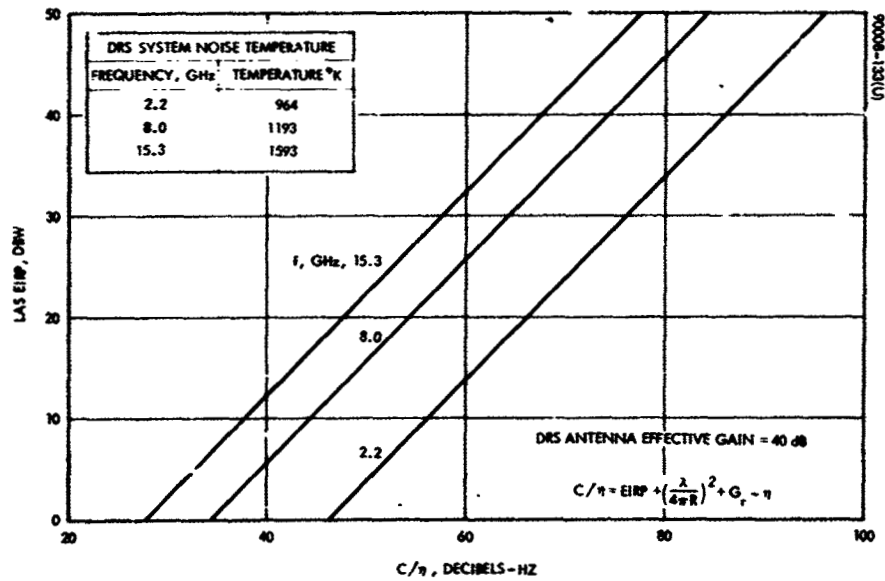


Figure 121. LAS EIRP Versus System Capacity



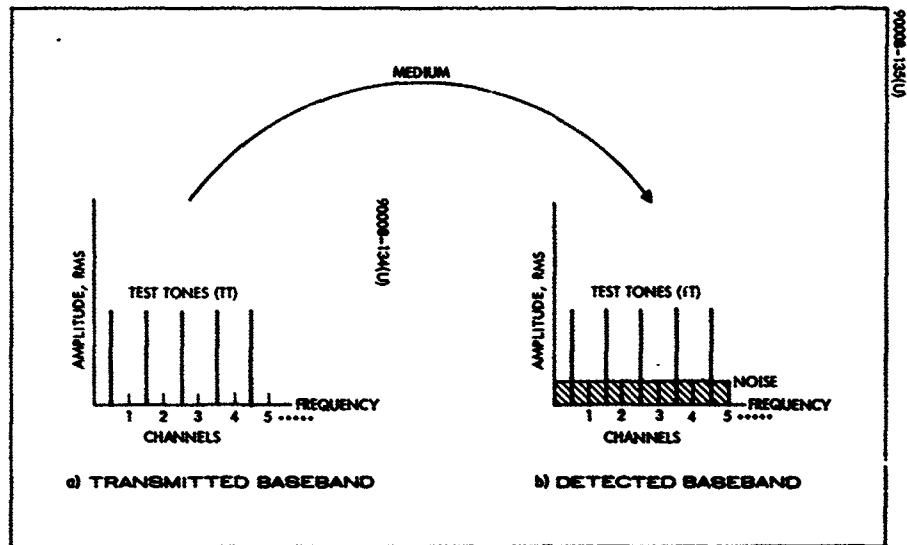


Figure 122. Data Link Model

equivalent noise added by the medium through which it has passed (transmitter, space, and receiver).

The detected baseband will be contaminated by distortion, intermodulation, and system noise which can be included in an equivalent channel noise. The channel quality can, therefore, be measured by the test-tone-to-noise ratio within limits determined by the system requirements.

## 6.5 SYSTEM NOISE

System noise consists of external and internal noise components. The internal noise is described by a receiver noise figure which varies with frequency. The external noise is due to background radiation as seen by the receiving antenna.

### 6.5.1 Background Radiation — External Noise

The DRS antenna will experience an equivalent noise temperature of 300°K due to the earth. The moon, when it is in the field of view of the DRS antenna, will contribute between 150° and 240°K, depending on its phase. When the moon is seen by the DRS antenna, it has that much less of the earth in its field of view. The 300°K temperature, therefore, will be used (worst-case) as the DRS antenna equivalent noise temperature due to background radiation.

The sun, when it is in the field of view of the DRS antenna, produces noise temperature sufficiently high that loss of communication may result (see Appendix II). This situation occurs rarely, and the DRS can be programmed to avoid the problem.

### 6.5.2 Internal Noise

The noise generated within a receiver increases with carrier frequency. For a typical receiver utilizing a tunnel diode and mixer, the following receiver noise figures in Table 8 are typical.

TABLE 8. RECEIVER NOISE FIGURES AND NOISE TEMPERATURES

Frequency, GHz	NF <sub>receiver</sub> , dB	T <sub>receiver</sub> , °K
2.2	5.3	664
8.0	6.1	893
15.3	8.0	1213

## 6.6 MODULATION TECHNIQUES

The carrier structure is determined in large part by the method used to modulate the baseband on it. Many methods might be used, but present and near-future practical considerations suggest frequency modulation, phase modulation, or a combination of both of these methods.

Frequency modulation and phase modulation are sometimes, for purposes of theoretical analysis, grouped together under the heading of angle modulation. However, the differences strongly influence their implementation and must, therefore, be closely considered.

It should be mentioned that pre-emphasis will be used with frequency modulation so that practically all portions of the baseband will threshold together. Because of this type of pre-emphasis, this method of frequency modulation is sometimes called broad-band phase modulation as opposed to the ordinary type of phase modulation. In this analysis, however, the term frequency modulation will be used.

Ordinarily, frequency modulation is detected by means of a discriminator. In the case of broad-band phase modulation, the discriminator is followed by an integrator so that the effect of pre-emphasis on the baseband amplitude will be corrected. The discriminator, however, will exhibit the customary threshold and will require the predetection signal-to-noise ratio to exceed this value. The threshold is approximately 10 dB for the normal discriminator and somewhat less for a threshold extension type of discriminator.

Phase modulation requires a phase detector in which a synchronous carrier is inserted in the proper phase. The inserted carrier is ordinarily obtained by phase locking to a remnant carrier in the original signal. A threshold (in the frequency modulation sense) does not exist for phase modulation. A major requirement is the existence of enough carrier for phase locking purposes, thus restricting the modulation index. In addition, intermodulation distortion increases rapidly with increasing modulation index, restricting operation to an essentially linear portion of the phase characteristic. For these reasons, frequency modulation (in the broad-band phase modulation sense) will be considered in detail as a preferred method of modulation.

## 6.7 FREQUENCY DIVISION MULTIPLEX/FREQUENCY MODULATION (FDM/FM)

The theoretical analysis of the FDM/FM system is given in Appendix II. Application of this analysis resulted in Figure 123 for the LAS-DRS link, which indicates trends, and thereby assists, in the next phase of this study.

The curves and notations in Figure 123a describe the tradeoff system parameters for a baseband of 2.5 MHz. Figures 123b through 123e are

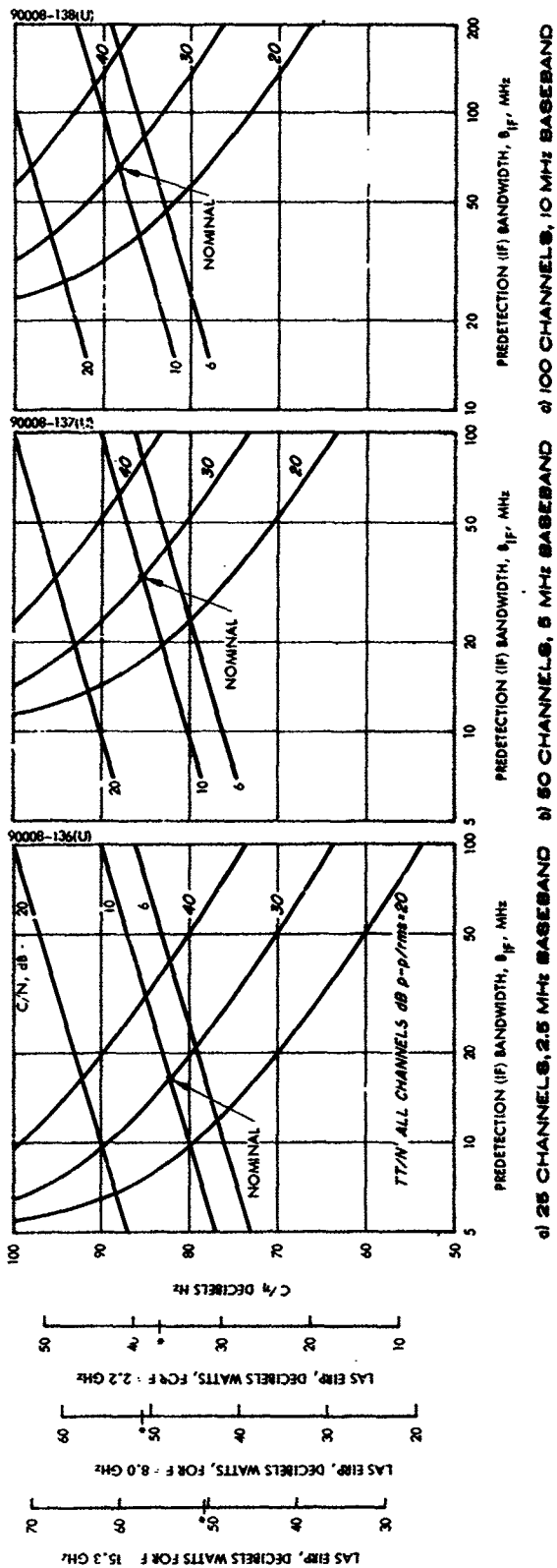
similar except for the basebands which range to 30 MHz. Each figure has two parametric families of curves. One set of curves ranges the value of  $C/N$  from 6 to 20 dB, and the other set of curves ranges the value of  $TT/N'$  from 20 to 40 dB, where  $N'$  is the noise power in a channel. The parametric coordinates are LAS EIRP for carrier frequencies of 15.3, 8.0, and 2.2 GHz versus the predetection (IF) bandwidth. For the purpose of Figure 123, it is assumed that the DRS antenna gain is 40 dB. The DRS noise temperature is 964°K at 2.2 GHz, 1193°K at 8.0 GHz, and 1513°K at 15.3 GHz. Asterisks have been placed on the EIRP ordinates indicating possible hardware implementation limitations. These are for trend information only, and will be varied in accordance with hardware availability and configuration.

The information contained in Figure 123 is sufficient to trade off the major parameters in the LAS-DRS broad-band link. These basic curves can be easily modified to reflect other parameter spreads that may be suggested by possible hardware availability. A most important aspect of these curves is their use in indicating trends. Such an application resulted in the data contained in Tables 9 and 10.

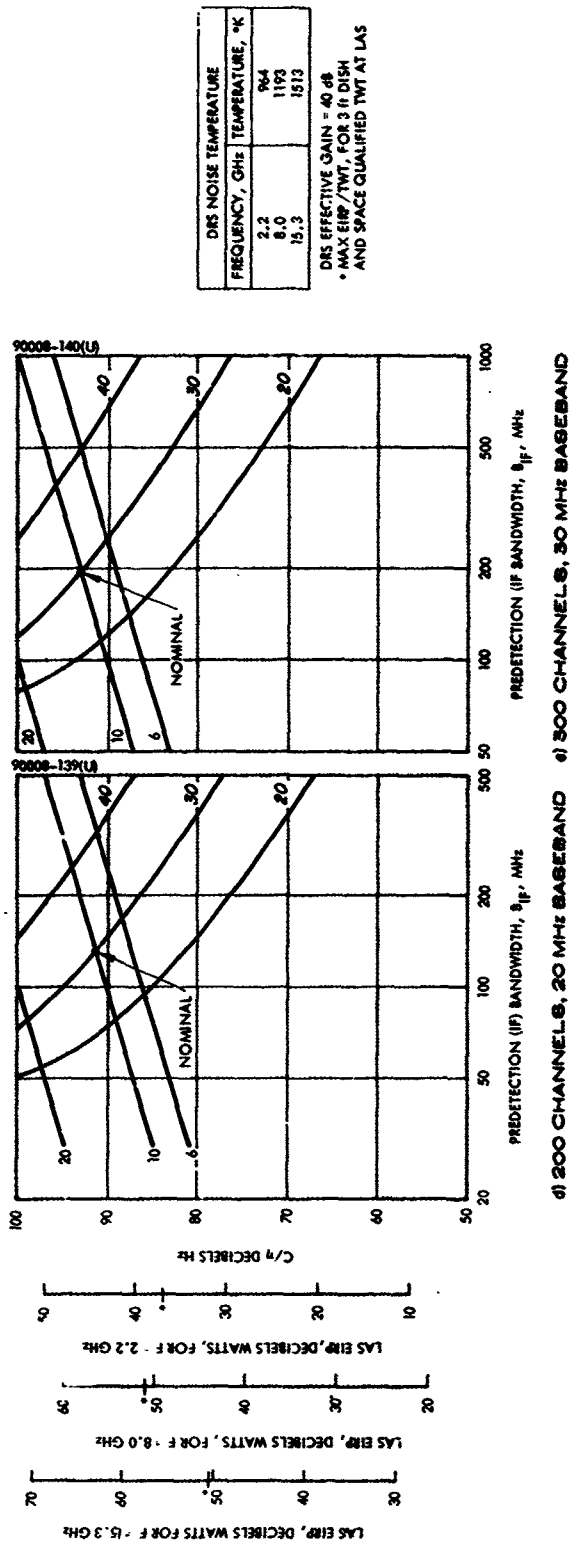
Table 9 was constructed by collecting the peripheral parameters surrounding a nominal system operating point. This point is indicated on Figure 123 and is the intersection of  $C/N = 10$  dB and  $TT/N' = 30$  dB. The values of  $C/N$  and  $TT/N'$  are of practical interest since they reflect parameters that might be applied to a possible spectral camera. In Table 9, it was assumed also that the DRS antenna gain was constant at 40 dB. This infers a reduction in antenna size with increasing frequency, which is to be expected for structural reasons.

For comparison, in Table 10, the DRS antenna was assumed to be 30 feet in diameter for all frequencies. The DRS antenna gain thus varied from 43.5 dB at 2.2 GHz to 60.0 dB at 15.3 GHz. It is important to note that the required LAS power shown in Table 9 is virtually independent of carrier frequency for each baseband. In Table 10, however, the required LAS power is reduced in proportion to the increased gain of the DRS antenna. It can be expected that the actual tradeoff system parameters will be bracketed by the values shown in Tables 9 and 10.

This communication system is compatible with the IRIG FDM Telemetry Standards, Document 106-66, Section 5.2. The subcarrier oscillators required for telemetry, together with IRIG bandwidths and guard bands, can be replaced by equivalent test tones and channels. Analysis is identical to that discussed above.



a) 25 CHANNELS, 2.5 MHz BASEBAND b) 50 CHANNELS, 5 MHz BASEBAND c) 100 CHANNELS, 10 MHz BASEBAND



d) 200 CHANNELS, 20 MHz BASEBAND e) 300 CHANNELS, 30 MHz BASEBAND f) 500 CHANNELS, 50 MHz BASEBAND

DRS NOISE TEMPERATURE	
FREQUENCY, GHz	TEMPERATURE, °K
2.2	964
8.0	1193
15.3	1313

DRS EFFECTIVE GAIN = 40 dB  
 • MAX EIRP/TWT, FOR 3 ft DISH  
 AND SPACE QUALIFIED TWT AT LAS

Figure 123. LAS-DRS Link FDM/FM Modulation

TABLE 9. SUMMARY OF LAS-DRS LINK FDM/FM MODULATION\*  
(DRS Antenna Gain Assumed Constant at 40 dB)

Baseband, MHz	IF Bandwidth, MHz	DRS Antenna Gain, dB	Carrier Frequency, GHz	LAS EIRP, dBw	3-foot Antenna Gain, dB	Required Transmis- sion Power, dBw
2.5	16.5	40	2.2	36.0	23.5	12.5
			8.0	48.0	35.0	13.0
			15.3	54.5	41.0	13.5
5.0	33.0	40	2.2	39.0	23.5	15.5
			8.0	51.0	35.0	16.0
			15.3	57.5	41.0	16.5
10.0	66.0	40	2.2	42.0	23.5	18.5
			8.0	54.0	35.0	19.0
			15.3	60.5	41.0	19.5
20.0	131.0	40	2.2	45.0	23.5	21.5
			8.0	57.0	35.0	22.0
			15.3	63.5	41.0	22.5
30.0	196.0	40	2.2	47.0	23.5	23.5
			8.0	59.0	35.0	24.0
			15.3	65.5	41.0	24.5

\* Higher DRS gain (lower LAS EIRP) potential at higher frequencies.

TABLE 10. SUMMARY OF LAS-DRS LINK FDM/FM MODULATION\*  
(Varying DRS Antenna Gain)

Baseband, MHz	IF Bandwidth, MHz	DRS Antenna Gain*, dB	Carrier Frequency, GHz	LAS EIRP, dBw	3-foot Antenna Gain, dB	Required Transmis- sion Power, dBw
2.5	16.5	43.5	2.2	32.5	23.5	9.0
		54.5	8.0	33.5	35.0	-1.5
		60.0	15.3	34.5	41.0	-6.5
5.0	33.0	43.5	2.2	35.5	23.5	12.0
		54.5	8.0	36.5	35.0	1.5
		60.0	15.3	37.5	41.0	-3.5
10.0	66.0	43.5	2.2	38.5	23.5	15.0
		54.5	8.0	39.5	35.0	4.5
		60.0	15.3	40.5	41.0	-0.5
20.0	131.0	43.5	2.2	41.5	23.5	18.0
		54.5	8.0	42.5	35.0	7.5
		60.0	15.3	43.5	41.0	2.5
30.0	196.0	43.5	2.2	43.5	23.5	20.0
		54.5	8.0	44.5	35.0	9.5
		60.0	15.3	45.5	41.0	4.5

\* Assumes a 30-foot diameter parabolic reflector with a 50 percent efficiency.

## 6.8 DIGITAL TRANSMISSION

As indicated in Section 6.4, the test tone (TT) format which was used to model the transmitted baseband can be used equally well to represent analog or digital data in the channels. Assuming non-coherent frequency shift keying (FSK) of subcarriers by the digital data, the channels shown in Figure II-2 (see Appendix II) which have a capacity of 80 kHz of analog data would be capable of handling 80 kilobits per second (kbps) bit streams of non-return to zero (NRZ-FM) data. The energy-per-bit to noise-spectral-density ratio required to ensure a bit error rate (BER) of  $10^{-4}$  is, according to Reference 1,

$$E/\eta = 12.2 \text{ dB} \quad (4)$$

The rms/rms TT/N required at the carrier discriminator output is identical to the S/N required at the input to the FSK bit detector. This signal-to-noise ratio is

$$S/N \text{ (dB)} = E/\eta \text{ (dB)} + \text{bit rate (dB)} - B \text{ (dB)} \quad (5)$$

where the bit rate and the subcarrier discriminator input filter bandwidth, B, are equal. Under these conditions, each channel requires a test-tone-to-noise-ratio of

$$TT/N = 12.2 \text{ dB, rms/rms} = 21.2 \text{ dB p-p/rms} \quad (6)$$

If a C/N of 10 dB is also required, the curves of Figure 123 indicate that the 25 channel system would require a  $C/\eta \approx 80 \text{ dB-Hz}$ . This system would be capable of transmitting 2 megabits per second of information with a BER of  $10^{-4}$ . A plot of  $C/\eta$  versus bit rate is shown in Figure 124.

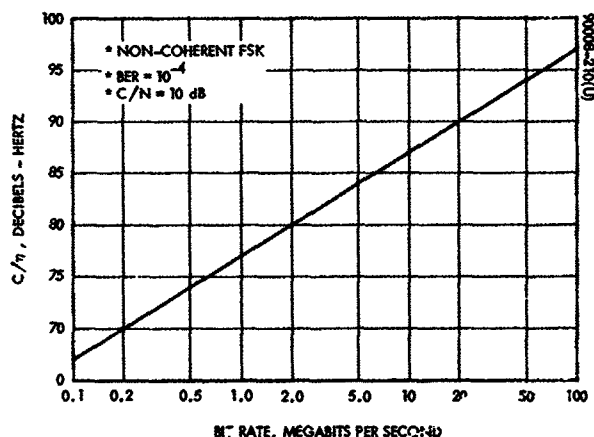


Figure 124. Carrier-to-Noise Density, Bit Versus Rate



## 6.9 DRS-LAS BROAD COVERAGE LINK

The use of a broad coverage DRS antenna and an omnidirectional antenna on the LAS would allow a communication link that would be independent of a critical antenna pointing requirement. The geometry is shown in Figure 125. As expected, however, the reduction in antenna gain requires a compensatory increase in transmitter power and/or a reduction in information rate.

From synchronous orbit, an earth coverage antenna would have a half-power beamwidth of 20 degrees, with a worst-case effective gain of 14 dB. The LAS omnidirectional antenna is assumed to have an effective gain of -4 dB. Figure 126a shows the DRS EIRP and DRS transmitter power as a function of LAS predetection bandwidth. A nominal C/N ratio of 10 dB is assumed at the carrier frequencies of 2.2, 8.0, and 15.3 GHz. From Figure 126a, it is evident that a DRS transmitter power of 10 watts at 2.2 GHz is required for an LAS predetection bandwidth of 100 Hz. The information rate for this bandwidth is of the order of 100 bits/sec.

The values of LAS system noise temperature used in Figure 126 are the receiver noise temperatures from Table 8. The external noise which the LAS would experience is galactic noise, which contributes a maximum of about 4°K at 2.2 GHz from the direction of the galactic plane and a negligible amount from directions away from the galactic plane (Reference 2). The noise decreases to a negligible amount at 8.0 GHz and higher frequencies. Therefore, only the receiver noise temperatures are used when considering the LAS with its omnidirectional antenna.

Figure 126b shows LAS EIRP and LAS transmitter power as a function of DRS predetection bandwidth. It is assumed also that the signal-to-noise ratio is 10 dB at carrier frequencies of 2.2, 8.0, and 15.3 GHz. The DRS system noise temperatures relative to those of the LAS show the effect of the earth's 300°K blackbody temperature. In this case, transmission of 500 bits/sec of telemetry data would require an LAS transmitter power of approximately 100 watts.

From the information contained in Figure 126, it can be concluded that the use of a broad coverage link is restricted to low data rate information, telemetry, and command.

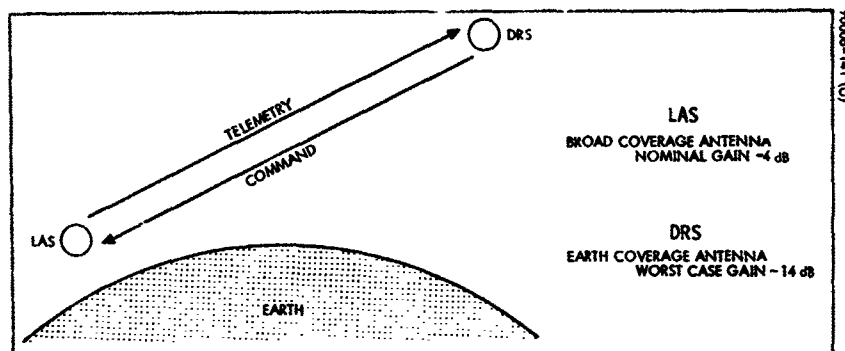
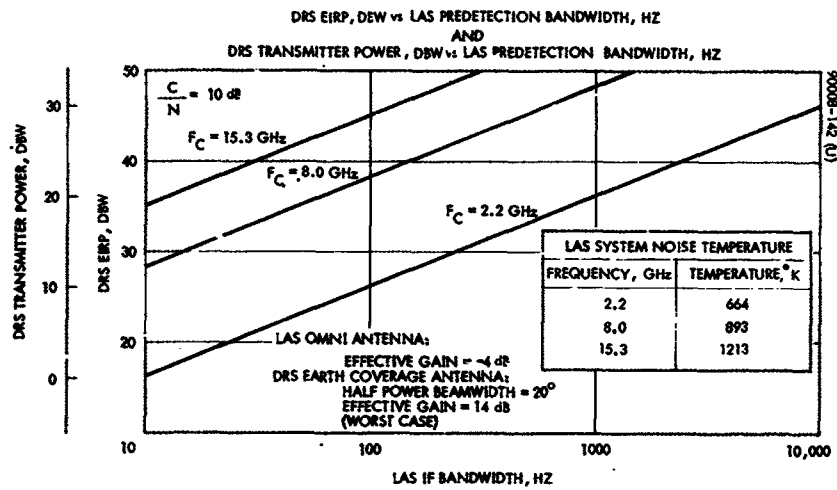
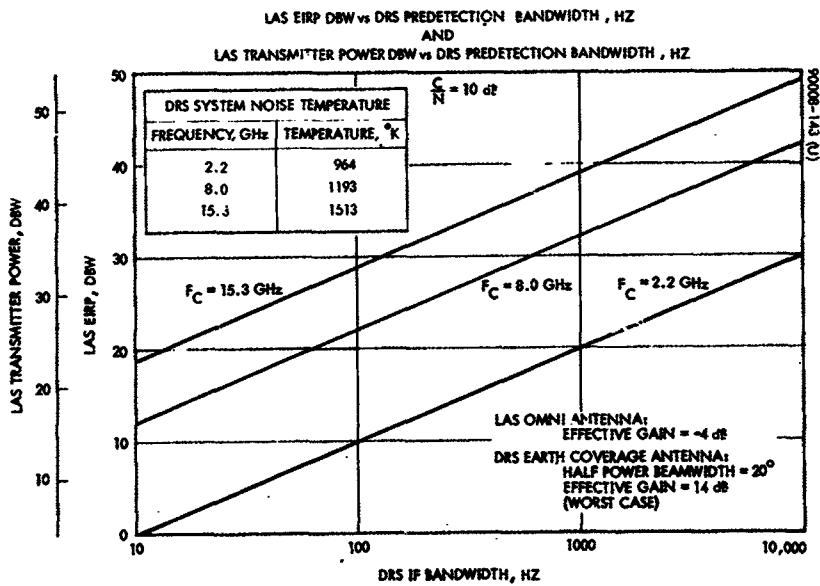


Figure 125. Low Data Rate Link



a) DRS-LAS



b) LAS-DRS

Figure 126. Broad Coverage Link

#### 6.10 REFERENCES

1. Paul D. Shaft, "Error Rate of PCM-FM Using Discriminator Detection," IEEE Trans. on Space Electronics and Telemetry, December 1963.
2. R.F. Felepowsky and E.I. Muehldorf, Space Communication System, Prentice Hall, 1965.

## 7. CONTROL

### 7.1 INTRODUCTION

In this section, attitude control concepts are discussed and compared. The effect of the LAS-DRSS communication link on the choice of the attitude control system is minimal. Since the purpose of this study is to evaluate the impact of this link on LAS systems, it should be stated at the outset that the impact is small. The attitude control method should accommodate a configuration which will allow one or two steerable antennas to be mounted on the spacecraft and allow generation of sufficient power. For payloads of the type discussed in Section 2, this latter requirement will result in deployable solar arrays. But as shown in Section 4, both of the two fundamental spacecraft concepts will accommodate both these requirements.

It is the satellite mission, and principally the pointing accuracy and angular rate limitations imposed by the sensors, which has the greatest bearing upon the choice of attitude control method. The continuous LAS-DRSS link will allow backup ground control capability in the event of the failure of an automatic system. But there appears to be no advantage to ground control except under the usual circumstance where spin stabilization is employed.

Descriptions and detailed analyses of the basic attitude control methods are available in books, journals, and industrial reports. The basic concepts have been extensively studied, and in most cases information concerning these methods has been available for several years. This section surveys these attitude control methods and discusses each in the light of earth observation requirements.

## 7.2 BASIC ATTITUDE CONTROL CONCEPTS

### 7.2.1 Gravity-Gradient Stabilization

Gravity gradient stabilization provides attitude control of the satellite by distributing the moments of inertia of the vehicle such that deviation from the desired earth-oriented attitude results in corrective torques produced by gravitational forces.

### 7.2.2 Mass Expulsion

Mass expulsion provides control by expelling gas such as hydrogen peroxide or hydrazine to produce corrective torques.

### 7.2.3 Magnetic Control

Magnetic control system provides corrective or control torques by controlling electric currents which produce magnetic fields, which in turn react with the earth's magnetic field.

### 7.2.4 Reaction Wheel System

The reaction wheel system, sometimes called an inertial wheel system, provides attitude control by producing angular momentum in three orthogonal reaction wheels to compensate the spacecraft angular momentum produced by disturbance torques. That is, the undesirable angular momentum of the earth-oriented spacecraft due to disturbance torques is transferred to the reaction wheels. Over a period of time, the speed of these wheels may become excessive, so another system is required to "unload" the angular momentum from these wheels. Either a mass expulsion or magnetic control system can be used for this purpose.

### 7.2.5 Spin Stabilization

Spin stabilization provides orientation of one spacecraft axis, the spin axis, by the gyroscopic effect resulting from the spinning motion of the satellite. Newton's law of motion states that the rate of change of angular momentum is in the direction of and proportional to the externally applied torque. Thus, if the angular momentum due to the spinning motion is large, small disturbance torques will produce only small deviations of the spin axis in a given period of time. That is, correction maneuvers need to be performed relatively infrequently. The torques required to correct the spin axis orientation may be provided by mass expulsion, magnetic control, or some other torque producing method. A satellite which is spinning, however, has limited use for earth observation because no axis can be continuously earth-oriented. As a result, the all-spinning vehicle is not considered further here.

#### 7.2.6 Momentum Bias System Type 1 (MBS Type 1)

The MBS Type 1 stabilization technique consists of two distinct parts—a spinning section and an earth-oriented, or despun, section. The spinning section provides spin stabilization while the earth-oriented section, which is mechanically despun, provides the structure for earth observation sensors. As with the spinning satellite, spin-axis correction maneuver torques must be produced by a system such as those discussed in Sections 7.2.2 and 7.2.3.

#### 7.2.7 Momentum Bias System Type 2 (MBS Type 2)

The MBS Type 2 technique also employs the advantages of spin stabilization, but differs from the MBS Type 1 in that a smaller, rigid inertial wheel is spun at a relatively high speed to provide the spin stabilization effect, rather than spinning a major portion of the spacecraft as is done with the MBS Type 1. Again, spin axis control can be obtained with the systems of Sections 7.2.2 through 7.2.4.

These systems, excluding all-spin stabilization, can be categorized as shown in Table 11.

TABLE 1 BASIC ATTITUDE CONTROL

Passive		
Gravity gradient		
Active		
Three-axis stabilization		
Mass expulsion reaction control		
Magnetic control		
Reaction wheels		
Unloading torques by magnetic control and mass expulsion		
Momentum bias		
Type 1	}	Mass expulsion and/or magnetic control for spin-axis pointing
Type 2		

### 7.3 DISTURBANCE TORQUES

The attitude control system must compensate for the motion of the satellite caused by external disturbance torques. It follows that some quantitative knowledge of these disturbances will be useful in evaluating the performance of a particular attitude control method. The sizing of the controlling elements, fuel or power required, and frequency of attitude correction is a function of the size and distribution of the disturbance torques. These torques in turn are a function of the spacecraft design, weight, area, surface material, cg location, etc. For preliminary design purposes, however, certain simplified models based on previous experience can be used to estimate the disturbance torque environment to within acceptable limits for sizing of the control elements.

#### 7.3.1 Solar Radiation Torques

A detailed analysis of solar radiation forces and torques on a surface is given in Appendix I. From Equation 27 of that appendix, the solar radiation torque  $T_s$  is given by the expression

$$\overline{T}_s = \int_A \overline{V} \times \overline{P}_n dA + \int_A \overline{V} \times \overline{P}_s dA \quad (1)$$

where  $\overline{V}$  is the vector distance from the origin (the LAS center of mass in this case) to the surface element  $dA$ .  $A$  refers to the intercepting surface, while  $P_n$  and  $P_s$  refer respectively to the components of the pressure vector producing normal and shear (tangential) forces.

To provide a quantitative estimate, assume that the spacecraft surface area exposed to the solar radiation is flat and normal to the sun vector. This is usually a worst-case assumption yielding the largest torques. Under these conditions

$$\overline{T}_s = P_n A \left( \frac{1}{A} \int_A \overline{V} \times \overline{n} dA \right) \quad (2)$$

where  $\overline{n}$  is the unit normal to the surface.  $P_n A$  is the force on the surface; the magnitude of the quantity in parentheses is, by definition, the distance,  $d$ , between the projection of the center of mass (cm) onto the surface and the surface center of pressure (cp). Thus, Equation 2 becomes

$$|\overline{T}_s| \equiv T_s = A d P_n \quad (3)$$

Substituting Equation 21 of Appendix I, with  $\theta = 0$  corresponding to the assumption of normal radiation incidence

$$T_s = A d P \left( 1 + \frac{2}{3}R + \frac{RD}{3} \right) \quad (4)$$

where  $P$  is the solar pressure constant  $= 9.48 \times 10^{-8}$  lb/ft<sup>2</sup>, and where  $R$  and  $D$  are the effective reflectivity and diffusivity coefficients, respectively.  $R = 1$  implies that all incident radiation is reflected and  $D = 1$  if the reflection is purely specular. A reasonable assumption for these coefficient spacecraft exterior materials and solar arrays is  $R = 0.7$  and  $D = 0.7$ , which reduces Equation 4 to

$$T_s = (1.55 \times 10^{-7}) A d \text{ ft-lb} \quad (5)$$

The surface area is a function of the basic spacecraft structure and the size of the solar array. The size of the solar array is, in turn, dependent on the required power. From the shroud dimensions of Figure 5, a normal surface area of 30 square feet is a reasonable estimate, and from Reference 1, about 0.1 square foot of solar array is needed per watt. Thus,

$$A \approx 30 + (0.1)(\text{power}) \text{ square feet} \quad (6)$$

To continue with the quantitative estimate, assume  $d = 3$  feet and that 500 watts of power is required. Then, from Equations 5 and 6

$$T_s = 3.72 \times 10^{-5} \text{ ft-lb} \quad (7)$$

For the normal incidence assumption, the disturbance torque will lie in the plane normal to the sun vector.

### 7.3.2 Aerodynamic Torque

At the altitudes considered for this spacecraft, the effect of aerodynamics is usually evaluated assuming free molecular flow interacting with the spacecraft surface by means of surface reflection coefficients for tangential and normal momentum,  $\sigma$  and  $\nu$ , respectively. When the coefficients are zero, there is no energy or tangential momentum exchange between the incident stream and the surface, and the reflection is said to be specular. When the coefficients are unity, the molecules are re-emitted randomly, and the reflection is said to be diffuse. The coefficients then represent the percentage of reflected molecules that are re-emitted diffusely. The geometry illustrating this is shown in Figure 127. Normally, diffuse reflection is assumed for spacecraft analysis.



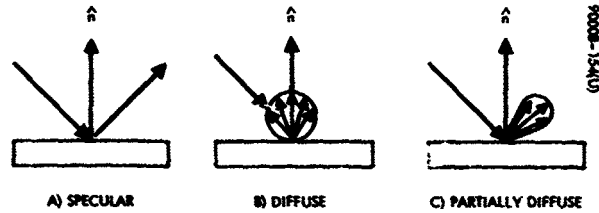


Figure 127. Reflection Geometry

The aerodynamic drag force, which leads to the disturbance torque, is computed from the equation

$$D = \left(\frac{1}{2} \rho V^2\right) A C_D \quad (8)$$

where

$\rho$  = atmospheric density, slugs/ft<sup>3</sup>

$V$  = spacecraft velocity, fps

$A$  = spacecraft area exposed to aerodynamic flow

$C_D$  = drag coefficient based on free molecular flow theory

For diffuse reflection  $C_D$  is given by the expression

$$\begin{aligned} C_D &= C_n \cos \theta + C_t \cos \theta \\ &= [(1 + 2 \cos \theta) + 2 \sin \theta] \cos \theta \end{aligned} \quad (9)$$

where  $\theta$  is the angle of incidence of the flow relative to the surface normal.

The total torque is actually given by an expression similar to that of Equations 1 and 2

$$\bar{T}_a = \left(\frac{1}{2} \rho V^2\right) \int_A \mathbf{r} \times \mathbf{n} C_D dA \quad (10)$$

As in the above analysis, assuming normal incidence of the particles over a surface of constant  $C_D$ , Equation 10 becomes

$$T_a = \frac{1}{2} \rho V^2 C_D A d \quad (11)$$

where  $d$  is the distance between the center of pressure and the center of mass projected onto  $A$ . The area  $A$  can again be estimated by Equation 6. Making the following assumptions

$$C_D = 3$$

$$\text{Altitude} = 500 \text{ n.mi. } (\rho = 1.94 \times 10^{-16} \text{ slug/ft}^3)$$

$$V \approx 24,000 \text{ fps}$$

$$\text{Power} = 500 \text{ watts}$$

$$d = 3 \text{ feet}$$

$$A = 80 \text{ square feet}$$

Then

$$T_a \approx 4.0 \times 10^{-5} \text{ ft-lb} \quad (12)$$

For the normal incidence assumed, the torque will lie in the plane normal to the velocity vector.

### 7.3.3 Gravity-Gradient Torques

A detailed derivation of the gravity-gradient torques about the spacecraft principal axes is presented in the following subsection. From that analysis, it can be seen that if the principal axes do not deviate greatly from the orbit axes (see Section 3.6), the magnitude of the resultant torque is approximately

$$T_g = 3\omega_o^2 \Delta I \sin \alpha \text{ ft-lb} \quad (13)$$

where  $\omega_o$  is the LAS orbital angular velocity in radians,  $\Delta I$  is the maximum difference between principal moments of inertia, and  $\alpha$  is the maximum angular deviation of the principal axes from the orbit axes.

For the weights and dimensions considered in Section 2, a value of  $\Delta I$  equal to 100 slug-ft<sup>2</sup> is possible. If the satellite has steerable solar arrays, and particularly if the orbit is sun synchronous with the sun-orbit angle greater than 20 degrees, the angular variation of the principal moments of inertia may easily be 5 degrees. For LAS orbits  $\omega_o \approx 10^{-3}$  rad/sec and so for the above assumptions

$$T_g \approx (3 \times 10^{-6})(100) \sin 5^\circ = 2.62 \times 10^{-5} \text{ ft-lb} \quad (14)$$

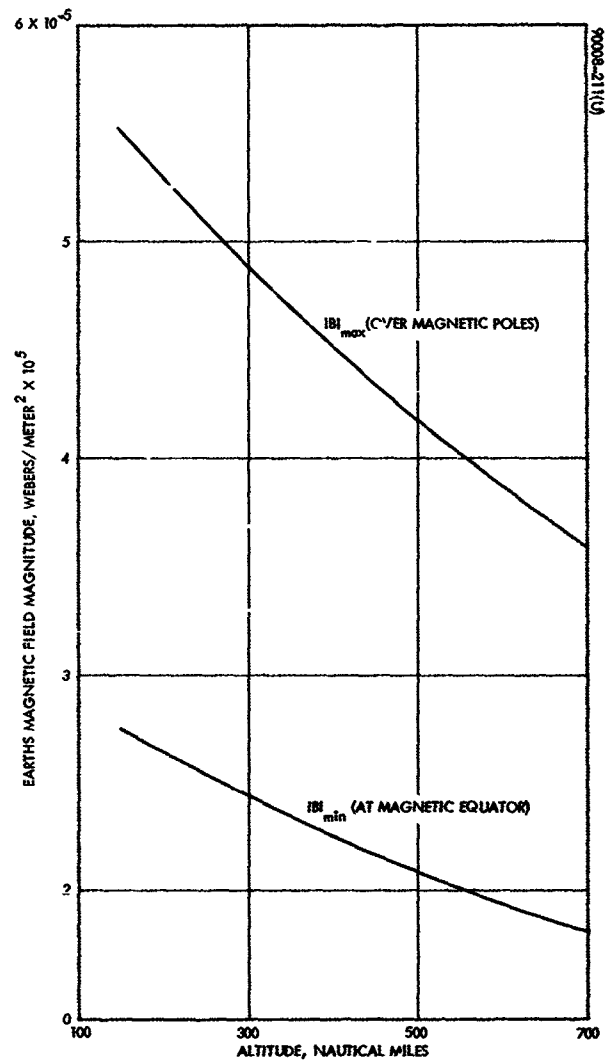


Figure 128. Earth's Magnetic Field Magnitude Versus Altitude

#### 7.3.4 Magnetic Torques

The magnitude of the earth's magnetic field is a function of the orbital altitude and magnetic latitude. The magnetic field has twice the magnitude over the magnetic poles as it does at the magnetic equator. The magnetic north vector deviates from geographical north by approximately 17 degrees. At the magnetic poles

$$|B|_p \approx \frac{2.56 \times 10^6}{R^3} \text{ webers per square meter} \quad (15)$$

where R is the orbital radius in nautical miles. The maximum and minimum values of the magnetic field magnitude are shown in Figure 128. For  $200 \leq h \leq 700$  n. mi.

$$3.6 \times 10^{-5} \leq |B_p| \leq 5.3 \times 10^{-5} \text{ webers per square meter} \quad (16)$$

If M is the component of the magnetic moment, in amp-square meter, perpendicular to the magnetic field vector, then the torque on the spacecraft is

$$T_m = M |B| \text{ newton-meters} \quad (17)$$

The specification on ATS-D required M to be less than 0.8 amp-square meter. Assuming this specification is relaxed to allow  $M \leq 2$  amp-square meter, then over the magnetic poles

$$7 \times 10^{-5} \leq T_m \leq 10.6 \times 10^{-5} \text{ newton-meters}$$

or

$$5.15 \times 10^{-5} \leq T_m \leq 7.8 \times 10^{-5} \text{ ft-lb} \quad (18)$$

For a 500 n. mi. altitude

$$T_m = 6.2 \times 10^{-5} \text{ ft-lb} \quad (19)$$

The magnetic field vector rotates with respect to nonrotating coordinates at the center of the spacecraft with twice orbital frequency, but the earth oriented spacecraft is rotating with orbital angular velocity. Thus, the torque with respect to a body fixed reference frame produced is cyclic with orbital frequency.

A secular effect is possible, however, if the magnetic moment vector changes magnitude or direction with respect to the spacecraft during an orbit.

#### 7.3.5 Comments

In addition to the average or maximum magnitude of the disturbance torque, its direction with respect to spacecraft coordinates is important as well as its functional dependence on time. These additional quantities require some knowledge of the LAS orbit and its structural configuration.

A few general comments are possible, however. As mentioned above, the magnetic disturbance torque is cyclical with respect to LAS body-fixed coordinates. A portion of both the solar torque and aerodynamic torque is cyclic while part is constant (secular) with respect to body fixed coordinates. Relative ratios of secular to cyclical torque depend on the LAS configuration, and particularly on the relative size of the solar array. The gravity-gradient disturbance torque may be either secular or cyclical depending on whether the cause for principal axes deviation is secular or cyclic with respect to body fixed coordinates.

## 7.4 GRAVITY-GRADIENT CONTROL

### 7.4.1 Gravity-Gradient Torques

The expressions for the gravity-gradient torque in the body reference coordinates of Section 3.6 are derived in Appendix III. These expressions are repeated below.

$$M_{gx} = 3 \omega_o^2 (I_z - I_y) a_{12} a_{13} \quad (20)$$

$$M_{gy} = 3 \omega_o^2 (I_x - I_z) a_{11} a_{13} \quad (21)$$

$$M_{gz} = 3 \omega_o^2 (I_y - I_x) a_{11} a_{12} \quad (22)$$

The matrix elements  $a_{11}$  are given in Equation 52 of Section 3.6. Examination of these factors reveals that Equations 20 and 21 are complex expressions involving sums and differences of products of trigonometric functions of the Euler angles defined in Section 3.6.

If small angle approximations are valid, i. e.,  $\sin \alpha = \alpha$ ,  $\cos \alpha = 1$ , etc., then

$$M_{gx} \approx - 3 \omega_o^2 (I_z - I_y) \alpha \theta \quad (23)$$

$$M_{gy} \approx 3 \omega_o^2 (I_x - I_z) \alpha \quad (24)$$

$$M_{gz} \approx - 3 \omega_o^2 (I_y - I_x) \theta \quad (25)$$

### 7.4.2 Control

Gravity-gradient control is implemented by designing the spacecraft so that when the principal axes are aligned with the orbital axes, the satellite is in the desired attitude. This requires providing moments of inertia such that the gravity-gradient torques correct attitude deviations. From Equations 23 through 25 it can be seen that this can be done by making both  $I_z$  and  $I_y$  larger than  $I_x$ .

To provide this large difference in moments of inertia it is usually necessary to extend booms with tip masses away from the main body.

#### 7.4.3 Pointing Capability

To estimate the pointing capability of this control method in the anticipated disturbance torque environment, consider the following example. In Sections 7.3.1 through 7.3.4 the following disturbance torques were estimated.

$$\begin{array}{rcl}
 \text{Solar radiation} & = & 3.7 \times 10^{-5} \text{ ft-lb} \\
 \text{Aerodynamic} & = & 4 \times 10^{-5} \text{ ft-lb} \\
 \text{Gravity-gradient} & = & 2.6 \times 10^{-5} \text{ ft-lb} \\
 \text{Magnetic} & = & 6 \times 10^{-5} \text{ ft-lb} \\
 \hline
 \text{Total} = T_d & = & 1.7 \times 10^{-4} \text{ ft-lb} \quad (26)
 \end{array}$$

$$R_{ss} \text{ total} = 8.5 \times 10^{-5} \text{ ft-lb} \quad (27)$$

Since the time dependence and direction of the disturbances depend on the spacecraft configuration, the  $R_{ss}$  total may result in a more valid evaluation. The total =  $1.7 \times 10^{-4}$  ft-lb represents a worst-case situation.

Using Equation 24, where for LAS altitudes,  $\omega_0 \approx 10^{-3}$  rad/sec, and assuming  $I_x - I_z = 1000 \text{ slug} \cdot \text{ft}^2$   $M_{gy}$  is equated to the disturbance torque. Using the  $R_{ss}$  total

$$8.5 \times 10^{-5} = (3 \times 10^{-6})(10^3) \alpha$$

or

$$\alpha_{R_{ss}} = 2.84 \times 10^{-2} \text{ rad} \approx 1.6 \text{ degrees} \quad (28)$$

For the worst-case total

$$\alpha_{\text{worst}} = 5.68 \times 10^{-2} \text{ rad} = 3.2 \text{ degrees} \quad (29)$$

For most earth observation missions, this magnitude of attitude error would not be tolerable. In addition, the extended booms required to produce the large moment of inertia difference will bend due to thermal gradients. This will produce additional pointing errors, possibly again as large as those above. Thus for the representative optical imaging mission chosen in this study, gravity-gradient control does not look attractive.

## 7.5 MAGNETIC TORQUE CONTROL

The generation of attitude control torques through the interaction of controlled spacecraft currents with the earth's magnetic field has received considerable attention in recent years. The most obvious advantage of such a technique is the elimination of fuel which is required of the more common mass expulsion systems. Thus, the lifetime of a vehicle with this method of attitude control is not limited by fuel storage capability. Other advantages over mass expulsion methods include the following: 1) the elimination of mechanical moving parts in valves, 2) only pure torques are produced, and 3) the elimination of concern about expelled propellant impinging on parts of the spacecraft. A distinct advantage is the ability to produce low torques over sustained periods as opposed to short impulsive torques.

The first step in analyzing a magnetic control system is to determine the earth's magnetic field in terms of body fixed coordinates and orbital parameters. Figure 129 defines spherical coordinates of a magnetic reference coordinate system,  $x_m, y_m, z_m$ . Figure 130a defines the parameters relating the magnetic Cartesian system to an inertial coordinate system,  $x_i, y_i, z_i$ , and Figure 130b defines the parameters relating the inertial coordinates to orbital coordinates  $i, j, k$ . These last two coordinate systems are discussed in Section 3.6

### 7.5.1 Earth's Magnetic Field

The earth's magnetic field may be approximated in the first order as the field due to a simple magnetic dipole at the center of the earth, with dipole axis inclined approximately 11 degrees to the earth's equator. This approximation is sufficiently accurate for considering magnetic attitude control of an orbiting satellite (see Reference 2).

The potential function for a magnetic dipole is given by:

$$\phi = - \frac{m \sin \gamma}{r^2}$$

where  $m$  is the dipole strength,  $r$  the magnitude of the radius vector from the dipole to the vehicle center of mass, and  $\gamma$  is the latitudinal position relative to the magnetic equator (Figure 129). The magnetic field,  $B$ , is then the negative gradient of the potential function,  $\phi$ :

$$B = - \nabla \phi = - \frac{m}{r^3} [2 \sin \gamma e_r - \cos \gamma e_\gamma] \quad (30)$$

where  $e_r$  and  $e_\gamma$  are the unit vectors directed along the vector  $r$  and normal to  $r$  in latitudinal direction. For the earth's magnetic field, the value of



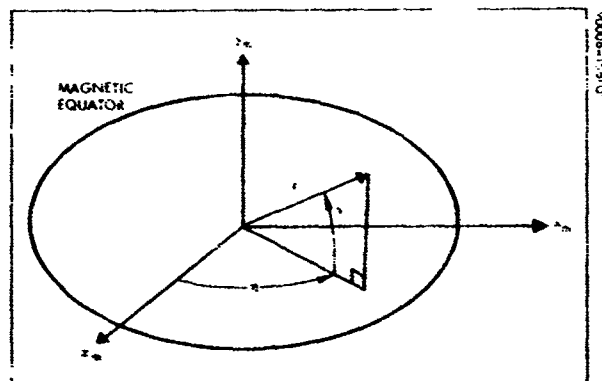


Figure 129. Magnetic Cartesian and Spherical Coordinates

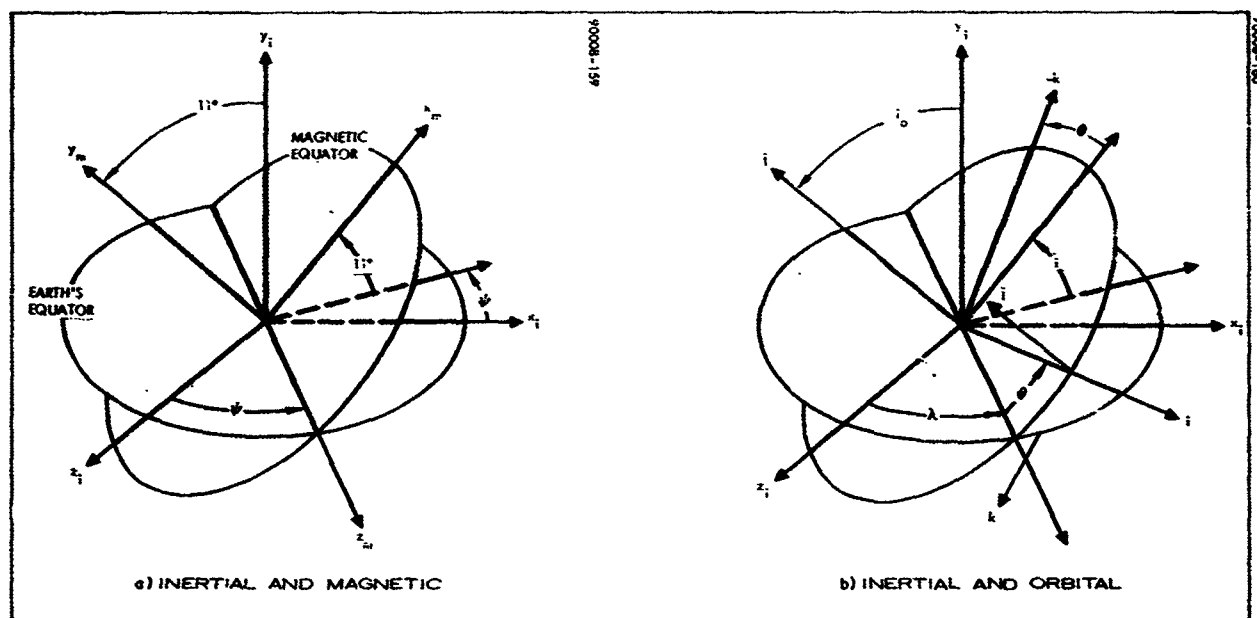


Figure 130. Coordinate Systems

$m$  is  $1.28 \times 10^{-6}$ , which gives the field in webers per square meter for  $r$  in nautical miles. The magnitude of the magnetic field,  $B$ , is given by:

$$|B| = \frac{m}{r^3} \sqrt{1 + 3 \sin^2 \gamma} \quad (31)$$

As seen from Equation 31, the magnetic field magnitude for a circular orbit increases as the geomagnetic latitude increases, and for a geomagnetic polar orbit, the maximum value is twice the magnitude of a geomagnetic equatorial orbit.

The position of a satellite relative to the  $x_m y_m z_m$  set may be defined in terms of the geomagnetic latitude,  $\gamma$ , and the geomagnetic longitude,  $\eta$ , as shown in Figure 129. Then, the transformation of vectors from the  $x_m y_m z_m$  set to the geomagnetic spherical set  $\eta \gamma r$  is given by:

$$\begin{pmatrix} e_r \\ e_\gamma \\ e_\eta \end{pmatrix} = C \begin{pmatrix} x_m \\ y_m \\ z_m \end{pmatrix} \quad (32)$$

where  $e_\eta$ ,  $e_\gamma$ ,  $e_r$ ,  $x_m$ ,  $y_m$ , and  $z_m$  are unit vectors and where

$$C = \begin{pmatrix} \cos \eta & 0 & -\sin \eta \\ -\sin \gamma \sin \eta & \cos \gamma & -\sin \gamma \cos \eta \\ \cos \gamma \sin \eta & \sin \gamma & \cos \gamma \cos \eta \end{pmatrix} \quad (33)$$

and

$$C^{-1} = C^T = \text{transpose of } C$$

The magnetic field, B, as expressed in Equation 30, may be transformed to the  $x_m, y_m, z_m$  coordinate system by the inverse of the transformation indicated in Equation 32. Thus

$$\begin{pmatrix} B_{xm} \\ B_{ym} \\ B_{zm} \end{pmatrix} = -\frac{m}{r^3} \begin{pmatrix} 3 \sin \gamma \cos \gamma \sin \eta \\ 3 \sin^2 \gamma - 1 \\ 3 \sin \gamma \cos \gamma \cos \eta \end{pmatrix} \quad (34)$$

In Section 3.6, the matrix transformations relating those coordinate systems are developed. In general terms,

$$\begin{pmatrix} x_i \\ y_i \\ z_i \end{pmatrix} = H \begin{pmatrix} x_m \\ y_m \\ z_m \end{pmatrix}$$

$$\begin{pmatrix} i \\ j \\ k \end{pmatrix} = G \begin{pmatrix} x_i \\ y_i \\ z_i \end{pmatrix}$$

Thus

$$\begin{pmatrix} i \\ j \\ k \end{pmatrix} = K \begin{pmatrix} x_m \\ y_m \\ z_m \end{pmatrix} \quad K = GH \quad (35)$$

From the definition of the magnetic spherical coordinates  $\eta\gamma r$  in Figure 129 and the orbital coordinates  $ijk$  in Figure 130b, it can be seen that

$$i = e_r$$

From Equations 32, 33, and 35,

$$\begin{aligned} e_r &= x_m \cos \gamma \sin \eta + y_m \sin \gamma + z_m \cos \gamma \cos \eta \\ &= k_{11}x_m + k_{12}y_m + k_{13}z_m = 1 \end{aligned}$$

Thus

$$\begin{aligned} k_{11} &= \cos \gamma \sin \eta \\ k_{12} &= \sin \gamma \\ k_{13} &= \cos \gamma \cos \eta \end{aligned} \quad (36)$$

From these equations,  $\gamma$  and  $\eta$  can be determined as functions of the orbital parameters  $\psi$ ,  $\theta$ ,  $i$ , and  $\lambda$ . From Equations 34 and 36,

$$\begin{pmatrix} B_{xm} \\ B_{ym} \\ B_{zm} \end{pmatrix} = -\frac{m}{r^3} \begin{pmatrix} 3k_{11}k_{12} \\ 3k_{12}^2 - 1 \\ 3k_{12}k_{13} \end{pmatrix} \quad (37)$$

and from Equation 35

$$\begin{pmatrix} B_i \\ B_j \\ B_k \end{pmatrix} = K \begin{pmatrix} B_{xm} \\ B_{ym} \\ B_{zm} \end{pmatrix} \quad (38)$$

and so combining Equations 37 and 38

$$\begin{aligned} B_i &= -\frac{m}{r^3} (3k_{11}^2 k_{12} + 3k_{12}^3 - k_{12} + 3k_{12}k_{13}^2) \\ B_j &= -\frac{m}{r^3} (3k_{11}k_{12}k_{21} + 3k_{12}^2 k_{22} - k_{22} + 3k_{12}k_{13}k_{23}) \\ B_k &= -\frac{m}{r^3} (3k_{11}k_{12}k_{31} + 3k_{12}^2 k_{32} - k_{32} + 3k_{12}k_{13}k_{33}) \end{aligned} \quad (39)$$

These expressions can be simplified by observing that the matrix  $K$  is a direction cosine matrix, i. e., a coordinate system rotation matrix, and hence is orthogonal which means that

$$KK^T = I \text{ (unit matrix)}$$

From this property, several useful relationships follow, namely

$$K^T = K^{-1}$$

$$\sum_{i=1}^3 k_{ij}k_{ip} = \sum_{i=1}^3 k_{ji}k_{pi} = \delta_{jp} = \begin{cases} 1 & j = p \\ 0 & j \neq p \end{cases}$$

Then from Equation 39

$$B_i = -\frac{m}{r^3} \left[ 3k_{12}(k_{11}^2 + k_{12}^2 + k_{13}^2) - k_{12} \right] = -2k_{12} \frac{m}{r^3} \quad (40)$$

$$B_j = -\frac{m}{r^3} \left[ 3k_{12}(k_{11}k_{21} + k_{12}k_{22} + k_{13}k_{23}) - k_{22} \right] = k_{22} \frac{m}{r^3} \quad (41)$$

$$B_k = -\frac{m}{r^3} \left[ 3k_{12}(k_{11}k_{31} + k_{12}k_{32} + k_{13}k_{33}) - k_{32} \right] = k_{32} \frac{m}{r^3} \quad (42)$$

And from Section 3.6, it can be shown that

$$\begin{aligned} k_{12} &= s_m \left[ \cos \theta \sin (\psi - \lambda) - \cos i \sin \theta \cos (\psi - \lambda) \right] + c_m \sin i \sin \theta \\ k_{22} &= c_m \cos i + s_m \sin i \cos (\psi - \lambda) \\ k_{32} &= s_m \left[ \cos i \cos \theta \cos (\psi - \lambda) + \sin \theta \sin (\psi - \lambda) \right] - c_m \sin i \cos \theta \end{aligned} \quad (43)$$

where

$$\begin{aligned} c_m &= \cos 11^\circ \approx 0.9816 \\ s_m &= \sin 11^\circ \approx 0.1908 \end{aligned}$$

The field components can be investigated using Equation 43.

It can be seen that for  $\sin \theta = 0$  and  $\sin (\psi - \lambda) = 0$ ,  $k_{12} = 0$  and thus  $B_i = 0$ . If

$$\sin \theta = \frac{c_m}{\sin i} \left( \begin{array}{c} c_m \leq \sin i \\ \text{or} \\ 73^\circ \leq i \leq 107^\circ \end{array} \right) \quad (44)$$

and

$$\cos \theta \sin (\psi - \lambda) - \cos i \sin \theta \cos (\psi - \lambda) = s_m$$

which implies that

$$\tan \psi = -\frac{\cot \theta}{\cos i} = \left( \frac{\sin^2 i}{c_m^2} - 1 \right)^{1/2} \sec i$$

Then

$$k_{12} = 1$$

and

$$B_i = 2 \frac{m}{r^3}$$

$$B_j = B_k = 0$$

Clearly by the above analysis, the minimum value for the magnitude of  $B_j$  is zero and the maximum occurs when

$$\cos (\psi - \lambda) = \text{sign of } \tan i$$

where

$$|k_{22}| = \left| \cos \left[ 11^\circ - i (\text{sign } \tan i_o) \right] \right|$$

For sun-synchronous orbits where  $i \approx 99.5$  degrees

$$|k_{22}| \approx |\cos(116.5^\circ)| \approx 0.45$$

The  $B_k$  component has a minimum magnitude of zero under the conditions of Equation 44 or if  $\cos \theta = 0$ ,  $\sin(\psi - \lambda) = 0$ , then  $B_k = k_{32} = 0$ . When

$$\cos \theta \sin i = -c_m$$

$$\cos i \cos \theta \cos(\psi - \lambda) - \sin \theta \sin(\psi - \lambda) = s_m$$

Then

$$k_{32} = 1 \text{ and } B_k = \frac{m}{r^3}, \quad B_j = B_i = 0$$

#### 7.5.2 Magnetic Control Concepts

The earth's magnetic field,  $B$ , will interact with a magnetic moment,  $M$ , which may be generated by currents or magnetized material, to produce a torque,  $T$ . All three quantities are vectors and the relationship between them is given by

$$T = M \times B \quad (45)$$

Suppose now that the spacecraft sensors and associated processing indicate that a control torque,  $T_c$ , should be applied to correct the vehicle's attitude. Consider the following vector operation involving  $T_c$ ; using Equation 45

$$B \times T_c = B \times (M \times B) \quad (46)$$

A useful vector identity yields

$$B \times (M \times B) = |B|^2 M - B (M \cdot B) \quad (47)$$

From Equation 45, it can be seen that the torque produced by the interaction of  $B$  and  $M$  is normal to both  $M$  and  $B$  and that the only component of  $M$  having any effect is that component normal to  $B$ . Thus, there is no advantage to be gained by having any component of  $M$  parallel to  $B$ ; and in fact if there is a parallel component, the power required to produce it is wasted. The conclusion here is that  $M$  should be generated normal to  $B$ , i. e.,

$$M \cdot B = 0 \quad (48)$$

Substituting Equation 48 into 47 and Equation 47 into 46, a control law for  $M$  is established:

$$M = \frac{1}{|B|^2} (B \times T_c) \quad (49)$$

The actual torque produced is obtained by substituting from Equation 49 into 45, yielding

$$T = \frac{1}{|B|^2} [(B \times T_c) \times B] = T_c - \frac{1}{|B|^2} (B \cdot T_c) B \quad (50)$$

Equation 50 indicates that the actual torque produced is not in the desired  $T_c$  direction unless  $T_c$  is normal to  $B$ , i. e.,  $B \cdot T_c = 0$ . Thus, the generated torque has a component  $T_d$  in the desired direction as well as an undesired component  $T_u$ . These vector relationships are illustrated in Figure 131 where it can be seen that.

$$T_d = |T| \cos \delta = \frac{T \cdot T_c}{|T_c|}$$

Using Equation 50 above

$$T_d = \frac{1}{|T_c|} \left[ (T_c \cdot T_c) - \frac{1}{|B|^2} (B \cdot T_c)^2 \right] = |T_c| \sin^2 \delta$$

and from Figure 131

$$T_u = T_d \cot \delta = |T_c| \sin \delta \cos \delta$$

Thus, both  $T_d$  and  $T_u$  approach zero as  $\delta$  approaches zero, but  $T_d \rightarrow T_c$  as  $\delta \rightarrow 90$  degrees, whereas  $T_u \rightarrow 0$  as  $\delta \rightarrow 90$  degrees.

Assuming that the attitude of the spacecraft is controlled so that the xyz body axes very nearly coincide with the ijk orbit axes, Equation 49 can be rewritten

$$\begin{bmatrix} M_x \\ M_y \\ M_z \end{bmatrix} = \frac{1}{|B|^2} \begin{bmatrix} B_y T_{cz} - B_z T_{cy} \\ B_z T_{cx} - B_x T_{cz} \\ B_x T_{cy} - B_y T_{cx} \end{bmatrix} \quad (51)$$



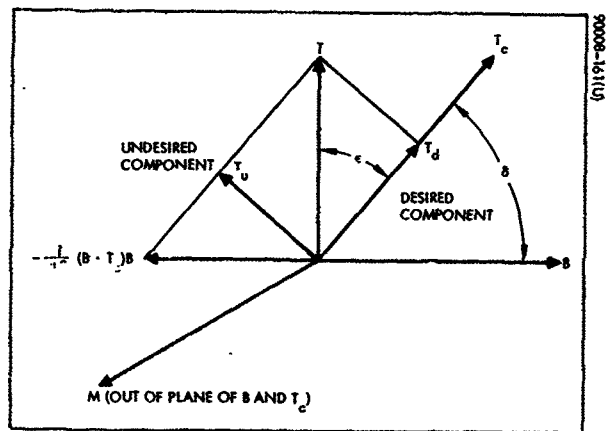


Figure 131. Vector Relationships  
With Magnetic Torque Control Law

If these magnetic moments are generated by currents in coils, as is discussed later, and

$$M_j = \frac{i_j}{L_j} \quad j = x, y, z$$

Then, the control currents are given by

$$\begin{aligned} i_x &= \frac{L_x}{|B|^2} (B_y T_{cz} - B_z T_{cy}) \\ i_y &= \frac{L_y}{|B|^2} (B_z T_{cx} - B_x T_{cz}) \\ i_z &= \frac{L_z}{|B|^2} (B_x T_{cy} - B_y T_{cx}) \end{aligned} \quad (52)$$

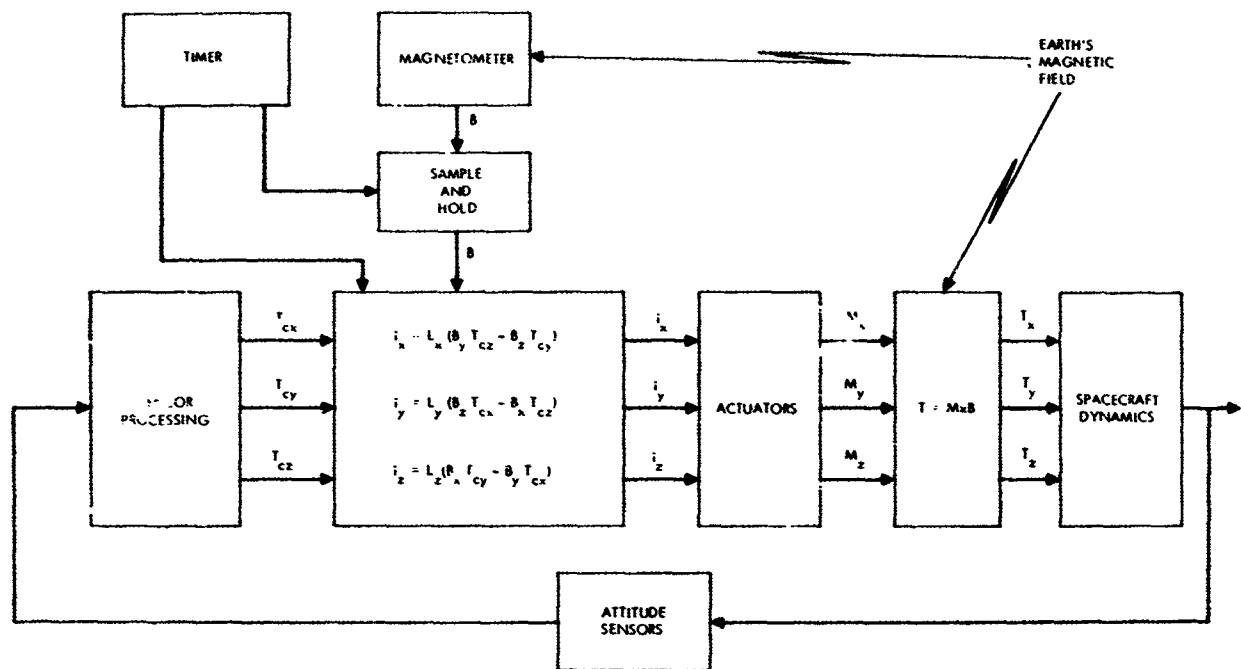
### 7.5.3 Implementation

A fundamental problem in implementing magnetic torque control is the determination of the earth's magnetic field. When the control currents  $i_x$ ,  $i_y$ ,  $i_z$  are flowing, the magnetic field near the spacecraft is altered so that correct measurements of the earth's magnetic field are difficult to obtain. This problem can be overcome in two ways: 1) shield the magnetometer (magnetic field sensor) from the spacecraft's magnetic field or place it on an extended boom out of the influence of the spacecraft's magnetic field or 2) turn off the currents periodically and make the measurements, then activate the current controllers based upon the just-sampled field measurements.

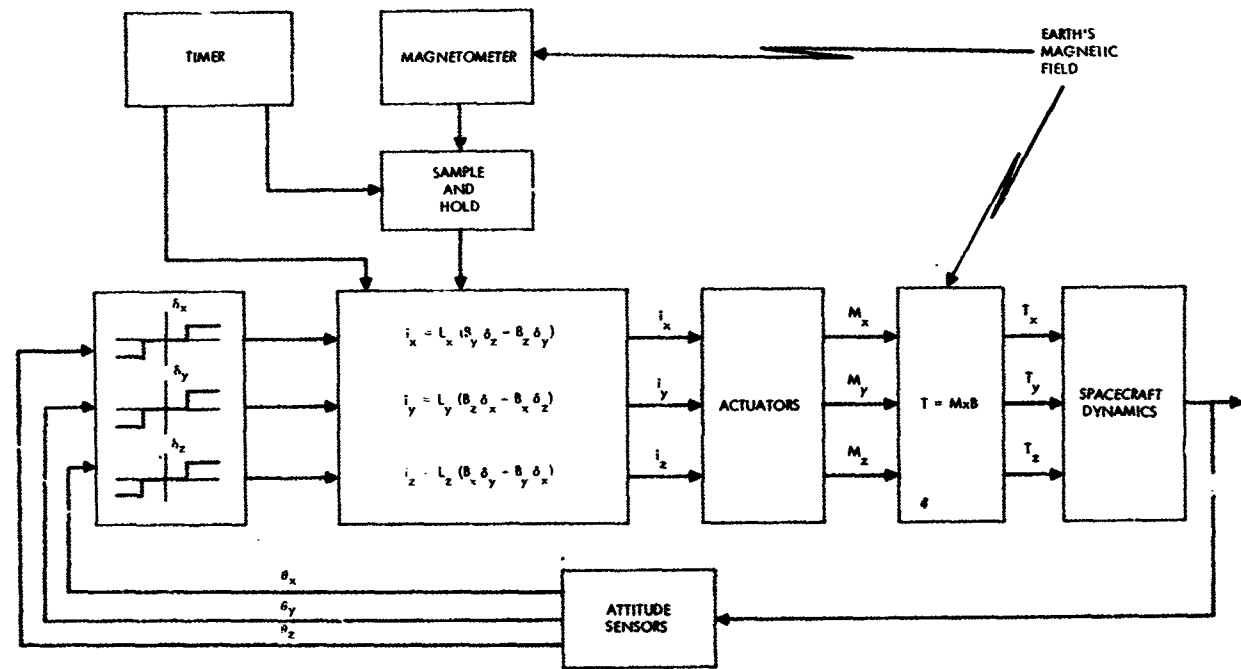
The latter method requires some timing and switching circuits, but eliminates the possibly even greater problems of mechanical extension and structural design necessary for isolating the magnetometer. Even with the extended sensor, the isolation is not complete.

In Equations 51 and 52,  $|B|^2$ , the square of the magnitude of the field vector, appears in the denominator. Evaluating  $|B|^2$  requires a complex computation, which, though not extremely difficult to mechanize electronically, is preferably eliminated. If  $|B|^2$  in Equations 50, 51, and 52 is replaced by a constant, then only the magnitude of  $M$  is affected. Then in Equation 52, for instance, the currents will depend on the magnitude of the field components. Since  $|B|$  varies by a factor of 2, the maximum value of the components will not vary by more. Thus, the result of replacing the  $|B|^2$  term in the magnetic moment and control current equations by a constant is a variable gain system with at most a gain variation of two.

90008-16210



a) CONTROL LAW SYSTEM



$\delta_i = -1, 0, 1 \quad (i = x, y, z)$

b) SIMPLIFIED SYSTEM (MULTIPLICATIONS ELIMINATED)

Figure 132. Magnetic Torquing Systems

But, inasmuch as the magnetic field components about each axis may vary from zero to some maximum values during an orbit, this additional variation is not critical. If the gain constants  $L_x$ ,  $L_y$ ,  $L_z$  absorb the  $|B|^2$  term, Equation 52 becomes

$$\begin{aligned} i_x &= L_x (B_y T_{cz} - B_z T_{cy}) \\ i_y &= L_y (B_z T_{cx} - B_x T_{cz}) \\ i_z &= L_z (B_x T_{cy} - B_y T_{cx}) \end{aligned} \quad (53)$$

A mechanization of a control system with a sampled magnetic field is shown in Figure 132a. In this diagram, the sensor processor is merely three amplifier circuits. The controller performs the multiplications and subtractions of Equation 53. This system can be even further simplified if the signal processor is an on-off device with a dead zone. In this case, the multiplications are eliminated, and the control torque signals  $T_{cx}$ ,  $T_{cy}$ ,  $T_{cz}$  are on-off switching signals. Such a system is shown in Figure 132b.

#### 7.5.4 Control Capability

Mission requirements will determine the necessary control capability in terms of angular rates and pointing accuracy. Pure magnetic control suffers from the fact that there are times when no control torque in the desired direction is possible due to the orientation of the spacecraft with respect to the earth's magnetic field.

A careful examination of Equations 40 through 42 will indicate the variation of the magnetic field component perpendicular to the control axes. This analysis is quite complex, but some assumptions can be made. Near the point where a transverse field component is zero, the maximum variation will be at approximately the LAS orbital frequency, while the worst that could occur is a variation with earth rotation frequency.

However, it is possible to perform an analysis using a general frequency  $\omega$  and assuming that the variation of the transverse field component near its zero varies sinusoidally with this frequency. Later, applicable values of  $\omega$  can be substituted in the resulting expressions.

Considering torque about one of the body axes, from Equation 45 the maximum available torque at any moment is given by

$$T = M_{\max} B_{\perp}$$

where  $M_{\max}$  is the upper limit of available magnetic moment along that axis. Since by the above assumption,  $B_{\perp} = (B_{\perp})_{\max} \sin \omega t$ , and so

$$T = T_m \sin \omega t$$

where

$$T_m = M_{\max} (B_{\perp})_{\max}$$

If the disturbance torque,  $T_d$ , is assumed constant for a period during which the maximum available torque becomes zero, then an estimate of vehicle angular rate and pointing error can be made. The angular acceleration is given by

$$\ddot{\theta} = \frac{1}{I} (T_d - T_m |\sin \omega t|)$$

where  $I$  is the moment of inertia, and  $T_d$  the disturbance torque. And if it is assumed that the angular velocity is zero until  $t$  seconds before the available torque becomes zero, then

$$\dot{\theta} = \frac{1}{I} \int_{-t}^t (T_d - T_m |\sin \omega s|) ds = \frac{2T_d}{\omega I} \left[ \omega t - \frac{T_m}{T_d} (1 - \cos \omega t) \right] \quad (54)$$

The maximum angular velocity occurs where  $\ddot{\theta} = 0$ , i. e., where

$$\omega t = \sin^{-1} \left( \frac{T_d}{T_m} \right) \quad (55)$$

Substituting Equation 55 into Equation 54

$$\dot{\theta}_m = \frac{2T_d}{\omega I} \left\{ \sin^{-1} \left( \frac{T_d}{T_m} \right) + \frac{T_m}{T_d} \left[ 1 - \left( 1 - \frac{T_d^2}{T_m^2} \right)^{1/2} \right] \right\} \quad (56)$$

The angular deviation is found from Equation 54 by integration

$$\theta = \frac{2T_d}{\omega I} \left[ \frac{\omega t^2}{2} + \frac{T_m}{T_d} \left( \frac{\sin \omega t}{\omega} - t \right) \right] \quad (57)$$

The maximum angular deviation occurs at  $t_m$  when  $\dot{\theta} = 0$ , that is, when

$$\omega t_m + \frac{T_m}{T_d} (\cos \omega t_m - 1) = 0 \quad (58)$$

For convenience, the following definitions will be made:

$$\alpha = \omega t_m \text{ and } \beta = \frac{T_d}{T_m}$$

It can be seen from Equation 58 that  $\alpha$  is the solution to

$$\alpha \beta + \cos \alpha - 1 = 0 \quad (59)$$

and the maximum angular deviation is found by substituting this value into Equation 57 to yield

$$\theta_m = \frac{.2T_d}{\omega^2 I} G(\beta)$$

where

$$G(\beta) = \frac{\alpha^2}{2} + \frac{1}{\beta} (\sin \alpha - \alpha)$$

with  $\alpha$  the solution to Equation 59. With this notation, Equation 56 becomes

$$\dot{\theta} = \frac{2T_d}{\omega I} H(\beta)$$

where

$$H(\beta) = \sin^{-1}(\beta) + \frac{1}{\beta} \left[ (1 - \beta^2)^{1/2} - 1 \right]$$

It can be shown that for Equation 59 to have a solution other than  $\alpha = 0$

$$|\beta| \leq 0.724611$$

The factors  $G(\beta)$  and  $H(\beta)$  are plotted in Figures 133 and 134, respectively.

It can be shown that for a small value of  $\beta$

$$G(\beta) \approx \frac{2}{3} \beta^2 \quad H(\beta) \approx \frac{\beta}{2}$$

For  $\beta$  less than 0.3, the above approximations are in error less than 4 percent and 0.8 percent, respectively. It is expected that to ensure control capability the system will be designed such that  $T_m \geq 5T_d$  or  $\beta \leq 0.2$ . Thus, the above approximation can be used for estimating the angular rate and pointing error.

$$\begin{aligned} \theta_m &\approx \frac{4T_d \beta^2}{3I \omega} \text{ radians} \\ \dot{\theta}_m &\approx \frac{T_d \beta}{I \omega} \text{ rad/sec} \end{aligned} \tag{60}$$

For a quantitative example, assume that  $\omega$  is equal to the orbital angular velocity which for orbital altitudes of 300 to 500 n.mi. has the approximate value  $10^{-3}$  rad/sec. For a spacecraft weighing 1000 pounds, moments of inertia in the vicinity of 300 slug-ft<sup>2</sup> can be expected; and the disturbance torque will be taken as the rss total calculated in Section 7.4.3 ( $8.5 \times 10^{-5}$  ft-lb). Let  $\beta = 0.1$ , then for these values

$$\begin{aligned} \theta_m &\approx 0.22 \text{ degree} \\ \dot{\theta}_m &\approx 1.63 \times 10^{-4} \text{ deg/sec} \end{aligned}$$

However, for many orbits, the rate of change of available torque is much less than that corresponding to orbital angular velocity.

In particular, for a sun-synchronous orbit, it can be shown that for significant portions of the LAS orbit the angular rate of change of the magnetic field vector with respect to the spacecraft is less than  $3 \times 10^{-5}$  rad/sec. Using this value for  $\omega$ , along with the above assumed quantities, Equation 60 yields

$$\theta_m \approx (2.4 \times 10^4) \beta^2 \text{ degrees}$$

A brief analysis indicates that for power and weight of the system to be kept less than 40 pounds and 30 watts, respectively,  $\beta$  must be greater than about 0.01. With this limit, the pointing error will be 2.4 degrees. For earth observation, an error this large will be unacceptable.

Since  $\beta = T_d/T_m$ , it may be noted that if  $T_m$  is fixed due to weight and power limitations then the pointing error is proportional to  $T_d^3$ , i.e., the pointing accuracy is very sensitive to the disturbance torque. The value of disturbance torque used above was only an approximation based on many assumptions (see Section 7.3). If by careful design the disturbance torque can be reduced below this value, a magnetic control system may provide the required pointing accuracy.

Since the pointing accuracy depends so critically on the disturbance torque, and since the satellite will have a solar array resulting in relatively large disturbance torques, it appears that a design with adequate safety margin would be excessively heavy or require large power. However, as can be demonstrated, combined with other attitude control concepts, magnetic torquing capability can be useful and attractive. The general analysis of the previous sections is applicable to other dual-mode control systems using magnetic torques.

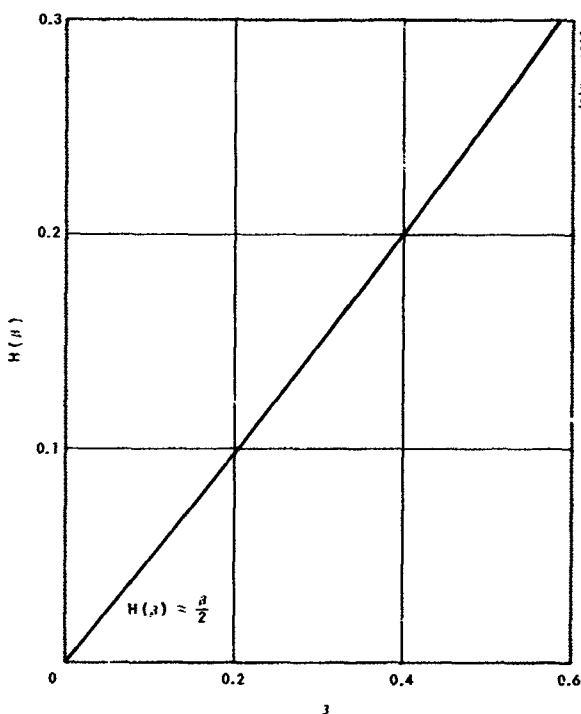


Figure 133.  $G(\beta)$  Versus  $\beta$

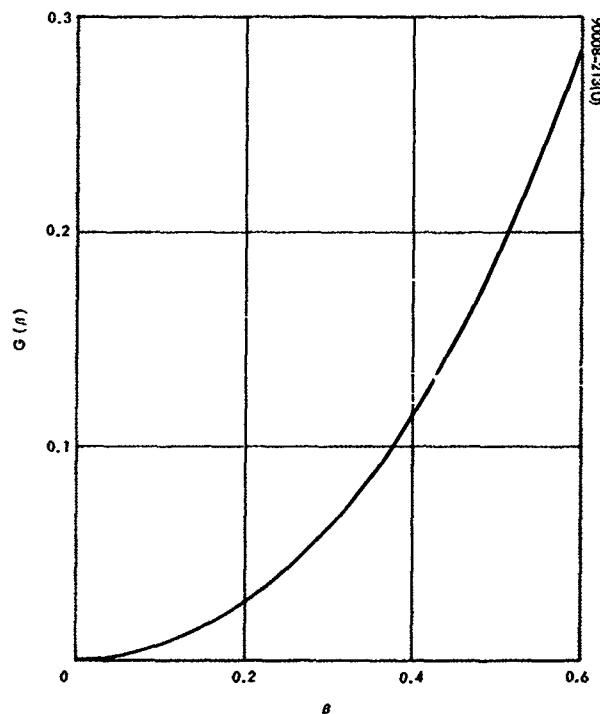


Figure 134.  $H(\beta)$  Versus  $\beta$



## 7.6 MASS EXPULSION CONTROL

Attitude control torques can be produced by expelling mass from the spacecraft, resulting in torque producing reactive forces. Since the mass is usually a gas expelled through a nozzle, this type of system is frequently referred to as a reaction jet system. The two expressions will be used here interchangeably. Similarly gas, propellant, or fuel refer to the expelled substance.

### 7.6.1 Specific Impulse and Propellants

One of the most important characteristic quantities of a propellant is its specific impulse,  $I_{sp}$ , defined by

$$W_F I_{sp} = \int_0^t F dt \quad (61)$$

where  $F$  is the force produced and  $t$  is the time required to expel  $W_F$  pounds of fuel. This quantity appears in any analysis of a mass expulsion system. Choice of attitude control propellants is at present essentially limited to cold gas ( $N_2$ ), hydrogen peroxide ( $H_2O_2$ ), and hydrazine ( $H_2N_2$ ).

Precise attitude control requirements necessitate very small total impulse per correction. For example, hydrazine cannot be used in a conventional manner because to perform properly, jet burn time must exceed 0.05 second at a thrust level greater than 0.1 pound. Otherwise, hydrazine has insufficient time on the catalyst bed and does not burn. This means that the minimum impulse available from hydrazine imparts a minimum  $\theta$  to a 100 slug-ft<sup>2</sup> vehicle of approximately 0.01 deg/sec.

It may be possible to use hydrazine in a different form. Hughes has developed a dual-mode hydrazine control system wherein stationkeeping is accomplished by hydrazine thrusting in the normal manner in the few pound region, while electrolyzed hydrazine is thrusting in the millipound region with an  $I_{sp} = 125$  seconds for attitude control. The electrolyzed hydrazine jet thruster has been laboratory tested but has not yet been space-proven.

Nitrogen as a cold gas is conventional for attitude control, but its low  $I_{sp} = 60$  seconds is inefficient from a weight viewpoint, as will be indicated later.

The high specific impulse of hydrogen peroxide (160 seconds) is very desirable. The main objection to its use is the contamination problem. The slightest impurity causes formation of oxygen, even in the tank, which causes tank pressure to increase.

### 7.6.2 Minimum Fuel Consumption

Minimum fuel consumption can be attained by continuously thrusting with a force sufficient to create a torque on the vehicle equal to the disturbance torque. Suppose it were possible to construct a system to provide this continuous control. If  $r$  is the moment arm for the expulsion nozzles, then

$$T_d = Fr = \text{disturbance torque} \quad (62)$$

Substituting in Equation 61 and rearranging

$$W_F = \frac{1}{r I_{sp}} \int_0^t T_d dt \quad (63)$$

If  $T_d$  is constant, this becomes

$$W_F = \frac{T_d t}{r I_{sp}} \quad (64)$$

If  $T_d = 8.5 \times 10^{-5}$  ft-lb, the rss total of the disturbance torques estimated in Section 7.3, and if  $r = 2.5$  feet, a reasonable value based on the shroud dimensions of Figure 5, then

$$R_F \equiv \text{fuel rate} \equiv \frac{W_F}{t} = \frac{1070}{I_{sp}} \frac{\text{lb}}{\text{year}}$$

Where the unit of  $I_{sp}$  is seconds. Thus, for  $I_{sp} = 100$  seconds

$$R_F = 10.7 \text{ lb/year} \quad (65)$$

### 7.6.3 Impulsive Systems

Continuous control is not possible with the conventional gas systems mentioned above because there is a lower limit to the thrust available, and values of torque in the range of the disturbance torque cannot be efficiently produced. Torques several orders of magnitude greater are applied for very short periods of time resulting in step changes in the angular velocity.

The integral on the right side of Equation 61 is defined as the thrust impulse for an on-time of  $t$  seconds. The torque impulse is merely

$$I_T = r \int_0^t F dt \quad (66)$$

From Newton's second law

$$r \int_0^t F dt = \int_0^t I \frac{d\omega}{dt} dt = \int_{\omega_1}^{\omega_2} I d\omega = I\Delta\omega \quad (67)$$

where  $I$  is the moment of inertia. But this also applies for the disturbance torque in place of  $rF$ . Consider then the one-sided limit cycle shown in Figure 135. The disturbance torque causes motion corresponding to the curve BCA. When the attitude deviation reaches the deadband limit, a torque impulse is applied over a relatively short time (milliseconds) exactly compensating the disturbance torque impulse imparted during the longer BCA portion of the limit cycle.

That is,

$$\int_0^{t_{AB}} rF dt = \int_0^{t_{BCA}} T_d dt \quad (68)$$

and since  $t_{AB} \ll t_{BCA}$ , Equations 63 and 64 are valid here. Thus, the one-sided limit cycle, with impulsive torques, uses minimum fuel.

But consider now the two-sided, hard-limit cycle shown in Figure 136. For constant thrust Equation 67 yields

$$I_T = rF t_{on} = I\Delta\omega = 2I\dot{\theta} \quad (69)$$

at each end of the limit cycle. For a full limit cycle

$$4I\dot{\theta} = W_F I_{sp} \quad (70)$$

$$\dot{\theta} t_{off} = 4\theta_o \quad (71)$$

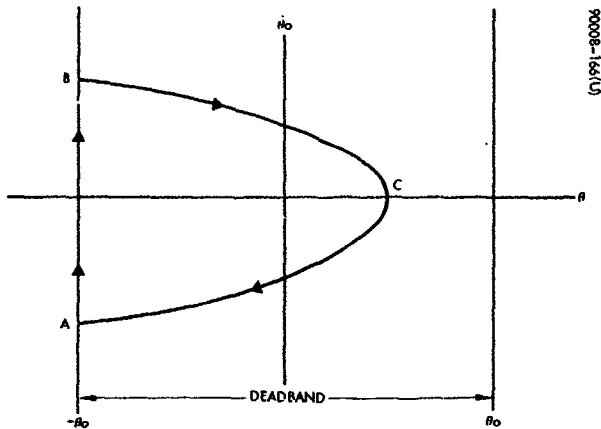


Figure 135. One-Sided Limit Cycle

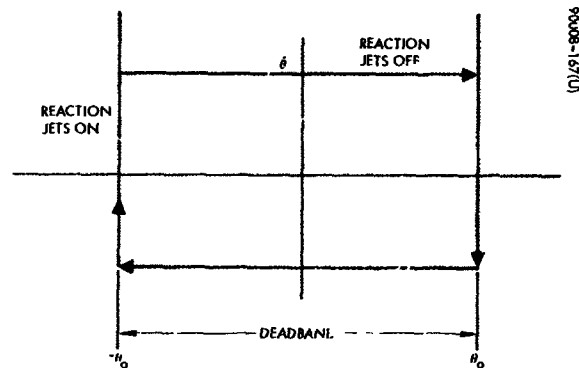


Figure 136. Two-Sided, Hard Limit Cycle

Since  $t_{\text{off}} \gg t_{\text{on}}$ ,  $t_{\text{off}} = t$ . Then, from Equations 70 and 71

$$R_F = \frac{W_F}{t} = \frac{I \dot{\theta}^2}{I_{sp} \theta_0} \text{ lb/sec} \quad (72)$$

or using the identity  $I_T = 2 I \dot{\theta}$

$$R_F = \frac{W_F}{t} = \frac{I_T^2}{4 I_{sp} I \theta_0} \text{ lb/sec} \quad (73)$$

From Equation 73, for this case, the fuel rate is proportional to the square of the torque impulse and inversely proportional to the deadband. The disturbance torque does not appear as a factor because, by the very nature of the hard-limit cycle, the disturbance torque has been overpowered and "swamped out."

As an example let  $I = 200 \text{ slug-ft}^2$ ,  $I_{sp} = 100 \text{ seconds}$ ,  $\theta_0 = 0.1 \text{ deg} = 0.00175 \text{ rad}$ , and let the torque impulse be chosen to  $\dot{\theta} = 0.01 \text{ deg/sec} = 1.75 \times 10^{-4} \text{ rad/sec}$ . Then from Equation 72,

$$R_F = 3.5 \times 10^{-5} \text{ lb/sec} \approx 1100 \text{ lb/year} \quad (74)$$

#### Comment

It can be seen that there is a considerable difference between this fuel rate and that given by Equation 65. The disturbance torques may vary over a wide range about any given spacecraft attitude control axis, making it

difficult to design for one-sided limit cycle operation. But from Equation 73 and the discussion of Section 7.6.2, the torque impulse should be made as small as possible consistent with the requirement that the system be able to cope with all disturbances.

#### 7.6.4 System Implementation

Figure 137 shows a typical reaction jet control system utilizing a dual-mode hydrazine reaction control system. The catalytic thrusters are used primarily for removal of injection errors. The remaining gas jets with much lower thrust rating are used for normal attitude and velocity maneuvers to obtain more precise control. The catalytic thrusters are the 5-pound thrusters developed for the ATS program, and the gas jets of about 100-millipound thrust are modifications of available designs.

The control of all axes is performed on board the spacecraft, which requires the use of a yaw reference gyro and a sun sensor to recalibrate the gyro periodically. It is a conceptually simple system with no development problems associated with it, but in comparison with the MBS Type 1 is slightly more complex (seven thrusters versus two, sun sensor, yaw gyro, nonspinning earth sensor) and less reliable. Also, since the fuel required is a function of the desired pointing accuracy (see Equations 72 and 73), the growth to more precise pointing missions is hampered with this system.

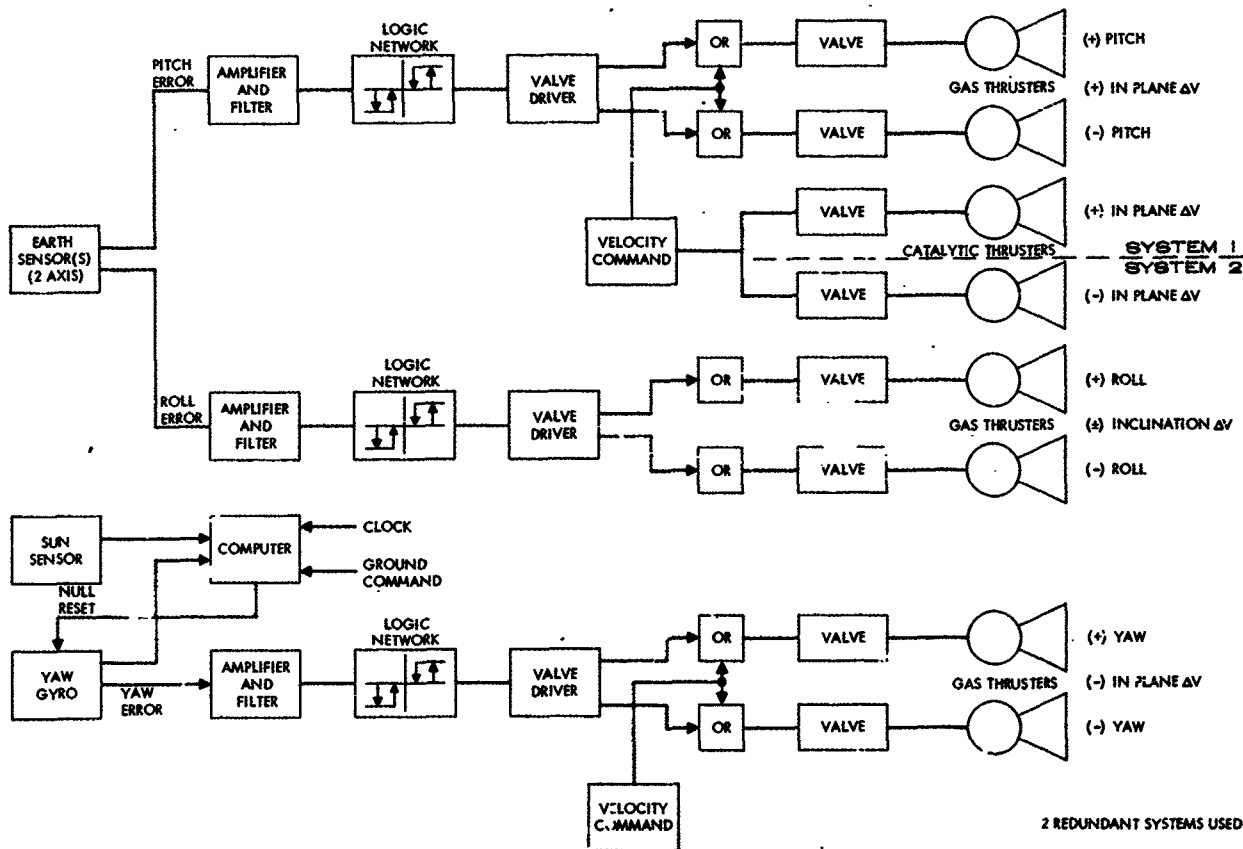


Figure 137. Mass Expulsion Control Block Diagram

## 7.7 REACTION WHEEL STABILIZATION

In many satellites actually launched or still being designed, flywheels are part of the stabilization system. The Nimbus weather-observation satellite uses three of these devices, one for each axis. Fine control of the Orbiting Astronomical Observatory's attitude is also obtained by means of flywheels.

To bring out the salient points of this method of control, a satellite is assumed to be provided with three flywheels, each oriented along one of the satellite's principal axes. The moment of inertia of a flywheel about its own axis of rotation is  $I$ ; the angular velocities of the flywheels relative to the satellite are  $\omega_x$ ,  $\omega_y$ , and  $\omega_z$  (Figure 138).

Euler's equations of motion now have to be slightly modified to allow for the presence of the flywheels. A derivation of these equations is based on the simple fact that the action of the flywheels does not change the total angular momentum of the combination of the satellite and the flywheels. The latter can merely interchange the angular momentum between the satellite and themselves.

$$M_x = I_x \dot{p} + (I_z - I_y) qr + I(\dot{\omega}_x + \omega_z q - \omega_y r)$$

$$M_y = I_y \dot{q} + (I_x - I_z) rp + I(\dot{\omega}_y + \omega_x r - \omega_z p)$$

$$M_z = I_z \dot{r} + (I_y - I_x) pq + I(\dot{\omega}_z + \omega_y p - \omega_x q)$$

In these equations,  $I_x$ ,  $I_y$ , and  $I_z$  include the contribution due to the mass of the flywheels. The ratio of the moments of inertia of the flywheel and the satellite may be very small, however, in the order of  $10^{-5}:1$ .

From the above equations, it can be seen that the influence of an external torque ( $M_x$ ,  $M_y$ ,  $M_z$ ) can be compensated by an appropriate change in the angular acceleration of one or more of the flywheels. In principle, the satellite's attitude or angular velocities need not change if the external torque could be measured directly. The flywheels can thus be considered as a means to isolate the satellite from disturbing torques. In practice, the satellite is stabilized in a certain attitude by making the flywheel's acceleration depend on the satellite's deviation from the desired attitude, as well as on the rates of change of these deviations.

A simplified block diagram of a single-axis control system using a flywheel is shown in Figure 139.

The modified Euler's equations also indicate that, in the general case, a change in angular velocity of one flywheel may have a rather complicated influence on the motions about the other axes. This disadvantage is avoided if a single inertia sphere is employed, instead of three inertia wheels.

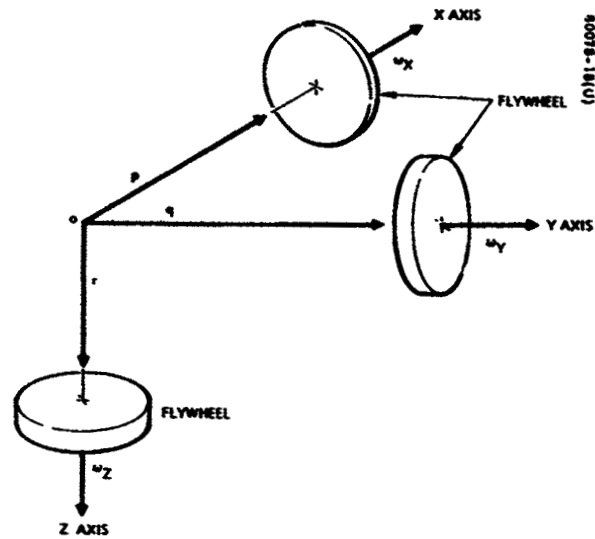


Figure 138. Simplified Arrangement of Flywheels

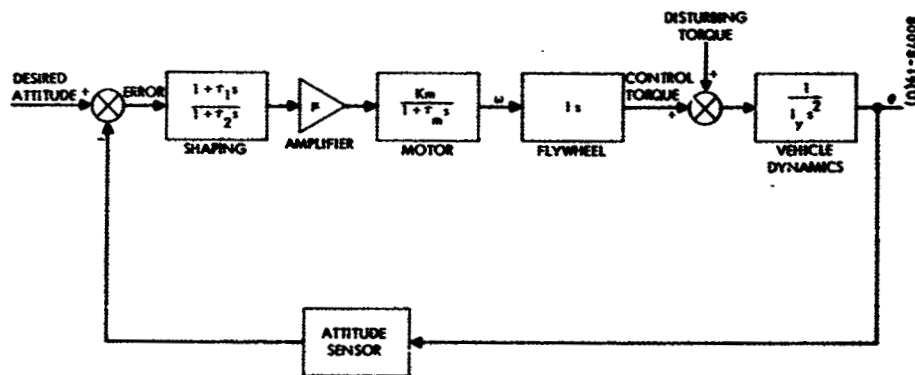


Figure 139. Block Diagram of Single-Axis Flywheel Control System

The use of this single-control element, free to rotate about any axis relative to the satellite, eliminates the crosscoupling terms otherwise present in Euler's equations.

Finally, a rather important conclusion can be drawn from these equations. An external torque acting all the time in the same direction has the effect of continuously increasing the angular velocity of at least one flywheel. For practical reasons, however, there is a maximum allowable speed for the flywheels, which simply means that a flywheel may become "saturated." If disturbing torques are expected to act in one direction only, the satellite has to be provided with still another mechanism to exert controllable torques. Magnetic torque or mass expulsion control may be used. The torque produced by one of these systems allows the angular momentum of the flywheels to be "unloaded" returning the speed to zero. Figure 140 presents a block diagram of such a dual-mode system.

When properly sized, this system allows storage of angular momentum due to cyclical disturbance torques; only momentum due to secular disturbance torques need be removed by the reaction jet or magnetic system. The shaping networks can be designed to provide either proportional or integral control for a steady orientation and a pointing error only slightly exceeding sensor error. Thus, a major improvement in fuel utilization is possible as compared with the pure mass expulsion system.

It remains then to estimate system weight and power drain. The size and weight of the flywheels are determined by the size of the disturbance torques. Since these vary with size and configuration of the spacecraft, results are shown as a function of disturbance torques.

#### 7.7.1 Calculation of Wheel Inertia and Weight

Let:

$T_s$  = secular disturbance torque

$T_c$  = cyclical disturbance torque

$t_p$  = orbit period

$t$  = time between momentum unloading

$J$  = wheel inertia

$\omega$  = wheel saturation velocity

The stored angular momentum of the wheel,  $J\omega$ , is the time integral of the disturbance torques acting on the vehicle. Secular torques are assumed constant. The angular momentum generated by the cyclical torques should integrate to nearly zero over one orbit. The cyclical torques are



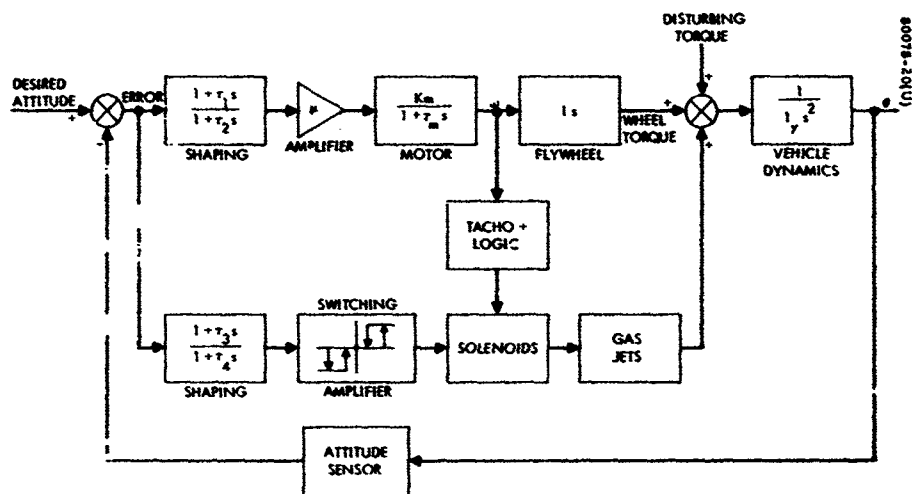


Figure 140. Block Diagram of Single-Axis Dual-Mode Control System

assumed to contribute maximum momentum in one half-period, then to decrease during the next half-period. Then

$$J\omega = T_s t + T_c \frac{t}{2} \quad (75)$$

Experience has shown that a maximum wheel speed of 1200 to 1500 rpm is a good compromise between weight, size, bearing life, reliability, etc.

Figure 141 shows wheel moment of inertia related to unloading time for various disturbance torques with a wheel speed at time of unloading of 1200 rpm.

The relation between rotating parts inertia and wheel weight, shown in Figure 142, was obtained from wheel data supplied by the Eclipse-Pioneer Division of Bendix Aviation Corporation.

From Figures 141 and 142, the relations between wheel weight and unloading time of Figure 143 were obtained.

In the calculations, an orbit period of 100 minutes was assumed. Also, the secular and cyclical torques were assumed equal (which, of course, will not be true). However, in a particular application, the two terms of Equation 75 can be prorated by inspection. A wheel unloading speed of 1200 rpm was assumed.

Other sources of momentum that the wheel must accommodate are initial spacecraft angular momentum, precession of the vehicle 1 deg/day about the pitch axis, and perhaps the momentum due to antenna slewing. The largest of these will probably be the initial spacecraft angular momentum. If, for example, the spacecraft angular velocity were 0.05 deg/sec with a moment inertia of 60 slug-ft<sup>2</sup>, the extra wheel momentum storage would be 0.06 lb-ft-sec. This is a significant quantity in a small vehicle and must be considered in wheel sizing unless provision is made for unloading soon after reference acquisition.

Momentum storage due to 1 deg/day precession about the pitch axis is negligible, and the resulting interaction torque caused about the other axes is an order of magnitude less than the outside disturbance torques about these axes. Likewise, the effects of antenna movement should not affect design of the wheels.

It is seen from the curves that, even for a disturbance torque of 10<sup>-4</sup> lb-ft, total wheel weight for three-axis control is only approximately 30 pounds. As shown below, weight of fuel consumed per year also is small.

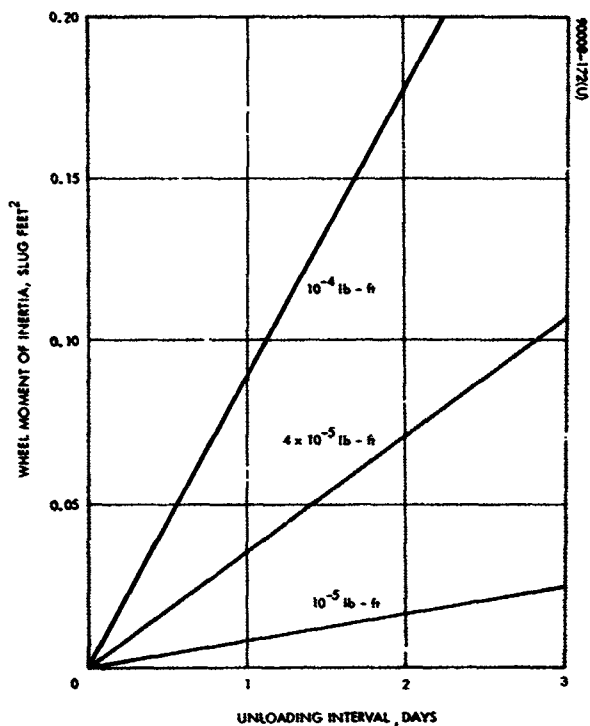


Figure 141. Wheel Moment of Inertia Versus Unloading Interval for Various Disturbance Torques

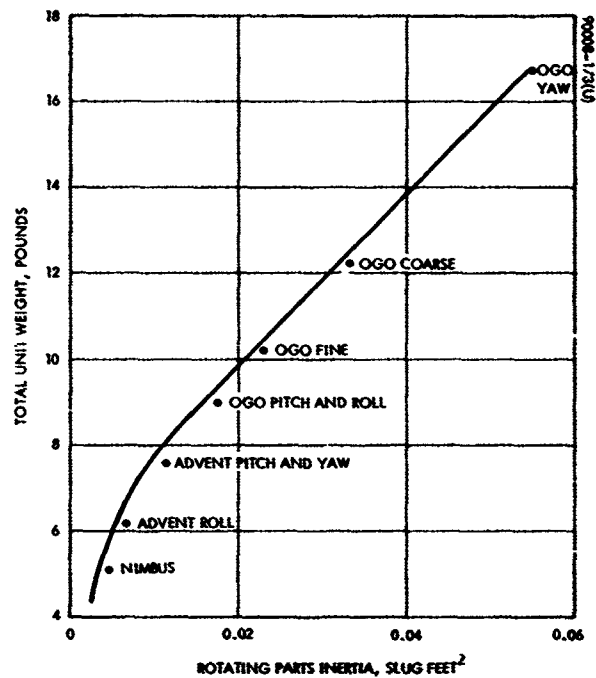


Figure 142. Inertial Wheel Total Unit Weight Versus Rotating Parts Inertia

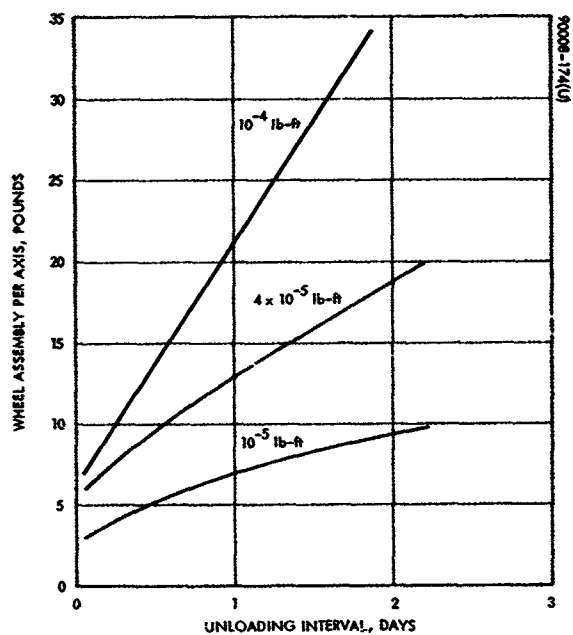


Figure 143. Wheel Assembly Weight Versus Unloading Interval for Various Disturbance Torques

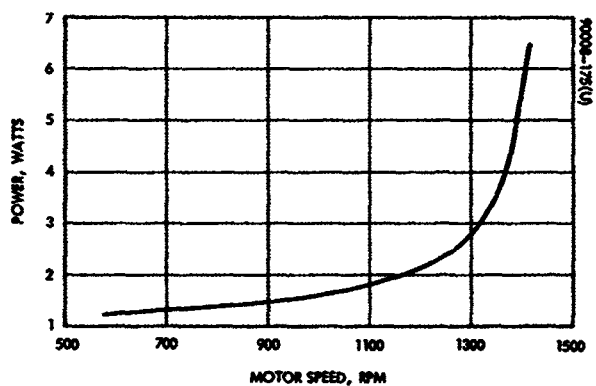


Figure 144. Power Versus Motor Speed for Typical Inertia Wheel

On the average, the moment exerted by the unloading jets must equal the secular disturbance torque,  $T_s$ . Then, since jet thrust = fuel flow rate times specific impulse (see Equations 80 and 83),

$$R_F = \text{fuel rate} = \frac{T_s}{r I_{sp}}$$

For example, let  $T_s = 10^{-4}$  lb-ft,  $r = 4$  ft,  $I_{sp} = 125$  sec. Then,

$$\text{Fuel} = \frac{10^{-4}}{4 \times 125} \times 3.15 \times 10^7 = 6.3 \text{ lb/year/axis}$$

and the stored weight for removing all disturbance torques for a large vehicle for 1 year of operation is less than 50 pounds.

#### 7.7.2 Power Consumption

The average power drainage due to the inertia wheels that must be provided for in the spacecraft power budget is the power the wheel motors must supply to overcome windage and bearing friction at unloading speed. For example, the possibility exists that all three wheels will operate at near unloading speed for a considerable time. The extra power required to overcome jet reaction torque during wheel unloading is of short duration and can be obtained from the battery.

The average power required to overcome secular torques is negligible as is shown by the following estimate. The total momentum imparted to a wheel in 1 year due to a secular torque of  $4 \times 10^{-5}$  lb-ft is 1200 lb-ft-sec. A typical inertia wheel motor will have an average torque (in reverse) of 50 oz-in. at an average power of 60 watts. The time for that torque to create a momentum of 1200 lb-ft-sec is 4800 seconds, which is the time the 60 watts must be applied in 1 year. Hence, average power drain is

$$60 \times \frac{4800}{3.15 \times 10^7} = 0.01 \text{ watt}$$

Power to maintain a wheel at a constant 80 percent of full speed is 1 to 3 watts, depending on size of the wheel, according to Bendix. This is illustrated in Figure 144 which is a plot of power versus steady-state wheel speed for a typical wheel. The unloading speed probably would be 120 rpm in this case.

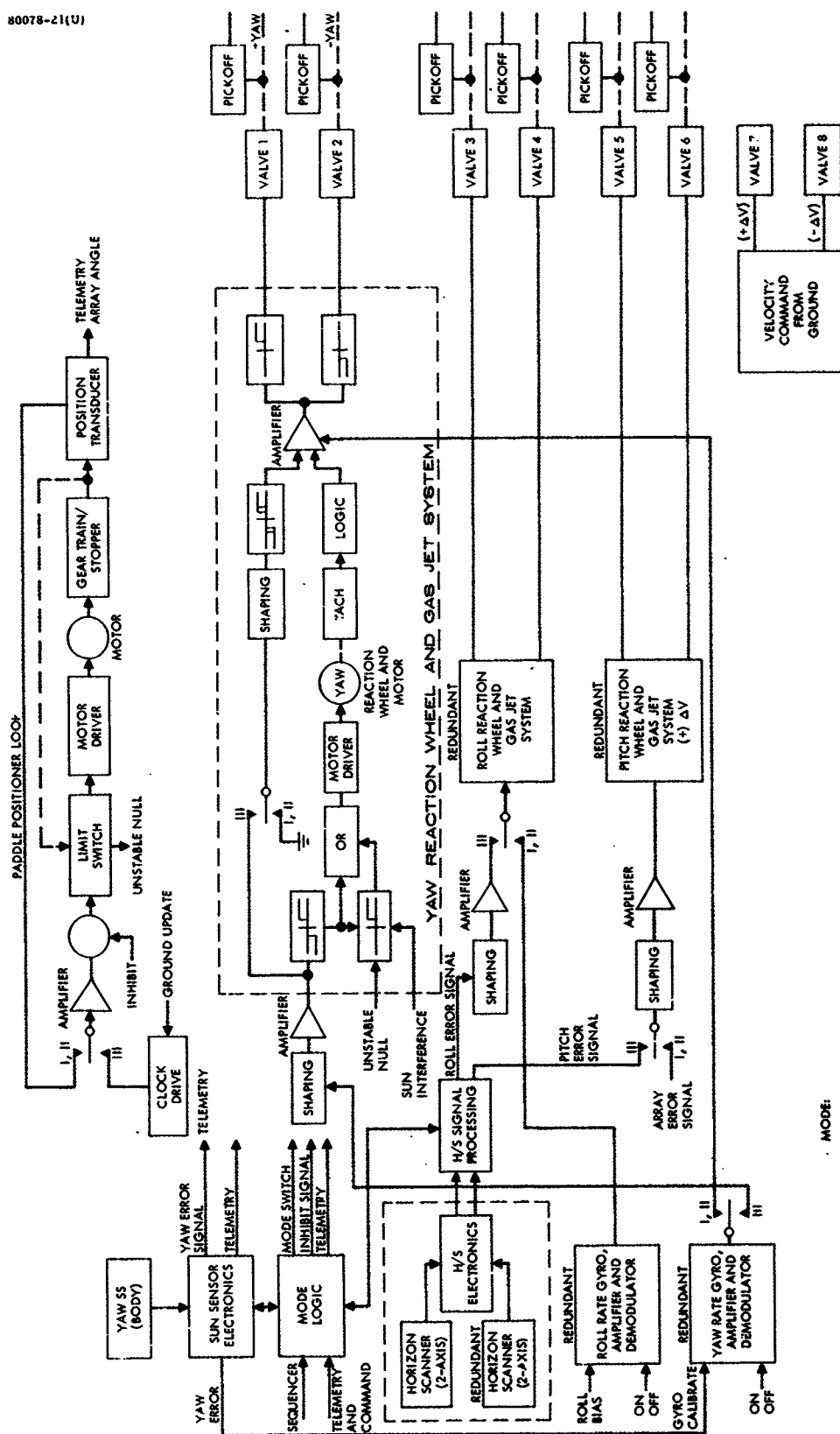


Figure 145. Three-Axis Attitude and Velocity Control for Reaction Wheel Control

### 7.7.3 Motor Characteristics

The main characteristic of the inertia wheel motor is that its stall torque exceeds the torque exerted by the unloading jets. Another motor requirement generally is a reasonably flat torque-speed curve over the speed range zero to  $\pm$  unload speed.

The motor time constant is given by

$$\tau = J \frac{\text{stall torque}}{\text{maximum speed}}$$

It usually lies between 2 and 20 seconds. The time required to unload the wheel is governed by motor stall torque and should always exceed motor time constant.

### 7.7.4 System Implementation

A complete functional block diagram of a reaction wheel system with gas jet unloading is shown in Figure 145. This system utilizes three reaction wheels. The three reaction wheels are motor-driven flywheels that provide storage of angular momentum. External (cyclic) torques are absorbed in the reaction wheel system without disturbing the attitude of the fixed portion of the spacecraft. This control scheme avoids the short-period, jet pulse limit cycle (deadband) characteristics of mass expulsion control three-axis spacecraft.

The wheels for this configuration were sized to require momentum unloading only once every five orbits. The resulting design is very close to the Orbiting Geophysical Observatory design and utilizes three 8-inch-diameter wheels mounted orthogonally and weighing 30 pounds. An on-board attitude control system is required to continuously sense and correct attitude errors. Two axes of control are obtained from scanning-type earth sensors. The third axis about the vertical (yaw axis) is controlled by a rate gyro reference, with updating information obtained from the sun sensor mounted on the solar panels. This sensor provides a fan-shaped field of view in the solar ecliptic plane.

The sun angle used to update the yaw reference gyro is measured by this sensor when the spacecraft yaw axis is normal to the ecliptic (twice each orbit). The gyro is also used with a second rate gyro to provide stability during the earth and sun acquisition phases after booster separation.

## 7.8 MOMENTUM BIAS SYSTEM TYPE 1

### 7.8.1 General Description and Stability

The MBS Type 1 is, generically, a spin-stabilized spacecraft with a despun platform. The unique feature of the MBS Type 1 is that the platform is virtually unlimited in size. The system is not constrained to have a pancake shape demanded by the familiar inertia ratio criterion used to design previous spinning satellites with or without despun platforms. Due to the pancake criterion, requiring spin about an axis of maximum inertia, these craft are limited in both overall length and despun platform size by launch vehicle shroud diameters. Also, since shrouds are longer than wide, the pancake constraint results in nonoptimum use of shroud volume.

Alternately, the MBS Type 1 may be described as a rotor-stabilized spacecraft differing from present designs of this type in a fundamental way. The MBS Type 1 is not constrained to have a perfectly rigid rotor, i. e., a metallic flywheel, dictated by the nutational stability criterion used to design satellites of this class. In essence, the MBS Type 1 is the broadest application of spin stabilization. It bridges the gap between present nonrigid spinners with despun platforms and perfectly rigid rotor-stabilized spacecraft. Free from the rigid rotor constraint, the MBS Type 1 rotor is used to perform many functions in addition to effecting gyroscopic stability. Examples of some of these additional uses are:

- 1) A gravity-fed liquid propellant attitude and velocity control system may be spun, thereby requiring merely two jets for all axis control. The jet system spin also makes the spacecraft essentially insensitive to the torques induced by leaks since they are averaged out every spin cycle.
- 2) Relatively simple attitude sensors may be rigidly mounted to the wheel and scan targets by virtue of spin. Ten arcsecond pointing accuracy may be achieved using one rigidly mounted star scanner. For less demanding missions, the sensor would be an IR earth scanner.
- 3) Solar panels may be body-mounted like ATS and Intelsat II or despun, utilizing a sun tracking system.
- 4) The wheel may also carry payload requiring spin, such as the ATS-I spin-scan meteorological camera.
- 5) Using the wheel as a spinning sunshield permits entirely passive thermal control for most missions.

Further, since the rotor, or spinning section, comprises a significant portion of the spacecraft, it has a large spin moment of inertia, and large gyroscopic stiffnesses may be achieved at very low spin rates of 10 to 100 rpm.

Thus, the MBS Type 1 provides a fully stabilized platform while maintaining features of well-proven spinner technology. In fact, all hardware aspects of the MBS Type 1 have developmental roots in the Syncom and OSO programs. This hardware has been combined into a new configuration long recognized as well-suited for many missions but, heretofore, considered dynamically unstable.

The MBS Type 1 concept is due quite simply to the discovery that it is possible and practical to passively stabilize the spin of a nonrigid body about an axis of least inertia if the body contains a counterrotating element on which a nonrigid energy dissipation mechanism, a nutation damper, may be placed. In present MBS Type 1 design, since the counterrotating element carries payload as well, it is large although it need not be. For example, a small counterrotating box containing a nutation damper can be used to stabilize a large, slender spinning liquid rocket or could have been used to stabilize Explorer I had the principle been known.

A study of the dynamics of two-body configurations was initiated at Hughes in early 1964. This study was motivated by the desire to add despun elements to Syncom-type satellites after the OSO program demonstrated that rotating elements could be operated in space for years. The object of the study was to determine whether stability of two-body configurations was governed by the well-known criterion for spinning monobodies. That is, a monobody must be spun about its axis of greatest inertia. By simple extension of analysis used for monobodies, it was learned that two-body stability does not necessarily require spin about a major axis, and that the distribution of energy dissipation between the two bodies plays a role (Reference 3). This same conclusion was reached by Landon and Stewart at RCA in a paper (Reference 4), which appeared at nearly the same time. Both of these works had an important shortcoming, however. To perform the simple extension of monobody theory, both analyses were limited to the special case of a two-body configuration in which only one of the bodies is nonrigid. With this assumption, detailed quantitative consideration of not well-understood nonrigid effects (i. e., energy dissipation) could be avoided. The important results of these analyses are: 1) if the spinning body is nonrigid, its spin moment of inertia must be greater than the combined configuration transverse moment of inertia, essentially the same as the inertia ratio criterion for monobodies; and 2) if the spinning member is perfectly rigid, a flywheel, the two-body configuration is practically free of inertia constraints. To attack the problem of a general two-body configuration wherein both bodies are nonrigid, it was clear that detailed understanding of the role of nonrigid effects was required.

By analyzing equations of motion of two-body systems with specific nonrigid elements, nutation dampers (Reference 3), physical understanding of the manner in which motion of dampers affected gross system motion was developed. The relationship between the amount of energy which a damper



dissipated into a dash pot, for example, and gross system motion was learned. With this understanding of specific cases, the classical energy-sink method was reconstructed (Reference 5) to deal with the general two-body nonrigid system. This energy-sink analysis yields the following stability criterion

$$\left| \begin{array}{c} \text{Energy dissipation} \\ \text{rate of spinning section} \end{array} \right| < \left| 1 - \frac{I_t}{I_s} \right| \times \left| \begin{array}{c} \text{Energy dissipation} \\ \text{rate of despun} \\ \text{platform} \end{array} \right|$$

Where  $I_t$  = the moment of inertia of the total vehicle about an axis through the center of mass normal to the spin axis, and  $I_s$  = moment of inertia of the spinning section about its spin axis.

This analysis deals only with the case where no appreciable coupling exists between the despin control system and the nutational dynamics of the spacecraft. When the platform despin axis is not coincident with a principal axis, control torques react with the nutational dynamics of the spacecraft. This can be either stabilizing or destabilizing (nutationally), depending on the response characteristics of the despin control loop at nutation frequency.

The nutational coupling is block diagrammed in Figure 146; for simplicity, the imbalance has been assumed to exist in a single plane. Path A-B represents the reaction torques introduced into the nutational dynamics by the despin torquer; path C-D represents the reaction torques introduced into the despin loop by the nutational dynamics. The control is synthesized such that the coupling produces nutationally stabilizing reaction torques.

#### Despun Solar Panel Coupling

An MBS Type 1 configuration for the representative LAS mission of Section 2 requires an additional rotating element — the despun solar panel assembly. This panel rotates relative to the main despun platform at 1 revolution per orbit as it remains pointing at the sun. Thus, there is a dynamic coupling link between the two control loops. A solar panel control with a constant rate and no outer position loop could not lead to limit cycling or even instabilities when coupled to the rotor drive control. Preliminary investigations indicate that as long as the solar panel stepper motor drive frequency is isolated from the spacecraft nutation frequency, there will be no stability problems. Some transient disturbances of the despun platform position will occur as the solar panel is stepped; however, the disturbance amplitude can be kept small by using high-frequency, low-amplitude steps to rotate the panel relative to the despun platform.

### Stability Conclusions

When the practical nature of the MBS Type 1 was established, considerable effort was devoted to thoroughly consider all system aspects. Complete dynamic analysis of real systems (Reference 7), including an active despin servo loop coupling the spinner and platform, was performed, using a digital computer simulation specifically designed for the MBS Type 1. Here, the dynamic integrity of a real system was established. Further, Reference 6 describes an air-bearing supported MBS Type 1 dynamic model that was fabricated and tested. The model corroborated theoretical conclusions. Reference 6 also compiles a number of analyses that treat the case of an MBS Type 1 with asymmetric platform complementing the analyses of References 3 and 5.

#### 7.8.2 Despin Control System (DCS)

The principal elements of a DCS are: 1) the earth sensor assembly located on the spinning section (rotor), 2) the despin control electronics located on the rotor, and 3) the bearing and power transfer assembly. The latter includes 1) the bearings, slipring assembly, and housing, 2) the despin motor (brush-type dc motor), and 3) the master index pulse (MIP) generator.

The operation of a typical DCS (see Figure 147) is as follows: the despun platform angular coordinate  $\phi$  is controlled by a motor, commanded in a manner to null the LOS error of the platform boresight with respect to the earth center plane. The error signal used to drive the torque motor is derived from sensed platform LOS error ( $\epsilon$ ) and rate ( $\dot{\epsilon}$ ).

An earth sensor mounted on the spinner generates leading and trailing earth-edge pulses. A frequency-lock loop (FLL) operating on these pulses generates two outputs: a single pulse per revolution (ppr) which occurs at the midpoint of the earth-edge pulses, and a 16 ppr pulse train synchronized to the earth sensor pulses. A mechanical shaft angle encoder (SAE) at the bearing interface provides two additional pulse trains: a single pulse per revolution aligned with the platform boresight is used for LOS position error computation MIP, and a 16 ppr pulse train is used for LOS rate error computation.

The basic operation of the DCS is as follows. In the steady-state tracking mode, the platform LOS error is determined once per revolution by phase comparison of the earth center pulse output of the FLL and the MIP output of the SAE. The sampled LOS error is then shaped and smoothed in the outer loop to produce a motor torque command based on position information. The inner rate loop processes the output pulses of the SAE in conjunction with the output pulses of the FLL. Thus, the rate loop processing is a sampled loop that updates the LOS rate information 16 times per rotor revolution, and commands a torque proportional to the rate error.

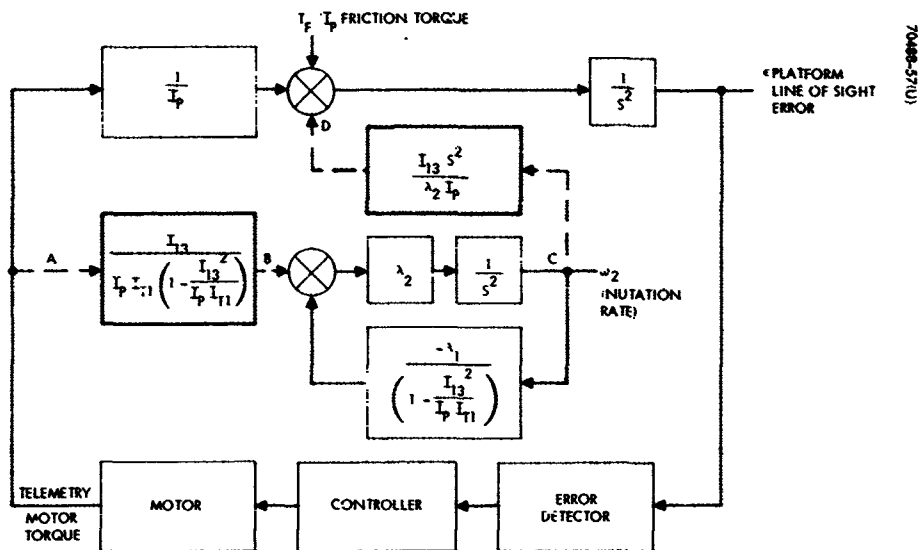


Figure 146. Representative Stabilization and Control Block Diagram Illustrating Crosscoupling

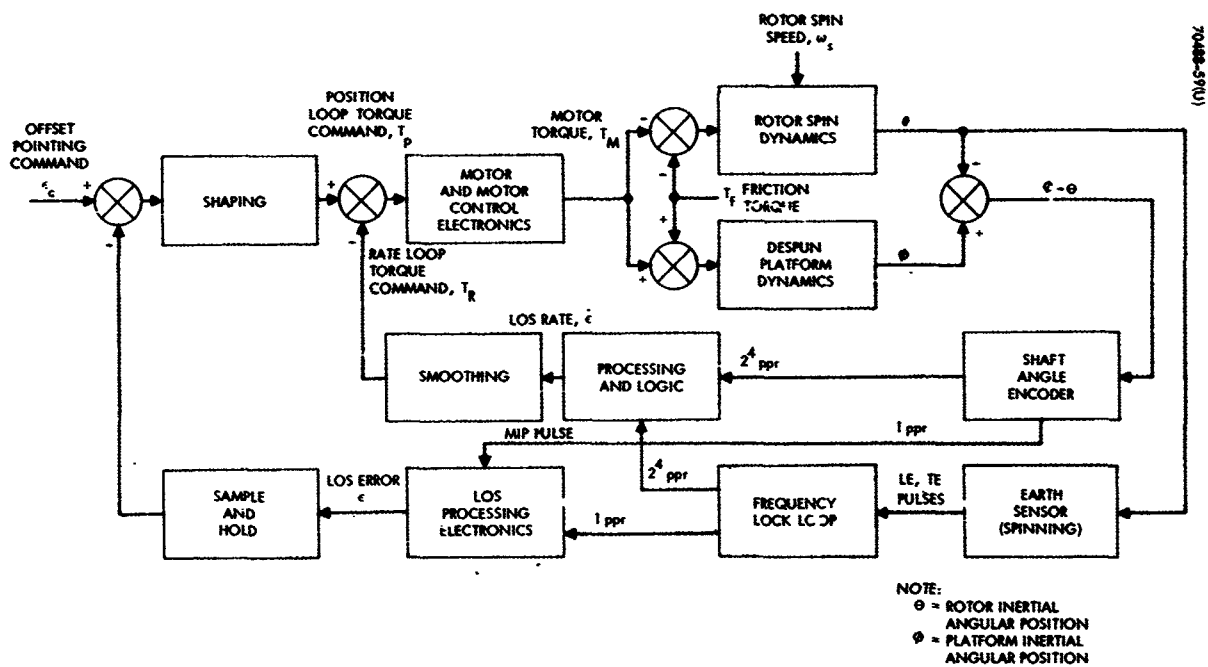


Figure 147. Typical Despin Control System Functional Block Diagram

The inner (rate) loop characteristic response time is selected to be fast relative to one rotor revolution, which requires a large torque-to-LOS rate gain ratio. This fast-response inner loop serves two purposes: 1) it senses and corrects for nutationally induced LOS motions, thus providing stable nutational damping via the coupling, and 2) the outer loop may be a low-gain loop; thus the earth sensor noise can be substantially smoothed without a LOS error penalty.

The operational modes of the DCS consist of an acquisition mode, a steady-state track mode, an offset pointing mode, and various failure mode capabilities. The characteristics of these operational modes are summarized in Table 12.

### 7.8.3 Velocity and Attitude Control

Attitude control here refers to spin-axis orientation. Velocity and attitude control are provided by a functional subsystem which provides the sensing, logic, and actuators necessary to perform velocity maneuvers and to maintain the proper inertial orientation of the spacecraft (spin axis normal to orbit plane).

A magnetic torque or mass expulsion system may be used for attitude control. No clear, general preference for one or the other of these systems is evident. However, a case can be made for mass expulsion control based on the fact that a mass expulsion velocity control system will be required in any case. The remainder of this subsection discusses such a system.

The hardware elements that comprise a mass expulsion velocity and attitude control subsystem are: 1) the hydrazine monopropellant reaction control system, 2) an ATS-type slit sun sensor, and 3) one passive nutation damper. The outputs of the two pencil-beam earth sensors are functionally used to determine the attitude error, but are considered part of the despin subsystem. The functional utilization of these elements is shown in Figure 148.

TABLE 12. SUMMARY OF DCS OPERATIONAL MODES

Acquisition mode	Provides initial capture capability from arbitrary LOS initial conditions
Track mode	Steady-state operation consists of a dual-loop configuration operating in a linear mode
Offset pointing mode	Provides command bias for null of static errors and for spacecraft mass imbalance correction during $\Delta V$ maneuvers
Failure modes	Hardware redundancy and automatic error sensing maintain attitude control without continuous ground monitoring

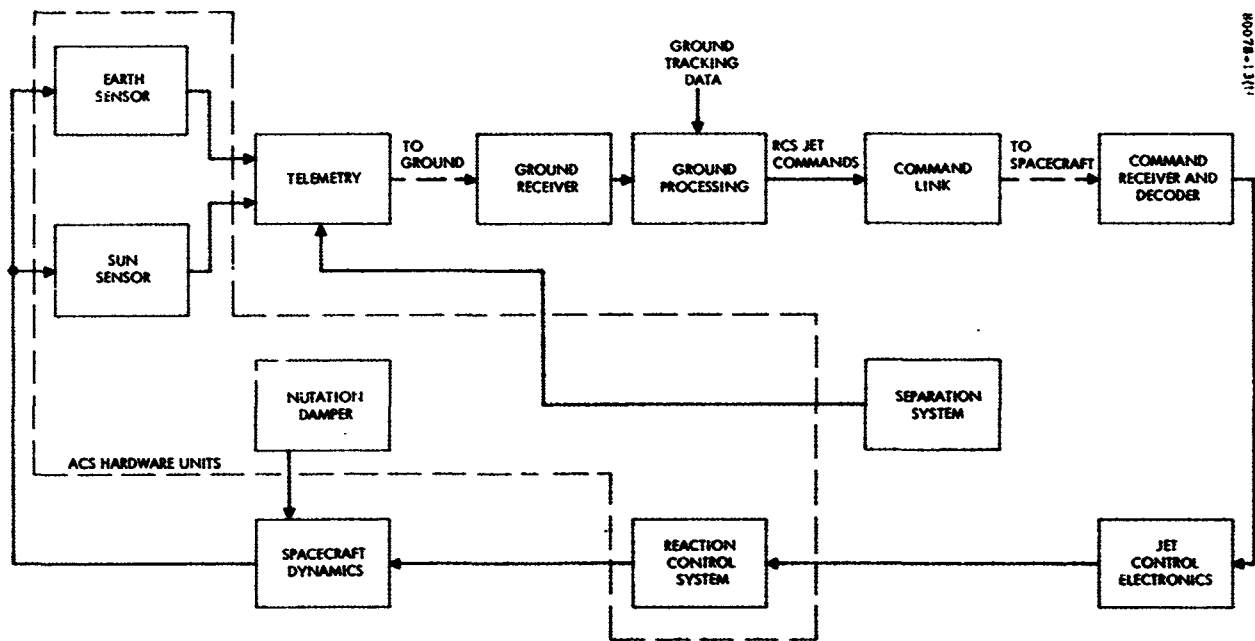


Figure 148. Functional Block Diagram of Velocity and Attitude Control Subsystem

The basic attitude control technique for the MBS Type I is a logical extension of the method used successfully on the Intelsat I and II programs. The familiar pulsed axial jet mode of operation of the reaction control system causes precession of the spacecraft spin axis when pulsed in synchronism with the spin period. The sun ( $\psi$ ) pulse is used for a reference direction as on past spacecraft, although the earth sensor can be used as a backup.

#### Attitude Control System Design Analyses and Tradeoffs

The following subsections describe the tradeoffs that led to the selection of particular techniques of the attitude control system. The principal attitude control system tradeoffs considered are: 1) combined versus separate velocity control and attitude control, 2) ground command versus automatic on-board velocity and attitude control, 3) spinup methods, and 4) nutation damping techniques.

Attitude and Velocity Control Methods. The first tradeoff consideration in the selection of velocity controls and attitude control methods involves a consideration of separate versus combined velocity control and attitude control systems. The primary tradeoff in this selection is the potential necessity for different thrust levels to perform the necessary velocity control and attitude control maneuvers.

The technique of spin stabilization to provide gyroscopic stiffness also permits the use of relatively large thrust levels for both attitude and velocity control without causing the allowed orientation drift to be exceeded. Large allowable thrust levels, along with the ability to use either pulsed or continuous thrusting from the reaction control system, permits identical thrust levels to be used for both velocity and attitude control. Syncom/Early Bird flight experience has proved this concept of combined velocity and attitude control using a single reaction control system operated in either a pulsed or continuous mode.

Since the equipment in the spacecraft (jet control electronics) and on the ground (ground processing equipment) must have the capability for selection of a particular jet, thrust duration, and thrust phasing for velocity control, combining this function with attitude control adds no additional equipment for the reaction control system. The only additional equipment required is for the computation of orientation and required corrections, computation that must be performed whether a separate or combined approach is utilized.

Based on proven Syncom/Early Bird flight experience and maximum system reliability, the combined velocity and attitude control method represents the obvious selection.

A second tradeoff involves the selection of either a ground command mode or an autonomous on-board mode for attitude control (velocity control will be considered separately). While the primary method of attitude control for the spacecraft is gyroscopic stiffness, external disturbance torques

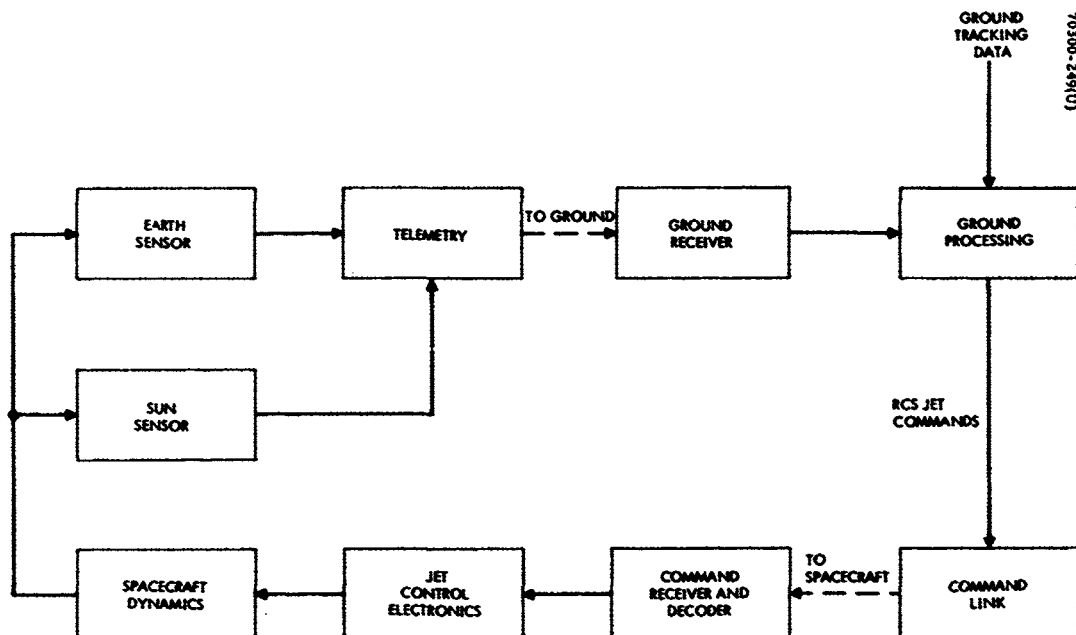


Figure 149. Ground Command Mode Block Diagram

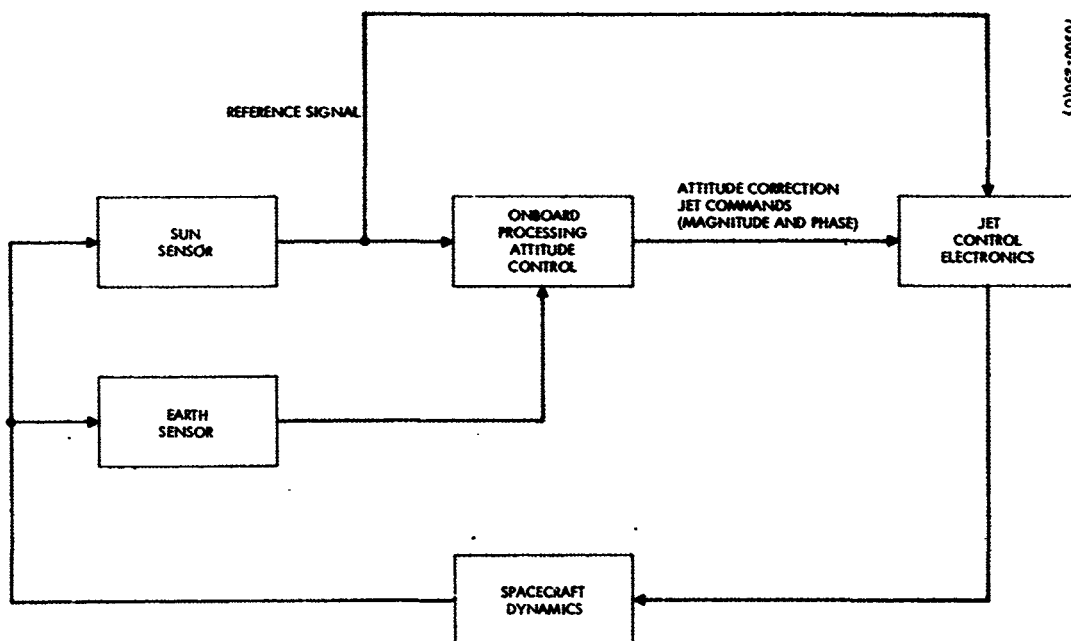


Figure 150. Block Diagram of Autonomous On-Board Attitude Control System for MBS Type 1

will cause a precession of the satellite angular momentum vector. Thus, periodic correction by the satellite reaction control system jets is required. The attitude control system is required to command the reaction control system jet firings such that the spacecraft spin axis remains within a given half-cone angle of the orbit normal.

One ground command method is similar to that used on Syncom, Early Bird, HS-303A, and the Applications Technology Satellites. The only difference is in the type of attitude sensor to be used; in this mission a pair of earth sensors is used since the earth sensor information is provided free from within the despin subsystem processing electronics and the earth sensors provide better orientation determination accuracy. Earlier Hughes satellites used sun sensors and antenna polarization measurements; in either case, the corrections are computed on the ground and a command link used to fire the reaction control system jets. A schematic block diagram for the ground command mode is given in Figure 149 illustrating the use of ground processing of the telemetered sensor outputs to determine orientation and command corrections.

The autonomous method is identical to the ground command mode except that all processing and sensor data smoothing are accomplished on board the spacecraft by appropriate electronics. This difference is significant in that the ground command mode takes advantage of the smoothing of sensor data to obtain better accuracy and to minimize the number of orientation computations required (one computation with smoothed data versus one computation per several spin revolutions). A schematic block diagram representing the autonomous mode is shown in Figure 150.

The components necessary to provide attitude control in the two modes being considered are summarized in Table 13. Examination of this table shows that the complexity is approximately equivalent in either system. This is expected since the functions performed are the same. However, the most complex function is the signal processing and smoothing and jet control logic. In the ground control mode, the major portion of this function is accomplished on the ground, while in the autonomous control mode it is accomplished on board the satellite. In addition, it is desirable that a manual override of the autonomous attitude control system be provided to enhance system reliability. In this case, the override system would be identical to the ground control mode, and the only function served by the on-board processing is to simplify the routine ground control operations.

The major factors involved in determining the optimum method of attitude control, in the order of decreasing importance, are: 1) reliability, 2) correction frequency, 3) accuracy, 4) flexibility, 5) cost, 6) weight, and 7) growth capability.



TABLE 13. ATTITUDE CONTROL COMPONENTS

Function	Ground Control	Autonomous
Sensor	Two-axis, spinning earth sensor; ATS sun sensor	Two-axis, spinning earth sensor; ATS sun sensor
Reaction control system	Axial control jet	Axial control jet
Telemetry link	Earth sensor signals, sun sensor signals	None required, but earth and sun sensor data furnished for data analysis
Command link	Single-channel binary-coded signal	None required, but manual override desirable
On-board signal processing	Decoder and storage of jet command logic (number of pulses, pulsing angle, jet number, and execute signal)	Sensor signal storage and smoothing, orientation determination and control logic, failure mode detection, and jet command logic
Ground signal processing	Smoothing of sensor signals and computation and coding of control signals	None required unless manual override mechanized

Reliability is judged to be the most important aspect since loss of attitude control capability can cause a gradual drift of the spin axis from the desired orientation. Comparing the two modes of control on the basis of reliability shows that the ground-based system is clearly more reliable since significantly fewer on-board components are used in the signal processing and command link circuitry. To surpass the ground-based control mode reliability, the autonomous mode would require backup manual override, which increases the cost. Comparing the two systems on a cost basis also favors the ground-based system since the cost of developing flight quality processing electronics would be significantly greater than that for developing ground-based processing electronics and software.

Correction frequency is another important factor because a short interval between corrections means that for ground control the attitude must be closely monitored.

As mentioned previously, because of the improved data smoothing possible on the ground, the accuracy of the ground-based control mode is somewhat better than the autonomous control. It is also easier to discriminate against low-frequency, high-amplitude noise pulses in a ground control mode. Noise pulses of this type could erroneously actuate the control sequence in the autonomous mode.

The weight factor appears to be relatively unimportant in this tradeoff. The additional weight of the control circuitry required in the autonomous mode signal processing is relatively insignificant in a satellite of about 1000 pounds.

Growth capability is another factor that has little bearing on the choice of control mode. The automatic mode can be implemented in future missions to avoid any dependence on a ground command link except in a failure mode.

The final comparison factor is the flexibility of operation of the reaction control system. For example, it is possible to switch jets and vary the pulse length or direction by ground commands. In general, the ground control link is more flexible in its usage than is the autonomous control mode, but the override feature negates this factor.

A summary of the attitude control mode tradeoff factors is shown in Table 14. In this summary, the autonomous control mode is presented both with and without the backup manual override feature. On the basis of the factors presented, the autonomous mode with ground override appears most favorable, primarily because of the correction frequency and flexibility.

Velocity Control Alternates. The initial orbit acquisition and velocity corrections must clearly be implemented by a ground command mode due to the dependence of these functions on ground orbit tracking data and ground decision making. However, operational velocity control may be performed in either an automatic or ground command mode.

The ground command mode of operation is illustrated in Figure 149 where all processing and reaction control system jet commands are generated on the ground. Inputs are required from the orbit tracking data to determine the necessity and magnitude of the velocity correction maneuver as well as from the sun sensor to properly phase the reaction control system jet commands.

The automatic mode requires the use of on-board processing electronics that measures the spin angle between the earth line of sight (LOS) and the sun LOS each day at the high noon condition (sun LOS in nominal longitudinal plane). In addition, a clock must be included on the spacecraft to determine when the high-noon condition occurs, and this clock must be periodically updated. The schematic block diagram of the combined altitude and velocity control method using an automatic on-board mode of operation is shown in Figure 151.

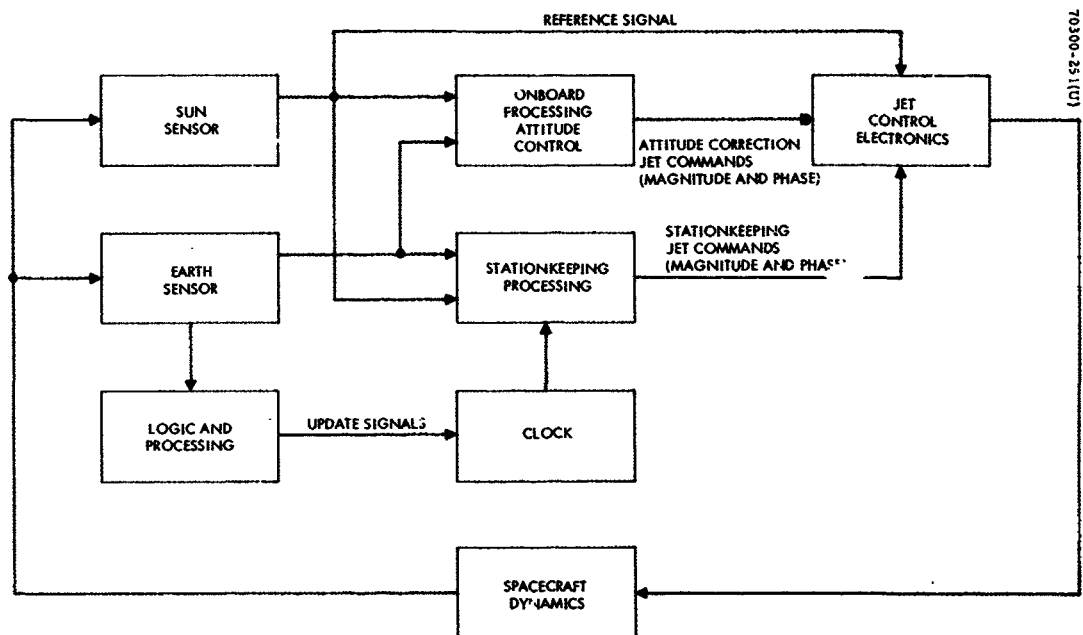


Figure 151. On-Board Velocity and Attitude Control System Block Diagram

TABLE 14. ATTITUDE CONTROL MODE TRADEOFF SUMMARY

Factor	Ground Control Mode	Autonomous Mode	Autonomous Mode With Manual Override
Reliability	Acceptable	Lowest	Best
Accuracy	Acceptable	Acceptable but lower	Same as mode being used
Cost	Lowest	High	Highest
Weight	Lowest	Acceptable	Acceptable
Command frequency	Approximately every 6 hours	None	Once every 6 hours if autonomous mode fails
Growth capability	Good	Lowest	Good
Flexibility	Very good	Lowest	Best

Although the automatic method presents excellent growth potential for future missions, the complexity and cost of the on-board processing and the infrequency (approximately once every 2 weeks) of required utilization of the command link for the ground command mode usually will lead to the selection of the ground command mode. The ground command capability must already exist to perform initial station acquisition and station changing, as well as a failure mode override; hence, the ground command mode presents the maximum reliability of the two approaches.

Spin Speed Selection and Control. The choice of the nominal spin speed for the spinning section of the spacecraft is based on tradeoffs involving several mission and system requirements. A high spin speed is desirable to increase the angular momentum, thus decreasing the rate of attitude deviation caused by solar torques. The period between corrections is directly proportional to the spin speed. On the other hand, the accuracy of the sensors (sun and earth) decreases as the spin rate increases due to the lower signal energy. The bearing and slipping wear and friction level wear is directly proportional to the spin speed, as is the weight of the spinup system. Finally, the despin servo loop and encoder design becomes more difficult as the spin speed increases.

The provision of a spin speed control capability to the spacecraft is relatively simple. The easiest way is to cant the two axial jets so that they provide a component of torque about the spin axis. The two jets would be canted in different directions so that one jet gives positive torques, while the other gives negative torques. Now the jet alignment problem is relatively simple. They would be canted at about  $1 \pm 0.4$  degree, which is easily achieved. Axial jet maneuvers would then be performed with alternate systems as required to maintain the spin speed within the desired band.

One problem with the method outlined is the loss in redundancy should one axial jet fail either open or closed. Due to the canted nozzles, the remaining fuel in the good system could not be used due to the spin torques that would be imparted. However, an additional set of axial jets can easily solve this problem if required.

#### 7.8.4 Pointing Accuracy

The primary distinction to be made between sources of pointing error concerns their frequency spectrum. Static or slowly varying errors will have little effect on the quality of photographic imaging; however, these errors must be limited, the limit corresponding to the amount of photographic overlap or antenna pointing requirements. Higher frequency error sources will degrade the photographic capabilities of the satellite by causing significant motion during a frame or scanning period, depending on the imaging device used.

Pointing errors can also be separated according to their plane of motion with respect to the orbit plane. Those errors whose plane of motion is perpendicular to the orbit plane are classified as crosstrack errors since this motion causes an earth-oriented axis to cross the orbit track on the earth's surface. Similarly, those errors whose plane of motion coincides with the orbital plane are along-track errors. This distinction is useful because several of the sources of error in the two directions have different causes. Along-track pointing is controlled by the despun control system about the rotor spin axis, while crosstrack pointing is controlled by spin stabilization plus a gas jet control system and is affected by spin axis wobble.

Below is a brief discussion of the sources of pointing error, broken down into four major categories and corresponding to Tables 15 and 16.

##### Along-track Low-Frequency Error Sources

These along-track low-frequency error sources include sensor misalignment, platform-to-rotor misalignment, and sensor inaccuracy. Based on experience with the AF MILCOMSAT satellite, the two misalignments can be limited to 0.05 degree each. Analysis of the Barnes earth sensor and associated signal processing indicates two sources of slowly varying error: electronic component variation due to temperature changes and variation in horizon radiance profile.

TABLE 15. ALONG-TRACK POINTING ERROR

Type	Error Source	3 $\sigma$ Error, degrees
High-frequency random	Earth sensor	0.02
	Friction noise	0.01
	Rate sensor	0.005
	Signal processing and electronics	0.01
	Rss Total	<u>0.025</u>
Low-frequency random	Earth sensor alignment	0.05
	Platform/rotor alignment	0.05
	Earth sensor	0.155
	Rss Total	<u>0.17</u>

TABLE 16. CROSSTRACK POINTING ERROR

Type	Error Source	3 $\sigma$ Error, degrees
High-frequency random	Bearing runout and jitter	0.01
	Dynamic unbalance	0.02
	Residual nutation	0.01
	Rss Total	<u>0.025</u>
Low-frequency random	Earth sensor	0.155
	Earth sensor alignment	0.05
	Payload alignment	0.10
	Rss Total	<u>0.195</u>
Fixed	Attitude control system dead zone	0.3
	Total fixed and low-frequency errors	<u>0.495</u>

The former results in a timing error of approximately 0.11 millisecond which corresponds to 0.04 degree at a spin speed of 60 rpm. Variation in the horizon profile results in a variation of the slope of the leading and trailing edges of the bolometer signal corresponding to the earth. The effective horizon width in the 15-micron frequency band at a tilt angle corresponding to an orbit latitude of 45 degrees and at an altitude of 500 n. mi. is approximately 1.0 degree. Variation in the horizon radiance profile will cause an error in horizon detection of not more than 15 percent of this value, i. e., about 0.15 degree. Thus the sensor rss error is 0.155 degree. The rss total of the three error sources is 0.17 degree.

#### Along-Track High-Frequency Error Sources

Along-track high-frequency pointing error is caused by relatively high-frequency noise inputs to the despin control system. There are four basic noise sources: 1) earth sensor noise, 2) bearing friction noise, 3) rate sensor noise, and 4) signal processing and electronics noise. The earth sensor noise is due principally to thermal noise in the detector which results in a relatively broad-band noise output from the sensor electronics, with an rms value of 0.03 degree. A phase-locked loop or filter can be used to reduce this to 0.0067 at the control system output. Thus, the  $3\sigma$  value can be limited to 0.02 degree.

Bearing and motor friction noise has not been thoroughly evaluated or measured. Analysis of despin control systems has led to operating torque-to-inertia ratios of about  $2.7 \times 10^{-3}$  rad/sec<sup>2</sup>. The noise torque-to-inertia ratio is estimated to have a peak value of 5 percent of this operating condition with the peak of the spectrum occurring at spin frequency. A tentative analysis of the response at the output indicates a  $3\sigma$  error of about 0.01 degree.

A rate sensor and rate loop within the despin control system will reduce the noise output due to friction noise, but will introduce another source of error as discussed below.

The rate sensor consists of an oscillator clock, a shaft encoder, which is a notched wheel on the rotor and a "notch sensor" on the platform, and digital electronics. The clock pulses between encoder pulses are counted and used as a measure of the relative spin rate between rotor and platform.

The quantization noise error is taken to be one-half the quantization level rate; thus, for a spin speed of 60 rpm and a clock frequency of about  $2^{18}$  pulses per revolution, the quantization noise is  $-360/2^{18} = 1.37 \times 10^{-3}$  deg/sec. In addition, there will be a significant noise contribution due to the mechanical asymmetries in the shaft encoder. Assuming 0.0005-inch machining tolerance for the encoder notches and a 3-inch radius, the  $3\sigma$  angular error is about 0.01 degree. If the encoder has 16 notches, the noise will occur principally at 16 times the spin frequency. The total system dynamics and control processing will reduce the transmission of this noise to the output.

As the gain of the feedback loop containing the rate sensor is increased, the transmission of the friction noise is decreased, but the transmission of the rate sensor noise is increased. The optimum setting of the rate loop gain results in the rms values of the pointing error due to friction noise and rate sensor noise being equal. Since with no rate sensor the friction noise results in a 0.01 degree  $3\sigma$  error, the introduction of a rate sensor must reduce the rss value of both sources to at least this value. But to be conservative and in the light of the many assumptions and approximations made, it will be assumed that the  $3\sigma$  pointing errors due to friction and rate sensor noises are 0.01 and 0.005 degree, respectively.

The noise caused by the electronics and signal processing including digital quantization error can only be roughly approximated. Preliminary analysis indicates that the  $3\sigma$  pointing error due to this error source is much less than 0.01 degree. The rss  $3\sigma$  value of the above four pointing errors is 0.025 degree.

#### Crosstrack Low-Frequency Error Sources

Crosstrack low-frequency error sources include the earth sensor inaccuracy, sensor misalignment, payload misalignment, and the attitude control system dead zone. As discussed above under Along-Track Low-Frequency Error Sources, the  $3\sigma$  pointing error due to sensor inaccuracy will be less than 0.155 degree. The sensor and payload misalignments can be limited to 0.05 and 0.1 degree, respectively, and the attitude control system dead zone has been set at 0.3 degree.

The alignment errors and sensor inaccuracy are random quantities, but the dead zone is fixed. Thus the rss error of the former must be directly added to the latter, yielding a total  $3\sigma$  error of 0.495 degree.

#### Crosstrack High-Frequency Error Sources

Crosstrack high-frequency error sources include bearing runout and jitter, dynamic unbalance, and residual nutation. Bearing runout and jitter depend on the quality of bearings used in the bearing assembly. Data from bearing manufacturers indicate that with two bearings separated by 10 inches this error can be kept below 0.002 degree. Assuming a smaller contact separation and low-quality bearings, this error can still be kept less than 0.01 degree. Dynamic unbalance is a result of balancing machine misalignments and sensitivity and propellant tank misalignments. Detailed analysis indicates a limit of 0.02 degree. Residual nutation occurs after attitude corrections and to a much lesser degree as a result of coupling between the DCS and transverse axis motion. Preliminary analysis yields a limit of 0.01 degree. The rss  $3\sigma$  pointing error of all sources is about 0.025 degree.

#### Comment

The values given above for error sources are estimates and are based on present knowledge and techniques. These error sources can be reduced by improved design, particularly the low-frequency, crosstrack errors.



## 7.9 MOMENTUM BIAS SYSTEM TYPE 2

The momentum bias system type 2 (MBS Type 2) utilizes a single flywheel rotating about an axis normal to the orbit plane for three-axis control. The system has a high angular momentum that provides dynamic stiffness to the spacecraft similar to a spin-stabilized satellite. The dynamic stiffness maintains the satellite orientation about the roll and yaw axes, while pitch rate is maintained at the orbital rate by controlling the flywheel speed with the flywheel motor. This method of control is similar to that for reaction wheel control except that a nominal amount of angular momentum (i. e., a bias) is specified for the wheel; whereas, in the conventional three-wheel reaction control, the nominal point is zero momentum. A reaction jet or magnetic control unloading system is required for the roll and yaw axes.

Considering now the large momentum wheel by itself. The measure of its stiffness is the amount it precesses under a given torque. Considering a single axis, the precession angle is given by time duration of disturbance torque, and by wheel inertia and speed. Let:

- T = disturbance torque
- J = momentum wheel inertia
- $\omega_1$  = wheel speed
- $\omega_2$  = precession rate
- $\theta_{\max}$  = pointing error tolerance
- k = wheel radius of gyration
- D = outside diameter of wheel
- t = spin axis control dead zone time
- m = wheel weight
- H = wheel angular momentum =  $J\omega_1$

Then

$$\underline{T} = \underline{H} \times \underline{\omega}_2$$

or

$$T = J\omega_1 \frac{\theta}{t}$$

$$J = \frac{m}{g} k^2$$

For a wheel,  $D^2 = 8k^2$ . Hence

$$m = \frac{8gtT}{D^2 \omega_1 \theta_{\max}}$$

If correction of precession angle is by reaction jet, the correction interval can be as short as desired. However, the correction interval should be no less than an orbit period. Otherwise, fuel will be wasted correcting cyclical torques. For example, assuming the magnitude of cyclical and secular torques is comparable, and corrections were necessary twice per orbit, reaction jet fuel would be increased by approximately a factor of three.

If magnetic interaction is the source of correction torque, wheel momentum must be sufficient to hold precession angle in the presence of both secular and cyclical torques within pointing error specification for some minimum time, during which the magnetic field coincides with the axis about which torque is desired. This minimum time will depend on the LAS orbit inclination. This magnetic dead time establishes wheel weight for a given set of disturbance torques.

Figure 152 shows inertia wheel weight as a function of correction time and a range of wheel diameters for a wheel velocity of 1200 rpm, with a disturbance torque of  $2 \times 10^{-5}$  ft-lb, and where pointing error is held to less than 0.5 degree.

Another requirement on the wheel is that its momentum be sufficient to maintain precession rates within specification when subjected to the sum of secular and cyclic torques, i. e., if  $\omega_2$  = precession rate, then wheel momentum,  $H$ , must obey the relation

$$H \geq \frac{T_c + T_s}{\omega_2}$$

Figure 153 shows the above relation for various disturbance torques. Even though the momentum increases very rapidly at small pointing error rates, the magnitudes represent small wheel weights. For example, let wheel speed = 150 rpm, diameter 2 ft,  $H = 3$  lb-ft-sec, then

$$H = J\omega_1 = \frac{m}{g} k^2 \omega_1 = \frac{m}{g} \frac{D^2}{6.25} \omega_1$$

$$m = 10 \text{ pounds}$$

Hence, angular error rate is not the dominant factor in wheel design.

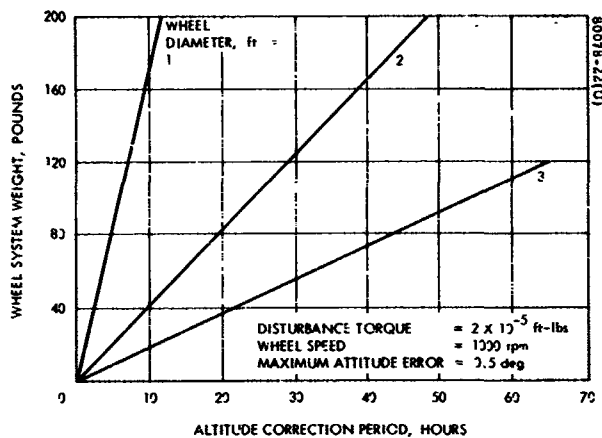


Figure 152. Momentum Wheel Sizing

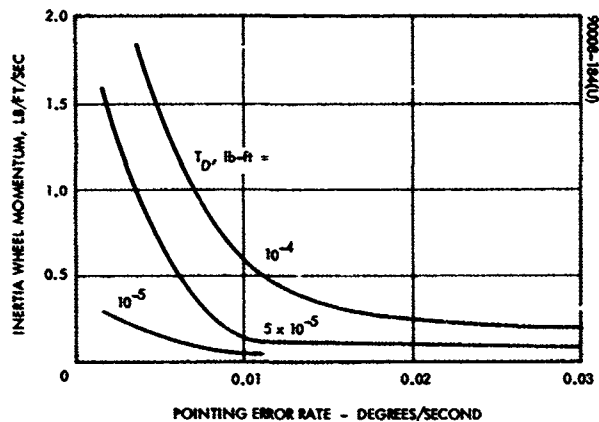


Figure 153. Inertial Wheel Momentum Required to Limit Pointing Error Rate

#### 7.9.1 Power Requirements

Power drain for other than the usual control electronics is minimal for an inertia wheel-type control system with reaction jet correction. The only extra power is that necessary to maintain constant wheel velocity, which should be less than 5 watts. In the case of magnetic correction, however, power consumption must be considered.

## 7.10 COMPARISON AND COMMENTS

It was shown in Sections 7.4 and 7.5 that for the anticipated disturbance torques on a representative LAS, both gravity-gradient and magnetic torque control lack sufficient pointing capability for optical imaging missions. A mass expulsion system will provide the required pointing accuracy, but, for conventional systems with lower limits on thrust impulse, the stringent pointing requirements of advanced missions will result in excessive use of fuel.

A mass expulsion system must use propellant to compensate for both secular (spacecraft-fixed) and cyclical disturbance torques which makes this system innately less fuel-efficient than the three remaining systems.

These three systems -- reaction wheels, MBS Type 1, and MBS Type 2 -- are dual-mode systems. The reaction wheel system requires, in addition to the reaction wheels, a torque-producing system to reduce the angular momentum of the wheels when it becomes too large. The MBS Type 1 and MBS Type 2 are dual-spin systems and require a torque-producing system to orient the spin axis. Either magnetic torque or mass expulsion systems may be employed for these secondary functions. If mass expulsion is used, then the primary system is sized so that correction torques from the mass expulsion system occur less often than once an orbit and, hence, compensate for only the secular disturbance torques. Table 17 presents the components for the above three systems.

The basic LAS requirement under consideration in this study is the ability to transmit data to, and receive from, a data relay satellite. For high data rate, optical imaging missions, this requirement necessitates a directive steerable antenna. But, as shown in Section 4.2, one or two such antennas can be accommodated by the two basic spacecraft configurations associated with the three candidate attitude control systems. Thus, the LAS-DRS communication link has little influence in making the choice from among these systems.

In Section 2, a representative, earth observation mission was selected. Based on LAS orbit geometry and the particular sensors chosen (see Section 2.3), the LAS pointing accuracy must be 0.1 degree and angular rates must be less than 0.01 deg/sec. Using the control system concepts of the preceding subsections along with available hardware knowledge for these stabilization requirements, the weight and power requirements of the preferred systems were estimated. The results are shown in Table 18.

It can be seen from Table 18 that all of these systems are comparable in weight and power. Although the MBS Type 1 is shown as being the heaviest, the weight estimate includes the bearing assembly which is a significant part of the spacecraft structure, and so, more equitably, part of the weight should be assigned to the structure rather than all to the control system. Thus, based on power and weight estimates and control capability,

no clear choice is evident from among the reaction wheel system, MBS Type 1, and MBS Type 2.

However, other considerations such as reliability, flexibility, growth capability, and cost may provide a basis for a selection.

A summary of the attitude control system conclusions is presented in Table 19.

TABLE 17. THREE VIABLE STABILIZATION METHODS

Factor	Momentum Bias System Type 1	Momentum Bias System Type 2	Reaction Wheel System
Attitude sensing	<ul style="list-style-type: none"> <li>• Spinning fan beam sun sensor</li> <li>• Spinning earth sensor</li> </ul>	<ul style="list-style-type: none"> <li>• Digital solar aspect indicator</li> <li>• Spinning optics for earth sensing</li> </ul>	<ul style="list-style-type: none"> <li>• Digital solar aspect indicator</li> <li>• Mechanically scanned earth sensor</li> </ul>
Attitude control with redundancy	<ul style="list-style-type: none"> <li>• Despin bearing assembly with motor</li> <li>• Four reaction jets or four magnetic torque coils</li> <li>• Nutation damper</li> <li>• Ground command spin axis control</li> </ul>	<ul style="list-style-type: none"> <li>• Momentum wheel with motor</li> <li>• Four magnetic torque coils</li> <li>• Nutation damper</li> <li>• Ground command control</li> </ul>	<ul style="list-style-type: none"> <li>• Three small wheels and motors</li> <li>• Twelve reaction jets or six magnetic torque coils</li> <li>• On-board control</li> </ul>
Velocity (orbit) control with redundancy	<ul style="list-style-type: none"> <li>• Two reaction jets</li> <li>• Ground command</li> </ul>	<ul style="list-style-type: none"> <li>• Two reaction jets</li> <li>• Ground command</li> </ul>	<ul style="list-style-type: none"> <li>• Two reaction jets</li> <li>• Ground command</li> </ul>
Fuel expulsion	<ul style="list-style-type: none"> <li>• Centrifugal feed</li> </ul>	<ul style="list-style-type: none"> <li>• Surface tension device</li> </ul>	<ul style="list-style-type: none"> <li>• Surface tension device</li> </ul>
Power generation	<ul style="list-style-type: none"> <li>• One solar panel</li> <li>• One stepper motor assembly and control</li> <li>• Two sliprings</li> </ul>	<ul style="list-style-type: none"> <li>• Two solar panels</li> <li>• One stepper motor assembly and control</li> <li>• One slipring</li> </ul>	<ul style="list-style-type: none"> <li>• Two solar panels</li> <li>• One stepper motor assembly and control</li> <li>• One slipring</li> </ul>

TABLE 18. ATTITUDE CONTROL SYSTEM COMPARISON

Accuracy: Pointing error < 0.1 degree  
Error rate < 0.01 deg/sec

	MBS Type 1	Reaction Wheels With Magnetic Torquing	Reaction Wheels With Reaction Jets	MBS Type 2 With Magnetic Torquing
Weight, pounds	66 including bearing, motor, fuel, instruments, redundancy	50 including redundant coils	64 (hydrazine) 110 (N <sub>2</sub> )	50 including redundant coils
Power, watts	28	30 maximum 24 average	24	26 maximum 22 average

TABLE 19. ATTITUDE CONTROL SYSTEM COMPARISON SUMMARY

<u>System</u>	<u>Comment</u>
Gravity-gradient	Do not provide adequate pointing capability
Magnetic torque control	
Reaction wheels	Provide adequate pointing capability
MBS Type 1	
MBS Type 2	System weight and power comparable
Mass expulsion	
	Provides adequate pointing capability, but may use excessive fuel
	Less fuel efficient than above three systems

## 7.11 REFERENCES

1. John Goldsmith, "Photovoltaic Power Systems," Advanced Propulsion Concepts: Proceedings of the Fourth Symposium, April 26-28, 1965.
2. Magnetic and Gravity Attitude Stabilization of Earth Satellites, Johns Hopkins University Applied Physics Report CM-996, May 1961.
3. A. J. Iorillo, "Nutation Damping," Hughes 2230.14/69, October 1964.
4. V. D. Landon and B. Stewart, "Nutation Stability of an Axisymmetric Body Containing a Rotor," J. Spacecraft and Rockets 1, 1964, pp. 682-684.
5. A. J. Iorillo, "Nutation Damping Dynamics of Axisymmetric Rotor Stabilized Satellites," ASME Winter Meeting, Chicago, Illinois, November 1965.
6. J. R. Velman, Attitude Dynamics of Dual-Spin Satellites, Hughes Aircraft Company, SSD 60419R, September 1966.

## 8. SUBSYSTEMS

Three major spacecraft subsystems of interest in this study are telemetry and command, power, and thermal control. The impact of the LAS-DRSS link on these subsystems is discussed below.

### 8.1 TELEMETRY AND COMMAND

The design of the telemetry and command subsystem is influenced strongly by the LAS-DRSS link, principally by the continuous communication capability. This implies that no LAS on-board storage is required for telemetry data to be sent to the ground or for commands to the spacecraft.

Elimination of command and telemetry storage on the LAS is the major impact of the LAS-DRSS link on these two systems. However, eliminating storage requires near continuous command and telemetry communication capability.

In Section 6.8 , a low data rate link was discussed which employed an omni or semi-omni antenna on the LAS and required only an earth coverage antenna on the DRS. Although the data rate must be low with such an antenna combination, this concept is attractive for a telemetry and command link because it allows continuous control of the spacecraft and ground reception of housekeeping data without requiring any antenna pointing.

In a typical command system (Figure 154), the output signal from the antenna is coupled to the command receivers which convert the command carrier to an IF signal, amplify it, and then detect the tones by a discriminator. A three-tone PCM-RZ command system can be used with one tone representing a "1", another tone indicating "0", and the third tone representing "execute". The audio output tones from the receivers go to the demodulator/decoders. Each demodulator/decoder time samples the receiver outputs, and the decoder being addressed locks onto whichever receiver has an output at the time a command is being sensed. The addressed demodulator/decoder then decodes the command. After the command stored in the decoder is verified via the telemetry link, an execute tone is sent, and the command is executed. An example of a command word format is shown in Figure 155.



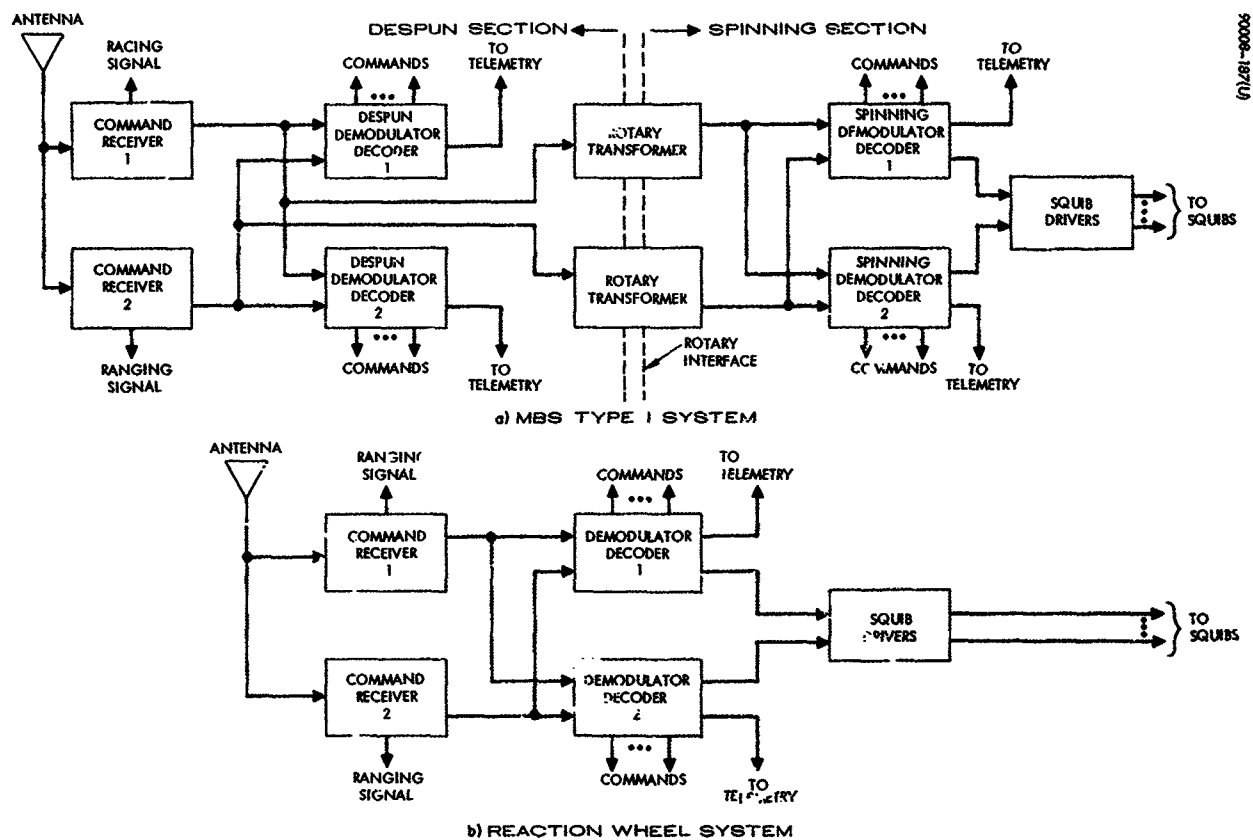


Figure 154. Command System Simplified Block Diagram

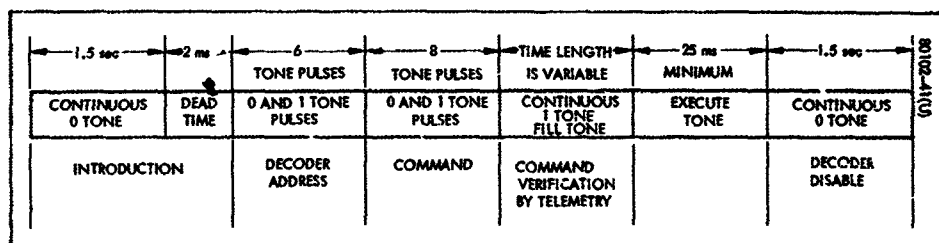


Figure 155. Command Word Format

The introduction portion of the command word is a continuous 0 tone of 1.5 seconds duration, followed by a 2-millisecond period of dead time. The decoder address and command portions of the word consist of a sequence of 0 and 1 tone pulses. The tone pulses are 2 milliseconds in duration, with 2 milliseconds of dead time between pulses. After the last tone pulse of the command portion is sent, a 2-millisecond dead time is followed by a continuous 1 tone period. The continuous 1 tone is present until the execute tone is sent, at which time a coincident pulse occurs on a decoder output line. If a command is to be continued as a sequential execution, the continuous 1 tone is maintained until the final execute tone. The last execute tone is followed by a continuous 0 tone of 1.5 seconds duration, which terminates the command word.

During the continuous 0 tone introduction, the demodulator stops sampling the two command receivers, locks onto one of them, and enables the decoder. The 14 tone pulses comprising the decoder address and command are stored by the decoder. The continuous 1 tone provides a signal to the demodulator to maintain lock to the receiver while the contents of the decoder register are being verified through telemetry data. The continuous 0 tone at the end of the command word provides for disabling of the decoder register and output circuitry.

Estimates of the weight, volume, and power requirements are presented in Table 20.

TABLE 20. COMMAND SUBSYSTEM  
WEIGHT, POWER, AND VOLUME

Unit	MBS Type 1			Three-Axis Stabilized		
	Weight, pounds	Power, watts	Volume, in <sup>3</sup>	Weight, pounds	Power, watts	Volume, in <sup>3</sup>
Demodulator/decoders, despun (2)	5.0	3.0	220	5.0	3.0	220
Demodulator/decoders spinning (2)	5.0	3.0	220	---	---	---
Command receivers (2)	9.0	3.2	460	9.0	3.2	460
Squib drivers	6.5	1.0	200	6.5	1.0	200
Rotary transformers	1.0	0.6	10	---	---	---
Total	26.5	10.8	1110	20.5	7.2	880

## 8.2 THERMAL CONTROL

The following features are important to consideration of the thermal control techniques to be used in the design of the LAS. These features apply both to spin-stabilized and three-axis stabilized versions of the spacecraft.

- 1) The low-altitude orbit is a relatively low external energy orbit. This means that some internal power dissipation is required to maintain acceptable temperatures.
- 2) The large external solar array will provide a large internal power dissipation density. This requires relatively large external radiating areas and careful attention to internal temperature gradients.
- 3) The above two features require that the primary feature of the overall thermal control system be based on either closely controlling the total amount of internal power dissipation about some average value or a variable external radiating area (active thermal control system).
- 4) An infrared camera with a requirement of a space radiating element will have an impact on the general arrangement.
- 5) The three-axis stabilized version and the nonspinning portions of the spin-stabilized version will have thermal gradients due to the concentration of the external solar load on one portion of the spacecraft.

### 8.2.1 Thermal Control System Selection

The low energy orbit and the high internal power dissipations are the primary features that must be considered in selection of a thermal control system. The orbit and mission requirements dictate a system that provides enough external radiating area to maintain adequate equipment temperatures at maximum power levels. With this system, the bulk spacecraft temperature is sensitive to internal power dissipation. For a passive system, this sensitivity is in the range of 0.5° to 1°F per watt. Therefore, large changes in internal power dissipation over the length of the mission are unacceptable. Power control either by thermostat-heaters, a system of limiters built into the power system, or some other similar system will be required with completely passive thermal control.

Temperature sensitivity to power as referred to here is a long-term overall function. The thermal capacity of the system is sufficient to damp out fairly large power changes over short-term periods, such as the 90-minute orbit period. For the same reason, the frequent eclipses will be a second-order perturbation on the internal equipment temperatures. A variable emissivity surface (active thermal control) will give a temperature sensitivity to internal power dissipation of 0.1° to 0.3°F per watt on the

internal bulk temperature. With an active thermal control system, minimum control over internal power dissipation is required. The type of thermal control system desired should be selected before the details of the thermal design are considered.

#### 8.2.2 High Internal Power Density

With the extended solar array, the power density available in the body of the spacecraft is on the order of twice that for a similar spin-stabilized body-mounted solar cell arrangement. With this larger amount of internal power combined with a sun-synchronous orbit which fixes the sun on one side of the spacecraft, particular attention to the thermal design will be required in order to reduce internal temperature gradients to a minimum. Depending on the type of overall thermal control system selected, the design will probably insulate the side of the spacecraft facing the sun to avoid external effects, locate the radiating areas on the nonsolar side, preferentially locate the high power dissipating equipment as close as possible to the radiating areas, and provide enough thermal conduction and radiation paths to reduce the temperature gradients. These designs would apply both to the three-axis stabilized version and the despun portions of the spin-stabilized version. For the spinning portion, the insulation requirement would be deleted.

#### 8.2.3 Infrared Camera Requirements

The selection and thermal integration of an infrared camera is the second most important feature to be decided after the selection of the basic overall thermal control system. Depending on which type of camera is selected, there will be an impact on the total design. Two of the candidate cameras require their own radiation systems for the low (100°K) temperatures required. If the infrared camera with the passive radiator is selected, a preferential location on the spacecraft where there are no back loads is required. For the present spacecraft designs, both with large extended solar arrays, such a location will present design difficulties because most of the spacecraft views either the earth, the sun, or the extended array.

#### 8.2.4 Ground Versus Automatic Control

Ground command through the relay link may be used to provide the control required by either a passive or active system, but the switching logic required in an automatic system is fairly simple so that little is added in weight, power, or complexity by employing automatic control, and fewer ground commands are needed. However, the continuous control capability afforded by the LAS/DRSS link allows backup control in case of automatic system failure.

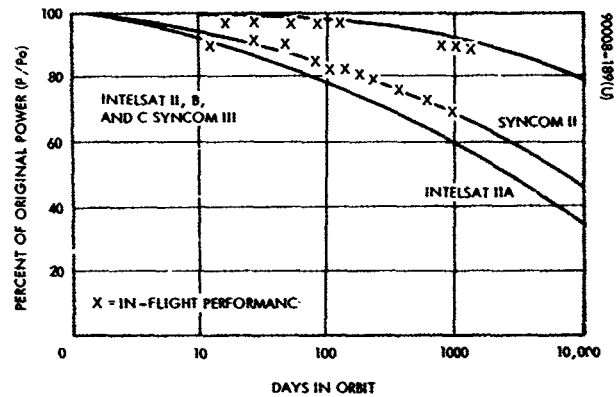


Figure 156. Solar Array Performance in Orbit

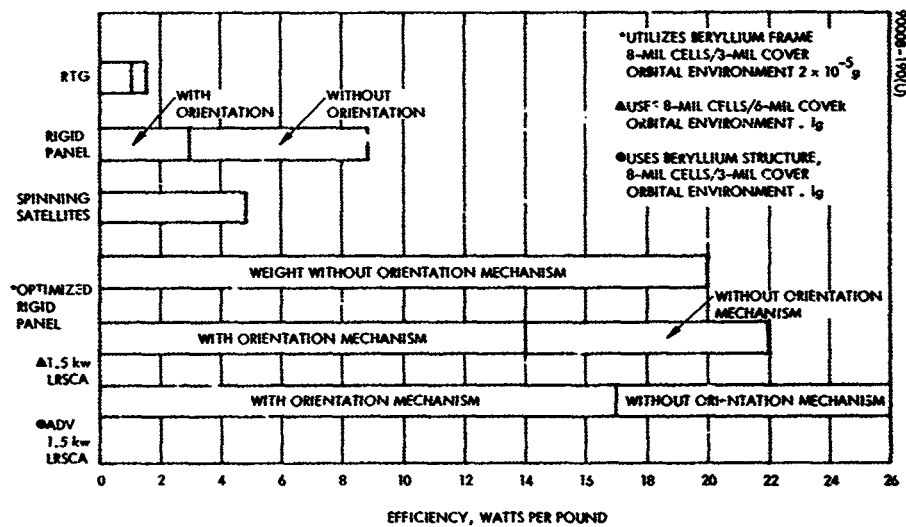


Figure 157. Gross Weight Efficiency for State-of-the-Art Solar Arrays

### 8.3 POWER SYSTEM

The power system consists of the solar array, solar array steering system, batteries, and charge-discharge controller. Each of these is discussed briefly below.

#### 8.3.1 Solar Array

Selection and optimization of the solar array configuration is dependent upon a number of factors which include:

- Orbital parameters (inclination and altitude)
- Spacecraft configuration and packaging constraints
- Environment
- Spacecraft power-time relationship
- Antenna shadowing
- Fabrication losses

Experience has shown that reliable solar arrays can be constructed. Figure 156 shows predicted and measured performance of solar panels for several satellites. Gross weight efficiency for state-of-the-art arrays is shown in Figure 157.

#### 8.3.2 Solar Array Steering System

The solar array steering system must point the array so that it is normal to the sun's radiation. In general, this will require two gimbal axes; but if the LAS orbit is sun-synchronous, only one gimbal axis, normal to the orbit plane, is required. Rotation about this axis must compensate for the rotational motion of the earth-oriented body, thus, the steering system provides relative rotation of the solar panel about this axis.

The steering control may be automatic or by ground command. An automatic system would employ a sun sensor and simple control electronics. Another type of automatic system would drive the single axis (sun-synchronous orbit) with constant speed. Position bias control by ground command would be provided to correct for the time of year and error buildup. Steering by ground command only would require one command every 15 seconds for 1 degree pointing accuracy.

Although the LAS/DRSS link will allow continuous ground commanded steering, there appears to be little advantage gained over an on-board system; and an automatic system will lessen the command link requirement and decrease ground processing and control operations. Ground control capability should be provided for backup, override, and initialization.

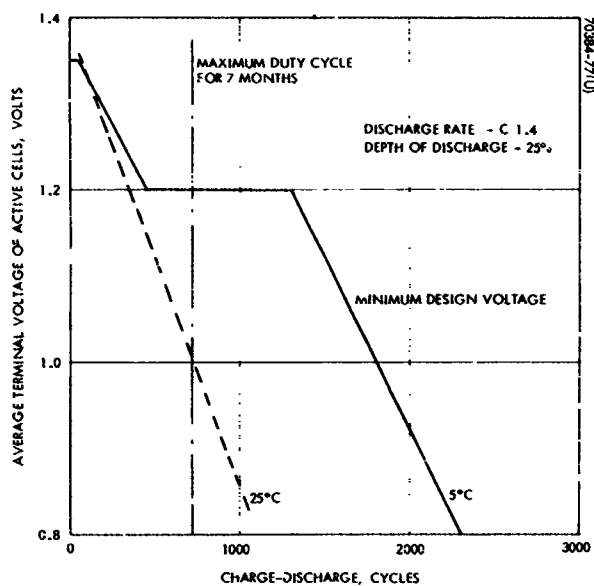


Figure 158. Average Silver-Cadmium Cell Voltage Versus Cycle as Function of Temperature

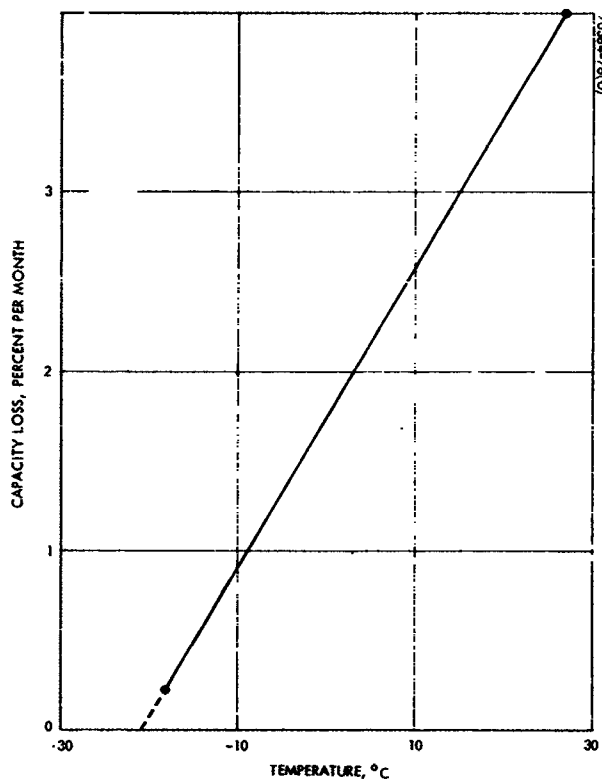


Figure 159. Estimated Open Circuit Stand Loss for Silver-Cadmium Batteries

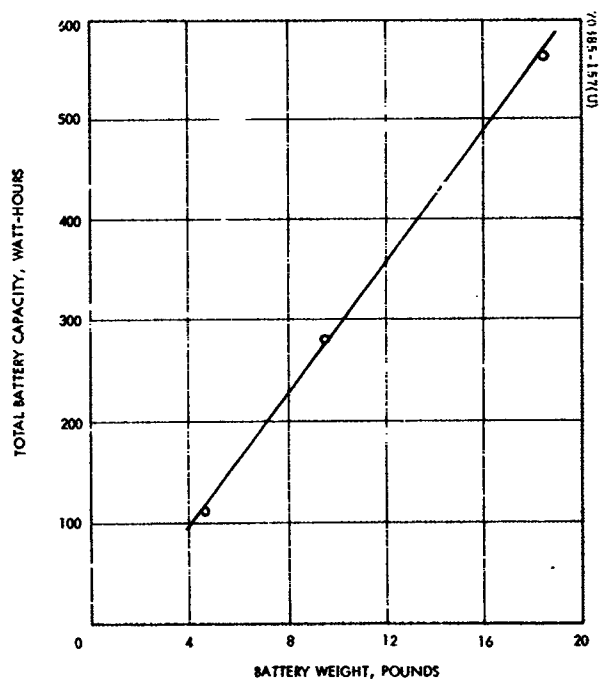


Figure 160. Battery Capacity Versus Temperature

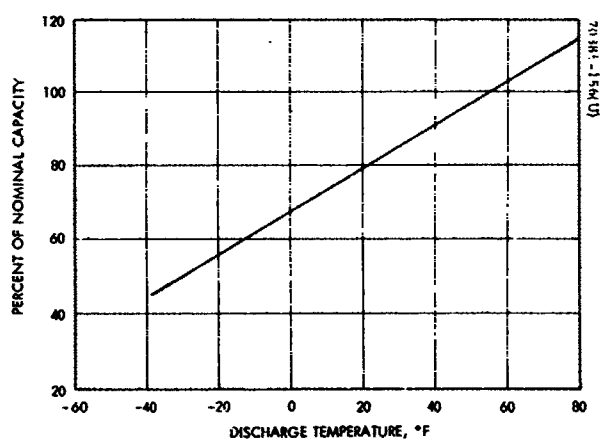


Figure 161. Silver-Cadmium Battery Weight Versus Capacity

### 8.3.3 Batteries

Although there are many different types of batteries in existence, only three types have been used. These are nickel-cadmium (Ni-Cd), silver-cadmium (Ag-Cd), and silver-zinc (Ag-Zn). Selection of the type of battery system is based on consideration of capacity, cycle life, and availability.

With excellent cycle life, coupled with good performance at low temperatures, nickel-cadmium cells are hermetically sealed to prevent loss of electrolyte and give maintenance-free performance, are easily recharged, and can provide fairly high peak currents. Limitations include a low energy output per unit of weight and volume. In addition, the Ni-Cd cell requires an overcharge for a full capacity input and exhibits limited charge retention.

Silver-cadmium cells combine some of the best features of the silver-zinc and nickel-cadmium types - i. e., they can provide a high capacity with a fairly long life. These cells also exhibit a high specific-energy-to-weight ratio, usually one and a half to two times greater than the nickel-cadmium cell, and have a greater charge retention. The silver-cadmium cell can be discharged to greater depths than the nickel-cadmium cell, can provide extended shelf life in both wet and dry conditions and a flat output voltage, and is mechanically rugged. Compared to silver-zinc, its limitations include lower cell voltage, lower specific energy ratio, and lack of availability. One significant feature of the silver-cadmium cell is that it is basically nonmagnetic.

The advantage of the silver-zinc cell over Ni-Cd and Ag-Cd cells lies principally in its ability to provide higher specific-energy-to-weight ratios. In addition, the Ag-Zn cells have an extremely high rate discharge capability.

Some parametric data on silver-cadmium batteries is presented in Figures 158 through 161.

### 8.3.4 Charge-Discharge Controller

The charge-discharge controller regulates the use of the solar array and batteries. When the solar array is exposed to the sun's energy, a portion of the solar array power is used to charge the batteries, and the rest is available for the required load. When the sun is eclipsed by the earth, the drop in solar array power is detected and the batteries discharge, supplying power to the load. As the LAS re-enters the sunshine, the rise in solar array power is detected and the batteries are charged. This controller can be simple and completely automatic. Ground control is necessary only for override.



## 9. CONFIGURATION

The principal factors in LAS configuration design are antenna mounting and pointing requirements, solar array size, method of stabilization, and shroud limitations. In Section 2.3, a representative LAS payload was selected; and in Section 2.4, it was estimated that this payload could be supported by a spacecraft of a weight well within the capability of the Thor-Delta booster. The shroud for this booster, shown in Figure 5, was taken as a basis for packaging design with the accompanying configuration consequences. One of these consequences is that the antenna(s) should be a square planar array(s), and that its side dimension must be limited to about 36 inches if it must be stowed between the spacecraft body and the shroud.

It was also estimated in Section 2.4 that the spacecraft requires approximately 350 watts of power. Assuming a sun synchronous orbit with a 35 percent eclipse time (Figure 9), the solar array must be capable of supplying 546 watts. When exposed to the sun, the spacecraft systems will require 65 percent or 350 watts, while 35 percent or 190 watts is used to charge batteries. During eclipse, the 350 watts is taken from the batteries.

The two fundamental stabilization configurations correspond to the MBS Type 1 and the three-axis methods, where, for this discussion, the latter includes the MBS Type 2. It was shown in Section 4.2 that both of these configurations can accommodate one or two antennas and a solar array. In that subsection, two mounting methods were also discussed — body mounting and solar panel mounting. The decision between one or two antennas depends on the requirement for data continuity. As discussed in Section 4.2, if no interruptions can be tolerated, two antennas must be used; whereas, only one is needed if two brief interruptions per orbit are allowed. Thus, there are three remaining choices influencing the configuration, as follows:

- |                       |                                     |
|-----------------------|-------------------------------------|
| 1) Number of antennas | One or two                          |
| 2) Mounting method    | Body-mounted or solar-panel mounted |
| 3) Stabilization      | MBS Type 1 or three-axis            |

All combinations yield eight different configuration and packaging concepts. In Section 4.8, solar panel mounting was not recommended, which leaves the following four combinations:

- 1) Two body-mounted antennas on an MBS Type 1
- 2) Two body-mounted antennas on a three-axis stabilized LAS
- 3) One body-mounted antenna on an MBS Type 1
- 4) One body-mounted antenna on a three-axis stabilized LAS

Configurations corresponding to combinations 1, 2, and 3, along with their packaging designs, for a 37-degree sun-synchronous orbit, are shown in Figures 162 through 164. Combination 4 can be visualized from Figure 163, where instead of two antennas, one would be mounted on the side facing away from the earth, i. e., outward from the plane of the drawing. Figure 165 indicates how two antennas might be mounted on the solar panels of a three-axis stabilized spacecraft. (Note the different shape of the solar arrays.) In Figure 163, the solar arrays extend relatively far from the spacecraft, whereas, in Figure 165, their long dimension is parallel to the orbit plane, allowing short feed lines to the antennas.

These figures are only for illustrative purposes to show the basic configuration concepts that are consistent with the packaging constraints and power requirements. More accurate and detailed configuration design requires specific knowledge of payload, power, thermal, and communication requirements.

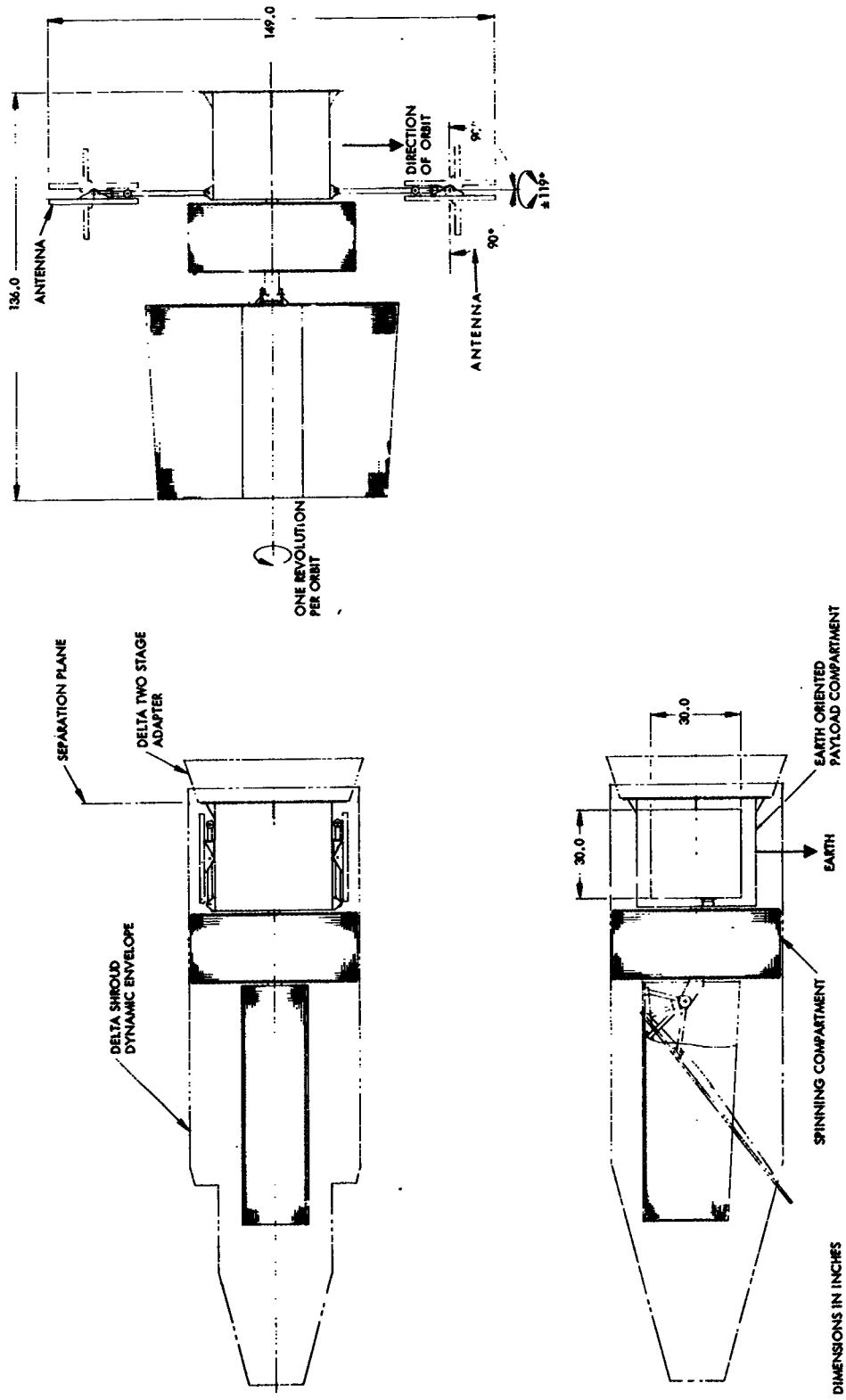


Figure 162. MBS Type 1 With Two Platform-Mounted Antennas

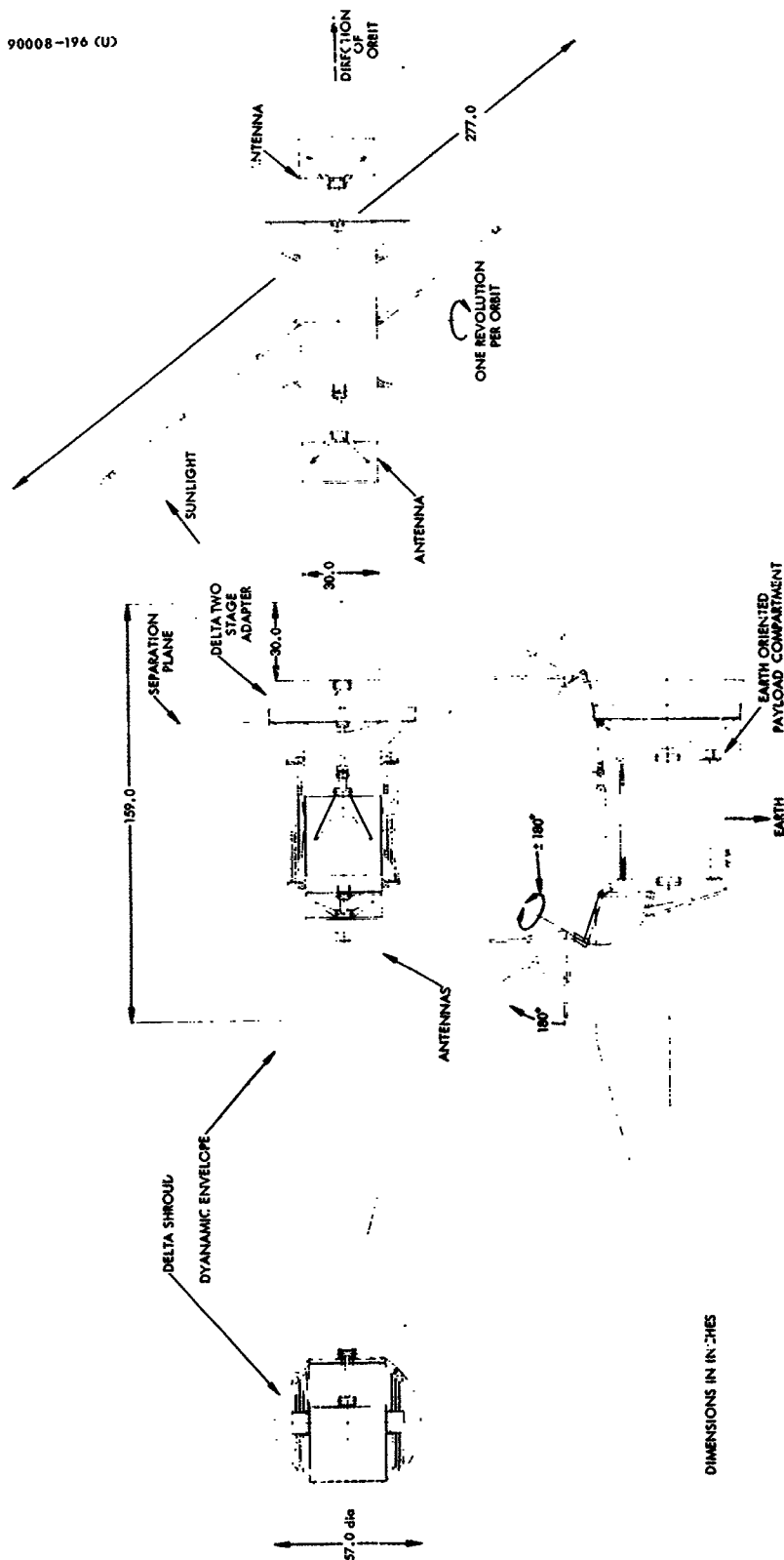


Figure 163. Three-Axis Stabilized With Two Body-Mounted Antennas

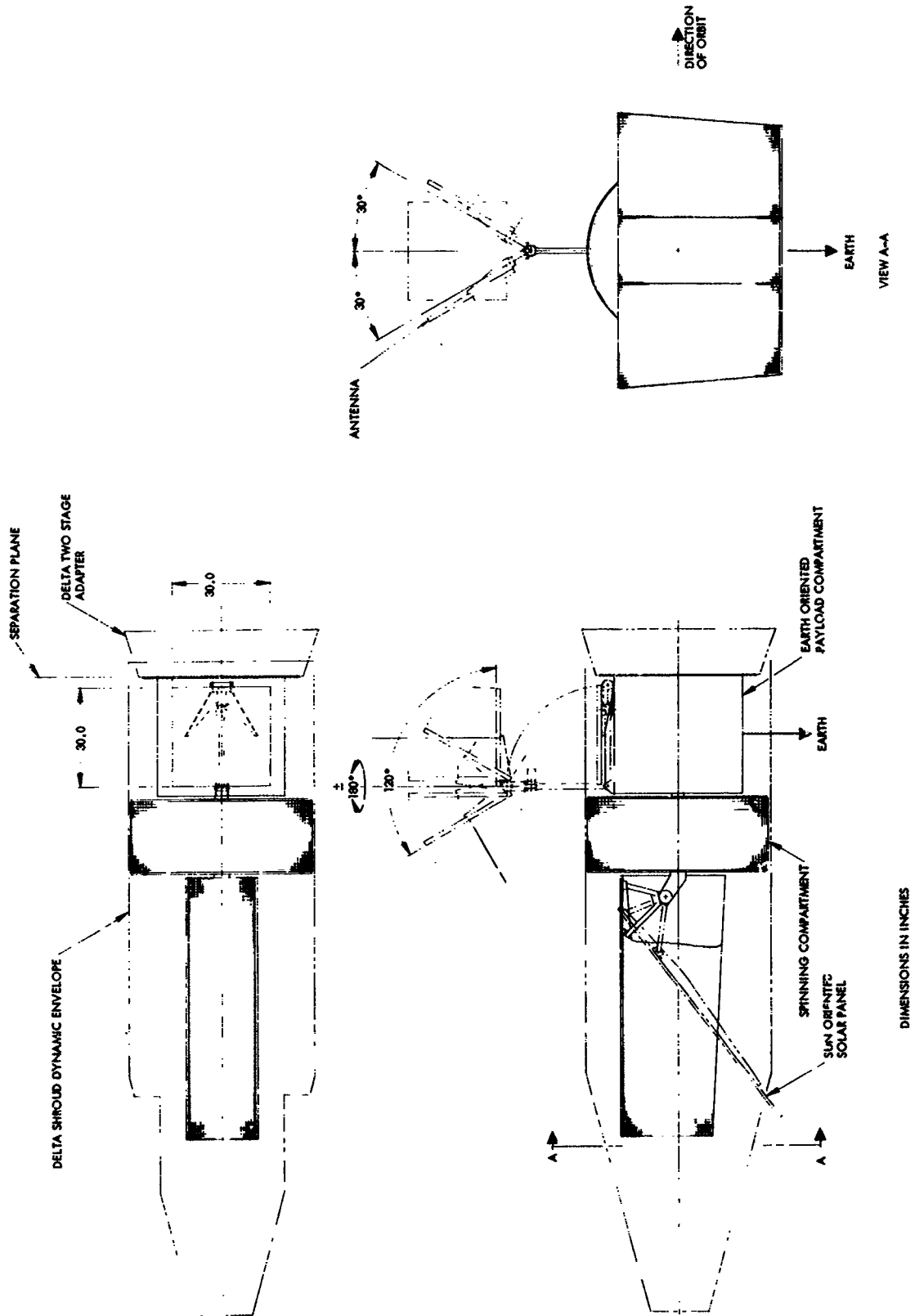


Figure 164. MBS Type 1 With One Body-Mounted Antenna

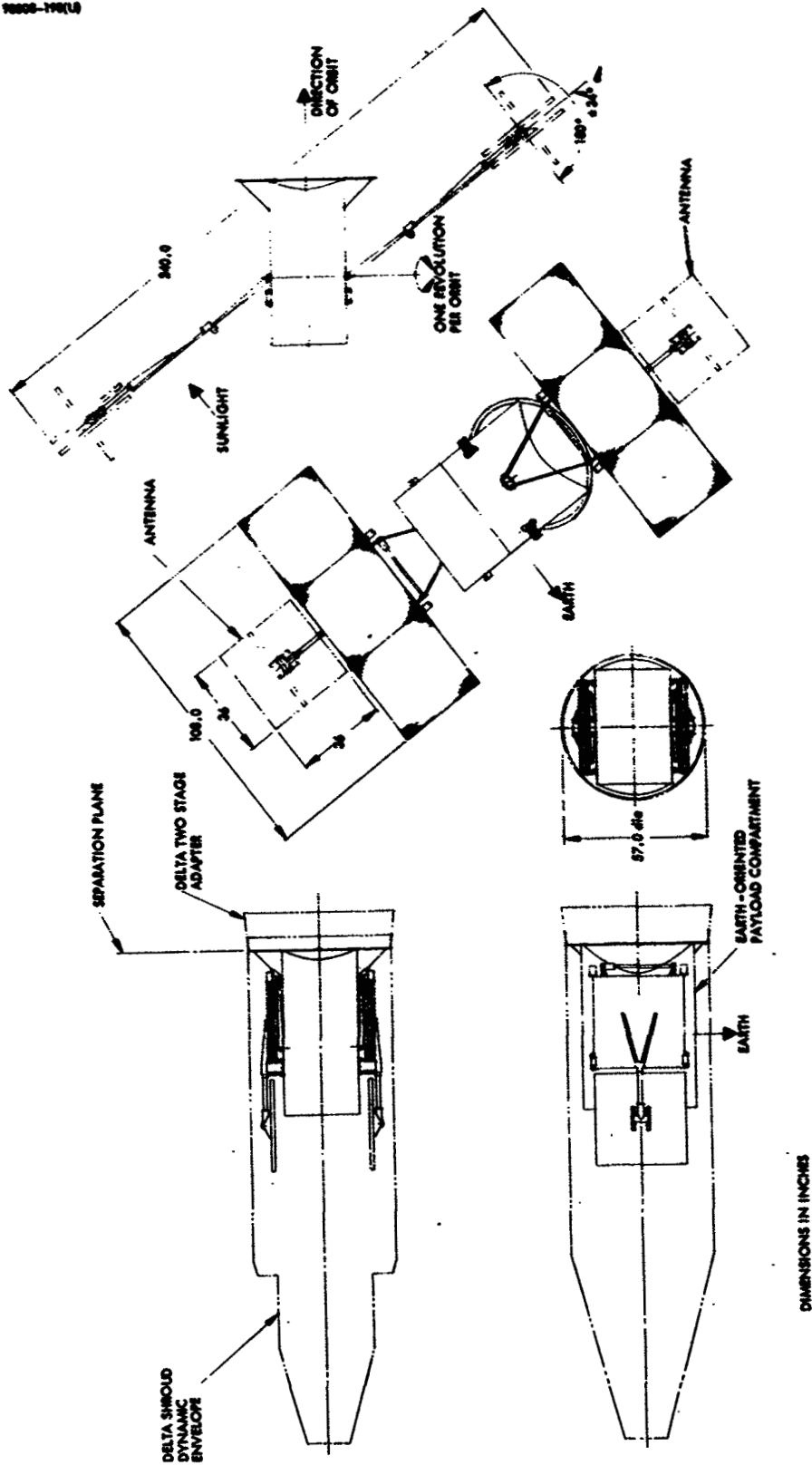


Figure 165. Three-Axis Stabilized With Two Solar Panel-Mounted Antennas

## 10. CONCLUSIONS AND RECOMMENDATIONS

The conclusions and recommendations presented here can be found within the preceding sections of this report, accompanied by analysis and discussion. They have been either briefly summarized or lifted word-for-word for presentation here. The topics are treated in order of their appearance.

### 10.1 MISSION, SENSORS, AND DATA BASEBAND

Earth observation has been selected as a representative mission for LAS-DRSS considerations because it is an important LAS application and provides the most stringent requirement on the LAS/DRSS system. A typical payload consisting of a four-spectral band scanning camera, remote interrogation package, and radar scatterometer will require a baseband of approximately 6 MHz. A spacecraft supporting this payload is within the capability of the Thor-Delta booster. Future earth observation payloads may have basebands of 20 or 30 MHz, or even larger.

### 10.2 LAS-DRSS VISIBILITY

For a DRSS consisting of two relay satellites and a single ground station, ground antenna elevation angles are small and accurate station-keeping will be required. The minimum percentage of visibility per orbit of an LAS from a single DRS will be 56 to 64 percent, corresponding to LAS altitudes from 200 to 700 n. mi., respectively.

### 10.3 ANTENNA POINTING

Uninterrupted data require two antennas, but with allowable interruptions a single antenna may be used. Based on the discussion of Sections 4.2 and 4.3, the following recommendations are made for these cases.

#### Two Antennas – Continuous Data

##### LAS Orbit Inclination Between 75 and 105 Degrees

The antennas should be mounted on extensions outward from the earth-oriented body in opposite directions along the axis coinciding with the velocity vector. These antennas should have two-gimbal steering systems with the primary axes in the LAS orbit plane oriented as shown in Figures 63 and 64.

##### LAS Orbit Inclination Less Than 75 Degrees and Greater Than 105 Degrees

The mounting should be the same as above, but the primary gimbal axes should be normal to the LAS orbit plane.

#### One Antenna – Interrupted Data

##### LAS Orbit Inclination Between 75 and 105 Degrees

The antenna should be mounted on an extension outward from the side of the spacecraft which faces away from the earth. The antenna should have three gimbal axes with the inertial axis (the one rigidly attached to the body-fixed extension) controlled by the solar panel steering system such that the primary axis remains normal to the sun vector.

##### LAS Orbit Inclination Less Than 75 Degrees and Greater Than 105 Degrees

The mounting should be the same as above, but a two-gimbal system can now be used with the primary axis normal to the orbit plane.



## 10.4 ANTENNAS

There are two fundamental antenna concepts: the electronically steered and the mechanically steered antenna. Because of the large required angular motion of the antenna, a mechanically steered array is recommended. For high gains, the saving in weight and power is considerable.

Four candidate antenna types for LAS application include the planar array, helical array, paraboloidal reflector, and rectangular horn.

Selection of one of these types involves a number of factors listed below:

- Shroud and packaging limitations
- Antenna size and shape
- Weight
- Gimbal and steering problems

Figure 116 allows a very crude comparison of size for a 15 GHz design frequency. Figure 118 shows a weight comparison for each frequency. From these four figures it can be seen that for every value of gain there is at least one antenna type which weighs less than a horn antenna. Thus, this antenna looks unfavorable on the basis of weight comparison. Also notice from these figures that, for every value of gain, either a helical array or parabolic reflector weighs less than a planar array, except for the lower frequencies. Figure 118 indicates that for 2.25 GHz there is a range of gain in the vicinity of 30 dB where the planar array weighs the least.

For design frequencies above 15 GHz, all antennas except the horn weigh less than 7 pounds for gains less than 40 dB, and this holds true at 8 GHz for gains less than 36 dB. Thus, for most applications, packaging considerations will influence the choice from among these antennas.

If a significant portion of the spacecraft has one or more flat exterior surfaces, the planar array is favored because it may be packaged within the booster shroud against the flat surface. If the stowed spacecraft structure can more easily accommodate volume rather than area, then either the helical array or parabolic reflector may be the best choice. For instance, the open conical structure of the Nimbus satellite can more easily accommodate a helical array than a planar array for a range of antenna gain. Figure 116 indicates that the helical array length and diagonal is less than the planar array side for gains less than 40 dB.

There are no obvious gimbaling or steering problems with any of the antennas about which general statements can be made.

Thus, from among the planar array, helical array, and parabolic reflector, for X-band frequencies and higher, the choice will depend mainly on the spacecraft structure and configuration and booster shroud limitations. For instance, for the Thor-Delta shroud shown in Figure 5, if the spacecraft has a box shape, a rigid, nonfoldable, square planar array must have a side dimension of less than about 36 inches if it is packaged between the spacecraft and shroud.

## 10.5 COMMUNICATIONS

The results of study in this area are not conclusions but, rather, parametric data from which trends can be noted and which may serve as a basis for communication system design. To evaluate the effect of carrier frequency variation, four representative frequencies were chosen to use in the analysis. These are 2.25, 8, 15.3, and 35 GHz. Frequency division multiplex/frequency modulation (FDM/FM) analysis combined with the range equation yielded the curves shown in Figure 123.

The information contained in Figure 123 is sufficient to trade off the major parameters in the LAS-DRS broad-band link. These basic curves can be easily modified to reflect other parameter spreads that may be suggested by possible hardware availability. A most important aspect of these curves is their use in indicating trends. Such an application resulted in the data contained in Tables 21 and 22.

Table 21 was constructed by collecting the peripheral parameters surrounding a nominal system operating point. This point is indicated on Figure 123 and is the intersection of  $C/N = 10$  dB and  $TT/N^1 = 30$  dB. The values of  $C/N$  and  $TT/N^1$  are of practical interest since they reflect parameters that might be applied to a possible multispectral camera. In Table 21 it was assumed also that the DRS antenna gain was constant at 40 dB. This infers a reduction in antenna size with increasing frequency, which is to be expected for structural reasons.

For comparison, in Table 22, the DRS antenna was assumed to be 30 feet in diameter for all frequencies. The DRS antenna gain thus varied from 43.4 dB at 2.2 GHz to 60.0 dB at 15.3 GHz. It is important to note that the required LAS power shown in Table 21 is virtually independent of carrier frequency for each baseband. In Table 22, however, the required LAS power is reduced in proportion to the increased gain of the DRS antenna. It can be expected that the actual tradeoff system parameters will be bracketed by the values shown in Tables 21 and 22.

The use of a broad coverage DRS antenna and an omnidirectional antenna on the LAS would allow a communication link that would be independent of a critical antenna pointing requirement. The geometry is shown in Figure 125. As expected, however, the reduction in antenna gain requires a compensatory increase in transmitter power and/or a reduction in information rate.

**TABLE 21. SUMMARY OF LAS-DRS LINK  
FDM/FM MODULATION  
(DRS Antenna Gain Assumed Constant at 40 dB)\***

Baseband, MHz	IF Bandwidth, MHz	DRS Antenna Gain, dB	Carrier Frequency, GHz	LAS EIRP, dBw	3 foot Antenna Gain, dB	Required Transmis- sion Power, dBw
2.5	16.5	40	2.2	36.0	23.5	2.5
			8.0	48.0	35.0	13.0
			15.3	54.5	41.0	13.5
5.0	33.0	40	2.2	39.0	23.5	15.5
			8.0	51.0	35.0	16.0
			15.3	57.5	41.0	16.5
10.0	66.0	40	2.2	42.0	23.5	18.5
			8.0	54.0	35.0	19.0
			15.3	60.5	41.0	19.5
20.0	131.0	40	2.2	45.0	23.5	21.5
			8.0	57.0	35.0	22.0
			15.3	63.5	41.0	22.5
30.0	196.0	40	2.2	47.0	23.5	23.5
			8.0	59.0	35.0	24.0
			15.3	65.5	41.0	24.5

\* Higher DRS gain (lower LAS EIRP) potential at higher frequencies.

TABLE 22. SUMMARY OF LAS-DRS LINK  
FDM/FM MODULATION

(Varying DRS Antenna Gain)\*

Baseband, MHz	IF Bandwidth, MHz	DRS Antenna Gain, dB	Carrier Frequency, GHz	LAS EIRP, dBw	3 foot Antenna Gain, dB	Required Transmis- sion Power, dBw
2.5	16.5	43.5	2.2	32.5	23.5	9.0
		54.5	8.0	33.5	35.0	-1.5
		60.0	15.3	34.5	41.0	-6.5
5.0	33.0	43.5	2.2	35.5	23.5	12.0
		54.5	8.0	36.5	35.0	1.5
		60.0	15.3	37.5	41.0	-3.5
10.0	66.0	43.5	2.2	38.5	23.5	15.0
		54.5	8.0	39.5	35.0	4.5
		60.0	15.3	40.5	41.0	-0.5
20.0	131.0	43.5	2.2	41.5	23.5	18.0
		54.5	8.0	42.5	35.0	7.5
		60.0	15.3	43.5	41.0	2.5
30.0	196.0	43.5	2.2	43.5	23.5	20.0
		54.5	8.0	44.5	35.0	9.5
		60.0	15.3	45.5	41.0	4.5

\* Assumes a 30-foot diameter parabolic reflector with a 50 percent efficiency.

Figure 126a shows the DRS EIRP and the DRS transmitter power as a function of LAS predetection bandwidth. A nominal C/N ratio of 10 dB is assumed at the carrier frequencies of 2.2, 8.0, and 15.3 GHz. From Figure 126a, it is evident that a DRS transmitter power of 10 watts at 2.2 GHz is required for an LAS predetection bandwidth of 100 Hz. The information rate for this bandwidth is of the order of 100 bits/sec.

Figure 126b shows LAS EIRP and LAS transmitter power as a function of DRS predetection bandwidth. It is assumed also that the signal-to-noise ratio is 10 dB at carrier frequencies of 2.2, 8.0, and 15.3 GHz. The DRS system noise temperatures relative to those of the LAS show the effect of the earth's 300°K blackbody temperature. In this case, transmission of 500 bits/sec of telemetry data would require an LAS transmitter power of approximately 100 watts.

From the information contained in Figure 126, it can be concluded that the use of a broad coverage link is restricted to low data rate information, telemetry, and command.

## 10.6 ATTITUDE CONTROL

It was shown in Sections 7.4 and 7.5 that for the anticipated disturbance torques on a representative LAS, both gravity-gradient and magnetic torque control lack sufficient pointing capability for optical imaging missions. A mass expulsion system will provide the required pointing accuracy, but for conventional systems with lower limits on thrust impulse, the stringent pointing requirements of advanced missions will result in excessive use of fuel.

A mass expulsion system must use propellant to compensate for both secular (spacecraft-fixed) and cyclical disturbance torques, which makes this system innately less fuel-efficient than the three remaining systems.

These three systems — reaction wheels, MBS Type 1, and MBS Type 2 — are dual-mode systems. The reaction wheel system requires, in addition to the reaction wheels, a torque-producing system to reduce the angular momentum of the wheels when it becomes too large. The MBS Type 1 and MBS Type 2 systems are dual-spin systems and require a torque-producing system to orient the spin axis. Either magnetic torque or mass expulsion systems may be employed for these secondary functions. If mass expulsion is used, then the primary system is sized so that correction torques from the mass expulsion system occur less often than once an orbit and, hence, compensate for only the secular disturbance torques. Table 17 presents the components for the above three systems.

The basic LAS requirement under consideration in this study is the ability to transmit data to, and receive from, a data relay satellite. For high data rate, optical imaging missions, this requirement necessitates a directive steerable antenna. But, as shown in Section 4.2, one or two such antennas can be accommodated by the two basic spacecraft configurations associated with the three candidate attitude control systems. Thus, the LAS-DRS communication link has little influence in making the choice from among these systems.

In Section 2, a representative, earth observation mission was selected. Based on LAS orbit geometry and the particular sensors chosen (see Section 2.3), the LAS pointing accuracy must be 0.1 degree and angular rates must be less than 0.01 deg/sec. Using the control system concepts of the preceding subsections along with available hardware knowledge for these stabilization requirements, the weight and power requirements of the preferred systems were estimated. The results are shown in Table 23.

It can be seen from Table 23 that all of these systems are comparable in weight and power. Although the MBS Type 1 system is shown as being the heaviest, the weight estimate includes the bearing assembly which is a significant part of the spacecraft structure, and so, more equitably, part of this weight should be assigned to the structure rather than all to the control system. Thus, based on power and weight estimates and control capability, no clear choice is evident from among the reaction wheel system, and the MBS Type 1 and MBS Type 2 systems.

However, other considerations such as reliability, flexibility, growth capability, and cost may provide a basis for a selection.

A summary of attitude control system conclusions is presented in Table 24.

## 10.7 SUBSYSTEMS

Three major spacecraft subsystems of interest in this study are telemetry and command, power, and thermal control. Of these three, the telemetry and command subsystem is most obviously affected by the LAS-DRSS communication link, for that link eliminates the need for LAS on-board storage of data or commands. The link makes possible continuous ground control of the power and thermal control systems, but there appears to be no general advantage to such control. Specific LAS payload and configuration requirements may dictate otherwise in special cases; but, in general, on-board control is preferable. However, backup, override, and initialization control of these systems by ground command through the relay link is recommended.

TABLE 23. ATTITUDE CONTROL SYSTEM COMPARISON

Accuracy: Pointing error < 0.1 degree  
Error rate < 0.01 deg/sec

	MBS Type 1	Reaction Wheels With Magnetic Torquing	Reaction Wheels With Reaction Jets	MBS Type 2 With Magnetic Torquing
Weight, pounds	66 including bearing, motor, fuel, instrum redundancy	50 including redundant coils	64 (hydrazine) 110 (N <sub>2</sub> )	40 including redundant coils
Power, watts	28	30 maximum 24 average	24	26 maximum 22 average

TABLE 24. ATTITUDE CONTROL SYSTEM COMPARISON SUMMARY

<u>System</u>	<u>Comment</u>
Gravity gradient	Do not provide adequate pointing capability
Magnetic torque control	
Reaction wheels	Provide adequate pointing capability
MBS Type 1	
MBS Type 2	System weight and power comparable
Mass expulsion	
	Provides adequate pointing capability, but may use excessive fuel
	Less fuel efficient than above three systems

## 10.8 CONFIGURATION

The two fundamental stabilization configurations correspond to the MBS Type 1 and the three-axis methods, where, for this discussion, the latter includes the MBS Type 2. It was shown in Section 4.2 that both of these configurations can accommodate one or two antennas and a solar array. In that subsection, two mounting methods were also discussed — body mounting and solar panel mounting. The decision between one or two antennas depends on the requirement for data continuity. As discussed in Section 4.2, if no interruptions can be tolerated, two antennas must be used; whereas, only one is needed if two brief interruptions per orbit are allowed. Thus, there are three choices influencing the configuration as follows:

- |                       |                                     |
|-----------------------|-------------------------------------|
| 1) Number of antennas | One or two                          |
| 2) Mounting method    | Body-mounted or solar-panel mounted |
| 3) Stabilization      | MBS Type 1 or three-axis            |

All combinations yield eight different configuration and packaging concepts. In Section 4.8 solar panel mounting was not recommended, which leaves the following four combinations:

- 1) Two body-mounted antennas on an MBS Type 1
- 2) Two body-mounted antennas on a three-axis stabilized LAS
- 3) One body-mounted antenna on an MBS Type 1
- 4) One body-mounted antenna on a three-axis stabilized LAS

Based upon the Delta shroud limitations and a requirement for a 540 watt solar array, configurations corresponding to combinations 1, 2, and 3, along with their packaging designs, for a 37-degree sun synchronous orbit, are shown in Figures 162 through 164. Figure 165 indicates how two antennas might be mounted on the solar panels of a three-axis stabilized spacecraft.

These figures are only for illustrative purposes to show the basic configuration concepts that are consistent with the packaging constraints and power requirements. More accurate and detailed configuration design requires specific knowledge of payload, power, thermal, and communication requirements.



## GLOSSARY

LAS	Low altitude satellite
DRS	Data relay satellite
DRSS	Data relay satellite system
LOS	Line of sight
Changeover	Process of steering a directive antenna from one DRS toward another
Primary gimbal axis	Antenna gimbal axis which orients secondary gimbal axis
Secondary gimbal axis	Gimbal axis fixed rigidly to antenna
Inertial (third) gimbal axis	Gimbal axis which is fixed to spacecraft structure and orients primary gimbal axis
Orbit sphere	Sphere defined by rotating a circular earth orbit in all directions

## APPENDIX I. SOLAR RADIATION FORCES

### I-1. INTRODUCTION

The electromagnetic energy radiated from the sun imposes a force on an intercepting surface. The following analysis develops the fundamental relationships required to determine the force acting on a body due to this radiation.

## I-2. ANALYSIS

### Solar Pressure

The solar constant near the earth is the rate at which energy is received at a unit surface. This number has been measured by several experimenters<sup>1</sup>. This quantity may be considered as a flux density with energy rate defined as the flux. The value of this constant<sup>1</sup> is  $S = 1.95 \text{ cal/cm}^2\text{-min}$ . The energy due to this radiation can be interpreted in two ways, both leading to the same result. First, consider the energy to be due to the kinetic energy of photons with cumulative mass,  $2m$ , so that

$$E = \text{energy} = mc^2$$

where  $c$  is the speed of light  $= 3 \times 10^8 \text{ m/sec}$ , which is the speed of the photons. This same result is obtained from Einstein's relationship, where  $m$  is the mass equivalent of the energy  $E$ . Then an equivalent momentum is given by

$$M = \frac{E}{c} = mc$$

Now as mentioned above,

$$S = \frac{dE}{dt} \text{ per unit area}$$

To determine the force on a totally absorbing unit area surface, or in other words the solar pressure constant  $P$ , Newton's law can be used, i. e., force is proportional to rate of change of momentum:

$$\begin{aligned} P &= \frac{dM}{dt} \text{ per unit area} \\ &= \frac{d}{dt} \left( \frac{E}{c} \right) \text{ per unit area} \\ &= \frac{1}{c} \frac{dE}{dt} \text{ per unit area} \\ &= \frac{S}{c} \end{aligned}$$

---

<sup>1</sup>A. J. Drummond, et al., 'The Eppley JFL Solar Constant Measurement Experiment,' XVII International Astronautical Congress Proceedings, Madrid, 1966.

Thus,

$$\begin{aligned}
 P &= \frac{1.95}{(3 \times 10^8)(60)} = 1.083 \times 10^{-10} \frac{\text{cal}}{\text{cm}^2 - \text{m}} \\
 &= (4.186 \times 10^7)(10^4)(1.083 \times 10^{-10}) \\
 &= 45.3 \frac{\text{dyne-cm}}{\text{m}^3} \\
 &= 0.453 \frac{\text{dyne}}{\text{m}^2} = 4.53 \times 10^{-5} \frac{\text{dyne}}{\text{cm}^2} \\
 &= 9.48 \times 10^{-8} \text{ lb/ft}^2
 \end{aligned} \tag{1}$$

#### Incident Radiation

For an arbitrary orientation of a surface element  $dA$  with unit normal  $\bar{n}$  to the radiation direction unit vector  $\bar{v}$ , the intercepted energy rate is

$$S_i = S \cos \theta \tag{2}$$

where  $\theta$  is the angle between  $\bar{n}$  and  $\bar{v}$ . The force on the surface element may be separated into two components: one normal to the surface and a shear force tangential to the surface. For completely absorbed radiation, i.e., the incident radiation

$$F_{nl} = P \cos^2 \theta dA$$

$$F_{sl} = P \cos \theta \sin \theta dA$$

These relationships follow from Equation 2 and the geometry of Figure I-1. It will be more convenient to deal with pressure in the subsequent analysis, so define

$$P_{nl} = \frac{F_{nl}}{dA} = P \cos^2 \theta \tag{3}$$

$$P_{sl} = \frac{F_{sl}}{dA} = P \cos \theta \sin \theta \tag{4}$$

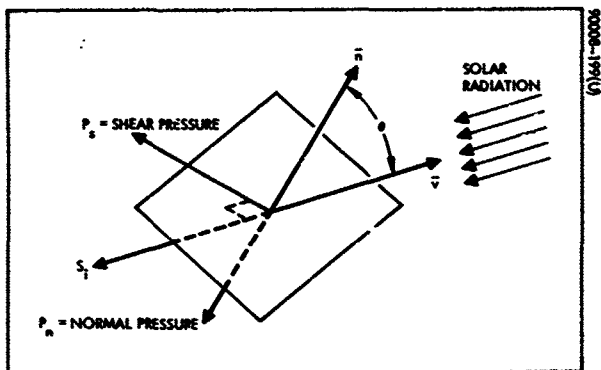


Figure I-1. Radiation-Surface Geometry

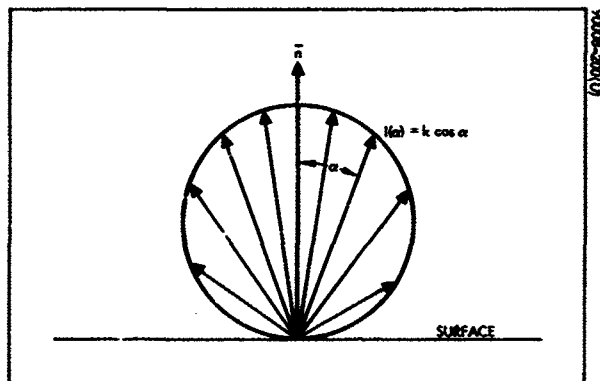


Figure I-2. Cosine Law Diffusion Pattern

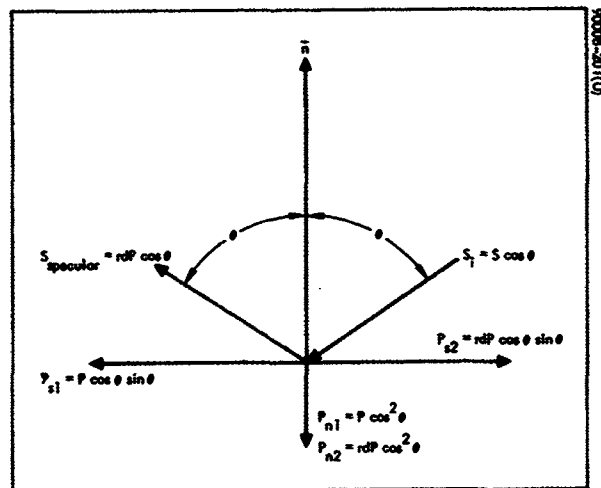


Figure I-3. Pressure Geometry

Three things can happen to this incident radiant energy: 1) it can be reflected, 2) it can be absorbed, and 3) the energy can be internally transmitted away from the surface element. But by continuity,

$$r + a + t = 1 \quad (5)$$

where

$r$  = reflectivity

$a$  = absorptivity

$t$  = transmissivity

### Reflected Radiation

Reflected radiation may be either specular or diffuse. Specular reflection refers to reflection obeying Snell's law of optics that the angle of incidence and angle of departure are the same. Diffusely reflected radiation is that energy which is spread in some pattern over all directions from the surface. The most common model of the diffused radiation pattern is the cosine law, i. e., that the intensity of diffused radiation from a point on the surface varies from the normal at that point as the cosine of the angle, but that the radiation is symmetric with respect to the normal. This intensity pattern is illustrated in Figure I-2 where a cross section of the symmetrical three-dimensional pattern is shown and where the length of the vectors are proportional to the intensity.

The relative amounts of specular and diffuse reflection are a function of the surface properties of the material, and so a characteristic of the material called the diffusivity is defined by

$$d = \text{diffusivity} = \frac{\text{specularly reflected radiation}}{\text{total reflected radiation}} \quad (6)$$

### Specular Reflection

The pressure due to specular reflection can be decomposed into its normal and shear components. From Figure I-3 it can be seen that

$$P_{n2} = rdP \cos^2 \theta \quad (7)$$

$$P_{s2} = -rdP \cos \theta \sin \theta \quad (8)$$

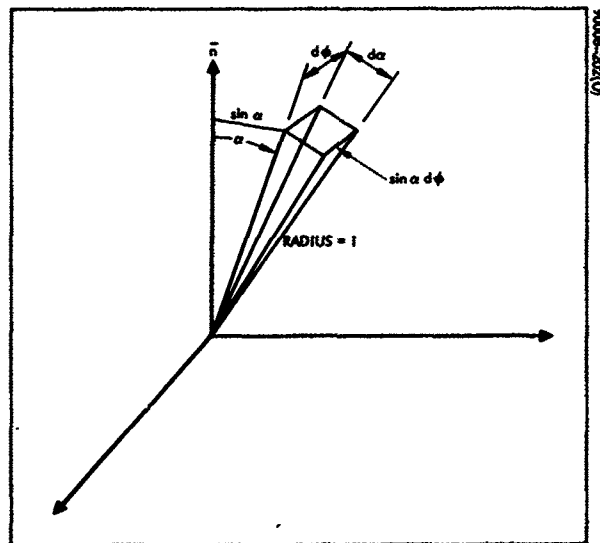


Figure I-4. Element of Hemispherical Surface

### Diffuse Reflection

Due to the postulated model of diffuse reflection with a symmetric pattern about the surface normal, the pressure and force due to this radiated energy is normal to the surface. To determine the pressure, consider Figure I-4 where a surface element of a hemisphere is shown. If the radiation flux intensity directed away from O is proportional to a function  $I(\alpha)$ , then the pressure normal to the surface can be expressed as

$$P_{n3} = r(1-d) P \cos \theta \int [I(\alpha)] dA \quad \text{normal to surface} \quad (9)$$

where, by continuity,  $I(\alpha)$  must be normalized such that

$$\int I(\alpha) dA = 1 \quad (10)$$

where the integration is over surface of the unit hemisphere. The model used here for diffuse reflection is the cosine law, i. e.,

$$I(\alpha) = k \cos \alpha \quad (11)$$

Then with  $dA = \sin \alpha \, d\alpha \, d\phi$ , Equation 10 becomes

$$\int_0^{2\pi} \int_0^{\frac{\pi}{2}} k \cos \alpha \sin \alpha \, d\alpha \, d\phi = k\pi = 1$$

or

$$k = \frac{1}{\pi}$$

Substituting this value into Equation 11 and Equation 11 into 9 and noting that

$$[I(\alpha)]_{\text{normal}} = I(\alpha) \cos \alpha$$

$$\begin{aligned} P_{n3} &= r(1-d) P \cos \theta \int_0^{2\pi} \int_0^{\frac{\pi}{2}} \frac{1}{\pi} \cos^2 \alpha \sin \alpha \, d\alpha \, d\phi \\ &= \frac{2}{3} r(1-d) P \cos \theta \end{aligned} \quad (12)$$



### Absorbed Radiation

The radiation of concern here is that which is absorbed but not transmitted away. The effect of such energy absorption is to raise the temperature of the surface, but if it is assumed that the surface is in equilibrium and that the temperature has been stabilized, then this energy must be re-radiated. Furthermore, it is assumed that this re-emission has a diffuse radiation pattern identical to that of diffuse reflection. Then, as in the previous discussion, the pressure is normal to the surface and given by

$$P_{n4} = \frac{2}{3} aP \cos \theta \quad (13)$$

### Combination of Effects

The expressions for the normal and shear pressures are merely the sum of the corresponding previous results. Thus, from Equations 3, 4, 7, 8, 12, and 13,

$$\begin{aligned} P_n &= P_{n1} + P_{n2} + P_{n3} + P_{n4} \\ &= P \cos^2 \theta + rdP \cos^2 \theta + \frac{2}{3} r(1-d) P \cos \theta + \frac{2}{3} aP \cos \theta \\ &= P \left\{ \cos^2 \theta (1+rd) + \frac{2}{3} \cos \theta [r(1-d) + a] \right\} \end{aligned} \quad (14)$$

$$\begin{aligned} P_s &= P_{s1} + P_{s2} = P \cos \theta \sin \theta - rdP \cos \theta \sin \theta \\ &= (1-rd) P \cos \theta \sin \theta \end{aligned} \quad (15)$$

Now, if the surface is well insulated and in equilibrium, then at each surface element very little energy will be transmitted away, i. e.,  $t \approx 0$ .

Assuming  $t = 0$ , from Equation 5

$$a = 1-r$$

and Equation 14 becomes

$$P_n = P \left\{ \cos^2 \theta (1+rd) + \frac{2}{3} \cos \theta (1-rd) \right\} \quad (16)$$

Suppose, however, that it is assumed that all incident energy is either reflected or transmitted away, i. e., that none is absorbed and re-emitted. Then,

$$a = 0 \quad t \neq 0 \quad \text{and} \quad t = 1 - r$$

$$P_n = P \left\{ \cos^2 \theta (1 + rd) + \frac{2}{3} \cos \theta [r (1 - d)] \right\} \quad (17)$$

What actually occurs lies somewhere between these two extremes, i. e.,  $a \neq 0$ ,  $t \neq 0$ . It is difficult to measure the absorptivity in addition to the reflectivity and diffusivity. Thus, in order to eliminate the absorptivity from Equation 14, as was done above in Equations 16 and 17 with rather dubious assumptions, define new parameters — the effective reflectivity,  $R$ , and the effective diffusivity,  $D$ , by

$$R + t = 1 \quad \text{or} \quad R = r + a \quad (18)$$

and

$$D = \frac{\text{specularly reflected radiation}}{\text{total reflected and re-emitted radiation}} \quad (19)$$

These are more practical definitions for which the parameters are more amenable to experimental determination, because in laboratory measurements it is difficult to separate reflected radiation from re-emitted radiation.

Following the analysis above, it can be seen that these definitions have the effect of making  $a = 0$  in Equation 14 and replacing  $r$  by  $R$  and  $d$  by  $D$ , so that

$$P_n = P \left\{ (1 + RD) \cos^2 \theta + \frac{2}{3} R (1 - D) \cos \theta \right\} \quad (20)$$

$$P_s = (1 - RD) P \cos \theta \sin \theta \quad (21)$$

The above analysis is summarized in block diagram form in Figure I-5.

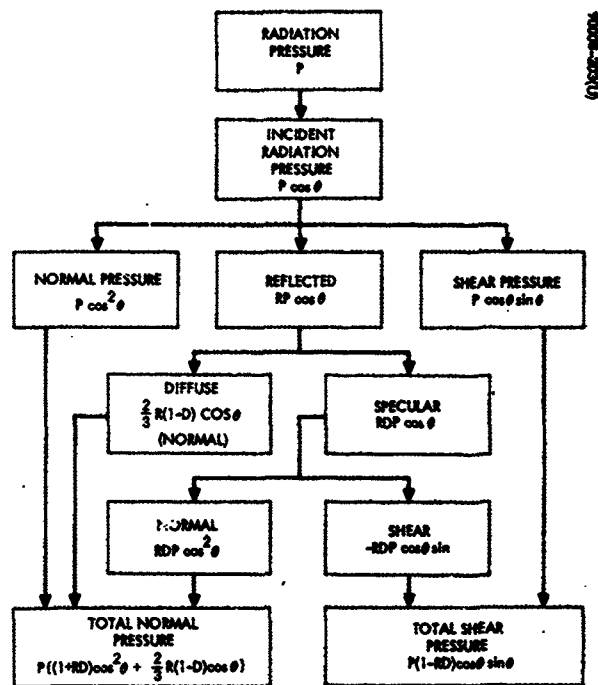


Figure I-5. Solar Radiation Pressure Computation Flow

### Vector Algebra

The above analysis could have been performed using vector algebra, but since the geometry is relatively simple it was felt that the above approach provides the most lucid development. However, from the expressions in Equations 20 and 21 and Figure I-1, the conversion to vector algebra is readily apparent. Since  $\bar{v}$  and  $\bar{n}$  are unit vectors,

$$\cos \theta = \bar{v} \cdot \bar{n}$$

$$\sin \theta = \bar{v} \times \bar{n}$$

and since  $\bar{n}$  is directed outward and likewise  $\bar{v}$  is directed outward but toward the sun,

$$0 \leq \theta \leq \frac{\pi}{2}$$

And so the correct directions for the two pressure components are given by

$$\bar{P}_S = (1-RD) P (\bar{v} \cdot \bar{n}) [(\bar{n} \times \bar{v})] \quad (22)$$

$$\bar{P}_n = -P \{(\bar{v} \cdot \bar{n})^2 (1+RD) + \frac{2}{3} (\bar{v} \cdot \bar{n})(1-RD)\} \bar{n} \quad (23)$$

### Forces and Torques

The forces on a surface A are given by

$$F_n = \int_A P_n dA \quad (24)$$

$$F_s = \int_A P_s dA \quad (25)$$

And the torque about a point 0 is given by

$$\begin{aligned} T &= \int_A \bar{V} \times d\bar{F}_n + \int_A \bar{V} \times dF_s \\ &= \int_A \bar{V} \times \bar{P}_n dA + \int_A \bar{V} \times \bar{P}_s dA \end{aligned} \quad (26)$$

where  $\bar{V}$  is the vector distance from 0 to the surface element dA.

## APPENDIX II. COMMUNICATION SYSTEM TECHNICAL ANALYSIS

This appendix contains the detailed analyses which serve as a basis for the conclusions of Section 6.

### II-1. ANALYSIS OF FDM/FM SYSTEM

The carrier-to-noise ratio  $(C/N)_{IF}$  in the carrier predetection bandwidth  $B_{IF}$  is

$$(C/N)_{IF} = \frac{C}{\eta_c B_{IF}} \quad (1)$$

where  $\eta_c$  is the noise power spectral density in the carrier predetection bandwidth. Lines of constant  $(C/N)_{IF}$  are plotted in Figure II-1.

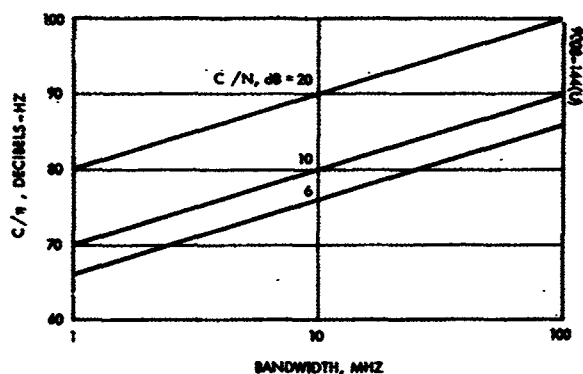


Figure II-1. Lines of Constant  
Carrier-to-Noise Ratio

The TT-to-noise ratio in the  $i^{\text{th}}$  channel at the output of the carrier FM demodulator is<sup>1</sup>

$$\left(\frac{TT}{N}\right)_i = \frac{3}{2} \left[ \frac{B_{IF} (\Delta f_{ci})^2}{(f_{ube}^3 - f_{lbe}^3)} \right] (C/N)_{IF} \quad (2)$$

<sup>1</sup>See Equation 59.

where<sup>2</sup>

$$(f_{ube}^3 - f_{lbe}^3) = 6\Delta f_i (f_i)^2 + 2(\Delta f_i)^3 \quad (3)$$

and

$$\Delta f_i = \frac{f_{ube} - f_{lbe}}{2} \quad (4)$$

If half the  $i^{th}$  channel bandwidth is much less than the  $i^{th}$  subcarrier frequency, the following approximation can be used<sup>3</sup>

$$(f_{ube}^3 - f_{lbe}^3) \approx 6\Delta f_i (f_i)^2, \Delta f_i \ll f_i \quad (5)$$

The exact expression, Equation 4, will be used here because  $\Delta f_i \ll f_i$  does not hold for the lower subcarriers.

Define

$$K_i = f_{ube}^3 - f_{lbe}^3 \quad (6)$$

From Equations 3 and 6

$$K_i = 6\Delta f_i (f_i)^2 + 2(\Delta f_i)^3 \quad (7)$$

From Equations 2 and 6, the TT-to-noise ratio in the  $i^{th}$  channel is

$$\left(\frac{TT}{N}\right)_i = \frac{3}{2} \left[ \frac{B_{IF} (\Delta f_{ci})^2}{K_i} \right] (C/N)_{IF} \quad (8)$$

---

<sup>2</sup>See Equation 61.

<sup>3</sup>See Equation 62.

and the FM improvement in the  $i^{\text{th}}$  channel is

$$I_i = \frac{\left(\frac{TT}{N^i}\right)_i}{(C/N)_{IF}} = \frac{3}{2} \left[ \frac{B_{IF} (\Delta f_{ci})^2}{K_i} \right] \quad (9)$$

On rearranging Equation 8 and substituting Equation 1,

$$(\Delta f_{ci})^2 = \frac{2}{3} \left(\frac{TT}{N^i}\right)_i \frac{K_i \eta_c}{C} \quad (10)$$

The above relation fixes the required peak carrier deviation due to each subcarrier,  $\Delta f_{ci}$ , as a function of:

$\left(\frac{TT}{N^i}\right)_i$  = required TT-to-noise ratio in  $i^{\text{th}}$  channel at output of carrier demodulator (this is function of subcarrier demodulator)

$K_i$  = function of location and width of  $i^{\text{th}}$  channel

$\frac{C}{\eta_c}$  = ratio of carrier power available to noise spectral density in carrier predetection bandwidth

Using Carson's Rule<sup>4</sup> to determine the predetection bandwidth  $B_{IF}$ ,

$$B_{IF} = 2(\Delta f_{cp} + f_m) \quad (11)$$

where  $\Delta f_{cp}$  is the peak carrier deviation and  $f_m$  is the highest modulating frequency. From Equation 11,

$$\Delta f_{cp} = \frac{B_{IF}}{2} - f_m \quad (12)$$

<sup>4</sup>This rule of thumb ensures that distortion of the signal because loss of sidebands outside  $B_{IF}$  is negligible.

Since the modulating subcarriers are assumed sinusoidal, the rms deviation of the carrier due to the  $i^{\text{th}}$  subcarrier is

$$\Delta f_{ci_{\text{rms}}} = \frac{\Delta f_{ci}}{\sqrt{2}} \quad (13)$$

and the carrier rms deviation is the root-sum-square of the rms deviations due to the individual subcarriers:

$$\Delta f_{c_{\text{rms}}} = \sqrt{\sum_{i=1}^n (\Delta f_{ci_{\text{rms}}})^2} \quad (14)$$

Combining Equations 13 and 14:

$$\Delta f_{c_{\text{rms}}} = \sqrt{\sum_{i=1}^n \frac{(\Delta f_{ci})^2}{2}} \quad (15)$$

Define a peaking factor  $P$  which relates peak to rms values for the  $n$  subcarriers:<sup>5</sup>

$$\Delta f_{cp} = P \Delta f_{c_{\text{rms}}} = P \sqrt{\sum_{i=1}^n \frac{(\Delta f_{ci})^2}{2}} \quad (16)$$

$$(\Delta f_{cp})^2 = \frac{P^2}{2} \sum_{i=1}^n (\Delta f_{ci})^2 \quad (17)$$

Combining Equations 17 and 10:

$$(\Delta f_{cp})^2 = \frac{P^2}{2} \sum_{i=1}^n \frac{2}{3} \left( \frac{TT}{N_i} \right) \frac{K_i \eta_c}{C} \quad (18)$$

---

<sup>5</sup>Section II-5 discusses peaking factors.



and making the TT-to-noise ratio identical in all channels:

$$\left(\Delta f_{cp}\right)^2 = \frac{P^2}{3} \left(\frac{TT}{N^i}\right) \frac{\eta_c}{C} \sum_{i=1}^n K_i \quad (19)$$

Combining Equations 12 and 19:

$$\left(\frac{B_{IF}}{2} - f_m\right)^2 = \frac{P^2}{3} \left(\frac{TT}{N^i}\right) \frac{\eta_c}{C} \sum_{i=1}^n K_i \quad (20)$$

Expanding the left side of Equation 20:

$$\frac{B_{IF}^2}{4} - f_m B_{IF} + f_m^2 = \frac{P^2}{3} \left(\frac{TT}{N^i}\right) \frac{\eta_c}{C} \sum_{i=1}^n K_i \quad (21)$$

#### Example: 25 100-kHz Channels

Assume LAS sensor data are in the form of 25 100-kHz wide channels. Guard bands of 10 kHz are included within the 100 kHz at upper and lower band edges. The total baseband is 2.5-MHz wide and is shown in Figure II-2.

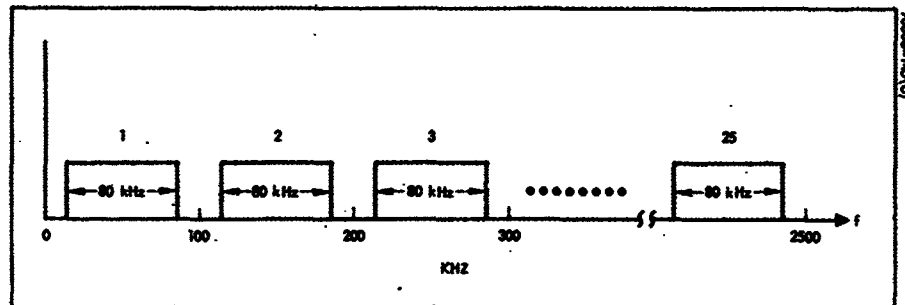


Figure II-2. Possible Baseband for Data From LAS

A baseband consisting of  $n$  channels results, each one of which will be represented by a test tone at frequency  $f_i$  which is centered in the channel of bandwidth  $2\Delta f_i$ . The highest baseband frequency is then

$$f_m = f_n + \Delta f_n \quad (22)$$

Using Equations 22 and 7 in 21, and multiplying through by 1:

$$B_{IF}^2 - 4(f_n + \Delta f_n)B_{IF} + 4(f_n + \Delta f_n)^2 = \frac{4}{3}P^2 \left( \frac{TT}{N^1} \right) \frac{\eta_c}{C} \sum_{i=1}^n \left[ 6\Delta f_i (f_i)^2 + 2(\Delta f_i)^3 \right] \quad (23)$$

The above equation is used to determine the lines of constant  $(TT/N^1)$  in Figure 123. For a given value of  $(TT/N^1)$ , and for a given set of sub-carrier channels ( $n$ ,  $f_i$  and  $\Delta f_i$  for  $i=1, 2, 3, \dots, n$ ), and an assumed peaking factor<sup>6</sup> $P$ , there is a relationship between  $B_{IF}$  and  $C/\eta_c$ .

For this example, the data-bearing portion of each channel is

$$B = \text{channel bandwidth} - \text{guard bands} \quad (24)$$

$$B = 100 - 2 \times 10 = 80 \text{ kHz} \quad (25)$$

The half-channel bandwidth is

$$\Delta f_i = \frac{B}{2} = 40 \text{ kHz for all } i \quad (26)$$

The TTs are at the center of the channels and are given by

$$f_i = (i - 0.5) (100 \text{ kHz}), i = 1, 2, 3 \dots n \quad (27)$$

where

$$n = 25 \quad (28)$$

<sup>6</sup>See Section II-5.

Now

$$\sum_{i=1}^n \left[ 6\Delta f_i (f_i)^2 + 2(\Delta f_i)^3 \right]$$

can be calculated for use in Equation 23 by using Equations 26, 27, and 28.

By computer, it is

$$\sum_{i=1}^n \left[ 6\Delta f_i (f_i)^2 + 2(\Delta f_i)^3 \right] = 1.24982 \times 10^{19} \quad (29)$$

Also,

$$f_n = 2.45 \times 10^6 \quad (30)$$

and

$$\Delta f_n = 4.0 \times 10^4 \quad (31)$$

Since  $n = 25$ , the statistically calculated peaking factor of 10 dB can be used (see Section II-5).

$$P = 10 \text{ dB} = 3.162 \quad (32)$$

This value was chosen so that the actual voltage (i. e., sum of all the sub-carriers) would exceed the calculated voltage more than 0.1 percent of the time but less than 1.0 percent of the time.

Solving Equation 23 using Equations 29 through 32 for  $(TT/N)_i$  of 20, 30, and 40 dB, p-p/rms yields the curves of Figure 123a.

Figures 123b through e are similar to Figure 123a except that basebands of 5, 10, 20, and 30 MHz were assumed. Figure 123 is summarized in Table II-1.

TABLE II-1. SUMMARY OF VALUES USED  
IN FIGURE 123

Figure	Number of Channels	Bandwidth of Each Channel, *	Total Baseband Bandwidth, MHz
123a	25	100	2.5
123b	50	100	5.0
123c	100	100	10.0
123d	200	100	20.0
123e	300	100	30.0

\* This includes the guard bands at the upper and lower band edges.

## II-2. DETAILED ANALYSIS OF FREQUENCY MODULATED TRANSMISSION LINK

A frequency modulated carrier is described by

$$V_{fm}(t) = A_c \cos \omega_c t + \frac{\Delta f_c}{f_m} \sin \omega_m t \quad (33)$$

where  $\omega_c$  is the nominal carrier center frequency,  $\Delta f_c$  is the peak frequency deviation, and  $f_m$  is the modulating frequency.

The peak carrier radian frequency deviation,  $2\pi\Delta f_c$ , is given by

$$2\pi\Delta f_c = K_1 A_m \quad (34)$$

and  $K_1$  is the carrier modulator constant, radians/volt.

The mean received carrier power is given by

$$C = \int_0^{2\pi} \frac{|A_c \cos(\omega_c t)|^2}{2\pi} d\omega t = A_c^2 \frac{\left[\frac{\omega t}{2} + \frac{\sin 2\omega t}{4}\right]_0^{2\pi}}{2\pi} \quad (35)$$

from which

$$C = \frac{A_c^2}{2} \text{ watts} \quad (36)$$

By use of the following relations

$$\cos(x \sin \theta) = J_0(x) + 2 \sum_{n=1}^{\infty} J_{2n}(x) \cos 2n\theta \quad (37)$$

$$\sin(x \sin \theta) = 2 \sum_{n=1}^{\infty} J_{2n-1}(x) \sin (2n-1)\theta \quad (38)$$

the frequency modulated carrier can be written in the following form:

$$\begin{aligned}
 V_{fm}(t) = A_c \left[ J_0 \left( \frac{\Delta f_c}{f_m} \right) \cos \omega_c t + \sum_{n=1}^{\infty} J_{2n} \left( \frac{\Delta f_c}{f_m} \right) \left[ \cos \left\{ \omega_c t + 2n\omega_m t \right\} \right. \right. \\
 \left. \left. + \cos \left\{ \omega_c t - 2n\omega_m t \right\} \right] - \sum_{n=1}^{\infty} J_{2n-1} \left( \frac{\Delta f_c}{f_m} \right) \left[ \cos \left\{ \omega_c t - (2n-1)\omega_m t \right\} \right. \right. \\
 \left. \left. - \cos \left\{ \omega_c t + (2n-1)\omega_m t \right\} \right] \right] \quad (39)
 \end{aligned}$$

where  $J_r(x)$  is a Bessel function of the first kind and order,  $r$ , with argument  $x$ .

It is clear that a frequency modulated wave requires a transmission bandwidth which is infinitely wide, since its spectrum is of infinite extent. In a real system of finite bandwidth, some of the spectral components must necessarily be rejected. The removal of these sidebands represents distortion of the modulating signal,  $s(t)$ , and loss of predetection signal power. However, for  $r > \Delta f_c / f_m$ ,  $J_r(\Delta f_c / f_m)$  decreases in amplitude very rapidly. This characteristic allows small, if non-zero, distortions of the signal to be realized in a band-limited situation. In the following analysis, it will be assumed that essentially all of the unmodulated carrier power is retained in the transmission bandwidth, and fully recovered in the predetection bandwidth.

The output signal voltage of the carrier demodulator is

$$V_o(t) = K_2 2\pi\Delta f_c s(t) \quad (40)$$

where  $K_2$  is the carrier demodulator constant in volts/radian.

The mean post-detection signal power is defined by

$$S_o = \int_0^T \frac{V_o^2(t) dt}{T} \text{ watts} \quad (41)$$

$T$  is the modulating signal period. Substituting Equation 40, Equation 41 becomes

$$S_o = \int_0^T \frac{[2\pi K_2 \Delta f_c s(t)]^2}{T} dt \text{ watts} \quad (42)$$

Note that the postdetection spectrum is double-sided, of both the signal and noise. If  $s(t)$  is a sinusoidal modulating signal, then Equation 42 becomes

$$\begin{aligned} S_o &= \frac{\int_0^{2\pi} [2\pi K_2 \Delta f_c \cos \omega_m t]^2 d\omega_m t}{2\pi} \\ S_o &= 2\pi K_2^2 (\Delta f_c)^2 \left[ \frac{\omega_m t}{2} + \frac{\sin 2\omega_m t}{4} \right]_0^{2\pi} \\ S_o &= 2\pi^2 K_2^2 (\Delta f_c)^2 \end{aligned} \quad (43)$$

This demodulated signal is uncorrupted by noise, which will be considered separately.

A simplifying assumption is made regarding the nature of the noise present in the carrier demodulator predetection bandwidth,  $B_{if}$ . It is assumed that the continuous noise variable can be represented by discrete spectral components spaced  $\Delta f$  cycles apart, of the same amplitude as the continuous uniform spectrum. This approximation can be observed in Figure II-3.

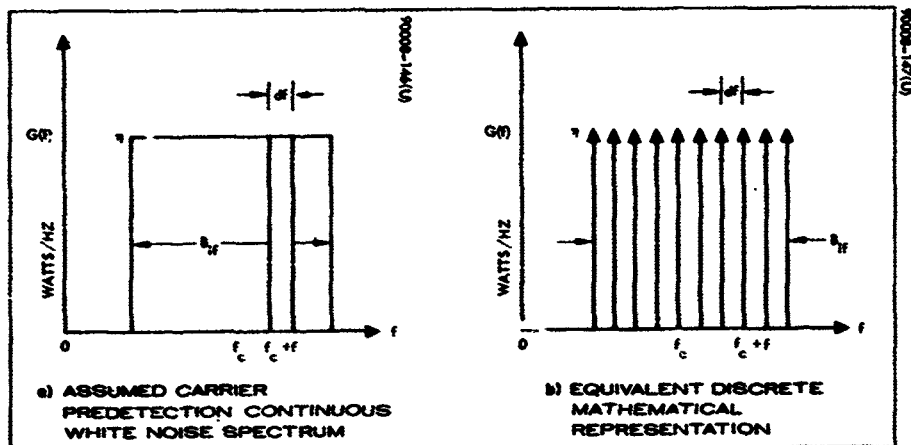


Fig re II-3. Noise Approximation

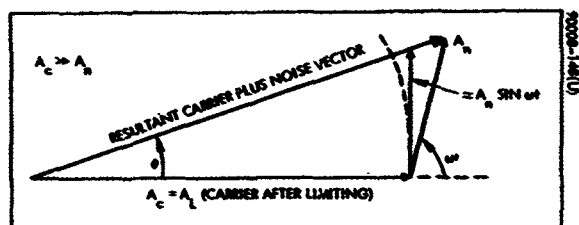


Figure II-4. Phasor Diagram of Carrier Plus Noise for Some Time, t



The noise variable in the predetection bandwidth is given by

$$n(t) = A_n \cos(\omega_c + \omega)t, \quad \frac{A_n^2}{2} = \eta_c \text{ watts/Hz} \quad (44)$$

An FM phasor diagram can be drawn to represent the situation of carrier plus noise (Figure II-4). It can be seen from this diagram that the noise signal produces both amplitude and frequency modulation of the carrier.

The limiter essentially removed the in-phase noise component, leaving only the quadrature component,  $A_n \sin \omega t$ . This graphical result can also be demonstrated analytically by combining the carrier and noise terms algebraically as

$$N_{fm}(t) = A_n \cos(\omega_c + \omega)t + A_c \cos \omega_c t \quad (45)$$

Using the trigonometric identity  $\cos(x + y) = \cos x \cos y - \sin x \sin y$ , Equation 45 can be rewritten

$$\begin{aligned} N_{fm}(t) &= A_n (\cos \omega_c t \cos \omega t - \sin \omega_c t \sin \omega t) + A_c \cos \omega_c t \\ &= (A_c + A_n \cos \omega t) \cos \omega_c t - A_n \sin \omega_c t \sin \omega t \\ &= A(t) \cos(\omega_c t + \theta) \end{aligned} \quad (46)$$

whose amplitude and phase components are<sup>7</sup>

$$\begin{aligned} A &= [(A_c + A_n \cos \omega t)^2 + (A_n \sin \omega t)^2]^{1/2} \\ \theta &= \tan^{-1} \left[ \frac{A_n \sin \omega t}{A_c + A_n \cos \omega t} \right] \end{aligned}$$

<sup>7</sup>From the identity:

$$A \cos \theta - B \sin \theta = \sqrt{A^2 + B^2} \cos \left[ \theta + \tan^{-1} \left( \frac{A}{B} \right) \right]$$

For the case of small mean noise power compared with mean carrier power ( $A_c \gg A_n$ ), these components of  $N_{fm}(t)$  become

$$A \approx A_c \left( 1 + \frac{A_n}{A_c} \cos \omega t \right) \quad (47)$$

$$\theta \approx \frac{A_n}{A_c} \sin \omega t \quad (48)$$

The condition  $A_c \gg A_n$  is usually realized in practice. An FM system is designed so that a minimum carrier-to-noise ratio  $(C/N)_{IF}$  is obtained (termed threshold), which satisfies this condition.

The noise modulated carrier is given at demodulator limiter output by

$$N_{fm}(t) = A_L \cos \left( \omega_c t + \frac{A_n}{A_c} \sin \omega t \right) \quad A_c \equiv A_L \quad (49)$$

The noise signal FM wave is identical in form to the information signal frequency modulated wave, where

$$\frac{A_n}{A_c} \text{ is analogous to } \frac{\Delta f_c}{f_m}; \text{ i. e., a deviation ratio } \ll 1 \quad (50)$$

The noise reduction mechanism is based on this last relationship. The noise components in the carrier predetection bandwidth produce small phase angle modulation of the carrier, whereas the data signal produces large variations of this angle. This makes the two carrier modulations separable.

The frequency deviation of the noise-modulated carrier, in this region of operation, is given by the time rate of change of the phase angle. Using Equation 48, the postdetection (output) noise voltage becomes

$$V_n(t) = K_2 \frac{d\theta}{dt} = K_2 \omega \frac{A_n}{A_c} \cos \omega t \quad (51)$$

This expression indicates that the contribution of the predetection noise components to the postdetection noise voltage will be proportional to their frequency spacing away from the carrier, i. e., components at predetection filter band edge will produce the greatest output voltage.

Since a sinusoidal form was assumed for each of the discrete predetection noise components, the incremental mean postdetection noise power for each component is given by

$$dN_o = \frac{K_2^2 \omega^2}{2} \left( \frac{A_n}{A_c} \right)^2 df = \left( \frac{K_2 \omega}{A_c} \right)^2 \eta_c df \quad (52)$$

The carrier postdetection noise spectrum is viewed by each channel filter. Figure II-5 shows the limits of the  $i^{\text{th}}$  channel bandwidth on the carrier demodulator output noise spectrum, namely

- $f_i$  = center frequency of  $i^{\text{th}}$  subcarrier channel, Hz
- $f_{lbei}$  = lower  $i^{\text{th}}$  channel band edge frequency, Hz
- $f_{ubei}$  = upper  $i^{\text{th}}$  channel band edge frequency, Hz
- $B_i$  = channel equivalent noise bandwidth, Hz; equal to  $(f_{ubei} - f_{lbei})$  for zonal case

Note that physically realizable predetection filters exhibit attenuation at band edges, tending to reduce this effect.

The noise power present in each of the channel bandwidths will next be computed. If the assumption is made that superposition holds (because  $A_n/A_c \ll 1$ ), and that no intermodulation of noise components occurs, then the total noise power present in the  $i^{\text{th}}$  channel bandwidth is given by

$$N_i = 2 \int_{f_{lbei}}^{f_{ubei}} \frac{K_2^2 \omega^2}{A_c^2} \eta_c df \text{ watts} \quad (53)$$

where the limits of the integration correspond to the band edges of the  $i^{\text{th}}$  subcarrier channel bandwidth,  $B_i$ .

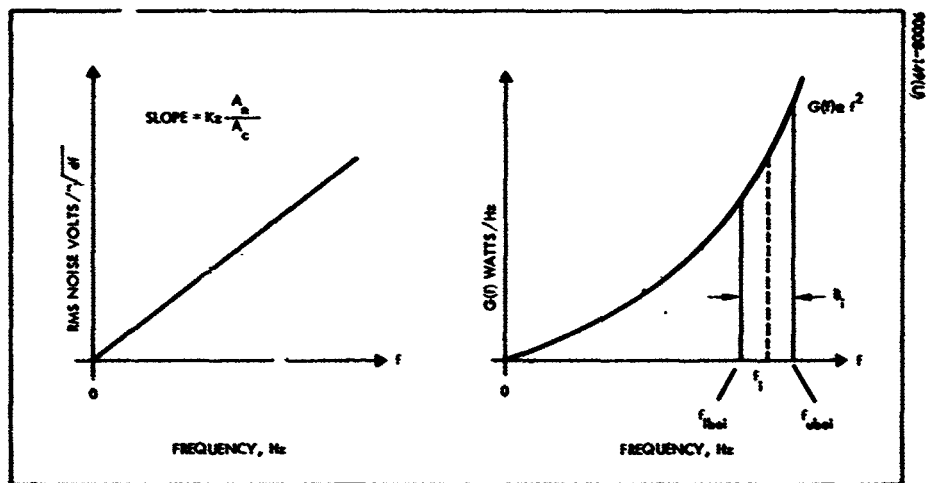


Figure II-5. Noise Voltage and Power Spectrum at Output of Carrier Demodulator

Carrying through, this integration results in

$$N_i = \frac{8\pi^2 K_2^2 \eta_c}{3A_c^2} (f_{ubei}^3 - f_{lbei}^3) \text{ watts} \quad (54)$$

Recognizing that  $C = A_c^2 / 2$ , Equation 54 can be rewritten as

$$N_i = \frac{4\pi^2 K_2^2 \eta_c}{3C} (f_{ubei}^3 - f_{lbei}^3) \text{ watts} \quad (55)$$

In order to relate this expression to the carrier predetection C/N, Equation 55 can be multiplied by  $B_{if}/B_{if}$ , the carrier noise bandwidth, to give

$$N_i = \frac{4\pi^2 K_2^2}{3B_{if}} (f_{ubei}^3 - f_{lbei}^3) \left(\frac{N}{C}\right)_{if} \quad (56)$$

since  $\eta_c B_{if} = N_{if}$ , the total noise power in the carrier predetection bandwidth.

The frequency modulating TT can be considered to be a simple sinusoidal modulating signal of frequency,  $f_i$ , with respect to the carrier. The mean signal power present in the  $i^{\text{th}}$  channel bandwidth is then given by Equation 42, where

$$S_i = \int_0^{2\pi} \frac{[2\pi \Delta f_{ci} K_2 \cos(\omega_i t)]^2}{2\pi} d\omega_i t \text{ watts} \quad (57)$$

$$\begin{aligned} &= 2\pi K_2^2 (\Delta f_{ci})^2 \left[ \frac{\omega_i t}{2} + \frac{\sin 2\omega_i t}{4} \right]_0^{2\pi} \\ &= 2\pi^2 K_2^2 (\Delta f_{ci})^2 \end{aligned} \quad (58)$$

where  $\Delta f_{ci}$  is the peak carrier deviation due to the  $i^{\text{th}}$  channel TT.

Combining Equation 57 with Equation 56, TT-to-noise ratio,  $(TT/N)$ , in the  $i^{\text{th}}$  channel bandwidth,  $B_i$ , is found to be

$$\left(\frac{TT}{N}\right)_i = \left[ \frac{3B_{if}(\Delta f_{ci})^2}{2(f_{ubei}^3 - f_{lbei}^3)} \right] (CNR)_{if} \quad (59)$$

Equation 59 can be put into somewhat more tractable form by substituting for the channel band edge frequencies,  $f_{lbei}$  and  $f_{ubei}$ , as follows:

$$\begin{aligned} f_{ubei} &= f_i + \Delta f_i \\ f_{lbei} &= f_i - \Delta f_i \\ (f_{ubei}^3 - f_{lbei}^3) &= (f_i + \Delta f_i)^3 - (f_i - \Delta f_i)^3 \end{aligned} \quad (60)$$

where  $\Delta f_i$  is equal to half the channel bandwidth.

Expanding this identity gives

$$(f_{ubei}^3 - f_{lbei}^3) = 6\Delta f_i(f_i)^2 + 2(\Delta f_i)^3 \quad (61)$$

Since  $\Delta f_i$  is a small fraction of the channel frequency, Equation 61 can be simplified using

$$(f_{ubei}^3 - f_{lbei}^3) \approx 6\Delta f_i(f_i)^2 \quad \Delta f_i \ll f_i \quad (62)$$

which can be substituted into Equation 59 to give

$$\left(\frac{TT}{N}\right)_i = \left[ \frac{B_{if}(\Delta f_{ci})^2}{4\Delta f_i(f_i)^2} \right] (C/N)_{IF} \quad (63)$$

Since  $B_i = 2\Delta f_i$  is the bandwidth of the  $i^{\text{th}}$  channel, Equation 63 becomes

$$\left(\frac{TT}{N}\right)_i = \left[ \frac{B_{if}(\Delta f_{ci})^2}{2B_i(f_i)^2} \right] (C/N)_{IF} \quad (64)$$

This computation can be performed for each of the  $i$  channels, by substitution of the proper values of peak carrier deviation due to a particular channel, and its corresponding upper and lower predetection band edge frequencies. Figure II-6 shows a typical carrier postdetection situation for  $i$  channels.

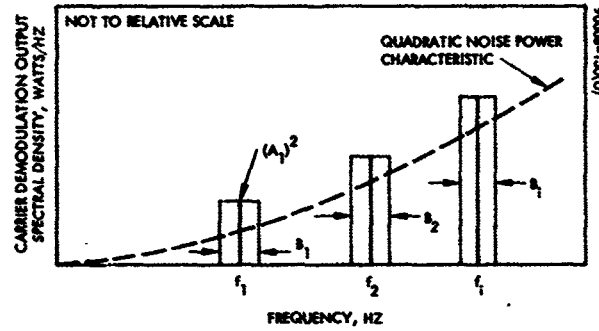


Figure II-6. Carrier Postdetection Spectrum With  $i$  Modulating Channels

### II-3. PRE-EMPHASIS

Figure II-6 also indicates a commonly encountered link characteristic, that of pre-emphasis. This pre-emphasis technique takes into account the quadratic output noise characteristic of the ideal carrier demodulator. In order to assure nearly simultaneous thresholding of each subcarrier channel, it is required that

$$(S/N)_{sc1} = (S/N)_{sc2} = \dots (S/N)_{sci} \quad (65)$$

Each subcarrier's amplitude (subcarrier/carrier modulation index) is adjusted so as to maintain the subcarrier predetection signal-to-noise ratio, i. e., the carrier demodulator output signal-to-noise ratio, constant. This indicates that subcarriers of increasing frequency require increasing amplitude levels.

Since the carrier demodulator output becomes the subcarrier demodulator input

$$\left(\frac{S}{N}\right)_{sci} = \left(\frac{T}{N'}\right)_i \quad (66)$$

Combining Equations 65 and 66, and Equation 63:

$$\frac{B_{IF}(\Delta f_{ci})^2}{4\Delta f_i (f_i)^2} = K \quad (\text{for all } i) \quad (67)$$

If the peak deviation of each subcarrier is identical, the following results

$$\Delta f_i = \text{constant} \quad (\text{for all } i) \quad (68)$$

Therefore

$$\left(\frac{\Delta f_{ci}}{f_i}\right)^2 = \frac{4\Delta f_i K}{B_{IF}} = K' \quad (69)$$

which shows that the peak deviation of the carrier due to the  $i^{\text{th}}$  subcarrier  $\Delta f_{ci}$  must be a function of the  $i^{\text{th}}$  subcarrier frequency  $f_i$ . This is implemented by amplifying the carrier baseband signal as a function of its frequency since the carrier modulation constant in rad/sec/volt is the same regardless of which subcarrier is doing the modulating. Thus the subcarrier/carrier modulation index is identical for all subcarriers, and is given by

$$\frac{\Delta f_{ci}}{f_i} = \beta = \text{subcarrier/carrier modulation index} \quad (70)$$

#### II-4. FM IMPROVEMENT VERSUS MODULATION INDEX

The TT-to-noise ratio in the  $i^{\text{th}}$  channel at the output of an FM discriminator is given by Equation 63 as:

$$\left(\frac{TT}{N'}\right)_i = \left[ \frac{B_{IF}(\Delta f_{ci})^2}{4\Delta f_i (f_i)^2} \right] (C/N)_{IF} \quad (71)$$

The FM improvement due to the carrier discriminator is

$$I_{FM} = \left(\frac{TT}{N'}\right)_i / (C/N)_{IF} \quad (72)$$



From Equations 71 and 72, and Equation 70:

$$I_{FM} = \frac{B_{IF}}{4\Delta f_i} \beta^2 \quad (73)$$

From Carson's Rule the predetection bandwidth is

$$B_{IF} = 2(f_h + \Delta f_c) \quad (74)$$

where  $f_h$  is the highest modulating frequency (modulating  $f_c$ ) and  $\Delta f_c$  is the peak carrier deviation due to all the subcarriers. For  $n$  sub-carrier channels each one  $2\Delta f_i$  wide and placed next to each other in the carrier baseband, the highest frequency is

$$f_h = 2n\Delta f_i \quad (75)$$

The peak carrier deviation  $\Delta f_c$  is the sum of deviations due to the individual subcarriers:<sup>8</sup>

$$\Delta f_c = \sum_{i=1}^n \Delta f_{ci} = \sum_{i=1}^n \beta f_i = \beta \sum_{i=1}^n f_i \quad \text{for } n < 7 \quad (76)$$

From Equations 74, 75, and 76:

$$B_{IF} = 2 \left( 2n\Delta f_i + \beta \sum_{i=1}^n f_i \right) \quad (77)$$

If the subcarrier channels are placed next to each other in the carrier baseband, and the subcarrier frequencies,  $f_i$ , are at the center of each channel these frequencies can be represented as

$$f_i = (2i - 1) \Delta f_i \quad (78)$$

---

<sup>8</sup>This is true for  $n < 7$ . For  $n \geq 7$  see Section II-5.

and Equation 77 becomes

$$B_{IF} = 2 \left( 2n \Delta f_i + \beta \sum_{i=1}^n (2i - 1) \Delta f_i \right) \quad (79)$$

$$B_{IF} = \Delta f_i \left[ 4n + 2\beta \sum_{i=1}^n (2i - 1) \right] \quad (80)$$

Combining Equations 73 and 80

$$I_{FM} = \frac{\Delta f_i \left[ 4n + 2\beta \sum_{i=1}^n (2i - 1) \right]}{4\Delta f_i} \beta^2 \quad (81)$$

$$I_{FM} = \left[ n + \frac{\beta}{2} \sum_{i=1}^n (2i - 1) \right]^2 \beta^2 \quad \text{for } n < 7 \quad (82)$$

## II-5. PEAKING FACTORS

A peaking factor  $P$  relates peak carrier deviation  $\Delta f_{cp}$  to rms carrier deviation  $\Delta f_{c_{rms}}$ :

$$\Delta f_{cp} \cong P \Delta f_{c_{rms}} \quad (83)$$

The rms deviation of the carrier due to all the subcarriers is the root-sum-square of the rms carrier deviations due to the individual subcarriers. Thus,

$$\Delta f_{c_{rms}} = \sqrt{\sum_{i=1}^n \left( \Delta f_{ci_{rms}} \right)^2} \quad (84)$$

If it is assumed that the modulating subcarriers are sinusoidal

$$\Delta f_{ci_{rms}} = \frac{\Delta f_{ci}}{\sqrt{2}} \quad (85)$$

Equations 84 and 85:

$$\Delta f_{c_{rms}} = \sqrt{\sum_{i=1}^n \frac{(\Delta f_{ci})^2}{2}} \quad (86)$$

Up to now there has been no restriction on  $n$ . But for a small number of subcarriers  $n$  (usually  $n < 7$ ) the peak carrier deviation is merely the sum of the peak deviations due to the individual subcarriers. This is true if the subcarriers are independent. Thus,

$$\Delta f_{cp} = \sum_{i=1}^n \Delta f_{ci} \quad \text{for } n < 7 \quad (87)$$

This indicates the possibility that the  $n$  subcarriers could all peak simultaneously.

From Equations 83, 86, and 87:

$$F = \frac{\Delta f_{cp}}{\Delta f_{c_{rms}}} = \frac{\sum_{i=1}^n \Delta f_{ci}}{\sqrt{\sum_{i=1}^n \frac{(\Delta f_{ci})^2}{2}}} \quad \text{for } n < 7 \quad (88)$$

Thus for a small number of subcarriers, the peaking factor is a function of the peak deviation the carrier due to the individual subcarriers.

## II-6. ANTENNA EQUIVALENT NOISE TEMPERATURE CAUSED BY SUN

An antenna beam intercepts an energy source at temperature  $T_S$  as shown in Figure II-7. If the antenna beam solid angle  $\Omega_A$  is completely covered by the source solid angle  $\Omega_S$ , then by thermal equilibrium considerations the equivalent noise temperature of the antenna  $T_A$  is given by

$$T_A = T_S \quad \text{for } \Omega_S \geq \Omega_A \quad (91)$$

But if the antenna beam solid angle is greater than the source solid angle

$$T_A = \frac{\Omega_S}{\Omega_A} T_S \quad \text{for } \Omega_S < \Omega_A \quad (92)$$

where

$T_S$  = source temperature, °K

$T_A$  = antenna equivalent noise temperature, °K

$\Omega_S$  = source solid angle, radians<sup>2</sup>

$\Omega_A$  = antenna beam solid angle, radians<sup>2</sup>

In the RF region of the spectrum, the Rayleigh Jeans Law, Equation 93, equates the brightness of an energy source and its temperature:

$$b = \frac{2kT_S}{\lambda^2} \quad (93)$$

$$T_S = \frac{b\lambda^2}{2k} \quad (94)$$

where

$b$  = brightness, watts meter<sup>-2</sup> Hertz<sup>-1</sup> radian<sup>-2</sup>

$k$  = Boltzmann's constant ( $1.38 \times 10^{-23}$  joule °K<sup>-1</sup>)

$T_S$  = temperature, °K

$\lambda$  = wavelength, meters

For a large number of subcarriers (usually taken to be  $n \geq 7$ ), the problem becomes a statistical one. The largest possible (i. e., worst-case) deviation of the carrier would occur when all the subcarriers peak simultaneously. But as  $n$  increases, the probability of all subcarriers peaking simultaneously decreases rapidly. Thus,

$$\Delta f_{cp} < \sum_{i=1}^n \Delta f_{ci} \quad \text{for } n \geq 7 \quad (89)$$

And, from Equations 83, 86, and 89:

$$P < \frac{\sum_{i=1}^n \Delta f_{ci}}{\sqrt{\sum_{i=1}^n \frac{(\Delta f_{ci})^2}{2}}} \quad \text{for } n \geq 7 \quad (90)$$

Values of  $P$  for  $n \geq 7$  can be determined by statistical methods where the ensemble of the subcarriers is modeled as a Gaussian random process of zero mean and three-sigma value of  $\pm 1$ . Previous work (Reference 1) has assumed a peaking factor of  $P = 10$  dB.

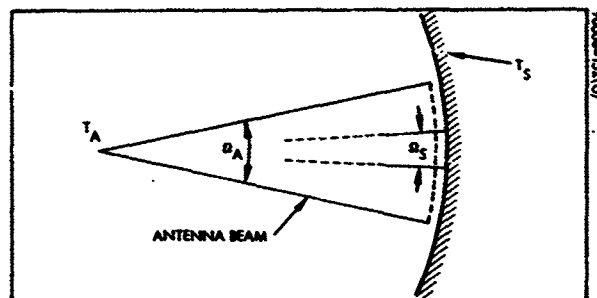


Figure II-7. Antenna and Energy Source

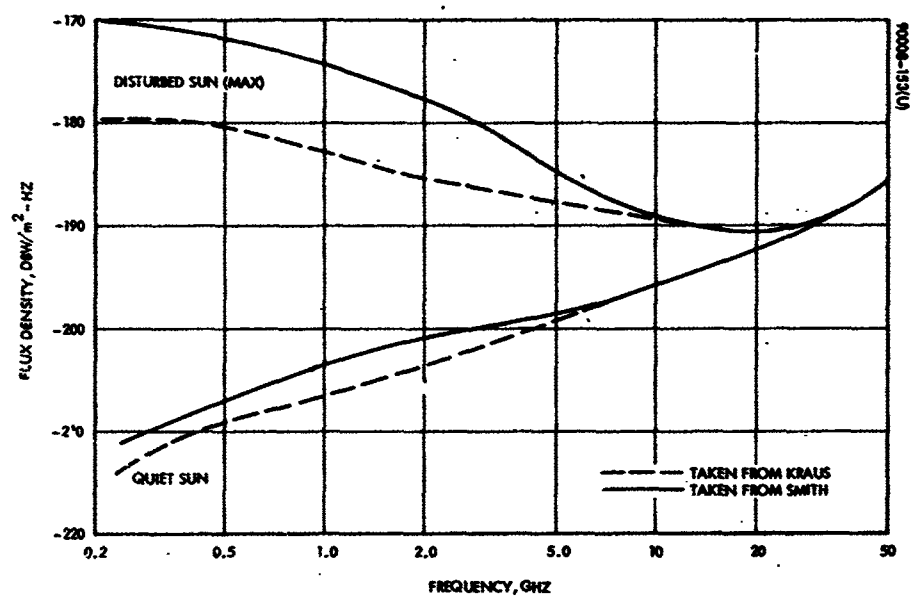


Figure II-8. Solar Radiation Flux Density Versus Frequency

The brightness of a source and flux density radiated by it are related by

$$S = b \Omega_s \quad (95)$$

where

$$S = \text{flux density, watts meter}^{-2} \text{ Hertz}^{-1}$$

From Equations 94 and 95

$$T_s = \frac{S \lambda^2}{2k \Omega_s} \quad (96)$$

From Equations 92 and 96

$$T_A = \frac{\Omega_s}{\Omega_A} T_s = \frac{S \lambda^2}{2k \Omega_A} \quad \text{for } \Omega_s < \Omega_A \quad (97)$$

The antenna beam solid angle is related to its effective aperture by

$$A = \frac{\lambda^2}{A_e} \quad (98)$$

where

$$A_e = \text{effective aperture, square meters}$$

From Equations 97 and 98

$$T_A = \frac{S A_e}{2k} \quad \text{for } \Omega_s < \Omega_A \quad (99)$$

Figure II-8 presents the flux density,  $S$ , of solar radiation as a function of frequency (curves as taken from References 2 and 3). Equation 99 can be used to convert flux density,  $S$ , into antenna equivalent noise temperature if the antenna beam solid angle is greater than source solid angle (0.5 degree for the sun). For example, Equation 99 can be used in conjunction with a 30-foot parabolic antenna only for frequencies less than about 5 GHz. At frequencies above 5 GHz, the antenna beam solid angle is less than 0.5 degree, and the equivalent noise temperature falls off at an additional 20 dB per decade.

## II-7. GLOSSARY

$B_{if}$	Carrier predetection equivalent noise bandwidth, Hz
$B_i$	Equivalent noise bandwidth of $i^{th}$ channel, Hz
$f_c$	Carrier center frequency, Hz = $\omega_c/2\pi$
$f_i$	Center frequency of $i^{th}$ channel, Hz
$\left. \begin{matrix} f_{lbe} \\ f_{ube} \end{matrix} \right\}$	Lower band edge and upper band edge frequency of $i^{th}$ channel, Hz
$f_m$	Carrier-modulating video baseband, Hz
$\Delta f_i$	Peak deviation of $i^{th}$ subcarrier or half the $i^{th}$ channel bandwidth, Hz
$\Delta f_{ci}$	Peak carrier deviation due to $i^{th}$ channel, Hz
$\Delta f_{ci}/f_i$	Modulation index of $i^{th}$ channel-carrier, Hz
$\left(\frac{TT}{N}\right)_i$	Test-tone-to-noise ratio in $i^{th}$ channel bandwidth
$(C/N)_{IF}$	IF carrier predetection SNR
$(SNR)_o$	Video postdetection SNR
$\eta_c$	Noise spectral density, watts/Hz, in carrier predetection bandwidth
$K_1$	Carrier modulator constant, radians/volt
$K_2$	Carrier demodulator constant, volts/radian
$A_c$	Peak carrier amplitude, volts
$A_L$	Peak carrier amplitude after limiting, volts
$A_m$	Peak modulating signal amplitude, volts
$s(t)$	General data signal, of frequency $\omega_m$



## II. 8 REFERENCES

1. Charles Cote, Paul Heffernan, George Hogan, and Charles Laughlin, A Proposal for a Technological Experiment Nimbus-E Data Relay Link Through ATS-F, Goddard Space Flight Center, Greenbelt, Maryland, March 1968.
2. J.D. Kraus, Radio Astronomy, McGraw-Hill, 1966.
3. A.G. Smith, "Extraterrestrial Noise as a Factor in Space Communications," Proceedings of IRE, April 1960, pp. 593-599.

### APPENDIX III. GRAVITY-GRADIENT TORQUES

Consider a general body whose center of mass is a distance  $r$  from the center of the earth as shown in Figure III-1. The force on an element of mass in the body is given by:

$$d\bar{F} = - \frac{G}{R^3} dm \bar{R} \quad (1)$$

where the bar above the letter denotes a vector and the letter alone denotes the magnitude.  $G = 9.563 \times 10^4 \text{ miles}^3/\text{sec}^2$  is the gravitational constant for the earth. From Figure III-1

$$\bar{R} = \bar{r} + \bar{\rho} \quad (2)$$

and by the law of cosines:

$$R^2 = r^2 + \rho^2 + 2(\bar{r} \cdot \bar{\rho}) = r^2 \left[ 1 + \frac{\rho^2}{r^2} + 2 \frac{(\bar{r} \cdot \bar{\rho})}{r^2} \right] \quad (3)$$

Substituting Equations 2 and 3 in 1

$$d\bar{F} = - \frac{G (\bar{r} + \bar{\rho})}{r^3 \left[ 1 + \frac{\rho^2}{r^2} + 2 \frac{(\bar{r} \cdot \bar{\rho})}{r^2} \right]^{3/2}} dm \quad (4)$$

The moment about the center of mass due to the force on an element of mass is given by

$$d\bar{M}_g = \bar{\rho} \times d\bar{F} \quad (5)$$

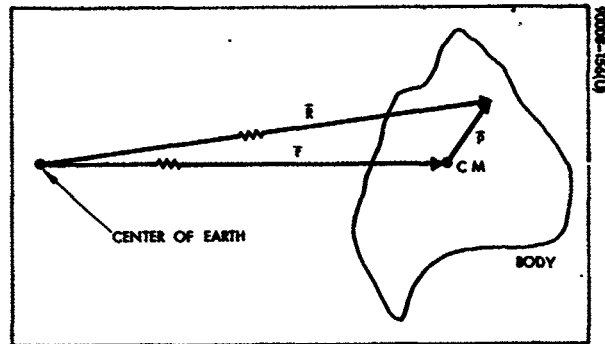


Figure III-1. General Gravity-Gradient Geometry

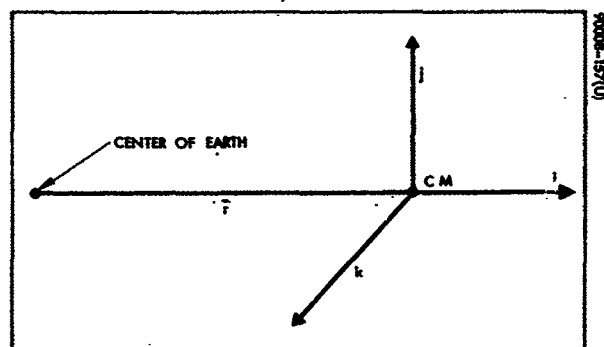


Figure III-2. Orbital Coordinates

Now, expanding the denominator expression of Equation 4 in a Taylor's series, and keeping terms of the order of  $\rho/r$ , the following results

$$\left[ 1 + \frac{\rho^2}{r^2} + 2 \frac{(\bar{r} \cdot \bar{\rho})}{r^2} \right]^{-3/2} \approx 1 - 3 \frac{\bar{r} \cdot \bar{\rho}}{r^2} \quad (6)$$

This is a good approximation, since for an LAS  $\rho/r < 10^{-6}$ .

From Figure III-2 it can be seen that

$$\frac{\bar{r}}{r} = e_i \quad (7)$$

where the letter e denotes a unit vector and the subscript denotes the direction.

Substituting Equations 6 and 7 into 5 the following results

$$d\bar{M}_g = - \frac{G}{r^2} \left[ 1 - 3 \frac{e_i \cdot \bar{\rho}}{r} \right] \left[ \bar{\rho} \times \left( e_i + \frac{\bar{\rho}}{r} \right) \right] dm \quad (8)$$

By definition of the vector product

$$\bar{\rho} \times \bar{\rho} = 0$$

thus Equation 8 becomes:

$$dM_g = - \frac{G}{r^2} \left( 1 - 3 \frac{e_i \cdot \bar{\rho}}{r} \right) (\bar{\rho} \times e_i) dm \quad (9)$$

Now express  $\bar{\rho}$  in terms of the body coordinates defined in Section 3.6

$$\begin{aligned} \bar{\rho} &= x e_x + y e_y + z e_z \\ \rho^2 &= x^2 + y^2 + z^2 \end{aligned} \quad (10)$$

From Section 3.6, Equation 52,

$$\begin{pmatrix} e_i \\ e_j \\ e_k \end{pmatrix} = A \begin{pmatrix} e_x \\ e_y \\ e_z \end{pmatrix} \quad (11)$$

Using Equations 10 and 11,

$$\begin{aligned} e_i \cdot \bar{\rho} &= (a_{11}e_x + a_{12}e_y + a_{13}e_z) \cdot (xe_x + ye_y + ze_z) \\ &= a_{11}x + a_{12}y + a_{13}z \\ \bar{\rho} \times e_i &= \begin{vmatrix} e_x & e_y & e_z \\ x & y & z \\ a_{11} & a_{12} & a_{13} \end{vmatrix} \\ &= (a_{13}y - a_{12}z)e_x + (a_{11}z - a_{13}x)e_y + (a_{12}x - a_{11}y)e_z \end{aligned}$$

$$\begin{aligned} (e_i \cdot \rho)(\rho \times e_i) &= (a_{11}a_{13}xy - a_{11}a_{12}xz + a_{12}a_{13}y^2 - a_{12}^2yz \\ &\quad + a_{13}^2yz - a_{12}a_{13}z^2)e_x + (a_{11}^2xz - a_{11}a_{13}x^2 \\ &\quad + a_{11}a_{12}yz - a_{12}a_{13}xy + a_{11}a_{13}z^2 - a_{13}^2xz)e_y \\ &\quad + (a_{11}a_{12}x^2 - a_{11}^2xy + a_{12}^2xy - a_{11}a_{12}y^2 \\ &\quad + a_{12}a_{13}xz - a_{11}a_{13}yz)e_z \end{aligned} \quad (12)$$

Integrating Equation 9, the following results

$$\bar{M}_g = -\frac{G}{r^2} \left[ \int (\bar{\rho} \times e_i) dm - \frac{3}{r} \int (e_i \cdot \bar{\rho}) (\bar{\rho} \times e_i) dm \right] \quad (13)$$

If the x, y, z axes are principal axes of inertia with origin at the center of mass, then:

$$\int x dm = \int y dm = \int z dm = 0 \quad (14)$$

$$\int xy dm = \int xz dm = \int yz dm = 0 \quad (15)$$

Then

$$\int (\bar{\rho} \times e_i) dm = 0 \quad (16)$$

Substituting Equations 12, 14, 15, and 16 into Equation 13, the expression for the gravity-gradient torque on the body is obtained:

$$\begin{aligned} \bar{M}_g = \frac{3G}{r^3} \int & \left[ a_{12} a_{13} (y^2 - z^2) e_x + a_{11} a_{13} (z^2 - x^2) e_y \right. \\ & \left. + a_{11} a_{12} (x^2 - y^2) e_z \right] dm \end{aligned} \quad (17)$$

By definition of the moments of inertia

$$I_x = \int (y^2 + z^2) dm$$

$$I_y = \int (x^2 + z^2) dm$$

$$I_z = \int (x^2 + y^2) dm$$

Thus,

$$\begin{aligned}
 \int (y^2 - z^2) dm &= \int \left[ (y^2 + x^2) - (x^2 + z^2) \right] dm = I_z - I_y \\
 \int (z^2 - x^2) dm &= \int \left[ (y^2 + z^2) - (x^2 + y^2) \right] dm = I_x - I_z \\
 \int (x^2 - y^2) dm &= \int \left[ (x^2 + z^2) - (y^2 + z^2) \right] dm = I_y - I_x
 \end{aligned} \tag{18}$$

Now, from Section 3.4, Equation 15

$$\omega_o^2 = \frac{G}{r^3} \tag{19}$$

Substituting Equations 18 and 19 into Equation 17

$$M_{gx} = 3\omega_o^2 (I_z - I_y) a_{12} a_{13} \tag{20}$$

$$M_{gy} = 3\omega_o^2 (I_x - I_z) a_{11} a_{13} \tag{21}$$

$$M_{gz} = 3\omega_o^2 (I_y - I_x) a_{11} a_{12} \tag{22}$$

The matrix elements  $a_{ij}$  are given in Equation 52 of Section 3.6 from which it can be seen that Equations 20 through 22 involve sums and differences of products of trigonometric functions of the Euler angles defined in Section 3.6.